Analytical Modelling of the Plastic Response of Thin Plates Under Impulsive Near-Field Blast Loadings

Saud Ayed Eid Alotaibi

This thesis is submitted for partial consideration towards the degree of Doctor of Philosophy in

The Department of Civil and Structural Engineering

at the University of Sheffield

15th July, 2024

dedicated to my father

my mother

my wife

my sons—Nawaf, Fahad & Salman

. . .

you are my world

Declaration

I, Saud Ayed Eid Alotaibi, certify that all the material contained within this thesis is my own work, except where it is clearly referenced to others. 15^{th} July, 2024.

Abstract

There has been significant scientific interest in studying the response of structures when subjected to extreme dynamic loading events such as blast and impact. Over the past three decades, there has been a rise in the number of explosion incidents globally. These often involve deliberate attacks where terrorists use high explosives to cause harm to civilians and public infrastructure through devastating blast waves. Blast loads from explosions can cause loss of human lives or severe injuries due to either the direct exposure of people to blast waves and/or as consequences of partial or overall collapse of structures, or their key structural elements. Through experiments, it is observed that the resulting deformations of structures under blast loadings are mainly plastic, and the magnitudes associated with typical blasts are found to exceed, by far, the quasi-static ultimate capacities of practical civilian structures. Furthermore, blasts from detonations of high explosives at close-in distances from the structures (called near-field blasts) are found to be highly transient and spatially non-uniform. This poses challenges to the structural engineering community that is required to provide reliable designs to protect the public and vital structures from such rising unconventional loading conditions. Most of the existing analytical techniques are either inapplicable or less accurate when the explosive threat corresponds to a near-field blast loading. Due to the high variability and sensitivity of the blast load to changes in the explosive threat's input variables, the utilisation of commercially available numerical tools (e.g., hydrocodes and sophisticated finite element solvers) is less attractive to practising blast engineers in the early phase of design due to their substantial computational costs. The present study focuses on developing a physically based and simple model to predict the plastic response of thin plates when subjected to near-field blasts so that it is fast-running and hence can be made available to practising blast engineers. The developed model is based on three idealising assumptions: the blast load is impulsive; the thin plate's material is rigid-perfectly plastic according to von Mises's criterion of yielding; and the plate responds in a pure membrane (or catenary) mode. These assumptions are necessarily taken to deem the ultimate model simple and easy to run, and they are considered reasonable based on a detailed review of the relevant literature. The model's accuracy is validated by comparisons to real experiments performed by others and high-fidelity finite element simulations performed by the author using LS-DYNA. The model is found reasonably accurate and provides additional insights on the response of thin targets to typical near-field blast loading.

Acknowledgements

I extend my deepest gratitude to Allah, the Lord of all worlds, for the strength and wisdom bestowed upon me.

My heartfelt thanks go to my supervisors, Professor Andrew Tyas, Dr Samuel Edward Rigby, and Dr Maurizio Guadagnini, for their invaluable guidance and trust throughout my research journey. Their expertise has been pivotal in enhancing my approach to engineering and research challenges, turning my work into a tangible achievement. I also express my appreciation to all members of the Blast and Impact Dynamics Research Group at the University of Sheffield for their unwavering support.

Special thanks to my father, Mr. Ayed Eid Khodher ibn Mobhij Alotaibi, whose steadfast support and sage wisdom have been the guiding stars of my journey. His belief in my abilities has been a constant source of motivation, leading me to this moment of accomplishment. I am eternally grateful for his sacrifices and love.

I am equally grateful to my mother, Mrs. Omaima Alotaibi, my beloved wife, Mrs. Maram Alotaibi, and my sons, Nawaf, Fahad, and Salman. Their enduring love and support have been my foundation during the most challenging phases of my PhD study and throughout my life.

My acknowledgements would be incomplete without mentioning the Department of Civil and Structural Engineering at the University of Sheffield for their exceptional research facilities and professional development support.

I extend my thanks to my sponsors, Qassim University, Saudi Arabia, the Saudi Arabian Cultural Bureau in the United Kingdom, and the Royal Embassy of Saudi Arabia in London for their generous financial and academic assistance.

Lastly, I am grateful to my all my colleagues and friends, whose support and insights have greatly contributed to my academic journey. Thank you for the shared wisdom and cherished moments that have shaped my path.

Thank you all, and all praise to Allah, the Lord of all worlds.

Contents

Declaration i
Abstract iii
Acknowledgements v
Contents vii
List of Figures xi
List of Tables xvii
Nomenclature xix
Acronyms and Abbreviations xxv

1 Introduction 1
1.1 Overview . . . 1
1.2 Motivations . . . 4
1.3 Intellectual Contribution . . . 7
1.3.1 Relevant Background . . . 7
1.3.2 Contribution by the Present Work . . . 8
1.4 Aims of the Thesis . . . 10

2 Literature Review 11
2.1 The Blast Loading . . . 11
2.1.1 Explosion . . . 11
2.1.2 Incident Blast Wave . . . 11
2.1.3 Blast Scaling Law . . . 12
2.1.4 TNT Equivalence of an Explosive . . . 14
2.1.5 Reflected Blast Wave . . . 14
2.1.6 Oblique Reflection . . . 16
2.1.7 Blast Clearing . . . 16
2.1.8 Blast Loading . . . 18
2.1.9 Blast Loading Characterisation . . . 20
2.1.10 Limitations of Available Fast-Running Blast Loading Models . . . 25
2.2 Response of Structures to Blast Loadings . . . 26
2.2.1 Overview . . . 26
2.2.2 Basis of the Main Analytical Technique . . . 28
2.2.3 Analytical Models . . . 29

2.2.4 Experimental Results . . . 33
2.2.5 Connection of the Near-Field Blast Loading to the Response of Structures . 34
2.2.6 Aims of the Present Study . . . 36
2.3 Summary . . . 37

3 Membrane Model **39**
3.1 Overview . . . 39
3.2 Structural Context of the Simple Membrane . . . 39
3.3 General Equilibrium Equations . . . 45
3.3.1 Overview . . . 45
3.3.2 A General Membrane . . . 46
3.3.3 A Simple Membrane . . . 47
3.3.4 Discussion . . . 47
3.4 Basic Review of Von Mises Plasticity . . . 50
3.4.1 Conditions Under Which $\varepsilon_{ij} = \lambda s_{ij}$ Holds . . . 53
3.5 Equilibrium Equation of a Simple Membrane Made of a Rigid-Perfectly Plastic Von Mises Material . . . 56
3.5.1 Discussion . . . 58
3.6 Deriving the Equilibrium Equation Using the Virtual Work . . . 59
3.6.1 Internal Virtual Work . . . 59
3.6.2 Total Virtual Work . . . 61
3.6.3 The Equilibrium Equation . . . 62
3.7 Implications of $\varepsilon_{ij} = \lambda s_{ij}$ on the Validity of the Solution . . . 63
3.8 Implications of $\varepsilon_{ij} = \lambda s_{ij}$ on the Stress State of the Simple Membrane . . . 65
3.8.1 Determination of Stress States for Special Cases of the In-Plane Strains . . 67
3.8.2 Principal Stresses for the General Strain Case . . . 71
3.8.3 Principal Directions for the General Strain Case . . . 75
3.8.4 Remarks on the Determination of the Stress States . . . 78
3.9 A Simplified Example of an Impulsively Loaded Simple Membrane . . . 79
3.9.1 General . . . 79
3.9.2 Membrane's Response Under Specific Impulse That Is Proportional to the First Mode Shape . . . 81
3.9.3 Determination of the Critical Time Instant . . . 81
3.9.4 Directions of the Principal Stresses . . . 83
3.9.5 Comparison of the First Mode Analytical Solution to a Numerical Solution Using LS-DYNA . . . 91

4 Validation of the Uniform Model **97**
4.1 Note . . . 97
4.2 Overview . . . 97
4.3 Theory . . . 98
4.3.1 Problem Definition . . . 98

4.3.2 Development of the Equation of Motion 99
4.4 Rectangular Membranes 103
4.4.1 Response of Rectangular Membranes 103
4.4.2 Uniform Specific Impulse Case (Rectangular Membrane) 105
4.5 Circular Membranes 107
4.5.1 Response of Circular Membranes 107
4.5.2 Uniform Specific Impulse Case (Circular Membrane) 108
4.6 Uniform Model Verification 109
4.6.1 Rectangular Membrane 109
4.6.2 Circular Membrane 113
4.6.3 Comparison of the Uniform Models to the Modified Nurick and Martin's Model 118
4.7 Overall Limitations and the Theory Drawbacks 120
4.8 Summary and Conclusions 120

5 Validation of the Non-Uniform Model 123
5.1 Background and Preamble 123
5.2 Introduction 125
5.3 Description of LS-DYNA Models 126
5.3.1 MM-ALE Set-Up 126
5.3.2 Lagrangian Only Set-Up 127
5.3.3 Summary of the ALE Method 130
5.3.4 Material and Equation of State (EOS) Models in LS-DYNA 136
5.4 The Non-Uniform Model Versus LS-DYNA 142
5.5 The Non-Uniform Model and LS-DYNA Predictions Versus Explosive Plate Experiments 145
5.6 Additional Analysis Results from LS-DYNA Simulations 148
5.7 Summary and Conclusions 159

6 Discussion 167
6.1 Overview of the Work 167
6.2 Notes on the Model's Applicability 168
6.3 On the Definition of the Near-Field Blast Loading and Its Non-Uniformity 173
6.4 Solutions for Irregularly Shaped Targets 174
6.5 The Two Solution Termination Strategies and the Solution Termination Dilemma . 177
6.6 On the Local Plastic Strain Distribution 182
6.7 Practical Engineering Applications of the Model 187

7 Summary and Conclusions 189
7.1 Conclusions 189
7.2 Final Remarks and Future Work 193

References 197

Appendices **211**

A Alternative Approach to Derive the Equilibrium Equation for the Rectangular Simple Membrane **211**

B Axi-Symmetric Membranes and the In-Plane Displacement Effect **215**

B.1 Axi-Symmetric Circular Membranes 215

B.1.1 Overview and the Problem Definition 215

B.1.2 Membrane Strains 216

B.1.3 Equilibrium Equations for a General Membrane 216

B.1.4 Equilibrium Equation for a Simple Membrane 217

B.2 In-Plane Displacement Effect 218

B.2.1 Cloete and Nurick's Case of Axi-symmetric Membranes 218

B.2.2 Extension of the Cloete and Nurick's Result 222

B.2.3 A General Membrane in Which $\sigma_1 = \sigma_2$ 230

C Assessment of the Error Due to Series Truncation **233**

D A Practical Method to Compute I_{mn} for Rectangular Membranes **237**

E Effect of Work-Hardening on the Response of an SDOF and a 2D Steel Plate **241**

E.1 Forced Response - SDOF 241

E.2 Impulsive Response - SDOF 243

E.3 Plate Response Using LS-DYNA 247

F MATLAB Function to Read LS-DYNA's binout Files **251**

F.1 Overview 251

F.2 Additional Functionality 253

F.3 Performance Remarks 253

F.4 Source Code of the MATLAB Function 254

G Illustration of the Solution Termination for a Rigid-Perfectly Plastic SDOF **255**

G.1 Overview 255

G.2 Problem Definition 255

G.3 Solution 257

G.4 Discussion 258

G.5 Systematic Derivation of the Non-Linear Equilibrium Equation of the SDOF . . . 259

List of Figures

2.1 Typical blast wave 17

2.2 Reflected peak overpressure versus distance. This is the trace of the peak reflected overpressures at different distances (or equivalently, for a fixed explosive charge, scaled distances) 17

2.3 Typical spatial variations of the positive phase blast parameters, associated with a typical near-field blast problem, over the surface of a rigid target . . 19

2.4 Reflected scaled blast parameters of a free air (spherical) blast wave 21

2.5 Incident scaled blast parameters of a free air (spherical) blast wave 22

2.6 Non-uniform specific impulse distribution (a) and the generated profile of initial velocity assuming a lower-bound (b) and an upper-bound (c) kinetic energy uptake, reproduced after Tyas and Pope (2003) 33

3.1 Qualitative classification of kinematic theories applicable for different plate-like structures 45

3.2 A generic Mohr's circle for plane-stress 69

3.3 Von Mises yield curve in the in-plane principal stress σ_1-σ_2 space 74

3.5 Trajectories of the first principal stress $\sigma_1 = 2/(\sqrt{3})\sigma_0$. The membrane is square, $k_y/k_x = L_x/L_y = 1$, of side length $L_x = 1$ 87

3.6 Combined trajectories (curves) of the first principal stress $\sigma_1 = 2/(\sqrt{3})\sigma_0$ (blue solid lines) and the second principal stress $\sigma_2 = (1/2)\sigma_1$ (black dashed lines) 89

3.7 A numerical representation of the directions of principal shear stresses, $\tau_{max} = \pm 1/(2\sqrt{3})\sigma_0$ 91

3.8 Trajectories of the principal shear stresses, $\pm\tau_{\max}$, which were obtained by solving the differential equation $dy/dx = \tan(\theta \pm \pi/4)$, where θ is the direction of the principal normal stress σ_1 92

3.9 Measuring the resemblance of the transverse displacement profile, $w(x, y, t)$, as predicted by LS-DYNA and the shape of the first mode, $\phi_{1,1}(x, y) = \phi_1(x, y)$, which solves the equilibrium equation predicted by the analytical model 94

3.10 Transient central displacement $w_c \equiv w(L_x/2, L_y/2, t)$ as predicted by the present model and LS-DYNA associated with the first mode solution 95

4.1 Problem definitions for the rectangular membrane: (a) plan view showing undeformed geometry and (b) side view showing a typical spatial distribution of specific impulse i. 99

4.2 Permanent displacement profile for rectangular membrane under three sets of impulses of constant amplitudes applied over central rectangular regions with loaded-to-total area ratios of (1) 0.062, (2) 0.25, and (3) 1.0 105

4.3 The converged value of truncated sum, S_0, for the rectangular membrane associated with uniform impulse case as a function of the membrane aspect ratio, L_y/L_x, where $L_y \leq L_x$. 106

4.4 Permanent displacement profile of an axi-symmetric circular membrane subjected to a uniform impulse which is applied over a localised region (1) with a loaded-to-total area ratio of 0.062 and over the whole area (2) of the membrane as predicted by the present solution. 108

4.5 Comparison of model predictions to experimental data (Nurick et al., 1985) in terms of central residual displacement w_c of rectangular and square membranes under uniform impulse of total magnitude of I_0. 110

4.6 Comparison of model predictions to experimental data (Nurick et al., 1985) and LS-DYNA numerical results in terms of central residual displacement w_c of (a) rectangular and (b) square membranes under uniform impulse of total magnitude of I_0 111

4.7 Comparison of model predictions to experimental data (Nurick et al., 1985) and LS-DYNA results in terms of central residual displacement w_c of circular membranes under uniform impulse of total magnitude of I_0. 114

4.8 Comparison of model predictions to experimental data (Gharababaei and Darvizeh, 2010) and LS-DYNA results in terms of central residual displacement w_c of circular membranes under uniform impulse. 115

4.9 Comparison of model predictions to results from LS-DYNA simulations corresponding to the experimental set-ups in Gharababaei and Darvizeh (2010) and Nurick et al. (1985) in terms of central residual displacement w_c of circular membranes under uniform impulse of total magnitude of I_0. . . . 116

4.10 Comparison of model predictions to experimental data (Nurick et al., 1996) in terms of central residual displacement w_c of circular membranes under uniform impulse of total magnitude of I_0. 116

4.11 Time history of the central displacement w_c from LS-DYNA simulation for a sample problem using input parameters given in Rigby et al. (2019a). . . 117

4.12 Comparison of model predictions to LS-DYNA results in terms of central residual displacement w_c of circular membranes under uniform impulse of total magnitude of I_0, in which the input parameters were taken from the parametric study in Rigby et al. (2019a). 118

5.1 Validation results for the prediction of specific impulse distribution, $i(r)$, using the MM-ALE method in LS-DYNA for a spherical PE4 charge of mass 100 [g] and clear stand-off distance of 55.4 [mm]. The numerical specific impulse (MM-ALE (2D)) is compared to the experimentally measured specific impulse by Rigby et al. (2019). 128

5.2 Preliminary mesh convergence analysis for a rectangular membrane problem. A mesh of 64 elements along each direction was chosen based on this analysis. 129

5.3 Comparisons of the model predictions to LS-DYNA results for rectangular membranes in terms of the central displacements, w_c, versus the energy-equivalent total impulse, I_k. 144

5.4 Comparisons of the model predictions to LS-DYNA results for circular membranes in terms of the central displacements, w_c, versus the energy-equivalent total impulse, I_k. 144

5.5 Explosive testing matrix of Curry and Langdon (2017) and their associated energy-equivalent total impulses (as predicted by the MM-ALE analyses in LS-DYNA) and the average values of the experimentally measured total impulses. 146

5.6 Area-integrated total impulses from LS-DYNA MM-ALE simulations (I_{dyna}) and Curry and Langdon (2017) experiments (I_{exp}) versus the equivalent impulses, I_k. 146

5.7 Experimental validation of model predictions for circular membranes in terms of the central displacements, w_c, versus equivalent impulse, I_k. The Model and LS-DYNA predictions are compared to the experimental data of Curry and Langdon (2017). 147

5.8 Numerically predicted (from MM-ALE LS-DYNA) specific impulse profiles that were generated from the detonations of cylindrical explosive charges. . 150

5.9 Residual (or permanent) deformed profiles, $w_p(r)$, of impulsively loaded circular targets as predicted by purely Lagrangian structural analyses in LS-DYNA. The targets were loaded by near-field blasts associated with non-uniform specific impulses. 151

5.10 Von Mises stress, σ_{e}, versus effective plastic strain, $\varepsilon_{\mathrm{e}}^{p}$, curves as deduced from the results of circular membrane responses under non-uniform specific impulses. The von Mises stresses and effective plastic strains correspond to the most stressed elements for each blast experiment. 152

5.11 Profiles of the von Mises stress, σ_{e}, versus the radial coordinate, r, of the circular membranes. The von Mises stress at a given point, r, is the average of the corresponding von Mises versus time curve at that point; the averaging is performed by time integration. 154

5.12 Time histories of the central transverse displacements, $w_c(t)$, of circular membranes loaded by non-uniform specific impulses. The impulses were generated from earlier explosive MM-ALE experiments in LS-DYNA. 155

5.13 Deformed profiles of a circular thin plate due to an impulsive near-field blast corresponding to a spherical PE4 explosive with a mass of 75 [g] and detonated at a clear stand-off distance (measured from the plate's centre) of 35 [mm]. Shown are the profiles predicted by the analytical model (based on the total solution termination strategy) and the corresponding ones from a purely Lagrangian LS-DYNA simulation. 157

5.14 Evolution of total kinetic energy of a circular thin plate due to an impulsive near-field blast corresponding to a spherical PE4 explosive with a mass of 75 [g] and a clear stand-off distance (measured from the plate's centre) of 35 [mm]. The kinetic energy as predicted by the analytical model (based on the total solution termination strategy) is compared to the corresponding one from a purely Lagrangian LS-DYNA simulation. 157

5.15 Specific impulse distributions from near-field blasts that are labelled by Mx-Sy where x is the mass in [g] of the spherical PE4 explosive, and y is the clear stand-off distance (measured from the plate's centre) in [mm]. . . 160

5.16 Maximum plastic strain-rate distributions in circular thin plates when subjected to near-field blasts. The blasts are labelled by Mx-Sy where x is the mass in [g] of the spherical PE4 explosive, and y is the clear stand-off distance (measured from the plate's centre) in [mm]. 161

5.17 Maximum (effective) plastic strain distributions in circular thin plates when subjected to near-field blasts. The blasts are labelled by Mx-Sy where x is the mass in [g] of the spherical PE4 explosive, and y is the clear stand-off distance (measured from the plate's centre) in [mm]. 162

5.18 Average effective (or von Mises) yield stress distributions in circular thin plates when subjected to near-field blasts. The blasts are labelled by Mx-Sy where x is the mass in [g] of the spherical PE4 explosive, and y is the clear stand-off distance (measured from the plate's centre) in [mm]. The corresponding specific impulses were given in Fig. 5.15. The effective yield stress at a point (in the profiles) is the average stress that is determined by integrating the von Mises stress versus effective plastic strain curve at that point. 163

5.19 Ratio of global dynamic yield stress to quasi-static yield stress versus total impulse. The global dynamic yield stress is the spatial average of the profiles shown in Fig. 5.18. The total impulses, I_0, are the spatial integrals of the specific impulse profiles shown in Fig. 5.15. 164

6.1 Kinetic (KE) energy and plastic work (PW) balance for a circular membrane under non-uniform specific impulse corresponding to the two solution termination strategies. The time histories of energies are given as predicted using the (total) solution termination strategy and the (sequential) termination strategy. The corresponding time histories from purely Lagrangian LS-DYNA simulation of the same input impulsive loading are given for reference. 182

6.2 Kinetic (KE) energy and plastic work (PW) balance for a circular membrane under uniform specific impulse corresponding to the two solution termination strategies. The specific impulse is uniform and energy-equivalent, according to Rigby et al. (2019a), to the non-uniform specific impulse that was used in Fig. 6.1. The time histories of energies are given as predicted using the (total) solution termination strategy and the (sequential) termination strategy. 183

E.1 Normalised residual displacement $x_r/x_{y,0}$ of elasto-plastic SDOF as function of the ratios of load duration to elastic period t_d/T_e and hardening modulus to elastic stiffness H/k. 242

E.2 Normalised transient displacement $x(t)/x_{y,0}$ of elasto-plastic SDOF (with work-hardening) as function of normalised time $t/t_{y,0}$; hardening modulus to elastic stiffness ratio is $H/k = 0.01$. The response is for an impulsively loaded SDOF, i.e., with non-zero initial velocity and zero external force. . . 246

E.3 Normalised transient displacement $x(t)/x_{y,0}$ of elasto-plastic SDOF (with work-hardening) as function of normalised time $t/t_{y,0}$; hardening modulus to elastic stiffness ratio is $H/k = 0.002$. The response is for an impulsively loaded SDOF, i.e., with non-zero initial velocity and zero external force. . . 246

E.4 Variation of JC current yield stress σ_y versus effective (von Mises) plastic strain $\varepsilon_{\mathrm{p,eff}}$ at the quasi-static plastic strain rate $\dot{\varepsilon}_0$. The curves correspond to different amount of strain-hardening in terms of B/A ratio. 248

E.5 Central transverse displacement w time history from LS-DYNA simulation (for $B/A = 1.7$) and the corresponding model prediction. 249

E.6 Histories of global energies from LS-DYNA (for $B/A = 1.7$), and the corresponding kinetic (KE) and plastic internal (IE) energies predicted by the model. From LS-DYNA, the internal (IE), kinetic (KE), total (TE), and hour-glass energies and external work (EW) are shown. The maximum response time t_{max} predicted by the model is shown as a vertical dashed line. 249

E.7 Effect of the degree of strain-hardening (in terms of B/A ratio) on the transient and residual central displacements from LS-DYNA. The model prediction assumes $\sigma_0 = A$. 250

E.8 LS-DYNA maximum (peak) and residual (res.) displacements at the plate's centre as functions of the degree of hardening (in terms of B/A). 250

F.1 A sample `binin` structure corresponding to a `binout` file that contains `matsum`, `glstat`, `nodout`, and `elout` databases. The `elout` field contains only `shell` since it is the type that was requested from LS-DYNA in the original model. 252

F.2 Content of the `matsum` database returned as part of the `binin`. To obtain the time vector (as an example), use `binin.matsum.data.time`. 253

List of Tables

2.1 Analytical works to study the dynamic response of rigid-plastic structures under extreme dynamic loadings 31

3.1 Used parameters' values for validating the first mode solution against numerical results from a simplified LS-DYNA analysis 94

4.1 The first seven roots of the zeroth order Bessel function $J_0(x)$ and their related quantities, which were computed using a MATALB function developed by Nicholson (2022). 108

4.2 Comparison of the present model against the modified Nurick and Martin's model proposed by Chung Kim Yuen et al. (2016) 119

5.1 Air parameters used in `*Eos_Linear_Polynomial` and `*Mat_Null` 138

5.2 PE4 parameters used in `*Eos_Jwl` and `*Mat_High_Explosive_Burn`. All values are adopted from Curry (2017) and Rigby et al. (2019a). 140

5.3 Domex-355 steel parameters in `*Mat_Modified_Johnson_Cook` which are adopted from Curry (2017) and Rigby et al. (2019a). 142

5.4 Input parameters for the MM-ALE explosive analyses and the corresponding energy-equivalent total impulses (Tyas and Pope, 2003; Rigby et al., 2019a), I_k, and area-integrated total impulses I_0. The total impulses are computed over the circular (cir.) and rectangular (rec.) plates. The Hopkinson-Cranz scaled distance Z are shown. 143

5.5 Blast input parameters in explosive MM-ALE simulations 149

Nomenclature

Latin symbols

a	-	Generic model coefficient
a_0	-	Arbitrary scalar
A	-	Area of structural target,
		Parameter in Johnson-Cook material model,
		Parameter in Jones-Wilkins-Lee EOS model
b	-	Exponential decay coefficient in the modified Friedlander blast waveform,
	-	Generic model coefficient
B	-	Parameter in Johnson-Cook material model,
		Parameter in Jones-Wilkins-Lee EOS model
c	-	Wave speed of membranes,
		Parameter in Johnson-Cook material model
c_p	-	Plastic wave speed, and occasionally written as c
C_a	-	Blast reflection coefficient of due to acoustic contribution
C_d	-	Blast reflection coefficient of due to dynamic contribution
D_{CJ}	-	Chapman-Joguet detonation velocity
e	-	The ratio $\frac{\varepsilon_{xy}}{\varepsilon_x}$,
		Internal energy per unit mass of fluid
e_0	-	Initial or ambient internal energy per unit mass
E	-	Internal energy per unit volume of fluid
E_k	-	Kinetic energy of membranes
E_0	-	Initial or ambient internal energy per unit volume
f	-	Generic function,
		Yield function
F	-	Force
h	-	Thickness of membranes
H	-	The Hamiltonian of a mechanical system
i	-	Blast-generated specific impulse (impulse per unit area)

i^- - Specific impulse of the negative phase

i_{so} - Incident or side-on positive specific impulse

i_r - Reflected positive specific impulse

I - Total impulse

I_0 - Total impulse due to uniform specific impulse

I_k - Energy-equivalent total impulse

I_{mn} - Total modal impulse of the $(m,n)^{\text{th}}$ mode in rectangular membranes

I_m - Total modal impulse of the m^{th} mode in axi-symmetric circular membranes

I_{M1} - Intensity of the first mode present in a generic response w

$j_{m,n}$ - The n^{th} zero of Bessel's function of order m

J_m - Bessel's function of order m

k_{exp} - TNT equivalency factor of specific explosive

k_{mn} - Wavenumber of the $(m,n)^{\text{th}}$ mode in rectangular membranes

K_{ub} - Upper-bound kinetic energy uptake

k_0 - Structural parameter for rectangular or circular membranes under uniform specific impulse

k_x - Wavenumber of a single mode in the x-direction

k_y - Wavenumber of a single mode in the y-direction

K - Kinetic energy

L_x - Side length along x-axis

L_y - Side length along y-axis

L^* - Characteristic length as ratio of rectangular membrane area to length of one diagonal

m - Parameter in Johnson-Cook model

n - Parameter in Johnson-Cook model,

- Generic model coefficient

n_1 - Component of the normal to von Mises yield curve in the principal in-plane stress space, along σ_1

n_2 - Component of the normal to von Mises yield curve in the principal in-plane stress space, along σ_2

p - Externally applied pressure on membranes ,
Fluid pressure,
Blast pressure

$\hat{p}$ - Internal hydrostatic pressure associated with stresses, $(1/3)\ \sigma_{ii}$

p_0 - Initial or ambient pressure

p_a - Atmospheric pressure (or the initial air pressure).

p_{CJ} - Chapman-Joguet detonation pressure

p_r - Reflected blast overpressure

$p_{r,0}$ - Normally reflected pressure

$p_{\text{r,max}}$ - Peak reflected blast overpressure

$p_{\mathrm{r,min}}$ - Minimum reflected blast underpressure

$p_{r,\theta}$ - Oblique reflected pressure

p_{so} - Incident or side-on blast overpressure

$p_{\mathrm{so,max}}$ - Peak incident or side-on blast overpressure

$p_{\mathrm{so,min}}$ - Minimum incident or side-on blast underpressure

r - Radial coordinate in axi-symmetric and circular domain

r_1 - Parameter in Jones-Wilkins-Lee EOS

r_2 - Parameter in Jones-Wilkins-Lee EOS

R - Radius of circular membrane,
Stand-off distance from target centre of explosive charge

s_{ij} - Deviatoric stress

$\dot{s}_{ij}$ - Rate of deviatoric stress

S - Surface area of the membrane

S_0 - Converged sum of the infinite series for rectangular membranes under uniform specific impulse

t - Time

t^* - Time of solution termination and critical time instant

t_a - Time of arrival of a blast wave

t_d - Duration of positive phase of a blast wave

t_d^- - Duration of negative phase of a blast wave

t_{max} - Maximum response time

T - Natural period,
Current absolute temperature in Johnson-Cook model

T_0 - Initial (or room) absolute temperature in Johnson-Cook model

T_m - Melting absolute temperature in Johnson-Cook model

u - In-plane displacement along x-axis

u_0 - In-plane displacement along x-axis at the plate's mid-plane

$\dot{u}_s$ - Particle's velocity of air behind the shock

U_p - Internal energy dissipation, plastic energy

v - In-plane displacement along y-axis,
Specific volume of fluid

v_0 - In-plane displacement along y-axis at the plate's mid-plane

V - Volume of membrane

w - Transverse displacement, i.e., along z-axis

$\dot{w}$ - Transverse velocity, i.e., along z-axis

$\ddot{w}$ - Transverse acceleration, i.e., along z-axis

w_0 - Transverse displacement at the plate's mid-plane

$\dot{w}_0$ - Initial transverse velocity, i.e., along z-axis

$\dot{w}_{0,\mathrm{lb}}$ - Lower-bound initial transverse velocity, i.e., along z-axis

w_c - Central residual transverse displacement

w_p - Permanent (or residual) transverse displacement

$\dot{W}_p$	-	Rate of plastic work
W	-	Mass of explosive charge
W_{exp}	-	Mass of explosive charge of specific explosive
W_p	-	Plastic work
W_{TNT}	-	TNT equivalent mass of an explosive
x	-	Cartesian coordinate
y	-	Cartesian coordinate
z	-	Cartesian coordinate
Z	-	Scaled distance, $R/w^{1/3}$

Greek symbols

α	-	Generic model calibration coefficient,
		Time-dependent amplitude of the first mode membrane solution
β	-	Generic model calibration coefficient
γ	-	Ratio of specific heat of gases
δ	-	Variational operator
δ_{ij}	-	Kronecker delta, $\delta_{ij} = 1$ if $i = j$, $\delta_{ij} = 0$ if $i \neq j$
δw	-	Virtual transverse displacement
Δ	-	Difference operator
ε_{ij}	-	Total strain,
		Plastic strain for a rigid-plastic material
$\dot{\varepsilon}_{ij}$	-	Strain rate
		Plastic strain rate for rigid-plastic material
$\ddot{\varepsilon}_{ij}$	-	Rate of plastic strain rate, or plastic strain acceleration
ε_{eff}	-	Effective (von Mises) strain
$\dot{\varepsilon}_{\text{eff}}$	-	Effective (von Mises) strain rate
ε_{vm}	-	Similar to ε_{eff}
$\dot{\varepsilon}_{\text{vm}}$	-	Similar to $\dot{\varepsilon}_{\text{eff}}$
$\dot{\varepsilon}^0_{\text{eff}}$	-	Quasi-static threshold of effective strain rate in Johnson-Cook model
ε^p_{ij}	-	Plastic strain
$\dot{\varepsilon}^p_{ij}$	-	Plastic strain rate
θ	-	Angle of incidence of blast wave upon reflection
		Direction of the first principal normal stress σ_1
θ_s	-	Direction of the maximum principal shear stress $\tau_{\max}$
λ	-	Total plastic multiplier
$\dot{\lambda}$	-	Plastic multiplier rate
$\ddot{\lambda}$	-	Acceleration of plastic multiplier
ρ	-	Mass density (mass per unit volume)
ρ_0	-	Initial or ambient mass density (mass per unit volume)
ρ_s	-	Density of air behind the shock
σ	-	Normal stress for Mohr's circle horizontal axis

σ_0	-	Initial uni-axial yield stress, Quasi-static yield stress, Characteristic yield stress
σ_1	-	First principal normal stress
σ_2	-	Second principal normal stress, $\sigma_1 \geq \sigma_2$
σ_{ij}	-	Cauchy (or true) stress
σ_{eff}	-	Effective (von Mises) stress
$\sigma_{d,y}$	-	Current (dynamic) yield stress for Johnson-Cook model
σ_{vm}	-	Similar to σ_{eff}
σ_x	-	Normal stress along x-axis
σ_{xy}	-	In-plane shear stress in the x-y plane
σ_y	-	Normal stress along y-axis
σ_z	-	Normal stress along z-axis
τ	-	Shear stress for Mohr's circle vertical axis, Normalised time for positive phase of blast wave
τ^-	-	Normalised time for negative phase of blast wave
$\tau_{\max}$	-	Maximum principal shear stress
ϕ	-	Mode shape of membranes
$\hat{\phi}_0$	-	Normalised impulse (or damage number) of Nurick and Martin
ϕ_1	-	Deformed shape of the first mode of rectangular membrane
ϕ_m	-	Deformed shape of the m^{th} mode in axi-symmetric circular problem
ϕ_{mn}	-	Deformed shape of the $(m,n)^{\text{th}}$ mode in rectangular membranes
ω	-	Angular frequency (radians per second), Parameter in Jones-Wilkins-Lee EOS
ω_m	-	Angular frequency of the m^{th} mode in an axi-symmetric circular membrane
ω_{mn}	-	Angular frequency of the $(m,n)^{\text{th}}$ mode in a rectangular membrane

Operator symbols

dx	-	(Total) differential element of x.
$\|f\|$	-	Norm of the function (or distribution) f, in two-dimensions $\|f(x,y)\| = \iint_A f^2(x,y)\, dA$.
$\|x\|$	-	Absolute value of the variable x
$\dot{x}$	-	First derivative of x with respect to time.
$\ddot{x}$	-	Second derivative of x with respect to time.
δ	-	Variational (or virtual) operator.
Δ	-	(Finite) difference operator.
∂x	-	Partial differential element of x.

Acronyms and Abbreviations

ALE	Arbitrary Lagrangian-Eulerian, a type of description of motion
CJ	Champan-Jouguet, a state of explosive at detonation point
CPU	Central Processing Unit
DIC	Digital Image Correlation
EOM	Equation of Motion
EOS	Equation of State
FE	Finite element. Also mentioned as FEA and FEM for finite element analysis and finite element method, respectively
FFT	Fast Fourier Transform
JC	Johnson-Cook, a material model suitable for ductile materials
JWL	Jones-Wilkins-Lee, an EOS for high explosive's detonation by-products
KB	Kingery and Bulmash, a semi-empirical model for blast parameters' predictions
LS-DYNA	General-purpose finite element software for non-linear dynamic analysis of continua and structures by Livermore Systems Technology, Ansys
MATLAB	A programming language for technical and engineering computations by Mathworks Inc.
MM-ALE	Multi-Material Arbitrary Lagrangian-Eulerian, a computational technique
NM	Nurick and Martin, a model to predict residual displacement of thin targets due to uniform impulse
PDE	Partial Differential Equation
PE4	Plastic explosive - composition 4, a type of chemical high explosive
SDOF	Single-degree-of-freedom, a mass-spring oscillator
SOD	Stand-off distance, a distance from a point to the explosion's centre
TNT	Trinitrotoluene, a type of chemical high explosive

UFC	Unified Facility Criteria, a guideline document for analysis and protection of structures against blast loading

Chapter 1

Introduction

1.1 Overview

The present work focuses on providing an analytical model to predict the transient and peak permanent response of a thin structural target subjected to a near-field blast loading. The main goal of the current research is to build a simple and efficient model so that it is fast-running and of considerably low computational expense. Thus, certain idealising assumptions based on observations of the various aspects controlling the overall behaviour are formulated such that they can be reasonable, i.e., without jeopardising the accuracy of the ultimate model. The basic assumptions underlying the model development are: (i) a rigid-perfectly plastic behaviour of the target's material; (ii) membrane mode of deformation without in-plane displacements; (iii) an impulsive blast loading, which is fully characterised by the specific impulse distribution so that the target's motion is initiated by the initial velocity field that is directly proportional to the specific impulse field.

Based on the first two assumptions, given above, an appropriate equation of motion was derived by means of the principle of virtual work. Then, according to the third assumption, i.e., the impulsive regime, the externally applied pressure, in the equilibrium equation, is set to zero, and the resulting equation becomes, then, a two-dimensional wave equation with the wave speed as a function of the yield stress in uni-axial tension. Since the wave speed is related to the yield stress, the equation of motion will be called the plastic wave equation. Initially, the equilibrium equation is expressed in a rectangular Cartesian co-ordinate system to describe the motion of rectangular targets, and using the standard transformation from rectangular to cylindrical coordinates, an equivalent equation of motion was obtained for circular targets that are assumed to be in axi-symmetric conditions. Therefore, overall, the target is found to be governed by the wave equation and responding in a free vibration manner where its motion is set by the initial velocity condition that is induced by the blast-generated specific impulse.

In the development of the equation of motion, the material behaviour was assumed as rigid-perfectly plastic as mentioned earlier, and the perfect plasticity is based on von Mises

yield criterion and its associated flow rule. However, since the classical von Mises relations are expressed in terms of plastic strain rates, they were found to lead to a highly non-linear equilibrium equation. Thus, in accordance with the form of the total strains of the considered membrane, it was recognised that if the plastic flow relations are expressed in the total plastic strains (instead of their rates), considerable simplifications are obtained. Hence, the total form of the flow rule was adopted, using which the final equation of motion, or the linear wave equation described above, is derived. However, the total flow rule imposed restrictions on the applicability of the thus-obtained equilibrium equation. This is summarised as follows. The response of the membrane is governed by the wave equation as long as it is under progressive yielding (i.e., as the total plastic strains are increasing, which means the strain rates are non-zero and hence the yield condition should be satisfied as assumed), and the solution of the wave equation must be terminated when a decrease in the total plastic strain takes place. In the absence of externally applied loading (as assumed in the present study), the condition when the total plastic strain starts to decrease is identical to the condition when the local kinetic energy starts to increase. Thus, the solution (of the wave equation) must be terminated when the kinetic energy increases. This important step (of terminating the solution) is essential to prevent the plastic work, or magnitude of the total plastic strain, from decreasing. The underlying basis of the solution termination condition is that the rate of plastic work must be always non-negative. That is, gained plastic work cannot be re-claimed (in particular, it cannot be converted back to kinetic energy); in the absence of external loading and rigid-body motion, the local kinetic energy can, then, only decrease.

Assuming the membrane is under progressive yielding, its response is given by the solution of the plastic wave equation. Since this equation is linear, it is solved by the eigen-expansion technique. For the rectangular membranes, the eigen-functions are the familiar Fourier components (or modes) of the solution. This is because each Fourier mode solves the wave equation, and the total solution is then the sum of the modes, due to the linearity of the (plastic wave) equation and the mutual orthogonality of the Fourier modes. For the circular membrane, the eigen-functions are the Bessel's functions of the first kind and, due to the axi-symmetric assumption, of zeroth order. The thus-obtained solution is considered valid up to an instant of time when the local kinetic energy reaches zero for the first time.

Therefore, overall, an analytical model is developed that consists of (i) the solution of the plastic wave equation and (ii) a solution-termination strategy to enforce the plastic work rate's non-negativity. The theoretical basis of the model is given in sufficient detail to address the implications of the adopted assumptions in constructing the model. Furthermore, some useful results or consequences of the implied assumptions on the overall response of the target are discussed.

The model is thoroughly validated using relevant experimental data available in the literature and results from numerical simulations using LS-DYNA performed by the present author. Based on the validation work, the model is demonstrated to be efficient and rea-

sonably accurate in predicting the overall behaviour and peak response of the thin target when loaded by blast-generated uniform and non-uniform specific impulses.

There are many experiments, available in the literature, for the case of uniform specific impulse, especially in the earlier studies. The peak transient and permanent displacements of uniformly loaded thin targets are measured in the experiments. The reported uniform specific impulses are directly used in the analytical model to provide the corresponding response predictions, which are then compared to the experimental findings. Recently, relatively fewer studies on the responses of thin targets, when subjected to near-field blasts and, hence, non-uniform specific impulses, became available. However, the majority of these latter non-uniform studies measure and report the total impulses instead of the actual specific impulse distributions. Thus, in order to provide predictions by the present analytical model, the blast event's set-up is replicated numerically using LS-DYNA to re-produce the specific impulse profiles. Then, this numerically obtained specific impulses are used in the model, and the predictions are compared to the experimentally measured displacements of the thin targets.

Two types of numerical analyses were performed for the purpose of validating the present analytical model. Firstly, the multi-material arbitrary Lagrangian-Eulerian (MM-ALE) technique, available in LS-DYNA, is utilised to run explosive blast events and hence predict the specific impulse distribution associated with a given explosive configuration. In this, the detonation of a high explosive (HE) charge that is placed in ambient air is simulated, and the resulting formation and subsequent propagation of a shock wave in the air are solved. Ultimately, the shock wave impinges onto a pre-defined target, which is modelled as perfectly rigid for an efficiency reason, thereby causing blast wave reflection. The reflected pressure on the rigid target is obtained, and from which the reflected overpressure (absolute pressure minus the initial ambient pressure) is computed. Then, the reflected overpressure is time integrated over the positive phase of the blast wave (defined as the time interval when the pressure relative to the ambient pressure is positive) to estimate the positive specific impulse. Secondly, given a specific impulse profile (uniform or non-uniform), additional purely Lagrangian structural analyses are performed to study the elasto-plastic responses of deformable thin plates where their motions are initiated by prescribed initial velocity fields, that are directly proportional to the specific impulses. In such Lagrangian problems, all effects regarding the target's linear and nonlinear behaviours are incorporated; namely, elastic deformations, membrane, bending, and transverse shear modes, plastic strain-hardening, and strain rate effects on the dynamic yield stress, are modelled. The results for the peak residual displacements from these structural simulations are then compared to the predictions by the present model for the considered prescribed specific impulse fields. The underlying theories of the various models and procedures in the numerical simulations are discussed in appropriate sections of the thesis, and the sources and numerical values of the various parameters as used in the present simulations are given.

1.2 Motivations

Over the past three decades, there has been an increasing number of incidents of explosions worldwide, particularly in the form of malicious attacks in which terrorists detonate high explosives to cause civilian destruction and/or public harm by means of the explosion-induced blast waves (Edwards et al., 2016). Blast loads from explosions can cause loss of human lives, severe injuries, or organ malfunctions due to either the direct exposure of individuals to the blast waves, see, e.g., Frykberg and Tepas (1988) and Denny et al. (2021), or as consequences of partial or overall collapses of structures, or their key structural elements, housing the human individuals (Teague, 2004; Edwards et al., 2016). Three major terrorist attacks that targeted building structures and resulted in significant structural collapse and related casualties include the Alfred P. Murrah building bombing in 1995, Oklahoma City, the United States; the Al-Khobar tower bombing in Dhahran, Saudi Arabia, in 1996; the United States Embassy bombing in Nairobi, Kenya, in 1998 (Arnold et al., 2004). Accidental explosions can also occur, such as the recent devastating incident that took place at the Port of Beirut on the 4^{th} of August 2020. This catastrophic event resulted in 190 deaths (Abouzeid et al., 2020), and about 240 buildings and 2,310 households were assessed as severely damaged (Strategy&, 2020). Beirut's blast was due to a transitioned detonation (Pasman et al., 2020) of 2.75 kilotons of ammonium nitrate, which is estimated by Rigby et al. (2020b) to be equivalent to [0.5-1.12] kilotons of TNT (trinitrotoluene); the overall damage-induced cost amounts to $\sim$ £1.3 billion (Strategy&, 2020).

There has been significant scientific interest in studying the response of structures when subjected to extreme dynamic loading events such as blast and impact. Through earlier experiments, it was observed that the resulting deformations of the given structures under such extreme loading conditions are mainly plastic. Furthermore, the actual magnitudes associated with typical blasts were found to exceed, by far, the quasi-static ultimate capacities of practical structures.

The blast load arises due to the reflection of a shock wave in the air as the shock impinges onto the exposed surface of the structure. The incident shock wave (just before reflection) is of extremely high pressure and the shocked air particles are of considerable momenta (product of the current density and particles' velocities). The air shock is initially formed due to a very rapid release of energy from an explosion of an explosive charge. For example, when a high explosive detonates, the inert explosive material is decomposed into extremely high-temperature and pressure gases (called the detonation by-products), which are then forced to expand very rapidly and thereby compressing the surrounding air and creating a high-pressure disturbance; owing to the high-pressure levels of this disturbance, it travels supersonically (or with a speed well above the speed of sound in air), i.e., as a shock. The intensity of the incident shock depends on the size of the charge (as this is directly related to the amount of the instantaneous energy deposition from the explosion) and the distance (called the stand-off distance) from the explosion's

centre such that it increases with the charge's mass and decreases with (roughly) the cube of the distance as the shock travels. As the exposed surface of the structure, when assumed as perfectly rigid, imposes a zero-velocity condition on the air particles (along the surface's normal), the air's pressure increases substantially, and this increased pressure is the reflected pressure that the structure will experience. As the structure restricts the motion of the shocked air particles in the normal direction (to its surface), the angle of incidence (defined as the angle between the normals of the shock front and that of the surface as the incident wave strikes the surface) plays a critical influence on the increased magnitude of the reflected blast wave; in general, the reflected pressure is higher as the angle of incidence is smaller. For structural applications, typically the pressure of interest is the pressure relative to the ambient pressure, which is called the overpressure. The time durations of blast waves (reflected pressure waves) are typically extremely short, e.g., in the order of several milliseconds.

In the early scientific investigations, blast loads arising from far-field explosions (i.e., the explosion centre is sufficiently far from the considered structure) were the main topic. Due to such blast configuration, the blast load is typically uniform over the exposed surface of the structure. However, as the explosive charge is detonated in proximity to the target (i.e., the structure), the resulting blast load has been confirmed experimentally to be highly non-uniform over the loading spans of the structure. This type of blast event is termed the near-field blast. Furthermore, in near-field blasts, the reflected blast wave is of extremely high peak overpressures, e.g., in tens or even hundreds of megapascals, and the blast wave duration is extremely short, e.g., few or sub-milliseconds. From the structural response's point of view, the complex nature of the near-field blast loading would induce modes of response that were not encountered in conventional structural problems. In particular, the response of the target would be mainly plastic, the deformation profiles can be highly transient and localised, and the overall response is more likely to be nearly impulsive. Thus, the commonly available analysis tools, methods, and techniques (that were developed mainly to address conventional loading regimes) are less applicable or less accurate.

The finite element method has been proven effective in terms of accuracy to numerically solve a wide range of mechanical problems and predict the (generally non-linear) responses of materials and complex structures when subjected to complex loading, initial, and boundary conditions. This is meant to be the case when the loading and the material behaviour are fully characterised and described by models that are validated against actual experiments. In particular, the transient response of arbitrarily shaped thin targets made of structural elasto-plastic materials under generic blast loadings resulting from detonations of high explosives can be simulated.

Nevertheless, the numerically obtained results can be considered reliable once the overall numerical model is validated first using relevant experiments, e.g., an actual experiment is replicated (or simulated) using the finite element program. The thus-validated model (or set-up) can then be adopted to predict the behaviours of real-world structures as the

various loading and geometric parameters are varied. However, in the implementation of the finite element method, several numerical artefacts are necessarily introduced to improve accuracy, stability, and/or efficiency. Thus, typically, it is recommended to ensure that the calculated response of the structure is practically insensitive to the actual values of the artificial parameters. Furthermore, the solution should not be sensitive to the mesh of the model, and typically a suitable mesh should be determined with which a variable of interest is shown to converge. Furthermore, due to the high rate of load application and the associated (highly) transient structural response, explicit time integrator schemes are typically used (and usually preferred) in the numerical calculations, and as such the time step sizes are required to be adequately small to avoid instability. The permitted time step size decreases as the mesh resolution is increased. Therefore, the modelling of real-world-sized problems can, sometimes, require appreciable computational times. Although the finite element method, as highlighted above, is an indispensable tool (and, in fact, is the current state-of-the-art) for solving complex blast problems, it can (as briefly explained above) be associated with user expertise and computational resources, e.g., data storage and CPU time.

As priorly discussed, the blast loading is highly variable, so in a typical real blast analysis, a designer would be interested to perform several analyses, where the blast input parameters are varied so that the effects of a large variety of possible loading cases and the associated structural responses are addressed. It is believed herein that the finite element method (due to its relatively considerable computational expense) is used to make a final detailed analysis or to verify a preliminary design that has been alternatively reached using some fast-running models, which are simple and very rapid to run as will be discussed briefly in the next section.

The reader should be aware that fast-running models are typically prone to some limitations due to the simplifications that are undertaken during the models' developments. Hence, during the final design stage, it is recommended that more accurate computational methods, e.g., the FE analysis, are utilised to obtain refined and more robust predictions. This is an example of the desirable integration, in practice, in solving engineering problems with an emphasis on the balance of accuracy-efficiency (or -simplicity). Furthermore, as another example where fast-running models and FE computations complement each other in engineering research, the high-fidelity computational (or numerical) methods can be of significant importance during the development of a fast-running model, e.g., to generate validation data to test the model's performance or to inform future research to improve existing approximate models. As compared to experimental methods, pre-validated numerical models are relatively more attractive and economical source for the generation of mechanically-rich validation data.

However, the availability of reliable fast-running models is indeed of a practical importance to obtain rapid first-order approximate predictions, in particular, in the initial design stage. Recently, other researchers, in the field of structural blast engineering, focused on developing remarkably fast-running models to characterise the near-field blast loading

that apply when the explosive charge is detonated at close-in proximity to the target. The present work is concerned with developing a fast-running model to predict the structural response of thin plates when they are subjected to a prescribed near-field blast loading. In the present model, the target is assumed to be loaded impulsively and hence the blast loading is *completely* characterised by the specific impulse distribution. Justifications for the above and other assumptions in the development of the present model were given in the previous subsection and to be discussed in more detail in the following chapters.

1.3 Intellectual Contribution

1.3.1 Relevant Background

As presented in the previous section, the present study focuses on the response of thin targets when subjected to near-field blast loading. Owing to the nature of near-field blasts, the loading is of extremely high magnitudes, extremely short durations, and is highly non-uniform spatially and highly transient temporally. Experiments on plates loaded by uniform and non-uniform blast loads and early theoretical studies on uniformly loaded structures both indicate that the structural target responses are mainly plastic (i.e., materially non-linear) and are accompanied by geometric non-linearities.

The problem (of predicting the structural response to blast loading) can be solved by using two broad approaches. The first is the utilisation of commercially available high-fidelity finite element software, in which all complexities are properly incorporated. However, this numerical approach is computationally expensive per one run and needs preliminary validations whenever a new problem setting is encountered. Furthermore, the numerically obtained solution (from an individual run) gives the prediction for one specific set of input parameters, e.g., load magnitude and distribution and sizes (or dimensions) of the structural target (assuming the material properties are deterministic, or constant, in nature); furthermore, such sophisticated tools require substantial user expertise and specialised training. It is meaningful, in the present context, to view the finite element solution as being an approximate solution of the more-or-less actual problem. A blast engineer, especially in the preliminary design stage, is typically interested in solving several (or more) problems so that varying combinations of the input parameters are considered to achieve a reliable initial design. Thus, demanding predictive models or methods (such as the finite element technique) are less attractive or, simply, inapplicable. This, naturally, leads to the importance of the second approach that utilises fast-running models. These efficient (or low-demanding) models offer exact or nearly exact solutions to a simplified (or idealised) version of the actual problem.

For a blast-loaded structure application, the fast-running models are subdivided into three main categories: to predict (i) the blast parameters given a blast threat configuration (i.e., explosive charge's mass and its position relative to the structure); (ii) blast load effects (e.g., the (likely) overall mode of the structural response) given the blast load type and its

parameters; (iii) structural response (e.g., plastic displacement) given a blast load type, its intensity, and mode of response. For the sake of definiteness, examples of the first category include the Kingery and Bulmash's (1984) model to predict the blast parameters for far-field blasts, and the one by Pannell et al. (2021) to predict the non-uniform specific impulse for near-field blasts from spherical charges. An example of the second category is the Tyas and Pope (2003; 2004) and Rigby et al. (2019) model stating that the effect of a near-field blast on thin targets is that the target responds impulsively, and hence the blast load is fully characterised by the specific impulse distribution, and the initial velocity field of the target is non-uniform and directly proportional to the specific impulse field. Lastly, Nurick and Martin model, described in Nurick and Martin (1989b), Nurick and Martin (1989a), Chung Kim Yuen et al. (2016), and Cloete and Nurick (2014), is an example for the third category, which predicts the normalised (with respect to the target's thickness) permanent displacement of the thin target as a function of the imparted total impulse. The present study is concerned with the last category of fast-running models, i.e., to predict the response of targets given a blast, of the near-field type, and with the likely overall structural response as being nearly impulsive (in correspondence with the nature of the near-field blast regarding the blast wave duration). It needs to be emphasised that fast-running models are, typically, either analytical and/or empirical (or semi-empirical) in nature.

Most of the available analytical models were developed in the early past, in which the blast load was always assumed as spatially uniform. Recent works in which non-uniform blast loads are addressed are available. Almost all the earlier and recent analytical solutions are based on the rigid-perfectly plastic idealisation of the structure, a theoretical tool that has been proven to be powerful and applicable for structures subjected to extreme dynamic events, such as in a blast problem. However, the available models extend the well-established (standard) plastic analysis framework to the dynamic regime when the externally applied loading exceeds the quasi-static collapse load. In these, the deformation profile needs to be assumed a priori based on the given fixed (or assumed) load distribution (this is made to be uniform in the early studies). The obtained solution, then, applies to that fixed load distribution.

1.3.2 Contribution by the Present Work

With the above background, the present study provides the following contribution: an analytical and fast-running model to predict the transient and maximum plastic response of a thin ductile plate when subjected to an arbitrarily non-uniform near-field blast loading. Important assumptions have been made in order to obtain a generic model that admits (or applies to) any blast load distribution. These are: (i) the blast loading is of extremely short duration such that the main structural response is impulsive, and hence the blast load is characterised by the specific impulse field, and the non-uniform specific impulse induces (proportionally) non-uniform initial velocity field; (ii) the intensity of the specific

impulse is significantly high such that the material can properly be assumed as rigid-perfectly plastic, and the thin plate responds mainly in purely membrane mode that is associated with the transverse displacement being extremely large. Furthermore, the von Mises yield condition and its associated flow rule are adopted. However, as the intended model is planned to be ultimately efficient and fast-running, the rate form of the flow rule is extended to be described in terms of the total plastic strains instead of their time rates, and the extended rule is called the total form of the flow rule. These assumptions were then used in the well-established virtual work principle, and a general equation of motion was ultimately derived, which governs the plastic response of the thin plate. This equation was then solved under the initial condition on the velocity field (which is related to the prescribed non-uniform specific impulse). Due to the introduced assumption on the total flow rule, the actual (plastic) response is the solution of the equation of motion as long as the restriction by the use of the total flow rule is not violated. Thus, the solution is then required to be terminated by a solution-termination strategy (which is discussed in detail in the thesis), and the subsequent response is held constant at the termination time. The basis of the termination strategy is to avoid the violation of the plastic work rate's non-negativity, which would take place whenever the incremental plasticity formulation is replaced by the total formulation (as assumed in the model development as described above).

Therefore, an analytical solution is developed in the thesis to predict the response of a thin target when subjected to a typical near-field blast. The model is believed to be fast-running (i.e., predictions are practically instant to be determined for given values of the structural, material, and loading parameters) and accurate (as the underlying assumptions are deemed reasonable and relevant; the model has been already validated using relevant experimental data and well-detailed numerical simulations). For a real blast problem, the model predictions can be considered reasonable approximations that would be highly useful for initial and preliminary design calculations, as the model demands relatively low computational cost. In addition, the analysis, discussion, and results that are presented in the thesis offer useful insights as the overall structural problem is reduced down to the most elemental (primitive) building blocks so that the important concepts and their scientific bases are (hopefully) lit and made evident. As a representative example, the model shows clearly that the mass density of the target is as structurally important (identically) as the yield strength of the material (as the functional form of the maximum plastic displacement is symmetric in terms of the two mentioned parameters) when the blast is of a near-field type and hence fully characterised by the specific impulse. Moreover, it is analytically derived that the time of maximum response of the target is (materially) a function of the inverse of the uni-axial yield stress, which is relatively quite small (when compared to typical elastic moduli), so that the maximum response time is relatively quite long. Hence, the response, due to a typical near-field blast load, is more likely to be impulsive; that is, if the impulsive regime can be justified for an elastic problem, then the plastic response is much more impulsive.

1.4 Aims of the Thesis

In setting out the scope and outline of the thesis, the following aims were formulated:

- Develop a physically-based theoretical model to quantify the overall effect of a near-field blast loading on a thin target;
- Keep the minimum required modelling features so that the model is simple and efficient to run;
- Identify relevant validation data and validation techniques to test the initial model;
- Assess the accuracy of the model and the implications of the necessarily to be taken assumptions, and propose modifications to address arising issues; and
- Investigate the consequences of the model and the significance of the results, and, if possible, highlight the basic mechanisms affecting the responses of targets when loaded by near-field blasts.

Chapter 2

Literature Review

2.1 The Blast Loading

2.1.1 Explosion

High explosives are chemical mixtures that when initiated undergo rapid and highly exothermic chemical decomposition, which is a process (called detonation) during which the inert explosive is transformed into detonation by-products of high temperature and pressure. The hot gaseous by-products are, then, forced to expand violently and hence disturb the surrounding medium, assumed as air. When air experiences pressure disturbance, the disturbance travels with a velocity that increases with the pressure magnitude so that higher pressures travel faster, resulting in a leading sharp front of the disturbance. A (pressure) disturbance that travels supersonically and of a steep or discontinuous front is called a shock wave. The detonation of high explosives, then, creates a strong shock wave in the surrounding air that travels (typically in all directions) away from the point of the explosion into the undisturbed air (Kinney and Graham, 1985). The wave is called an incident wave as it propagates freely in the undisturbed air.

2.1.2 Incident Blast Wave

The initial intensity of the incident wave is an increasing function of the amount of energy that was suddenly released from the explosive's detonation, while its current intensity decays with the distance from the explosion's centre. The reduction of the blast intensity with distance is because the initial energy is constant and gets progressively distributed over larger volumes of air as the shock travels further. The energy released during the explosion is typically related to the mass of the charge. It is well-established that the incident wave intensity (as will be demonstrated in the following subsections) is determined by the scaled distance, which is defined as

$$Z = \frac{R}{W^{1/3}}, \tag{2.1.1}$$

where R is the stand-off distance and W is the charge's mass. The stand-off distance is defined as the distance of a point (where the blast intensity is measured) from the explosive's centre.

As the incident wave arrives at a (fixed) point in air initially at ambient conditions, the air pressure abruptly increases (or discontinuously jumps) to a high maximum value, then it decays exponentially over time, drops below the ambient pressure, attains a minimum value, and eventually returns to the ambient level by the end of the wave. Relative to the initial atmospheric pressure, the maximum point is termed the peak overpressure, whereas the minimum point is called the minimum underpressure. The incident blast wave is therefore composed of an earlier positive phase, during which the relative pressure is positive, and then a subsequent negative phase, when the relative pressure is negative. A typical incident blast wave is shown by the dashed curve in Fig. 2.1, which will be presented in Section 2.1.5. The durations of each phase are important blast parameters.

The area under the relative pressure-time curve is called the specific impulse (i.e., impulse per unit surface area). The positive specific impulse is the area associated with the overpressure time history, $p(t)$, during the positive phase, $i = \int_{t_\mathrm{a}}^{t_\mathrm{a}+t_\mathrm{d}} p(t)\ dt$, or,

$$i = t_\mathrm{d} \int_0^1 p(\tau)\, \mathrm{d}\tau, \tag{2.1.2}$$

where the normalised time, τ, is

$$\tau = \frac{t - t_\mathrm{a}}{t_\mathrm{d}}, \tag{2.1.3}$$

in which t_a is the time of arrival of the blast wave and t_d is the duration of the positive phase; note that $dt = t_d d\tau$. Similarly, the corresponding area of the relative pressure curve over the negative phase defines the negative specific impulse. The negative phase exists due to the over-expansion of air molecules owing to the early increase of their momenta (when they were shocked) and to their instantaneous inertia so that pressure drops below the ambient value (Kinney and Graham, 1985). Throughout the remaining of the present section, the peak overpressure of the incident wave is considered as the measure of the main blast intensity.

2.1.3 Blast Scaling Law

The incident blast parameters are commonly predicted by scaling the given blast to a reference blast problem associated with a charge of unit mass of a reference explosive (typically taken as TNT), according to the well-established scaling law formulated independently by Hopkinson (1915) and Cranz (1926). Baker et al. (1991) discusses the applicability and usefulness of Hopkinson-Cranz scaling and shows that the scaling law is obeyed at a wide range of distances from explosions produced by varying amounts of explosive charges. The

scaled parameters are determined at a scaled stand-off distance, and once the scaled parameters are known, the corresponding actual values are obtained by undoing the scaling operation. Scaled quantities are the actual quantities divided by their scaling lengths. The scaling lengths for pressure and velocity are equal to unity. Whereas, the scaling lengths for distance, time, and specific impulse are all equal to the cube root of the actual mass, denoted by W. Therefore, the scaled stand-off distance (or simply the scaled distance), as was given earlier in Eq.(2.1.1), is

$$Z = R/W^{1/3} \ ,$$

where R is the actual stand-off distance. All scaled parameters are (empirically) found to be (distinct) functions of the scaled distance alone (Baker et al., 1991). This is one of the most important implications of blast scaling from the modelling perspective. Associated with a scaled distance for a given problem, the scaled parameters are determined using some empirical models that are based on experiments with a unit mass of a standard type of explosive (which, as mentioned earlier, is commonly taken as TNT). Then, the actual blast parameters for the actual blast problem can be easily found by simple multiplications with the respective scaling lengths. For example, the actual peak overpressure is just the scaled peak overpressure, and the actual positive specific impulse is the scaled positive specific impulse times $W^{1/3}$.

At the very simplified level, the blast wave can be summarised as being generated by an instant deposition of energy (from the detonation), E, into the air that creates a disturbance, and the disturbance wave then propagates spherically in three dimensions in the air. Hence, the intensity of the wave in terms of peak overpressure at some distance R (from the blast source point) can be said to be in proportion to E/R^3 (Baker et al., 1991). Here, R^3 represents the volume over which the input (or source) energy, E, is spent (or converted into heat and mechanical work in the medium, i.e., the surrounding air). Simplifying further, if the input energy is replaced by the mass (or amount) of the explosive, W, the blast intensity is then proportional to $\sim W/R^3$. Therefore, using Hopkinson-Cranz scaled distance, if R is substituted with $ZW^{1/3}$, the blast intensity, or the peak overpressure, is proportional to $\sim W/(ZW^{1/3})^3 = 1/Z^3$. Hence, the blast intensity is condensed down to be a function of a single parameter Z, which demonstrates the importance and usefulness of the concept of the scaled distance in blast predictions. Also, this simplified analysis shows that the intensity (say in terms of peak overpressure) of a given blast rapidly decreases as Z increases. That is, *maintaining a clear stand-off distance between a sensitive (or critical) structural member and the explosive charge greatly reduces the blast pressures it would experience* (Cormie et al., 2009).

2.1.4 TNT Equivalence of an Explosive

It is well-known that the initial deposition of energy depends on the type of explosive being detonated, and there are a wide variety of explosives, then (for practical reasons) it is common practice to relate the blast strength of a given explosive to some reference explosive that has been extensively documented through many experiments. Traditionally, TNT is taken as the standard explosive (Esparza, 1986). In addition, it is common to replace the energy yield of an explosive by simply its amount (or mass) because they are quite proportional to one another, and the measurement of mass is much easier. This leads to the notion of the equivalence factors of various explosives, which estimate the equivalent mass of TNT required to re-produce the same blast intensity (or effect) at some predefined (or reference) stand-off distance as a unit mass of a particular explosive of interest. That is, $W_{\mathrm{TNT}} = k_{\mathrm{exp}} W_{\mathrm{exp}}$, in which k_{exp} is the equivalence factor of the explosive with mass W_{exp}, and W_{TNT} is the equivalent mass of TNT. In the literature, equivalence factors are evaluated based on, e.g., the peak incident overpressure or incident positive specific impulse as the parameter of measuring the blast strength; although, some other publications report the TNT equivalence factor in terms of the heat of detonation of an explosive relative to that of TNT (Command, 1975).

Therefore, models developed to predict the blast parameters from TNT explosions can be used to predict the corresponding parameters associated with other types of explosives. However, it should be noted that the equivalence factors for a given explosive are generally dependent on the choice of the blast strength parameter (e.g., whether it is based on overpressure or specific impulse) and sometimes on the scaled distance at which such parameters were measured, see Cooper (1994), Esparza (1986), and Bogosian et al. (2016).

2.1.5 Reflected Blast Wave

In addition to the substantial increase in pressure, the passage of the shock wave through a region of air increases its density and particle velocities that, in turn, lead to significant increases in air's momentum and kinetic energy. When the incident wave encounters a structure, reflection occurs, and the reflected wave is the load that the structure will experience. The blast load, in this thesis, refers to the reflected blast wave and its associated specific impulse.

The reflected pressures are substantially larger than the original incident pressure of the incident wave (Kinney and Graham, 1985). This is because the presence of the structure (when treated as ideally rigid) imposes a zero velocity constraint on air particles, and consequently the initial kinetic energy and momentum (before reflection) lead to increases in the pressure (upon reflection). This significant rise in pressure is traditionally decomposed into acoustic and dynamic contributions under the simplifying assumption that the molecular structure of air (and hence its specific heat ratio) is unchanged. However, more accurate analysis shows that dissociation and ionisation of air (molecules) take place un-

der some strong shock conditions, which result in an additional increase of the reflected pressure (Command, 1975). The ratio of the reflected to incident pressures is known as the reflected pressure coefficient, C_r.

The intensity of the reflected wave depends primarily on three factors:

- Intensity of the incident wave;
- Orientation of the structure's surface relative to the direction of travel of the blast wave; and
- Lateral extent of the structure's surface.

An additional but less important factor is the relative rigidity of the reflecting surface compared to that of shocked air; it is common practice to conservatively treat a practical structure as perfectly rigid. The peak reflected overpressure is, typically, multiple times the peak incident overpressure. A parameter called the angle of incidence is defined as the angle between the inward normal of the incident shock front and the outward normal of the reflecting surface. Since reflection restricts the component of air particle velocity in the normal direction to the reflecting surface, the amplitude of the reflected wave is therefore dependent on the angle of incidence. When this angle is zero, a normal reflection takes place as the incident wave strikes the surface. When the angle of incidence approaches 90 degrees, no reflection occurs and the structure merely experiences the incident (or side-on) pressure.

Normal reflection is an upper limit on the reflected wave intensity for moderate to strong incident waves. Under normal reflection, the reflected pressure coefficient, C_r, is the sum of C_a (due to acoustic contribution) and C_d (due to the dynamic contribution). The dynamic contribution relates the dynamic pressure, $p_d = (\gamma+1)\left[(1/2)\rho_s \dot{u}_s^2\right]$ to the incident overpressure, p_{so}, such that $p_d = C_d p_{so}$, where ρ_s and $\dot{u}_s$ are the air's density and particle velocity behind the incident shock and γ is the ratio of specific heats of air; when these air's properties behind the shock are expressed in terms of the incident pressure, the dynamic coefficient of reflection can be determined, see Kinney and Graham (1985, Eq. (5-12), p. 72) assuming constant γ for the shocked air. When an acoustic (compressive) wave encounters a rigid reflecting surface, it reflects as a compressive wave of equal magnitude so that the reflected pressure is the superposition of the original incident (of overpressure magnitude p_{so}) and reflected waves (which has a magnitude of p_{so}, as just explained), and hence the total reflected pressure (due to the acoustic effect) is $p_{a,r} = C_a p_{so} = 2p_{so}$.

As indicated above, C_a is always 2, while C_d is an increasing function of the magnitude of the peak incident overpressure. When the incident intensity is sufficiently low, the effect of air's dissociation and ionisation is typically negligible, and C_d can be as high as 6. Therefore, under strong air blasts, the normally reflected pressure can be at least 8 times as high as the incident pressure, when air is assumed as perfectly ideal gas (Command, 1975; Kinney and Graham, 1985). However, as discussed above, the actual normally reflected to incident pressure ratio can be even higher than the cited value above (e.g., 20 or more,

see references cited in Command (1975)), owing to the expected real-gas effects, i.e., the dissociation and ionisation of air molecules, under strong shock conditions (Cormie et al., 2009).

From the above discussion, the normally reflected pressure requires knowledge of the intensity of the incident pressure and evaluations of the dynamic contribution, which is a function of the density and particle velocity of the air behind the incident shock, including the contribution from the dissociation and ionisation of the shocked air. Due to the difficulty in quantifying the last contributions, the normally reflected pressures are measured directly by appropriate sensor set-ups in blast experiments, using which empirical models are developed to predict the normally reflected blast parameters. Since reflection affects pressure, it also affects the specific impulse. However, the time durations and (obviously) the time of arrival were found to be unaffected by reflection.

A typical reflected blast wave, showing the reflected pressure-time history (indicated by the solid line), is shown in Fig. 2.1; the corresponding incident pressure-time history is also shown in the figure by the dashed line to highlight the substantial increase of pressure due to the reflection. Similar to the incident blast wave parameters, the normally reflected parameters were observed to obey Hopkinson-Cranz scaling, and the scaled reflected parameters depend only on the scaled distance Z (Baker et al., 1991). The actual variation of the peak reflected overpressure against the scaled distance, Z, is depicted in Fig. 2.2 for $Z \leq 5$ m/kg$^{1/3}$.

2.1.6 Oblique Reflection

Oblique reflection results when the wave incidentally strikes the structure at angles θ between 0 and 90 degrees. Within that range, a critical sub-range (generally for $\theta \approx [40 - 50]$ degrees) exists for which an abnormal phenomenon emerges, known as the formation of the Mach wave (coalescence of incident and reflected waves) and its corresponding front (referred to as Mach's stem). The exact range of angles of incidence leading to Mach stem's formation depends on the incident wave's intensity.

In general, the magnitude of the reflected wave is at maximum under normal reflection, and its intensity decreases as the angle of incidence increases. However, there is a gradual increase and then decrease in the reflected wave intensity as the angle of incidence (increasingly) passes through the critical range described above. For a rigid and infinite reflecting surface, the reflected pressure is solely a function of the incident pressure and the angle of incidence (Kinney and Graham, 1985).

2.1.7 Blast Clearing

When the structure is of finite dimensions (as is always the case in reality), the actual transient reflected pressure can be substantially reduced due to a phenomenon called blast clearing, discussed in detail by Rigby (2014). Such a process develops due to the

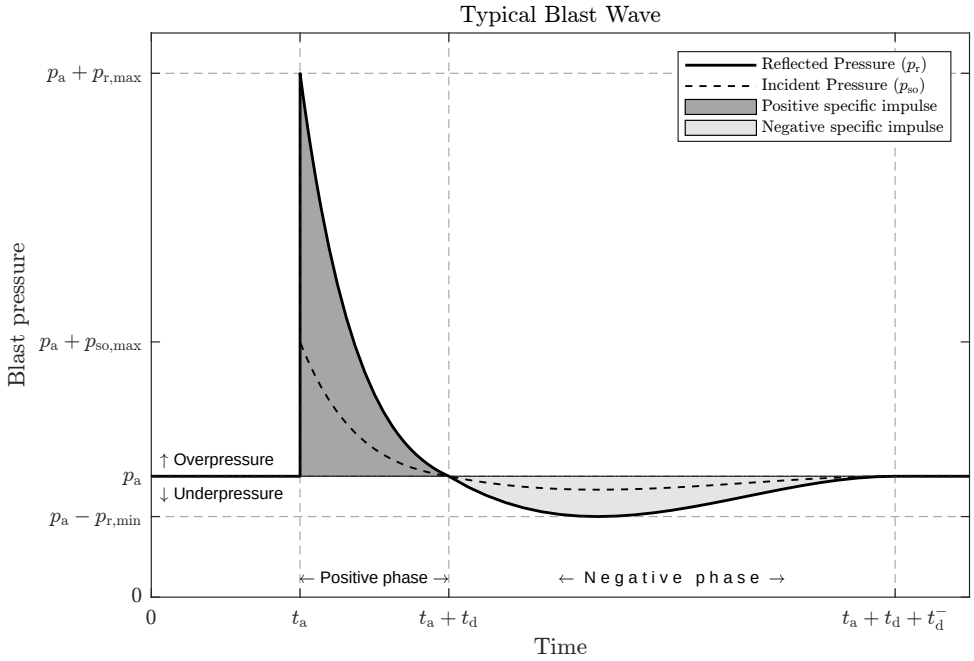

Fig. 2.1. Typical blast wave. Shown are the reflected pressure (solid line) and incident pressure (dashed line) time histories. t_a, t_d, t_d^- denote the time of arrival (of the shock wave), the duration of positive phase (when the pressure, p, is above the atmospheric pressure, p_a), the duration of the negative phase (during which $p \leq p_a$). The peak relative pressure (or peak overpressure) is $p_{r,max}$, and the minimum relative pressure (or minimum underpressure) is $p_{r,min}$. The time interval $t_a \leq t \leq t_a + t_d$ defines the positive phase, whereas $t_a + t_d \leq t \leq t_a + t_d + t_d^-$ defines the negative phase of the blast wave. Shaded areas represent the reflected positive and negative specific impulses.

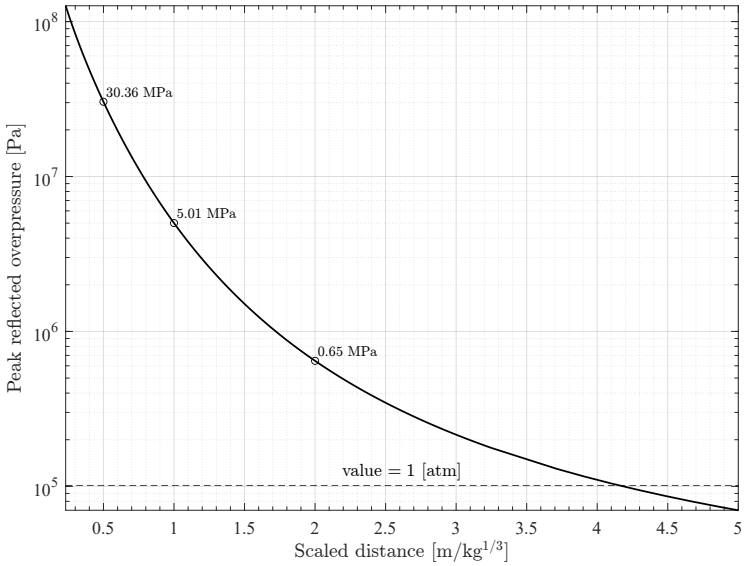

Fig. 2.2. Reflected peak overpressure versus distance. This is the trace of the peak reflected overpressures at different distances (or equivalently, for a fixed explosive charge, scaled distances). As can be seen, the distance from the blast centre plays an important role in the peak reflected overpressures generated by the blast. The horizontal dashed line corresponds to a pressure value of 101.23 [kPa], i.e., equivalent to 1 atmospheric pressure. This figure was generated using ConWep formulae for free air blast and a TNT charge of 10 kg; although, the overpressure is independent of the actual mass of charge used to construct the graph, as it depends only on Z. The ordinate values of the three labelled data points (at $Z = [0.5, 1, 2]$ m/kg$^{1/3}$) were rounded to the nearest 0.01 MPa. Note that a Log-scale is used for the vertical (overpressure) axis. Notice that the given pressures are the blast overpressure, i.e., the pressure in excess of the atmospheric pressure.

formation of rarefaction waves along the edges (free boundaries) of the loaded surface of the structure. This is due to an initial existence of pressure differentials since the reflected pressure distribution is not smooth over regions joining two surfaces with abrupt changes in their respective angles of incidence.

The rarefaction (or clearing) waves, which are expansive and emanating from the free edges, then propagate towards the interior of the loaded surface and, hence, reduce the current reflected overpressure. Therefore, blast clearing waves can substantially affect the actual amount of positive specific impulse and shrink the positive phase of the reflected blast wave at some points on the loaded surface of the structure, depending on how far the points are from the nearest free edges (Rigby, 2014). Clearing waves travel at sonic speed.

2.1.8 Blast Loading

The blast load, therefore, is the reflected blast wave, which itself is caused by the reflection of an incident wave of high pressure and large momenta of shocked air particles. Blast loads are classified into two main types: far- and near-field blast loadings (Tyas, 2019), depending primarily on (i) the shortest stand-off distance of the structure from the charge's centre and (ii) the size of the charge in relation to the shortest stand-off distance and the dimensions of the structure's exposed surface.

A far-field blast load corresponds to the case when the structure is sufficiently far from the explosion's centre (Tyas, 2019), and thus it is generally associated with the following features:

- Planar shock wave front;
- Little or no variations of stand-off distances, angles of incidence, and times of arrival over the exposed surface of the structure;
- Moderate reflected peak overpressures;
- Relatively long positive phase durations; and
- Possibly significant negative specific impulses.

On the other hand, near-field blasts, which correspond to the case when the structure is close to the explosive's centre, are associated with the following characteristics (Tyas, 2018; Tyas and Pope, 2003; Tyas, 2019; Rigby et al., 2015):

- High curvatures of the blast wave front;
- Considerable variations of stand-off distances, angles of incidence, and times of arrival over the structure's exposed area;

- Extremely high reflected overpressures, especially in localised areas associated with the smallest stand-off distances and angles of incidences;
- Very short positive phase durations; and
- Significant positive specific impulses (and their spatial profiles follow that of the reflected pressures above).
- Shape and directional effects of the charge could be significant;
- Instabilities and fireball-shock front interaction might influence local pressure levels;

The combination of the last features indicates the very complicated nature of near-field blast loadings. In particular, near-field blasts are of high peak pressures, large specific impulses, extremely short durations, and considerable spatial non-uniformities or localisations (Tyas, 2019; Rigby et al., 2015). Also, different regions of the structure start to be loaded at different times, which may induce sharp transverse shear differentials. Fig. 2.3 shows typical spatial distributions of the important blast parameters in the near-field range; the profiles of the various parameters were normalised by their maximum values.

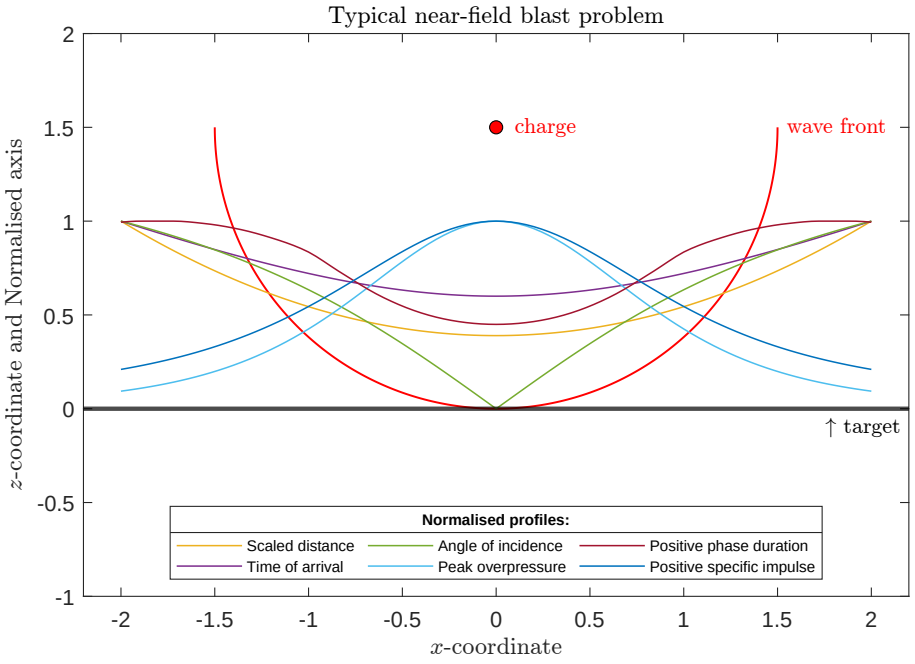

Fig. 2.3. Typical spatial variations of the positive phase blast parameters, associated with a typical near-field blast problem, over the surface of a rigid target. The charge (small red circle at $(x = 0, y = 0, z = 1.5)$) is detonated above the target (solid black line at $z = 0$); thus, the smallest stand-off distance is 1.5 unit of length. The red (inverted) semicircle represents a vertical section (at $y = 0$) of the spherical profile of the shock front when the wave just touched the target for the first time. The various blast parameter profiles were normalised with respect to their maxima to ease the visualisation. As can be seen, the blast parameters (namely the peak overpressure, positive specific impulse, and positive phase duration) are highly localised, and this is mainly because the charge is very close to the target. Note: Mach's stem effect was not included.

A thorough characterisation of the near-field blast loading is provided by Tyas and his team (2015; 2015) of the Blast and Impact Engineering research group at the University

of Sheffield. The team developed a robust experimental apparatus, called the Characterisation of Blast Load (or CoBL), to resolve both the temporal and spatial distributions as air's shock waves reflect off practically rigid targets. Several split-Hopkinson's pressure bars (split-HPBs), which are long and thin rods, are used as high-resolution pressure sensors. Certain arrangements of the split-HPBs are constructed to record reflected near-field blast waves at varying stand-off distances and angles of incidence. The authors provide quantitative evidence of the following: the spatial profiles of the peak reflected pressures and positive specific impulses are highly non-uniform (or localised), as is schematically shown in Fig. 2.3, the peak reflected pressures are typically in the tens or even hundreds of megapascals [MPa], the durations of the positive phase are typically in sub-milliseconds [ms] range, the negative phase is negligible (Tyas, 2018; Tyas, 2019; Rigby et al., 2015). The experimental diagnosis of the near-field blast load is recently improved by utilising the high-speed video (HSV) imaging technique (Rigby et al., 2020a), where the intensity and full-field distribution of the reflected near-field blast waves are correlated to the kinematics of the rising fireball generated by a high explosive's detonation.

Tyas (2019) defines the near-field blast as the one when the scaled distance is approximately less than 0.5 [m/kg$^{1/3}$], for which instabilities from the fireball do not appear; (Rayleigh-Taylor) instabilities may form and influence the reflected pressures in the range of scaled distances of about 0.5-2 [m/kg$^{1/3}$]. Furthermore, Gel'fand et al. (2004) suggest that the near-field domain size R_{nf} could be defined as $0 \leq R_{\text{nf}} \leq 20r_{\text{charge}}$, where r_{charge} is the characteristic dimension of the explosive charge.

2.1.9 Blast Loading Characterisation

The blast loading on a structure is characterised by the blast parameters of the positive and negative phases of the reflected blast wave. Once the parameters are known, the transient reflected pressure can be described using the modified Friedlander's function during the positive phase and the Granström's cubic polynomial (in terms of time) for the negative phase.

The reflected blast parameters under normal reflection can be determined using the semi-empirical model of Kingery and Bulmash (KB) (1984), which is available in graphical format in U.S. Army (2008). The parameters for oblique reflection can be estimated (for any angle of incidence) when the normally reflected and original incident wave parameters are known. The incident wave parameters can also be determined from the KB model (1984). Predictive models for the incident and normally reflected negative phase parameters are discussed in Rigby et al. (2014b).

The KB model predicts the blast parameters in terms of the Hopkinson-Cranz scaled distance, Z, and the cube root of the TNT equivalent mass, W_{TNT}, and it was developed from (i) a large compilation of experimental data from various sources during the second half of the last century (for moderate to large Z), and (ii) numerically reproduced data from computational explosive analyses (for the smallest values of Z). This fast-running

model is extensively shown to be accurate for the predictions of the incident and normally reflected blast parameters that are associated with free air and ground surface explosions from detonations of spherical and hemispherical TNT charges (Cheval et al., 2010; Cheval et al., 2012; Rigby et al., 2014a). The model accuracy is especially high for far-field blasts, but it becomes more questionable as the target becomes very close to the explosion's centre, i.e., in the near-field blast range (Rigby et al., 2015; Bogosian et al., 2002). A computer program known as ConWep and developed by (1992) provides predictions based on the model of KB.

Fig. 2.4 gives the normally reflected *scaled* blast parameters of the positive phase of the blast wave in terms of the scaled distance Z, according to the KB model; the blast is assumed to be due to a *spherical* TNT charge and the wave is propagating in free air before it is (normally) reflected at a perfectly rigid plane. On the other hand, the corresponding incident peak overpressure and incident positive specific impulse can be obtained from Fig. 2.5; in this figure, the ratios of the reflected to incident values of peak overpressure and scaled positive specific impulses are also shown to demonstrate the previously discussed substantial increases in blast parameters upon the normal reflection of the blast wave at a rigid target. Note that the time parameters for the incident wave are identical to those for the reflected wave, as was shown in Fig. 2.4.

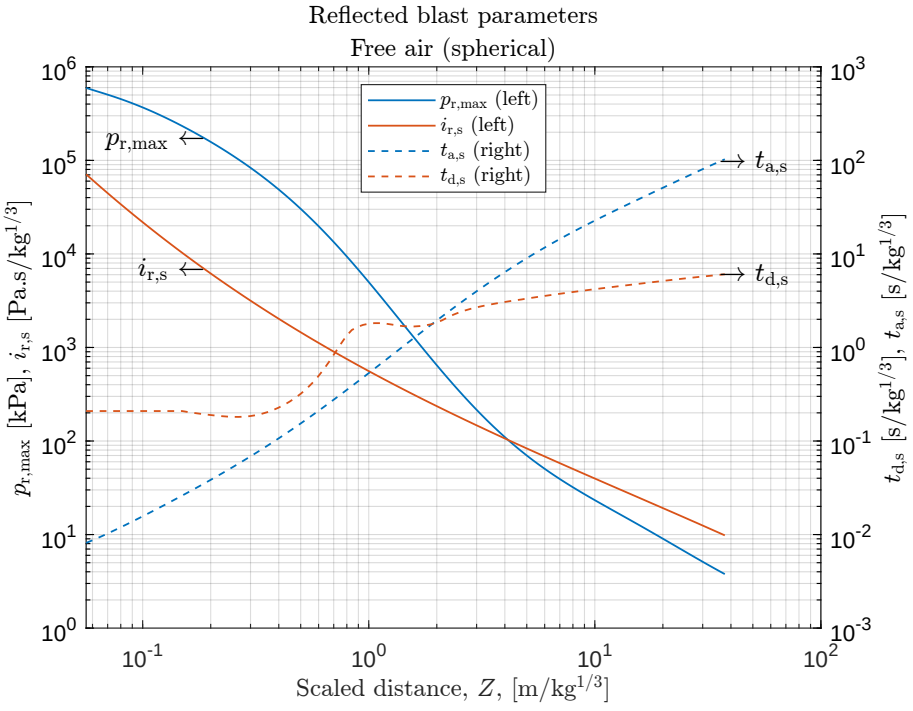

Fig. 2.4. Reflected scaled blast parameters of a free air (spherical) blast wave. The values of the peak reflected overpressure $p_{r,max}$, scaled positive specific impulse $i_{r,s}$, scaled time of arrival $t_{a,s}$, and scaled positive phase duration $t_{d,s}$ are given in terms of the Hopkinson-Cranz scaled distance $Z = R/W_{TNT}^{1/3}$. The actual specific impulse, positive phase duration, and time of arrival can be obtained by multiplying the scaled values (shown in the figure) by $W_{TNT}^{1/3}$. For visual convenience, the pressure and specific impulse curves correspond to the left vertical axis, whereas the time parameters are associated with the right vertical axis, as shown in the legends and by the arrows in the respective graphs. These curves are reproduced after the KB model.

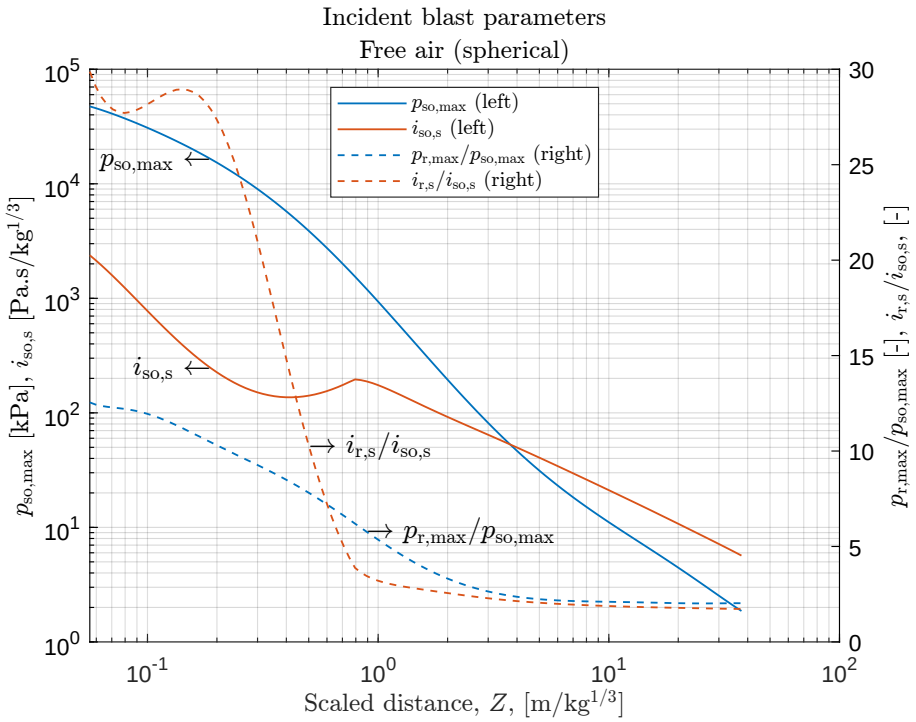

Fig. 2.5. Incident scaled blast parameters of a free air (spherical) blast wave. The values of the peak incident overpressure $p_{so,max}$, scaled positive specific impulse $i_{so,s}$ are given in terms of the Hopkinson-Cranz scaled distance $Z = R/W_{TNT}^{1/3}$. The actual specific impulse is obtained by multiplying the scaled values (shown in the figure) by $W_{TNT}^{1/3}$. The incident overpressures and specific impulses are associated with the left vertical axis. Additionally, the ratio of peak reflected overpressure $p_{r,max}$ to peak incident overpressure and scaled reflected positive specific impulse $i_{r,s}$ to scaled incident positive specific impulse for various scaled distances are shown as the dashed lines, which corresponds to the right vertical axis; note that the right-hand axis is not associated with the (log-spaced) horizontal grid lines. The reflected parameters correspond to normal reflection. These curves are reproduced after the KB model.

During the positive phase, the transient reflected pressure, $p_r(t)$, is represented by the following modified Friedlander function

$$p_r(\tau) = p_{\mathrm{r,max}}(1-\tau)e^{-b\tau},$$

where the normalised time τ is

$$\tau = \frac{t - t_{\mathrm{a}}}{t_{\mathrm{d}}}, \quad 0 \le \tau \le 1,$$

and b is known as the exponential decay coefficient, which, after Rigby (2014), can be evaluated by the iterative solution of the equation of the positive specific impulse,

$$\begin{aligned} i_r &= t_{\mathrm{d}} \int_0^1 p_r(\tau)\, d\tau \\ &= t_{\mathrm{d}}\ p_{\mathrm{r,max}} \int_0^1 (1-\tau)e^{-b\tau}\, d\tau \\ &= t_{\mathrm{d}}\ p_{\mathrm{r,max}} \left[\frac{b + e^{-b} - 1}{b^2}\right]. \end{aligned}$$

In the above, i_r, $p_{\mathrm{r,max}}$, and t_{d} are the (normally reflected) values, respectively, of the positive specific impulse, peak overpressure, and positive phase duration, as predicted from the KB model. The blast wave arrival time is t_{a}.

There is a publicly available chart, see, e.g., Kinney and Graham (1985, Figure 5-5(a) and Figure 5-8), Cormie et al. (2009, Figure 3.9), and Rigby et al. (2020a, Fig. 9) to estimate the reflected pressure under an oblique reflection in terms of the angle of incidence and peak incident overpressure which accounts for Mach's stem formation at the critical angles of incidence associated with the respective intensities of the incident waves. However, as an alternative approximate method, the dependence of the actual reflected pressure can be reduced in terms of the incident pressure and also the normally reflected pressure (to grossly contain the effects of the dynamic and air's dissociation contributions during the wave reflection) for a given angle of incidence. Therefore, the obliquely reflected pressure, $p_r(\theta) \equiv p_{r,\theta}$, can be predicted in terms of the angle of incidence (in radians), θ, the incident (or side-on) pressure, p_{so}, and the normally reflected pressure, $p_{r,0} \equiv p_r(\theta = 0)$, according to

$$p_{r,\theta} = \left[1 + \cos(\theta) - 2\cos^2(\theta)\right] p_{so} + \left[\cos^2(\theta)\right] p_{r,0}$$

Note that $p_{r,\theta}$ is being interpolated (trigonometrically) from $p_{r,0}$ when $\theta = 0$ down to p_{so} when $\theta = \pi/2$. The formula applies to the transient (time-varying) pressure at homologous times, i.e., the pressures $p_{r,\theta}$, p_{so}, and $p_{r,0}$ correspond to the same time instant and the relationship can be applied for all time instants. However, this approximate formula should not be applied near the range of critical angles of incidences (generally for $\theta \approx [40 - 50]$ degrees) where Mach's wave would form. The specific impulse due to oblique reflection can

also be predicted using the above trigonometric interpolation formula where all pressures are replaced by the corresponding specific impulses, i.e., to predict the oblique reflected specific impulse $i_{r,\theta}$ (for any angle θ) in terms of the incident i_{so} and normally reflected $i_{r,0}$ specific impulses; Namely,

$$i_{r,\theta} = \left[1 + \cos(\theta) - 2\cos^2(\theta)\right] i_{so} + \left[\cos^2(\theta)\right] i_{r,0}$$

The (reflected) pressure in the negative phase is modelled by Granström's cubic equation,

$$p_r(\tau^-) = (27/4)\, p_{\mathrm{r,min}} \tau^- \left(1 - \tau^-\right)^2,$$

where $\tau^- = \left[t - (t_\mathrm{a} + t_\mathrm{d})\right]/t_\mathrm{d}^-$, $0 \leq \tau^- \leq 1$. $p_{\mathrm{r,min}}$ is the peak (reflected) underpressure, and t_d^- is an estimate of the negative phase duration that preserves the negative specific impulse, i_r^-, i.e.,

$$t_\mathrm{d}^- = (16/9)\, i_\mathrm{r}^- / p_{\mathrm{r,min}}$$

In the definition of τ^-, $(t_\mathrm{a} + t_\mathrm{d})$ is the starting time of the negative phase. The blast negative parameters, $p_{\mathrm{r,min}}$ and i_r^-, can be predicted using available models (U.S. Army, 2008).

An extensive review of the mathematical modelling (or predictions) of the blast wave parameters is available in Rigby (2014), Command (1975), and Cormie et al. (2009), from which the present material is taken. Although, the reader should be aware that most of the available predictive models for the blast load characterisation have been validated for the far-field blast cases, and the near-field blast characterisation is still under active research (Tyas, 2019; Tyas, 2018; Rigby et al., 2015; Rigby et al., 2018), as will be discussed later in Section 2.1.10.

In the present work, the focus is on the prediction of the response of thin targets (thin plates or membranes) when subjected to near-field blasts. Furthermore, owing to the extremely short duration of a typical (near-field) blast wave, the target is assumed to be impulsively loaded, i.e., the external blast pressure pulse is completed whilst the target is practically intact (not deforming). Consequently, the thin target is said to be loaded by the specific impulse. A recently developed model to predict the specific impulse profile over a target is the one proposed by Pannell et al. (2021). The model applies to near-field blasts induced by the detonation of spherical charges made of PE4, and the specific impulse is described in terms of (a spatially varying) angle of incidence and the shortest stand-off distance (which corresponds to the zero angle of incidence) and the mass of the PE4 charge. According to Pannell et al., the specific impulse profile $i(\theta)$ is given by the following Gaussian model

$$i = aZ^{-n} \exp\left(\frac{-\theta^2}{b}\right) W^{1/3},$$

where θ is in degrees, Z is the smallest scaled distance (corresponding to $\theta = 0$), W is the

mass of the spherical PE4 charge, and a, n, and b are the model's coefficients: $a = 0.557$, $n = 1.663$, and $b = 2007$ which are valid for $0.11 \leq Z \leq 0.55$ [m/kg$^{1/3}$]. The authors also give refined values of the coefficients as $a = 0.383$, $n = 1.858$, and $b = 1829$ that provide more accurate predictions for the extreme near-field case for which $0.11 \leq Z \leq 0.21$. The spatial profile of i can then be determined once θ is evaluated at the various spatial points on the target.

2.1.10 Limitations of Available Fast-Running Blast Loading Models

It should be re-emphasised that the available fast-running models, namely the KB model (U.S. Army, 2008; Kingery and Bulmash, 1984), to predict the parameters of the blast wave are shown to be accurate for the moderate- to far-field blast cases, i.e., when Z is relatively large, e.g., $Z \geq 4$ [m/kg$^{1/3}$], since the models were mainly developed using data corresponding to these blast scales (Rigby et al., 2014a). Moreover, the available models apply to idealised blast settings, e.g., spherically shaped charges detonated in free air and reflecting upon infinitely wide rigid targets (Command, 1975). Tyas (2019) discusses the significant overprediction of the positive reflected specific impulses of the ConWep (the computer implementation of the KB model) in the near-field range. Also, the models require the estimation of the TNT-equivalence factor of a given explosive type, the values of which (if available) vary from source to source in the literature (Cooper, 1994). In addition to the reduced accuracy for near-field blast cases, the effects of angles of incidence, given their localisations, are cumbersome to accurately model. Almost all available fast-running models are deficient in describing the effect of the rising fireball and its interaction with the nearby target and the likely occurrence of the after-burn effect (Tyas, 2019; Tyas, 2018).

In an attempt to overcome the above limitations and to accurately predict the blast loading, the blast event is numerically simulated using some commercially available computational fluid dynamics solvers (or hydrocodes) and/or specialised finite element software (Rigby, 2014; Pannell, 2022; Curry, 2017; Pope, 2002). Although this approach might be associated with computational cost, it provides valuable means to predict the blast loading associated with (practically) any blast problem. In the present work, the blast event is modelled using the finite element method in combination with the multi-material arbitrary Lagrangian-Eulerian (MM-ALE) framework using LS-DYNA.

Using the latter approach, the air is modelled by its equation of state and is assumed at ambient conditions initially, and the explosive is modelled explicitly before detonation. The explosive is set to detonate at a particular point, and its detonation is modelled using the explosive's Chapman-Jouguet's properties that allow predicting the final state of the explosive upon detonation. These post-detonation states are then taken as the initial states of the detonation by-products (the hot gaseous products). The gaseous by-products are treated as a single (gaseous) material, and it is then modelled by its equation of state. Through the interaction of this detonation by-product with the surrounding ambient air, a

shock wave develops in the air and travels outwardly (from the centre of the inert explosive) with supersonic speed, i.e., the shock wave formation and its propagation through the air are modelled explicitly. Eventually, the propagating shock impinges on a priorly defined structural target. The reflected overpressures (i.e., absolute pressures minus the initial ambient air pressure) at various points on the exposed side of the target are recorded. The specific impulse profile is then generated by time-integrating the reflected overpressure time histories corresponding to the various points. In this approach, the domain is described using an ALE mesh, an effective technique that combines the advantages of a purely Lagrangian and purely Eulerian meshes and avoids some of their limitations, an overview of which will be given in Section 5.4. Furthermore, the adopted approach employs the novel multi-material element technology that allows more than one material to occupy the same element, each of which has its distinct material interface. This approach has been demonstrated to provide accurate predictions of general blast loadings. Excellent guidelines for this approach are given in Rigby (2014, Chapter 3) and Curry (2017).

2.2 Response of Structures to Blast Loadings

2.2.1 Overview

One of the simplest and most popular analytical methods for the analysis of blast-loaded structures is the equivalent single-degree-of-freedom (SDOF) model, which is originally developed by Biggs (1964), in which the actual structure is replaced with an equivalent mass-spring oscillator having effective structural properties, which are related to the actual ones by means of the mass, stiffness, and load transformation factors; the factors are functions of the assumed mode shape (of the actual structure's displacement). In essence, the transformation operation removes the spatial dependence, and the resulting SDOF becomes a single ordinary differential equation in time. Such simple idealisation enables important concepts to be easily understood and useful results to be derived. For example, the SDOF technique highlights and explains the notion of the pressure-impulse diagram. Furthermore, this analysis gives the important result that structures would respond impulsively when the pressure pulse's duration becomes very small compared to the time the structure requires to attain its maximum response. When the response is nearly impulsive, the exact magnitude of the pressure and the shape of the pressure pulse are irrelevant, only the impulse and the duration of the load are significant. This topic is extensively covered by U.S. Army (2008), Kinney and Graham (1985), Biggs (1964), and Cormie et al. (2009).

Although, the SDOF model assumes that the mode shapes correspond either to the first vibrational mode of the actual structure in question or to the static elastic or elasto-plastic displacement mode of the structure; the latter assumption is the most common in practice (U.S. Army, 2008, Sections 3.16-3.17). That is, the central assumption of the SDOF model is that the deformed shape is known a priori as given by the "static" mode that

depends on the spatial distribution of the external load and the geometry of the structure, and the transformation factors are, thus, already tabulated in design manuals for certain special cases, e.g., a uniformly loaded and simply supported Euler-Bernoulli beam. As the load becomes spatially non-uniform and/or the response of the structure's material becomes non-linear, the SDOF model loses its simplicity as the calculations of the transformation factors become quite involved. Moreover, under near-field blast loading, the actual displacement profile is far from being close to the static mode of the structure (Pope, 2002; Curry, 2017). In fact, the mode (shape) is highly transient (or time evolving) when the blast pressure magnitude far exceeds the plastic capacity of the structure, this is the case even when the blast loading is uniform (Hopkins and Prager, 1954).

Following the development of the modern theory of plasticity (i.e., the flow theory) and the theorems of static plastic analysis (Drucker et al., 1952; Prager, 1942; Prager, 1948), the analysis of the transient dynamic response of various structures under intense dynamic loads has been an active research field; in particular, such activity dates back to the early 1950s (Hopkins and Prager, 1954; Wang and Hopkins, 1954; Hudson, 1951), see Jones (1996) for an extensive list of references. Only the conclusions of the earlier works will be presented herein.

It has been consistently argued that under intense but extremely short dynamic loading due to blast or impact events, structures respond mostly impulsively and the resulting deformations are mainly plastic. As in the classical limit analysis of structures under static loading, the rigid-plastic material idealisation has been proven powerful and successful in describing the structural response in the dynamic regime (Jones, 2010; Jones, 2012). In the rigid-plastic material idealisation, elastic deformations are neglected, and a structure made thereof remains rigid unless its plastic capacity is reached at a given point (or section) within the structure; when the later condition is met, the structure undergoes purely plastic deformations.

The first step in carrying out a dynamic rigid-plastic analysis is the specification of the plastic limit curve (or yield surface) in the principal stress space; this surface is the geometric representation of the material's yield condition. When a stress point (in that space) is within the interior region bounded by the surface (but not on it), the material is said to be rigid. A stress point on the surface represents a state of yielding of the material, and this latter case is accompanied by increments (or rates) of plastic strains. The increment (or rate) of plastic strain is expressed by the flow rule. Inspired by the well-established fact that, for elastic materials, the elastic strain is the gradient (or derivative) of a well-defined function (called the elastic complementary energy, or the elastic complementary potential) with respect to the stress, the rate of plastic strain is formulated to be proportional to the gradient of an assumed function (called the plastic potential) with respect to the stress when the stress state satisfies the yield condition. The proportionality factor is called the rate of plastic multiplier. When the plastic potential function is identically the yield function, the plastic strains are said to be described by an "associated" flow rule. For materials obeying the associated flow rule, the plastic strains are always normal to the

yield surface (expressed in terms of stresses) and pointed to the exterior; this is called the normality rule. The plastic multiplier rate is required to be always non-negative, and it can be non-zero only when the current stress state is on the yield surface (i.e., the yield condition is satisfied). Further details of the development and results of the flow theory of plasticity can be found in Chen and Han (1988).

If the yield surface is a function of total plastic strain, plastic strain rates, or both, then the material is said to be strain-hardening, strain-rate sensitive (or visco-plastic), or both, respectively. A general rigid-plastic model incorporates all the above effects when they are applicable, depending on the type of material in question. Their inclusions, however, generally increase the level of complexity of the analysis. The most basic and computationally attractive case is the rigid-perfectly plastic model, described in great detail for the static regime by Prager and Hodge (1951) and the dynamic regime by Jones (2012), in which the yield surface is assumed constant (and fixed) throughout the motion of a given structure. Two widely used yield conditions for metallic structures are those due to von Mises's and Tresca's, explained in Chen and Han (1988), which are both pressure-independent; that is, yielding of a material obeying these criteria is induced by shearing action only (i.e., by shear or deviatoric stresses). Since the volumetric and deviatoric behaviours are mutually orthogonal, then when a von Mises's or Tresca's material yields, only distortional or shearing deformations take place (i.e., no volume change occurs, and for this reason, the material is said to be plastically incompressible).

In the literature, there are several closed-form solutions obtained by various researchers for dynamically loaded structures, in particular where the load is impulsive. Some works belong to the second half of the last century, such as the works of Hudson (1951) and Hopkins and Prager (1954) as mentioned earlier, but there continue to be recent works such as the analytical models of Cloete and Nurick (2014) and Mehreganian et al. (2019b). Most of the available models were based on the "rigid-perfectly plastic" assumption of the material's behaviour. The investigated structures include beams and (circular and rectangular) plates with various boundary conditions. However, the earlier (from the 1950s until the late 1980s) models were limited to uniform blast loading; it transpires that near-field blasts were not an issue or unrevealed at the time. A thorough review of the analytical and experimental studies during this period regarding the dynamic response of plastic structures can be found in Jones (1989), Jones (1996), and Symonds (1967).

2.2.2 Basis of the Main Analytical Technique

The field of investigating the response of engineering structures under intense dynamic loads has attracted the interest of many researchers. By far, the idealisation of a rigid-plastic material behaviour has been the basic framework based on which several approximate closed-form solutions were obtained. In the earlier works, responses to uniform dynamic pressure and uniform impulse were the main topics. Both small and large displacement regimes were considered in the response of circular and rectangular plates and

beams with various boundary conditions. Some works will be discussed in the next subsection.

Again, structures were idealised as rigid-plastic, and the particular spatial form of the dynamic load is assumed a priori. The first step is to find the "quasi-static" limit load by means of the upper and lower limit analysis theorems and to assume the incipient collapse mechanism. The mechanism should be consistent with the underlying yield function, its associated flow rule, and the boundary conditions. At the static collapse load, motion follows the "quasi-static" mechanism. As the dynamic load intensity increases further, the determination of the resulting dynamic mechanism becomes highly involved, and hence it is typically assumed. Then, the exact dynamic equilibrium equation is formulated in which the acceleration derives from the assumed collapse mechanism. The equation is then solved while avoiding any violation of the yield condition and the flow rule. If yield violation cannot be avoided, then the initially assumed mechanism is wrong. In this case, another initial mechanism must be chosen, and the process is repeated. The solution is valid when equilibrium, yield conditions, flow rule, and the boundary conditions are all satisfied. Thin plates are found to initially respond in flexure, and as displacement increases further, membrane effects evolve and become dominant. The load-free membrane response is typically driven by some initial displacement and velocity conditions, which are the final states of the initial flexural phase of the response.

Typically, the eventual correct solution could be associated with a "dynamic" collapse mechanism that is substantially different from the "quasi-static" mechanism. Since the material is rigid-plastic, then the motion will eventually end, which happens when the external loads are removed and the instantaneous velocity is zero everywhere (i.e., current kinetic energy and external work are simultaneously zero; note that accumulated plastic energy is dissipative, and hence it is not available to the structure to drive further motion).

The methodology behind the earlier works has been continued recently where non-uniform blast loads are also studied, which will be discussed below. However, the so-obtained solutions apply to the initially specified spatial forms of the loading function. Response to arbitrary loading has not been obtained. Furthermore, no solution for membranes' responses due to initial conditions imposed directly by the blast load (namely in terms of the blast-generated specific impulse) is available.

2.2.3 Analytical Models

Hudson (1951) presented a simplified analytical method to predict the permanent deformation of thin ductile circular membranes loaded by uniform impulsive pressures arising from underwater explosions and conducted experiments to validate the predictions. The load was replaced with an idealised impulse and, hence, was converted into an instantaneous uniform initial velocity profile.

Hopkins and Prager (1954) developed the concept of stationary and travelling plastic

hinge circles in analysing circular plates under uniform blast pressures. The small displacement regime was assumed to exclude the membrane action, and the plate was simply supported along its edge. The fully clamped problem was addressed later by Hopkins and Wang (1954). Hopkins (1957) discussed the theory in a separate work. Wang (1955) solved a similar problem but idealised the blast load as a uniform impulse such that the plate picks an instantaneous uniform velocity field, similar to the treatment in Hudson (1951) discussed above; that is, the circular plate was load-free during its entire motion. Florence (1966) conducted several blast experiments and compared the measurements to the predictions of Wang (1955).

The one-dimensional version of these works was treated by Parkes, who studied the evolution of deformation of cantilever (1955) and fixed-fixed (1958) beams subjected to point impacts of concentrated masses. The author compared the obtained solutions to his experimental results. Parkes's cantilever model was reviewed by Wang and Yu (1991) and also in Symonds and Fleming (1984). The first analytical treatment of non-circular targets was addressed by Cox and Morland (1959) where the dynamic response of a uniformly blast-loaded rectangular plate is investigated.

In all these pioneering works, the structure's material is modelled as rigid-perfectly plastic, an idealisation that neglects elastic deformations. The systematic technical procedures involved in the works discussed so far are illustrated at an elementary level in the books of Chakrabarty (2010, Chapter 8) and Jones (2012).

The large-displacement problem of the circular membrane under uniform impulsive load was considered by Jones (1967) and Mihailescu-Suliciu and Wierzbicki (2002). Wierzbicki and Nurick (1996) solved a similar case but with a localised uniform impulsive load applied over partial regions of the circular plate. In the latter works, the eigen-function expansion method was used to solve the derived *linear* partial differential equation (PDE) governing the plate's motion, in particular during the final phase in which membrane action prevailed. Wierzbicki (1974) discussed the possibility of extending the eigen-expansion method (or the principle of superposition) to plasticity problems when the loading regime is monotonic. Martin (1964) utilised the fundamental principles of mechanics to derive theoretical bounds on the motion of rigid-plastic structures in response to impulsive loading, although under the assumption of small displacements. Similar bounding theorems were extended to the large-displacement case by Ploch and Wierzbicki (1981) and Ronter and Martin (1972).

Symonds and Fryer (1988) critically examined the applicability of the perfect-plasticity assumption in the dynamic regime, which later led to the development of the well-known and widely used Cowper-Symonds's (1957) model for the dynamic yield stress as a function of strain rate. However, elastic deformations were shown to be still negligible as the load approaches the impulsive regime (Symonds and Fryer, 1988).

Martin and Symonds (1965) developed an approximate theory to predict the displacement of rigid-plastic structures by the so-called mode approximation technique, in which a kinetic energy-based functional is minimised to adjust the assumed velocity field which gives

Table 2.1. Analytical works to study the dynamic response of rigid-plastic structures under extreme dynamic loadings

	Small displacement (flexure)	Large displacement (membrane)
Circular plate	(Hopkins and Prager, 1954), (Wang and Hopkins, 1954; Wang, 1955), (Micallef et al., 2012; Micallef et al., 2014)	(Hudson, 1951), (Jones, 1967), (Mihailescu-Suliciu and Wierzbicki, 2002), (Wierzbicki and Nurick, 1996), (Cloete and Nurick, 2014), (Tyas and Pope, 2003), (Rigby et al., 2019a)
Rectangular plate	(Cox and Morland, 1959), (Mehreganian et al., 2019b)	(Mehreganian et al., 2018a; Mehreganian et al., 2019a), (Gharababaei and Darvizeh, 2010), (Jones, 2014), (Lomazzi et al., 2021)
Beam	(Parkes, 1955; Parkes, 1958), (Wang and Yu, 1991),(Symonds and Fleming, 1984)	(Symonds and Mentel, 1958)
Theory	(Hopkins, 1957), (Martin, 1983), (Martin and Symonds, 1965)	(Ploch and Wierzbicki, 1981), (Ronter and Martin, 1972)

the time-independent mode. Martin (1983) mathematically derived that an impulsively loaded structure (plate as an example) eventually converges to a mode-form response. It is remarkable to notice that the current practice of structural blast analysis, namely the SDOF method is related to Martin-Symonds's theory. The SDOF method is adopted in U.S. Army (2008), which is available at (UFC, 2022), and is applied in Rigby et al. (2014c) for the response of an elasto-plastic plate under realistic blast loading. As outlined earlier in Section 2.2.1, the SDOF technique utilises transformation factors based on the static deformation mode of the structure being analysed and is due to Biggs (1964). The main difference between Biggs's and Martin-Symonds's techniques is the choice of the mode shape.

The reader is referred to the three papers written by Jones (1996; 1989; 1978) for more discussion on the earlier developments in the field. Throughout his scientific contributions, see Li (2016), Jones consistently shows that the rigid-plastic material idealisation is an indispensable and suitable tool for blast analysis of structures. A summary of the earlier and recent publications that studied the dynamic response of rigid-plastic structures under extreme dynamic loadings (e.g., blast and impact) is provided in Table 2.1. Additional references can be found in Jones (2012), J. Chakrabarty (2010), Jones (1996), Jones (1989), Jones (1978), and Lomazzi et al. (2021).

In 1989, Nurick and Martin (1989a; 1989b) published the two-part paper, and their findings were recently revisited by Chung Kim Yuen et al. (2016). The three papers provide excellent predictive models for the permanent peak displacement of extremely thin plates, i.e., membranes, subjected to spatially uniform specific impulses; rectangular and circular membranes are considered. Their model is based on theoretical and dimensional analysis considerations. The authors derived an important parameter, called the normalised impulse or the damage number, $\hat{\phi}_0$, that is a function of the total impulse I_0. The resid-

ual displacement, when normalised to the plate's thickness, is found to be linear in the normalised impulse, $\hat{\phi}_0$, and the authors formulated their final model by linear fitting to a large set of experimental data. Their model will be presented and discussed in Section 4.6.3. Later, Cloete and Nurick (2014) obtained a closed-form approximate solution for the response of ductile circular membranes subjected to uniform impulsive loads that almost matches the original equation of Nurick and Martin (1989), the difference being a constant factor (see the above-cited paper where direct comparison is highlighted). In Cloete and Nurick (2014), an assumed (namely quadratic) displacement mode shape was used, and the authors devised a form of the balance of global initial kinetic and plastic (or dissipation) energies to find the eventual solution: the amplitude of the assumed displacement profile and the time when (the purely plastic) motion ends.

More recently, some analytical solutions considered spatially non-uniform impulsive loadings applied to different types of structures including thin and thick beams and plates under small- and large-displacement regimes (Micallef et al., 2012; Mehreganian et al., 2018a; Thil et al., 2019). However, in these models, the assumed (localised) distribution of the impulsive blast load does not follow the actual specific impulse distribution from a typical near-field blast as predicted by Pannell et al. (2021) for spherical charges. Their solutions apply to materials obeying Tresca's yield criterion. Modelling a material with Tresca's yield condition is typically simpler; however, this is only so when the directions of the principal stresses are known or can be found (or anticipated) in advance. In general conditions, determination of the principal axes are not trivial; hence, the model simplicity is lost when Tresca yield condition needs to be formulated in terms of the Cartesian components of the stresses. Moreover, Tresca yield curve (in the in-plane principal stress space) is not smooth, and the plastic strains do not uniquely determine the stress state. The corresponding von Mises's curve neither suffer from these limitations nor require an initial guess of the principal stress directions (Chen and Han, 1988).

In studying the response of thin plates under non-uniform blast loads, Rigby et al. (2019a) and Rigby et al. (2019b) established two important relationships. Firstly, the local initial velocity, $\dot{w}_0$, of the target (with density ρ, thickness h, and exposed area A) is confirmed to be a linear function of the imparted non-uniform specific impulse field, i,

$$\dot{w}_0 = \frac{i}{\rho h},$$

which is based on the upper bound kinetic energy. That is, non-uniform specific impulse generates non-uniform initial velocity, see Fig 2.6 (c). This initial velocity field contrasts with the "lower-bound" initial velocity field,

$$\dot{w}_{0,lb} = \frac{\int_A i \, dA}{\rho h A}$$

which is uniform and is interpreted as the rigid-body velocity (i.e., total impulse divided by total mass), see Fig 2.6 (b).

Secondly, the maximum permanent displacement is a linear function of the energy-equivalent total impulse, I_k, which is also based on the upper bound kinetic energy uptake, K_{ub}, developed by Tyas and Pope (2003), see Fig. 2.6,

$$K_{ub} = \frac{1}{2\rho h}\int_A i^2\, dA, \quad \text{and} \quad I_k = \sqrt{A\int_A i^2\, dA}.$$

The authors showed that the blast load can be replaced by a prescribed initial velocity field, which remarkably simplifies the analysis. This observation highlights the importance of the actual spatial variation of the specific impulse. According to the authors, the imparted energy from the blast onto a thin plate cannot be higher than K_{ub} or lower than the kinetic energy computed with $\dot{w}_{0,lb}$, provided the regime is impulsive.

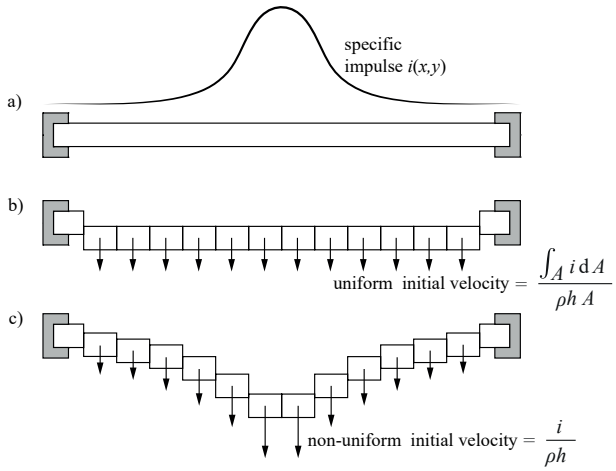

Fig. 2.6. Non-uniform specific impulse distribution (a) and the generated profile of initial velocity assuming a lower-bound (b) and an upper-bound (c) kinetic energy uptake, reproduced after Tyas and Pope (2003). Lengths of the downward arrows indicate qualitatively the magnitude of the initial transverse velocity field.

As discussed in Section 2.1.9, Pannell et al. (2021) proposed a model that predicts the non-uniform distribution of specific impulses arising from near-field blasts with scaled distances of 0.11-0.55 m/kg$^{1/3}$. Determining the specific impulse profile is critical in analysing structures under near-field blast loading, as discussed in Rigby et al. (2019a).

2.2.4 Experimental Results

Bodner and Symonds (1979) reported the results from experimental tests on circular plates under uniform blast loads applied over the whole and central regions of the plates. Nurick and his collaborators (1996; 1985; 1989; 1996; 1991) presented extensive experimental data for circular and rectangular plates under uniform impulsive loads and different boundary conditions.

As discussed in Section 4.2, the team of the Blast and Impact Engineering research group at the University of Sheffield confirmed experimentally that near-field blasts produce spatially

non-uniform specific impulses (Rigby et al., 2020a; Rigby et al., 2015; Tyas, 2019; Tyas and Pope, 2003). Furthermore, the researchers and their collaborators presented experimental and numerical studies of the transient deformation of thin ductile plates subjected to near-field blast (Rigby et al., 2019b). In their study, both the blast load and the full-field transient displacement of the target were measured locally: (a) the dynamic pressures histories at different spatial points were measured by the Characterisation of Blast Loading (CoBL) apparatus, which is described in detail in Rigby et al. (2015) and Clarke et al. (2015), providing the spatial variations of the specific impulses; (b) full-field transient displacements of the targets were measured using high-speed imaging, a technique that is described further in Curry and Langdon (2017); and (c) the total impulse was measured using a ballistic pendulum.

Furthermore, G. Langdon and her collaborators studied the response of steel plates under near-field blast experimentally (Curry and Langdon, 2017; McDonald et al., 2018; Mehreganian et al., 2018b). It was observed that a localised blast load induces central dishing (or bulging) in the targets. Gharababaei and Darvizeh (2010) performed blast experiments on steel, aluminium, and copper thin circular plates, which were loaded by detonating thin cylindrical charges of high explosives. The authors used rigid tubes to guide the propagation of the shock waves as they travel towards the specimens. Large plastic deformations were observed in the tests.

In addition, from the team of SIMLab, Aune et al. (2016) and Aune et al. (2017) presented experimental and numerical studies on the response of thin plates under free-air blasts, and similar studies were conducted by Elveli et al. (2022) on the response of thin plates to blasts produced in a shock tube facility. Additional air-blast experiments are also reported by Spranghers et al. (2012b) and Spranghers et al. (2013). The plates are made of ductile materials (structural steel and aluminium) and were observed to be primarily responding impulsively and plastically.

2.2.5 Connection of the Near-Field Blast Loading to the Response of Structures

As clearly indicated by the previous subsections, there is significant scientific interest in studying the structural response in the inelastic range when structures are subjected to extreme dynamic loadings, such as those arising from missile impacts and explosions. Extremely high magnitudes and short durations characterise loads generated from near-field blasts, see Rigby et al. (2020a), Rigby et al. (2015), Tyas (2019), and Tyas (2018), and are expected to cause mainly plastic deformations in the structures.

Simplified dynamic analysis of an idealised mass-spring oscillator suggests that the response tends to be impulsive as the ratio of the load duration to the (fundamental) structural period tends to zero; the impulsive response of the structure (or the oscillator here) is sensitive to the total impulse only, regardless of the magnitude of the peak force or the shape of the force-time function. Finally, in such a simplified analysis, the impulse can be

replaced with an initial velocity condition (U.S. Army, 2008, p. 611).

Recent experimental studies show that near-field blast waves are characterised by extremely short positive phase durations and a substantial specific impulse of the positive phase; in addition, owing to the closeness of the charge to the target in this blast type, the specific impulse distribution is spatially non-uniform. Rigby et al. (2019c) and Rigby et al. (2019b) show that thin plates (or membranes) respond impulsively to a near-field blast load; furthermore, the authors developed a simplified analytical model to convert the specific impulse distribution directly into an initial velocity field of the thin target. That is, the structural response is likely to be sensitive to the specific impulse in a near-field blast.

More recently, Pannell et al. (2021) developed a model to predict the specific impulse distribution from spherically shaped PE4 (plastic explosive) charges; according to their model, the specific impulse distribution follows a Gaussian distribution with respect to the angle of incidence. The model determines the specific impulse profile by knowledge of the charge's weight and normal (or the shortest) stand-off distance characterising the near-field blast threat. As it was specifically built for such blast problems, the model is applicable for scaled distances in the range $0.11 \leq Z \leq 0.55$ [m/kg$^{1/3}$]. Although, when the charge is cylindrical but still made of a PE4 explosive, its spherical equivalence should be first calculated in order to use Pannell et al.'s model; Rigby et al. (2021) proposed a method for calculating the spherical equivalence factor for cylindrical PE4 charges.

Rigby et al. (2020a), Rigby et al. (2015), Tyas (2019), and Tyas and Pope (2003) provided experimental evidence that near-field blasts generate spatially non-uniform spontaneous pressures that, subsequently, decay exponentially. Such intense loading could induce large displacement, strain rate-dependent, and material failure effects in the structural response, see, e.g., Jones (2010).

For these reasons, in addition to geometric complexities and boundary effects, the blast analyst typically resorts to making use of advanced computational methods, e.g., hydrocodes and finite element (FE) programs, attempting to simulate the complete problem. The commercially available FE programs can simulate the non-linear structural response under specific blast settings (Rigby et al., 2019a; Aune et al., 2017; Spranghers et al., 2013; Rigby et al., 2018; Curry, 2017). In solving the relevant problem numerically, additional preliminary computations could be necessary to ensure the solution is insensitive to some artificial parameters, e.g., those related to hour-glassing, artificial damping, structural (i.e., membrane or shear) and material (i.e., incompressibility) locking, extra contact and leakage controls, etc., which were introduced to improve the numerical solution's accuracy and/or to prevent instabilities.

However, the latter approach could, sometime, be relatively computationally expensive. The challenge becomes more critical once it is recognised that the input data of the blast threat are never known in advance, as pointed out by Tyas (2019). Furthermore, the material characteristics are prone, to some extent, to potential variabilities. Thus, to

design robust structures, it is more appropriate not to perform a single simulation but rather sufficiently many, to fully characterise the likely response and associated confidence intervals. What, then, suits the analyst in this regard is the availability of models that can be evaluated more rapidly.

2.2.6 Aims of the Present Study

The discussions in Sections 2.2.1–2.2.6 serve as a short account of some notable works investigating the response of structures to blast loads. As mentioned, some researchers discuss the theory and provide analytical solutions, while others give experimental insights and observations to strengthen or refine existing theories.

The trend of simplifying the problem and obtaining analytical and fast-running models is of considerable practical importance. Especially, rapid models are most suitable for probabilistic-based blast analyses where the cost of computation (per run) is a key concern since the framework requires, typically, many repeated calculations as the design input parameters are varied. That is, the situation (of variability of the problem inputs and the need for rapid computations) would naturally lead to the interest in building analytical solutions (or models) to a reasonably idealised version of the problem because of their relatively low computational expense. This is the rationale of the present work. It should be re-emphasised that once a first-order approximate solution is obtained through a fast-running model during the initial design stage, then a more robust analysis, e.g., based on high-fidelity computational methods (e.g, FE analysis), is typically required during the final design stage to ensure the reliability of the ultimate design.

The present work aims to develop an analytical solution to predict the transient and permanent displacement of thin ductile plates subjected to near-field blast loadings. The model utilises the following simplifying idealisations: impulsive blast load, rigid-perfectly plastic material behaviour, and membrane mode of deformation, according to observations from the already discussed literature.

That is, the problem to be analytically investigated is a thin plate made of a rigid-perfectly plastic ductile material, and the plate's response to the near-field blast loading is perfectly impulsive. Furthermore, in Chapter 3, the kinematics of the plate will be simplified such that the plate deforms as a pure membrane without in-plane displacements. Although the perfect impulsive regime and the rigid-perfect plasticity idealisations do not exist in reality, they have been shown to be of great practical importance in approximating the observed responses that are obtained experimentally and through high-fidelity numerical simulations. Nevertheless, the idealisations, to be practically valid, are subject to some applicability limits. As already mentioned, the present model is based on the aforementioned idealisations; hence it is vital to discuss the applicability of the model in (reasonable) detail. Practical guidelines on when the model should be applicable will be provided, later, in Chapter 6. In particular, discussions and practical considerations on the definition of the impulsive regime, the rigid-plastic material assumption, and the near-field blast and

the non-uniformity of its corresponding specific impulse distribution, will be addressed. The reason for the postponed discussion is to connect the model's limitations (which will be made clear after the model's validation) to the adopted assumptions, and hence to provide clear direction for future research as necessary. Discussion on the direct impact of the model, after its development in Chapter 3 and subsequent validation in Chapters 4 and 5, on engineering applications will be given in Section 6.7. This topic is vital to emphasise the practical importance of the present work, despite the limited nature of its applicability due to the adopted assumptions.

The well-established extended Hamilton's or the virtual work principles will be applied to the above-defined problem of impulsively loaded rigid-perfectly plastic membrane, in Chapter 3 and briefly in Section 4.3.2, to obtain a general equation of motion that applies to any target's geometry without a prior assumption on the initial field of motion. Hence, the then-derived equation and solution will accommodate any distribution of the blast-induced specific impulse.

2.3 Summary

From the reviewed literature concerning the dynamic response of near-field blast loaded plates, the following main conclusions are identified:

- Section 2.1:
  - Near-field blasts are associated with extremely short duration of the positive phase and non-uniform (highly localised) specific impulses;
  - The widely used semi-empirical blast parameter predictive models are less applicable to near-field blasts;
  - A generic near-field blast event can be numerically simulated using commercially available special-purpose hydrocodes and general-purpose explicit finite element solvers, e.g., LS-DYNA, when combined with the MM-ALE technique.
- Section 2.2:
  - Current practice of analysing the blast-loaded dynamic response of structures is the equivalent SDOF technique, which is based on the assumption that the mode shape (of response) is known a priori and taken as the quasi-static deformed profile. From this, it is concluded that a structure tends to respond impulsively when the blast load duration becomes relatively shorter than the maximum response time;
  - Experiments and early theoretical studies on the dynamic plastic response of plates, when subjected to extreme blast load intensity, show that the deformation mode is by far different from the quasi-static mode, and the deformation profile is highly transient, i.e., not a mode-response;

– Available analytical solutions of the plastic displacements of thin plates under both uniform and non-uniform blast loading are based on the extension of the conventional (i.e., for static regimes) plastic analysis to the dynamic regime. This method requires that the initial incipient and subsequent dynamic deformation shape (a dynamic plastic mechanism) is assumed a priori, corresponding to a given load distribution (whose spatial profile is fixed). Thus, the analytically derived solutions apply only to such a fixed loading profile. These studies show that the rigid-perfectly plastic idealisation is powerful and applicable for the analysis of blast-loaded structures. Furthermore, it is concluded that the responses of blast-loaded plates become eventually dominated by the membrane mode of deformation as the blast load intensity and transverse displacements increase substantially;

– Experiments and well-detailed numerical simulations on near-field blast-loaded thin targets show clearly that the resulting structural responses are mainly plastic and nearly impulsive. When thin plates are loaded by near-field blasts generated from close-in high explosive detonations, it is confirmed that the blast load is fully characterised by the specific impulse alone. The non-uniform specific impulse induces a proportionally non-uniform initial velocity field.

Chapter 3

Membrane Model

3.1 Overview

A model to predict the response of thin plates against impulsive blast loading will be developed. The plates will be assumed to respond in pure membrane mode, and their material are treated as rigid-perfectly plastic according to von Mises's yield conditions. The equation of motion governing the dynamic response of the plates will be derived.

First, the kinematics of the membrane to be considered, which will be called a simple membrane, is introduced with reference to the well familiar plate theories. Then, the general equilibrium equations will be developed based on the purely geometric assumptions. That is, the equilibrium equations will be obtained by direct application of the principle of the virtual work, which, hence, is applicable regardless of the constitutive relations (i.e., no matter how stresses are related to the strains). Then, a short overview of von Mises's plasticity is presented for a rigid-perfectly plastic material. Finally, the equilibrium equation of the simple membrane is specialised for this particular material behaviour, i.e., when the membrane is made of rigid-perfectly plastic von Mises material.

3.2 Structural Context of the Simple Membrane

A very powerful systematic tool to derive the governing equilibrium equation(s), of a given structural problem, is the virtual work principle, which requires the specification of the appropriate forms of the strains associated with the dominant behaviour of the considered problem (Reddy, 2002; Washizu, 1975). Various structural theories exist that apply to particular plate problems, see, e.g., Reddy (2007) and Ventsel and Krauthammer (2001). The main differences between these are the assumptions made on the form of strains.

In this section, the goal is to relate the simple membrane to other familiar plate theories. For this purpose, first the primary kinematic variables are defined. Consider a general plate of thickness h, and let its mid-plane be lying on the x-y plane, and the z axis being perpendicular to it. Let the displacement components be (u, v, w) for any point (x, y, z).

Furthermore, let the components of the displacement at any point on the mid-plane, $z = 0$, be (u_0, v_0, w_0); observe that these displacements (of the mid-plane) are functions of (x, y) only, by definition. The (u, v) and (u_0, v_0) are called the in-plane displacements, and w (and w_0) is the transverse displacement (measured along the thickness or the z axis).

When the plate is thin and the transverse displacement w is small, then Kirchhoff plate theory is applicable, and accordingly, the kinematics of the plate are

$$\begin{aligned} w(x,y,z) &= w_0(x,y) \\ u(x,y,z) &= u_0(x,y) - z\frac{\partial}{\partial x}\left[w_0(x,y)\right] \\ v(x,y,z) &= v_0(x,y) - z\frac{\partial}{\partial y}\left[w_0(x,y)\right], \end{aligned} \tag{3.2.1}$$

owing to the well-known Kirchhoff's hypotheses: perpendicular plane sections remain perpendicular and plane, and the plate's thickness is inextensible, see, e.g., Timoshenko and Woinowsky-Krieger (1959).

According to the above kinematic assumptions, the strains in a Kirchhoff plate are

$$\begin{aligned} \varepsilon_x^{(\mathrm{K})} &= \frac{\partial u_0}{\partial x} - z\frac{\partial^2 w_0}{\partial x^2} \\ \varepsilon_y^{(\mathrm{K})} &= \frac{\partial v_0}{\partial y} - z\frac{\partial^2 w_0}{\partial y^2} \\ 2\varepsilon_{xy}^{(\mathrm{K})} &= \frac{\partial v_0}{\partial x} + \frac{\partial u_0}{\partial y} - 2z\frac{\partial^2 w_0}{\partial x \partial y} \\ 2\varepsilon_{xz}^{(\mathrm{K})} &= 0 \\ 2\varepsilon_{yz}^{(\mathrm{K})} &= 0 \\ \varepsilon_z^{(\mathrm{K})} &= 0, \end{aligned} \tag{3.2.2}$$

where the three transverse strains are identically zero due to the form of the displacement components given earlier. The superscript (K) is used to refer to Kirchhoff. It should be emphasised that the transverse displacement is independent of z, i.e., $w = w_0(x, y)$, and hence w is uniform across the thickness.

It will be referred to the three non-zero strains, $\varepsilon_x^{(\mathrm{K})}$, $\varepsilon_y^{(\mathrm{K})}$, $\varepsilon_{xy}^{(\mathrm{K})}$, as the in-plane strains. These strains can be split into two parts: a membrane part associated with the derivatives of the in-plane displacements, u_0 and v_0, and a bending part associated with the (second-order) derivatives of the transverse displacement w_0. The above forms of the in-plane strains apply when the transverse displacement is small. For this reason, the membrane and bending behaviours are geometrically uncoupled (Reddy, 2007).

Discussion of Kirchhoff's thin plate theory is ended at this point. However, it is helpful

to note the following. The theory is an approximate structural theory that applies to thin plates under small displacement because Kirchhoff's assumptions well describe the motions of such plates. It is a simplification of the general three-dimensional case which is applicable when the structure is a thin plate under small w_0. For such problems, the significant kinematics of the actual behaviour are those retained in the theory of Kirchhoff, outlined above (Ventsel and Krauthammer, 2001).

When the transverse displacement w_0 becomes large, non-linear terms will appear in the definition of the strains. However, attempts are made to again avoid considering the general case by including all such non-linear terms but instead just retain the most significant, based on further kinematic assumptions. That is, one seeks another simplified (or approximate) plate theory that is applicable and practical. When large transverse displacement, w_0, occurs in a thin plate, it induces large rotations, which are given by $\frac{\partial w_0}{\partial x}$ and $\frac{\partial w_0}{\partial y}$. Von Kármán established a thin plate theory that accounts for large transverse displacement; von Kármán plate is the extension of Kirchhoff plate in which the large rotation effects are included, see, e.g., Reddy (2007). According to von Kármán, only the following quadratic terms need to be retained in the non-linear strains: $(1/2)(\frac{\partial w_0}{\partial x})^2$, $(1/2)(\frac{\partial w_0}{\partial y})^2$, and $(1/2)\frac{\partial w_0}{\partial x}\frac{\partial w_0}{\partial y}$, while the remaining quadratic terms (that would appear from the definitions of the non-linear strains) can be neglected as they are considered relatively very small. Again, the justification is that the retained (quadratic) terms correspond to the large rotations induced when w_0 gets larger (Reddy, 2007).

Hence, the von Kármán strains can be written as

$$\begin{aligned}
\varepsilon_x^{(\mathrm{VK})} &= \varepsilon_x^{(\mathrm{K})} + \frac{1}{2}\left(\frac{\partial w_0}{\partial x}\right)^2 \\
\varepsilon_y^{(\mathrm{VK})} &= \varepsilon_y^{(\mathrm{K})} + \frac{1}{2}\left(\frac{\partial w_0}{\partial y}\right)^2 \\
2\varepsilon_{xy}^{(\mathrm{VK})} &= 2\varepsilon_{xy}^{(\mathrm{K})} + \left(\frac{\partial w_0}{\partial x}\frac{\partial w_0}{\partial y}\right) \\
2\varepsilon_{xz}^{(\mathrm{VK})} &= 2\varepsilon_{xz}^{(\mathrm{K})} + 0 = 0 \\
2\varepsilon_{yz}^{(\mathrm{VK})} &= 2\varepsilon_{yz}^{(\mathrm{K})} + 0 = 0 \\
\varepsilon_z^{(\mathrm{VK})} &= \varepsilon_z^{(\mathrm{K})} + 0 = 0,
\end{aligned} \tag{3.2.3}$$

where the superscripts (VK) refers to von Kármán strains, and (as before) the superscript (K) refers to Kirchhoff strains, which were given earlier. Note that the bending parts of the in-plane strains in the von Kármán plate are identically the same as those in the Kirchhoff plate. However, the membrane strains now have additional contributions due to the transverse displacement, w_0, being large, which are the quadratic terms appearing in the von Kármán in-plane strains. Both Kirchhoff and von Kármán strains apply to thin plates; on the other hand, Kirchhoff strains apply when the transverse displacement, w_0,

is small, whereas von Kármán strains apply when w_0 becomes large (Reddy, 2007).

Next, the transverse displacement w_0 is kept to be large, i.e., starting with von Kármán thin plate, and focus is made on the limit as the plate becomes infinitely thin (or when the thin plate becomes a membrane). In this limiting process, the contribution of the behaviour pertaining to bending tends to disappear. The reason for the vanishing of bending action is due to the absence of bending stresses, not bending strains (i.e., curvatures). That is, the following quantities are the ones that tend to zero as the thickness becomes infinitely small,

$$\begin{aligned}\int_{-h/2}^{h/2} \sigma_x \varepsilon_x^{(\mathrm{B})}\, dz &= -\int_{-h/2}^{h/2} \sigma_x z \left(\frac{\partial^2 w_0}{\partial x^2}\right)\, dz \\ &= -\left(\frac{\partial^2 w_0}{\partial x^2}\right) \int_{-h/2}^{h/2} \sigma_x z\, dz \\ &\approx -\left(\frac{\partial^2 w_0}{\partial x^2}\right) \sigma_x \int_{-h/2}^{h/2} z\, dz \equiv 0\end{aligned} \tag{3.2.4}$$

and similarly

$$\int_{-h/2}^{h/2} \sigma_y \varepsilon_y^{(\mathrm{B})}\, dz = 0$$

$$\int_{-h/2}^{h/2} \sigma_{xy} \varepsilon_{xy}^{(\mathrm{B})}\, dz = 0,$$

since the in-plane stresses, σ_x, σ_y, and σ_{xy}, become uniform across the thickness in the limit as it tends to zero. The superscript (B) was used to refer to the bending part of the corresponding strains. So, it is clear that the vanishing of the bending contribution for an infinitely thin plate is due to the product with the thickness coordinate, z, appearing in the bending strains.

Thus, in the limit as the plate becomes infinitely thin, the appropriate form of in-plane strains become those of von Kármán where the terms multiplied with the thickness coordinate, z, are removed (since their integration over the infinitely small thickness will vanish). That is, for membranes (or infinitely thin plates) under large displacement, the

strains take the form

$$\begin{aligned}
\varepsilon_x^{(\mathrm{M})} &= \frac{\partial u_0}{\partial x} + \frac{1}{2}\left(\frac{\partial w_0}{\partial x}\right)^2 \\
\varepsilon_y^{(\mathrm{M})} &= \frac{\partial v_0}{\partial y} + \frac{1}{2}\left(\frac{\partial w_0}{\partial y}\right)^2 \\
2\varepsilon_{xy}^{(\mathrm{M})} &= \frac{\partial v_0}{\partial x} + \frac{\partial u_0}{\partial y} + \left(\frac{\partial w_0}{\partial x}\frac{\partial w_0}{\partial y}\right) \\
2\varepsilon_{xz}^{(\mathrm{M})} &= 0 \\
2\varepsilon_{yz}^{(\mathrm{M})} &= 0 \\
\varepsilon_z^{(\mathrm{M})} &= 0,
\end{aligned} \tag{3.2.5}$$

where the superscript (M) refers to pure membranes. A membrane whose strains are as defined above is called the general membrane. In the literature, the general membrane formulation is credited to Föpple and is, simply, a modified version of von Kármán theory with the flexural parts removed due to extreme thinness of the plate see, e.g., Marker and Jenkins (1997). Note that the thickness does not necessarily need to approach zero for the general membrane theory to be valid. For example, Reddy (2007) discussed the general membrane theory as an approximation of the mechanics of thin plates when bending action is negligible compared to the membrane action, e.g., due to the large transverse deformation. In the above development, the final result is reached using the more direct mathematical limiting process, which is the approach of Föpple, see, again, Marker and Jenkins (1997).

Extending from the general membrane kinematics, there can emerge a further limiting case in which the transverse motion of the thin plate is dominantly depending on the contribution to in-plane strains by the derivatives of the large transverse displacement (w_0) in comparison to the contribution by the in-plane displacements (u_0 and v_0). That is, the stretching of the membrane is said to be due only to a purely transverse motion. Duffey (1967) and Cloete and Nurick (2014) argue that the internal plastic work of a (general perfectly plastic) membrane in the large displacement regime that is associated with large transverse blast loading is independent of the in-plane displacements.

In the following, the latter membrane kinematics are investigated by requiring that $\frac{\partial u_0}{\partial x}$, $\frac{\partial v_0}{\partial y}$, and $(\frac{\partial v_0}{\partial x} + \frac{\partial u_0}{\partial y})$ are very small (compared to the derivatives of the transverse displacement) that, in turn, imply that $u_0 = const.$, and $v_0 = const.$ Hence, when it is further considered that the membrane is to be fixed at its outer edges, then one finds that

$$u_0 \equiv 0$$

$$v_0 \equiv 0$$

A membrane that is free of in-plane displacements will be called a *simple membrane*.

Therefore, the strains in a simple membrane (in which the in-plane displacements, u_0 and v_0, are zero) can be defined as

$$\begin{aligned}
\varepsilon_x &= \frac{1}{2}\left(\frac{\partial w_0}{\partial x}\right)^2 \\
\varepsilon_y &= \frac{1}{2}\left(\frac{\partial w_0}{\partial y}\right)^2 \\
\varepsilon_{xy} &= \frac{1}{2}\left(\frac{\partial w_0}{\partial x}\frac{\partial w_0}{\partial y}\right) \\
\varepsilon_{xz} &= 0 \\
\varepsilon_{yz} &= 0 \\
\varepsilon_z &= 0
\end{aligned} \tag{3.2.6}$$

The overall summary is that the starting point is Kirchhoff's plate, which is thin and subjected to small displacement w_0. Then, a transition is made from Kirchhoff to von Kármán as w_0 increases, where additional membrane strains emerge from w_0 being large, while the bending strains remained as given by Kirchhoff. Then, the bending contribution was eliminated as the plate becomes infinitely thin (i.e a membrane) to obtain the general membrane. The in-plane displacement effects in all three cases (i.e., Kirchhoff and von Kármán thin plates and the general membrane) remained the same as in the Kirchhoff plate. Ultimately, it was considered a further limiting case (emerging from the general membrane) when w_0 becomes exceedingly large so that the in-plane strains become dominated by its derivative in comparison to the contributions from the derivatives of the in-plane displacements (u_0 and v_0), which, in turn, imply that the total displacement is identically the transverse displacement w_0, and the in-plane displacements are set zero. The last limiting case was called the simple membrane. The strains in the simple membrane are given by the last set of equations, i.e., Eq.(3.2.6). The simple membrane formulation will be the basis of the kinematic description of the membrane response of thin plate that are subjected to intense lateral loading arising from near-field blasts. The effects of the in-plane displacements were neglected to reduce the dimensions of the problem, i.e., to deal with a point-wise single degree-of-freedom which is the transverse displacement, w_0. This simplifying step is thought reasonable after the important conclusion of Cloete and Nurick (2014) that the transverse response of blast-loaded circular thin plates is independent of the in-plane (namely, the radial) displacement. The relationship between the different plate-like theories is depicted in Fig. 3.1.

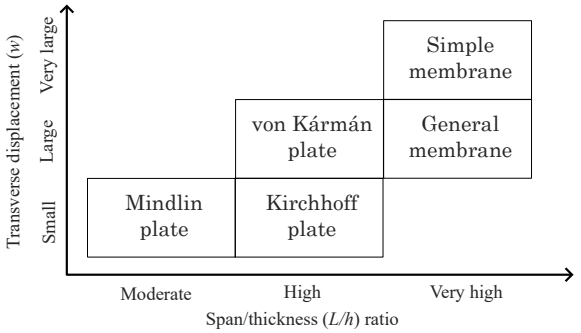

Fig. 3.1. Qualitative classification of kinematic theories applicable for different plate-like structures. In the literature, Kirchhoff plate is also known as Kirchoff-Love theory, von Kármán plate is known as Föppl-von Kármán, Mindlin plate is also known as Reissner-Uflyand-Mindlin theory. Von Kármán plate extends Kirchhoff plate by including strains associated with large transverse displacement (i.e., large rotations). The general membrane, or Föpple membrane, is obtained from von Kármán plate with bending effects neglected. The simple membrane is derived from the general one after removing the strains associated with the in-plane displacements.

3.3 General Equilibrium Equations

3.3.1 Overview

A membrane problem is considered in which the in-plane displacements u_0 and v_0 of the membrane's mid-plane are negligible compared to the transverse displacement w_0. This is viewed as the limiting case of the general von Kármán plate when: (i) bending strains are omitted in the limit as thickness becomes infinitely small, and (ii) in-plane displacements (u_0 and v_0, along the x and y axes, respectively) have negligible contribution to the membrane strains.

However, in the following, the general membrane is considered first in which the in-plane displacements (u_0, v_0) are present (in addition to the transverse displacement w_0), and its equilibrium equations are provided. Then, discussion of the special case (which will be called a simple membrane) is made when the in-plane displacements can be assumed negligible compared to the large transverse displacement w_0, and its equilibrium equation is given. Again, the equilibrium equations will be developed using the virtual work principle, following the approach in Reddy (2002) and Washizu (1975), such that they are applicable regardless of the material constitution. The starting points are the kinematics of the two membranes, as given in the previous section.

3.3.2 A General Membrane

If the in-plane components u_0 and v_0 are retained, the non-zero strains are the in-plane strains given below

$$\begin{aligned} \varepsilon_x &= \frac{\partial u_0}{\partial x} + (1/2)\left(\frac{\partial w_0}{\partial x}\right)^2 \\ \varepsilon_y &= \frac{\partial v_0}{\partial y} + (1/2)\left(\frac{\partial w_0}{\partial y}\right)^2 \\ 2\varepsilon_{xy} &= \left(\frac{\partial v_0}{\partial x} + \frac{\partial u_0}{\partial y}\right) + \frac{\partial w_0}{\partial x}\frac{\partial w_0}{\partial y} \end{aligned} \tag{3.3.1}$$

whereas the other three (transverse) strains are assumed zero. However, note that the in-plane shear strain, ε_{xy}, is generally non-zero. For a membrane with its non-zero strains as given above, it is governed by the following (three) equilibrium equations

$$\begin{aligned} \frac{\partial \sigma_x}{\partial x} + \frac{\partial \sigma_{xy}}{\partial y} &= 0 \\ \frac{\partial \sigma_{xy}}{\partial x} + \frac{\partial \sigma_y}{\partial y} &= 0 \\ \sigma_x \frac{\partial^2 w_0}{\partial x^2} + 2\sigma_{xy}\frac{\partial^2 w_0}{\partial x \partial y} + \sigma_y \frac{\partial^2 w_0}{\partial y^2} + \frac{p}{h} &= \rho \ddot{w}_0, \end{aligned} \tag{3.3.2}$$

where the in-plane accelerations $\ddot{u}_0$ and $\ddot{v}_0$ were made zero (this is a very usual assumption). The parameters are as follows: h is the membrane's thickness, ρ is the mass per unit volume, and p is the externally applied pressure (in the direction of z and w_0). Note that the stresses σ_x, σ_y, and σ_{xy} were assumed uniform across the thickness (in line with its smallness, and since no bending effects can develop). The above equilibrium equations were obtained by a direct application of the principle of virtual work. Note, also, that three equations are obtained since there are three independent motion variables, namely u_0, v_0, and w_0, in such a membrane problem. The membrane is assumed to be supported along all its outer edges.

As long as the strains are given by Eq. (3.3.1), which are due to Föpple as discussed in the previous section, then the equilibrium equations, Eqs. (3.3.2), are applicable regardless of the material constitutive relations, i.e., without restrictions about how the stresses are related to the strains. This is because the virtual work applies in general (Reddy, 2002). Hence, they apply to elastic, elasto-plastic, or even rigid-plastic membranes. Note that the in-plane shear stress σ_{xy} appears in the equilibrium equations. The corresponding equilibrium equations for a circular general membrane, which is under axi-symmetric conditions, are provided and discussed in Section B.1.3 of Appendix B.

3.3.3 A Simple Membrane

The simple membrane is defined as the one that is the limiting case of the earlier general membrane where the contributions of the in-plane displacements, u_0 and v_0, to the in-plane strains, are negligible. That is, $u_0 = const.$, and $v_0 = const.$ Since the membrane will be assumed to be supported on all its outer edges, then one lets $u_0 \equiv 0$, and likewise, $v_0 \equiv 0$. Therefore, the non-zero strains are taken as

$$\begin{aligned} \varepsilon_x &= \frac{1}{2}\left(\frac{\partial w_0}{\partial x}\right)^2 \\ \varepsilon_y &= \frac{1}{2}\left(\frac{\partial w_0}{\partial y}\right)^2 \\ \varepsilon_{xy} &= \frac{1}{2}\frac{\partial w_0}{\partial x}\frac{\partial w_0}{\partial y} \end{aligned} \tag{3.3.3}$$

and the remaining three transverse strains are still taken to be zero, as in the general membrane case.

When the above strains, in Eq. (3.3.3), are used in the virtual work equation, the simple membrane becomes governed by the following single equilibrium equation

$$\frac{\partial}{\partial x}\left(\sigma_x \frac{\partial w_0}{\partial x} + \sigma_{xy}\frac{\partial w_0}{\partial y}\right) + \frac{\partial}{\partial y}\left(\sigma_{xy}\frac{\partial w_0}{\partial x} + \sigma_y \frac{\partial w_0}{\partial y}\right) + \frac{p}{h} = \rho \ddot{w}_0, \tag{3.3.4}$$

where the parameters, h, ρ, and p, are as defined following Eq. (3.3.2). Again, the simple membrane is assumed to be supported along all its outer edges. The equilibrium equation Eq. (3.3.4) applies to any membrane (irrespective of the material constitution) for which the strains are as given in Eq. (3.3.3). Note that the application of the virtual work provided one equilibrium equation since the simple membrane (the present case) has only one degree of freedom for the motion, namely the transverse displacement, w_0. This simple membrane can only resist externally applied pressure along the z axis (i.e., in the direction of w_0). The corresponding equilibrium equation for an axi-symmetric circular simple membrane is treated in Section B.1.4 of Appendix B.

3.3.4 Discussion

When the membrane is assumed to be made of a rigid-perfectly plastic material, the strains (whenever non-zero) are the plastic strains. The increments of these strains can be non-zero only when the stress state satisfies the yield condition of the material. The accumulations (over time) of such increments give the total (plastic) strain (Chen and Han, 1988). The equilibrium equations, in Eqs. (3.3.2) for the general membrane and in Eq. (3.3.4) for the simple membrane, involve the spatial derivatives of w_0, and if such derivatives are non-zero, they lead to non-zero strains (according to the definitions of the

strains given earlier). Therefore, the stresses in the equilibrium equations need to satisfy the yield condition, otherwise, their coefficients (i.e., the spatial derivatives of w_0) would be zero. Next, when the material is known to follow a particular yield condition, e.g., von Mises plasticity, a stress state satisfying the yield condition needs to be determined. For the present two membranes' problems, the stress state is a plane-stress state. However, the collection of plane-stress states satisfying the yield condition represents a surface called the yield surface (Chen and Han, 1988); every point (i.e., stress state) on the surface satisfies the yield condition (and there are infinitely many such points since the surface is continuous).

Since the membrane is under a plane-stress state, then the third principal stress axis is the z axis (because there are no transverse shear stresses, σ_{xz} and σ_{yz}); then, the other two principal axes must lie on the x-y plane, i.e., on the membrane's mid-plane, since the principal axes must be mutually orthogonal.

Then, if it can, somehow, be shown that the whole membrane is free of in-plane shear stress σ_{xy}, the remaining two principal axes coincide with the Cartesian axes, x and y; this is because the principal directions are, by definition, those with respect to which there are no shear stresses.

For such case ($\sigma_{xy} \equiv 0$ throughout the membrane), then one has for the general membrane (from Eq. (3.3.2))

$$\sigma_1 \frac{\partial^2 w_0}{\partial x^2} + \sigma_2 \frac{\partial^2 w_0}{\partial y^2} + \frac{p}{h} = \rho \ddot{w}_0,$$

and likewise, for the case $\sigma_{xy} \equiv 0$ in the simple membrane, one (from Eq. (3.3.4)) has

$$\frac{\partial}{\partial x}\left(\sigma_1 \frac{\partial w_0}{\partial x}\right) + \frac{\partial}{\partial y}\left(\sigma_2 \frac{\partial w_0}{\partial y}\right) + \frac{p}{h} = \rho \ddot{w}_0,$$

where σ_1 and σ_2 are the in-plane principal stresses, and the Cartesian axes x and y are the principal axes.

However, in the principal plane (which coincides, for the present case, with the x-y plane), the collection of the stress states (σ_1, σ_2) satisfying the yield condition represents a continuous curve (a 45^o rotated ellipse for von Mises material in the two-dimensional σ_1-σ_2 space), see, e.g., Chen and Han (1988). But, since the membrane cannot develop negative membrane stresses, the physically valid region is the first quadrant $\sigma_1 \geq 0$ and $\sigma_2 \geq 0$.

Next, if one further assumes that the membrane is, throughout, free of any in-plane shear stress σ_{xy} in "all orientations", then the two stresses σ_1 and σ_2 (also σ_x and σ_y) must be equal (it is helpful to think of this with reference to the Mohr circle, which happens to be a circle with radius zero, i.e., a point if in-plane shear stresses must be zero in all orientations). For both von Mises and Tresca materials, the state of stress satisfying either yield conditions and for which $\sigma_1 \geq 0$, $\sigma_2 \geq 0$ and $\sigma_1 = \sigma_2$ is the following: $\sigma_1 = \sigma_2 = \sigma_0$, where σ_0 is the uni-axial yield stress (in tension) of the material. This solution follows immediately from the characteristics of the mentioned yield criteria (Chen and Han, 1988).

Hence, if the membrane throughout is free of in-plane shear stress, i.e., $\sigma_{xy} \equiv 0$, and in all possible orientations, then the stress state satisfying both Tresca and von Mises yield conditions, is $\sigma_x = \sigma_y = \sigma_1 = \sigma_2 = \sigma_0$, and σ_0 is constant. For such particular stress state, the general membrane equilibrium equation is

$$\sigma_0 \left(\frac{\partial^2 w_0}{\partial x^2} + \frac{\partial^2 w_0}{\partial y^2} \right) + \frac{p}{h} = \rho \ddot{w}_0$$

The first two equations in Eq. (3.3.2) are identically satisfied. Furthermore, under the same stress state as above (i.e., when setting $\sigma_x = \sigma_1 = \sigma_y = \sigma_2 = \sigma_0$ and recalling that σ_0 is a constant), the simple membrane is governed by

$$\sigma_0 \left(\frac{\partial^2 w_0}{\partial x^2} + \frac{\partial^2 w_0}{\partial y^2} \right) + \frac{p}{h} = \rho \ddot{w}_0, \tag{3.3.5}$$

which is identical to that of the general membrane. In both of the last two equations, σ_0 is the uni-axial tensile yield stress, h the membrane thickness, ρ its mass per unit volume (density), and p is the externally applied pressure along the direction of the transverse displacement, w_0. That is, if the stress state is $\sigma_x = \sigma_y = \sigma_0$ throughout the membrane's area, then $\sigma_{xy} = 0$, and there appears no distinction between the simple or general membrane kinematics in describing the motion of a membrane due to a purely transverse loading, and the membrane is fully supported along its periphery.

The validity of the last equilibrium equations depends on the validity of the assumption that the in-plane shear stress, σ_{xy}, is zero everywhere on the membrane and in all orientations. That is, the above equations are subject to the condition that $\sigma_{xy} \equiv 0$ and $\sigma_x = \sigma_y$. If this is known to be the case or has been verified, then the last (duplicate) equilibrium equation governs the responses of either membrane type.

The foregoing discussion concerns the motions of rigid-plastic (general and simple) membranes, where an initial guess on the stress state has been made. Membranes made of ductile materials obey the associated flow rule. However, in the associated flow plasticity, the stress state needs not be assumed but rather be associated with plastic strain rates that are normal to the yield surface (or curve for plane-stress problems) at that stress state. Furthermore, if, in particular, the von Mises's yield criterion is adopted, then the stress state (which is a particular point on the yield curve) is automatically (and uniquely) determined by the plastic strain rates themselves whenever they are non-zero. In addition, the plastic incompressibility (a feature of von Mises materials) of the material poses restrictions on the stress state.

The equation of motion for a membrane made of rigid-perfectly plastic von Mises material will be derived systematically in the sequel without a prior assumption on the stress state; however, an overview of the plastic relations for von Mises materials will be discussed first.

3.4 Basic Review of Von Mises Plasticity

The membrane is assumed rigid before yielding and perfectly plastic during yielding, according to von Mises plasticity. Hence, the strains, ε_{ij}, and their rates, $\dot{\varepsilon}_{ij}$ are the plastic strains, ε^p_{ij}, and their rates, $\dot{\varepsilon}^p_{ij}$. So, throughout, the superscript (p) will be omitted in the sequel. In the following, the classical (or incremental) theory of von Mises plasticity will be briefly introduced, and the material is based on the work of Chen and Han (1988); the reader is referred, among others, to this cited source for detailed discussion of the classical theory. The *incremental* plasticity of von Mises is the basis for the subsequent extension of the formulation in terms of *total* plasticity, which will be introduced and discussed later on.

According to (the classical) von Mises yielding theory, the condition of yielding is $s_{ij}s_{ij} = (2/3)\sigma_0^2$, and σ_0 is the uni-axial tensile yield stress which is assumed constant due to the perfect-plasticity assumption. s_{ij} is the deviatoric part of the total stress, σ_{ij}. That is, $s_{ij} = \sigma_{ij} - \hat{p}\delta_{ij}$, in which $\hat{p}$ is the (hydrostatic) pressure, and δ_{ij} is Kronecker delta. Since σ_0 is constant, one also has (by differentiating the yield condition): $s_{ij}\dot{s}_{ij} \equiv 0$. When the yield condition is satisfied, rates of (plastic) strains would develop according to the "associated" flow rule, i.e., by

$$\begin{aligned} \dot{\varepsilon}_{ij} &= \dot{\lambda}\frac{\partial}{\partial \sigma_{ij}}\left[(1/2)s_{kl}s_{kl} - (1/3)\sigma_0^2\right] \\ &= \dot{\lambda}s_{ij}, \end{aligned} \tag{3.4.1}$$

where $\dot{\lambda}$, known as the plastic multiplier rate, is a non-negative scalar. $\dot{\lambda}$ can be non-zero only when the yield condition is satisfied, i.e., s_{ij} satisfies the yield condition, given earlier. By using the flow rule and the yield condition, the plastic multiplier rate is given by

$$\dot{\lambda} = 1/\left[\sqrt{(2/3)}\sigma_0\right]\sqrt{\dot{\varepsilon}_{ij}\dot{\varepsilon}_{ij}}, \tag{3.4.2}$$

whenever the stresses s_{ij} satisfy the yield condition, i.e., s_{ij} is on the yield surface; otherwise, $\dot{\lambda} \equiv 0$, and, in turn, $\dot{\varepsilon}_{ij} = 0$. Note that repeated indices imply summation; for example, $\sigma_{kk} = \sigma_{xx} + \sigma_{yy} + \sigma_{zz}$, and furthermore, for simplicity σ_{xx} is replaced with σ_x.

Now, since $\dot{\varepsilon}_{ij}$ are the plastic strain rates, due to the rigid-plastic assumption, then whenever $\dot{\varepsilon}_{ij}$ are non-zero (and $\dot{\lambda} > 0$) means that s_{ij} must satisfy the yield condition and is given by $s_{ij} = \dot{\varepsilon}_{ij}/\dot{\lambda}$,

$$\begin{aligned} s_{ij} &= \frac{\dot{\varepsilon}_{ij}}{\dot{\lambda}} \\ &= \sqrt{(2/3)}\sigma_0\ \frac{\dot{\varepsilon}_{ij}}{\sqrt{\dot{\varepsilon}_{kl}\dot{\varepsilon}_{kl}}} \end{aligned} \tag{3.4.3}$$

whenever $\dot{\varepsilon}_{ij} > 0$. This can be viewed as a (deviatoric) stress-strain (rate) relation of a rigid-perfectly plastic von Mises material. The above relation suggests that s_{ij} is uniquely

determined by the strain rates $\dot{\varepsilon}_{ij}$, when $\dot{\varepsilon}_{ij} > 0$, which is equivalent to the statement that s_{ij} satisfies the yield condition, $s_{ij}s_{ij} = (2/3)\sigma_0^2$. In other words, the strain rates whenever non-zero determine (by themselves) the appropriate point (stress state) on the yield surface. It is well-known for a perfectly plastic von Mises material that only the ratios (proportions) of plastic strains (relative to one another) are what determine the stress state, irrespective of their absolute values, and this is attributed to the normality rule which will be discussed later.

The rate of plastic work (per unit volume) is given by $\sigma_{ij}\dot{\varepsilon}_{ij}$, and for the material at hand, it evaluates to

$$\begin{aligned} \sigma_{ij}\dot{\varepsilon}_{ij} &= (s_{ij} + \hat{p}\delta_{ij})\dot{\varepsilon}_{ij} \\ &= s_{ij}\dot{\varepsilon}_{ij} + \hat{p}\dot{\varepsilon}_{ii} \\ &= s_{ij}\dot{\varepsilon}_{ij} + \hat{p}\dot{\lambda}s_{ii} \\ &= s_{ij}\dot{\varepsilon}_{ij}, \end{aligned} \tag{3.4.4}$$

where the flow rule has been used, and in arriving at the last equality, the fact that $s_{ii} = 0$ was used. Furthermore, using the last equality and substituting the flow rule again, one has for the rate of plastic work

$$\begin{aligned} \sigma_{ij}\dot{\varepsilon}_{ij} &= s_{ij}\dot{\varepsilon}_{ij} \\ &= \dot{\lambda}s_{ij}s_{ij} \\ &= (2/3)\dot{\lambda}\sigma_0^2 \end{aligned} \tag{3.4.5}$$

Hence, for the rate of plastic work (i.e., the left-hand side of the above) to be non-negative, one must have $\dot{\lambda}$ to be non-negative at all times. Note that the rate of plastic work can be rewritten as $\sigma_{ij}\dot{\varepsilon}_{ij} = (2/3)\dot{\lambda}\sigma_0^2 = \sigma_0\sqrt{(2/3)\dot{\varepsilon}_{ij}\dot{\varepsilon}_{ij}}$, and hence by noting that $\sigma_0 = \sqrt{(3/2)s_{ij}s_{ij}}$ is the effective (or von Mises) stress, then the quantity $\sqrt{(2/3)\dot{\varepsilon}_{ij}\dot{\varepsilon}_{ij}}$ is the so-called effective (or von Mises) plastic strain rate, $\dot{\varepsilon}_{\text{eff}}$; the rate of plastic work can, in turn, be rewritten more compactly as $\sigma_0\dot{\varepsilon}_{\text{eff}}$. It is important to note that since $\dot{\lambda}$ is non-negative, and according to the flow rule, $\dot{\varepsilon}_{ij} = \dot{\lambda}s_{ij}$, one should have: the signs of $\dot{\varepsilon}_{ij}$ and s_{ij} are equal.

The above is the classical analysis of a rigid-perfectly plastic von Mises material that is universally accepted as a successful formulation to describe its plasticity; for more discussion and applications, the reader is referred to Chen and Han (1988). It is a rate form formulation since it is based on the rates of (plastic) strains.

If the simple membrane, whose equilibrium is governed by Eq. (3.3.4), is assumed to be made of a rigid-perfectly plastic von Mises material, for which $s_{ij} = \dot{\varepsilon}_{ij}/\dot{\lambda}$ holds whenever $\dot{\varepsilon}_{ij} > 0$, then its equilibrium equation takes the following form

$$\frac{\partial}{\partial x}\left[\frac{1}{\dot{\lambda}}\left(\dot{\varepsilon}_x\frac{\partial w_0}{\partial x}+\dot{\varepsilon}_{xy}\frac{\partial w_0}{\partial y}\right)\right]+\frac{\partial}{\partial y}\left[\frac{1}{\dot{\lambda}}\left(\dot{\varepsilon}_{xy}\frac{\partial w_0}{\partial x}+\dot{\varepsilon}_y\frac{\partial w_0}{\partial y}\right)\right] + \frac{\partial}{\partial x}\left(\hat{p}\frac{\partial w_0}{\partial x}\right)+\frac{\partial}{\partial y}\left(\hat{p}\frac{\partial w_0}{\partial y}\right)+\frac{p}{h}=\rho\ddot{w}_0, \tag{3.4.6}$$

where $\sigma_x = s_x + \hat{p}$, $\sigma_y = s_y + \hat{p}$, $\sigma_{xy} = s_{xy}$ have been used, then the three deviatoric stresses were related to the corresponding three strain rates. $\hat{p}$ is the internal pressure, $\hat{p} = (1/3)\sigma_{kk}$, and the notation $\hat{p}$ is used to distinguish it from the externally applied pressure, p.

The internal pressure cannot be associated with strains in a rigid perfectly plastic von Mises material (Washizu, 1975), unless the strain rates (as given by the derivatives of the displacements, i.e., the total strains) satisfy the incompressibility identically. Hence, its appearance in the above equation needs to be looked at as a "reaction", and it could be interpreted as an attempt by the membrane to satisfy the incompressibility. Note that the strains appearing in the above equilibrium equation are purely deviatoric.

However, since the flow rule, in its classical form, is incremental, and it appears to result in non-linearity in the constitutive relation, the "total" form of plastic deformation, i.e., dealing with total (plastic) strains instead of their increments or rates, becomes of interest. From the flow rule, $\dot{\varepsilon}_{ij} = \dot{\lambda}s_{ij}$, the total strains can be found by direct integration (with respect to time t) of this relation to get

$$\varepsilon_{ij} - \varepsilon_{ij}^{(0)} = s_{ij}\lambda - s_{ij}^{(0)}\lambda^{(0)} - \int_{t_0}^{t}\lambda\dot{s}_{ij}\,dt,$$

where the superscripts (0) denote the initial values of the quantities, or initial conditions, at time $t = t_0$. Next, the case of interest is the one where: (i) the initial conditions, for ε_{ij} and λ, can be dropped, and (ii) when $\dot{s}_{ij}$ can be set zero to eliminate the time integral altogether. That is, the following total form of flow rule, $\varepsilon_{ij} = \lambda s_{ij}$ is sought. This is discussed in the next subsection below. The reader should be aware that notion of the total (or deformation) plasticity is, in fact, an existing branch of the mathematical plasticity (Chen and Han, 1988); although such formulation is not as popular as the modern (or incremental) plasticity theory, see, e.g., the critical comments by Drucker (1956). For completeness, a well-known application of the total plasticity theory is the yield (or slip) lines theory, which is credited to Henky, that develop in plane-strain problems under monotonic loadings, e.g., in quasi-static indentation of a semi-infinite plate (Chen and Han, 1988).

3.4.1 Conditions Under Which $\varepsilon_{ij} = \lambda s_{ij}$ Holds

On integrating the flow rule, ($\dot{\varepsilon}_{ij} = \dot{\lambda} s_{ij}$), over time t, and then integrating the right-hand side by parts, one gets the total (plastic) strain as

$$\varepsilon_{ij} = s_{ij}\lambda - \int_0^t \lambda \dot{s}_{ij}\, dt, \tag{3.4.7}$$

assuming zero initial conditions for ε_{ij} and λ. This expression for the total strain, ε_{ij}, is valid as long as the initial conditions as assumed above are zero. That is, it applies to monotonic loading paths, since for such paths, the initial conditions are those at the start of motion which can be assumed zero for an initially unstrained membrane.

The flow rule also states that $s_{ij} = \dot{\varepsilon}_{ij}/\dot{\lambda}$, and after using the expression of $\dot{\lambda}$, given earlier, the rate of s_{ij} can be evaluated by direct differentiation to get

$$\dot{s}_{ij} = \frac{\ddot{\varepsilon}_{ij} - s_{ij}\ddot{\lambda}}{\dot{\lambda}}, \tag{3.4.8}$$

which is valid when $\dot{\lambda} > 0$, i.e., when s_{ij} continues to satisfy the yield condition.

Now, differentiating both sides of $[\dot{\lambda} = 1/(\sqrt{(2/3)}\sigma_0)\sqrt{\dot{\varepsilon}_{ij}\dot{\varepsilon}_{ij}}]$, one finds that

$$(2/3)\sigma_0^2\ddot{\lambda} = s_{ij}\ddot{\varepsilon}_{ij},$$

which is also valid only when the stresses s_{ij} satisfy the yield condition. Now because the yield is satisfied, i.e., $(2/3)\sigma_0^2 = s_{ij}s_{ij}$, the last relation can be written as $(s_{ij}s_{ij}\ddot{\lambda} = s_{ij}\ddot{\varepsilon}_{ij})$, which in turn implies that

$$0 = s_{ij}\left(\ddot{\varepsilon}_{ij} - s_{ij}\ddot{\lambda}\right) \tag{3.4.9}$$

From the above, Eq. (3.4.9), either $s_{ij} = 0$, the quantity inside the parentheses is zero during yielding, or s_{ij} is orthogonal to $\left(\ddot{\varepsilon}_{ij} - s_{ij}\ddot{\lambda}\right)$, by viewing the above as a dot product. If one lets

$$\ddot{\varepsilon}_{ij} = \ddot{\lambda} s_{ij}$$

to hold, then it implies that $\ddot{\varepsilon}_{ij}$ is a scalar multiple of s_{ij}, the multiplier being $\ddot{\lambda}$ (note that $\ddot{\lambda}$ is not restricted to be non-negative). Hence, $\ddot{\varepsilon}_{ij}$ is parallel to s_{ij} and hence normal to the yield surface (since s_{ij} is the normal to von Mises yield surface). Furthermore, $s_{ij}\dot{s}_{ij} = 0$ (presented earlier) also implies that s_{ij} and $\dot{s}_{ij}$ are normal to each other. So, the condition that $\dot{s}_{ij}$ is zero, is equivalent to saying that $\ddot{\varepsilon}_{ij}$ is normal to the yield surface as is the strain rate $\dot{\varepsilon}_{ij}$. Hence, it is a condition of progressive yielding where the stresses s_{ij} remain on the yield surface at the same point throughout the response.

Hence, for progressive yielding, one has $\ddot{\varepsilon}_{ij} = \ddot{\lambda} s_{ij}$, and for which $\dot{s}_{ij}$ becomes

$$\dot{s}_{ij} = \frac{0}{\dot{\lambda}} = 0 \tag{3.4.10}$$

whenever $\dot{\lambda} > 0$.

Hence, during the monotonic loading path and during progressive (continuing) yielding, the total (plastic) strain ε_{ij} is found as

$$\varepsilon_{ij} = \lambda s_{ij}, \tag{3.4.11}$$

as the deviatoric stresses continue to satisfy the yield condition, $s_{ij}s_{ij} = (2/3)\sigma_0^2$. From this total form of the flow rule, λ is found as

$$\lambda = \frac{\sqrt{\varepsilon_{ij}\varepsilon_{ij}}}{\sqrt{(2/3)}\sigma_0}, \tag{3.4.12}$$

given the yield condition is *and* remains satisfied.

Now, $\varepsilon_{ij} = \lambda s_{ij}$ is valid when the initial conditions are zero and when $\dot{s}_{ij} = 0$. It was shown that $\dot{s}_{ij} = 0$ is valid when $\ddot{\varepsilon}_{ij} = \ddot{\lambda} s_{ij}$.

Next, suppose that $\dot{\varepsilon}_{ij}$ at some time is initially positive (i.e., yielding is already established) but its value decreases (as the structure under consideration approaches its end of (the purely plastic) motion). Hence, the value of the instantaneous $\ddot{\varepsilon}_{ij}$ is negative, and so is the value of $\ddot{\lambda}$; note that s_{ij} is positive since $\dot{\varepsilon}_{ij}$ is so, and the two quantities must have similar signs. The response is now investigated during a small time interval Δt from the instant of time $t = t_0$ at which the response is as assumed above. In particular, what is investigated is the evolution of the quantity $\dot{\lambda}$ over the small time increment Δt. For this, one can write: $\dot{\lambda}(t_0 + \Delta t) \approx \dot{\lambda}(t_0) + \frac{\partial}{\partial t}(\dot{\lambda})|_{t_0}\Delta t = \dot{\lambda}(t_0) + \ddot{\lambda}(t_0)\Delta t$. Now, recalling that $\dot{\lambda}$ must be non-negative, and given the present assumption that $\ddot{\lambda}$ is negative, then there is a critical Δt beyond which the condition $\dot{\lambda} \geq 0$ would be violated. For the present hypothetical example, the critical Δt is defined when the left-hand side becomes zero for the first time, which gives $\Delta t = -\dot{\lambda}(t_0)/[\ddot{\lambda}(t_0)]$, where $\ddot{\lambda} < 0$ by assumption, and hence the value of the critical Δt is well-defined (i.e., finite and non-negative). If the response is not terminated at the time $t_0 + \Delta t$, where Δt is as given above, then $\dot{\lambda}(t_0 + \Delta t)$ would then be negative (according to the assumption $\ddot{\lambda} < 0$), which is not valid (not physical) and implies a decreasing plastic work. This can be considered as a basis for the idea of terminating the solution at some critical time instant when the "total" flow rule relation $\varepsilon_{ij} = \lambda s_{ij}$ is assumed to hold at the beginning of the response of a rigid-perfectly plastic structure. The reader is referred to Capurso (1972) and Maier (1968) for the numerical procedures to detect the critical time instant (beyond which a negativity of the plastic multiplier rate would occur) in an impulsively loaded rigid-perfectly plastic structure. This topic will be revisited in Section 6.4, when discussing solutions of irregularly shaped membranes.

From the foregoing discussion (in the present section), it is seen that there will be a critical time instant whenever $\dot{\varepsilon}_{ij}$ and $\ddot{\varepsilon}_{ij}$ have opposite signs, i.e., when the strain rate is initially positive and is decreasing, or when it is initially negative and increasing. Thus, equivalently, a critical time instant is preceded by $\dot{\varepsilon}_{ij}\ddot{\varepsilon}_{ij} \leq 0$; that is, when this inequality

is met, a critical time instant is approaching. Note that it was earlier established that $(2/3)\sigma_0^2\ddot{\lambda} = s_{ij}\ddot{\varepsilon}_{ij}$. This can also be rewritten as $(2/3)\sigma_0^2\dot{\lambda}\ddot{\lambda} = \dot{\varepsilon}_{ij}\ddot{\varepsilon}_{ij}$. Hence, since $(2/3)\sigma_0^2\dot{\lambda}$ is always non-negative, then whenever $\dot{\varepsilon}_{ij}\ddot{\varepsilon}_{ij} < 0$, one has $\ddot{\lambda} < 0$. Finally, since again $\dot{\lambda}$ must be non-negative at all times, then there is a critical time instant associated with $\ddot{\lambda}$ being negative (so that $\dot{\lambda}$ does not turn negative as time evolves), or equivalently with $\dot{\varepsilon}_{ij}\ddot{\varepsilon}_{ij}$ being negative.

On the other hand, since the critical time instant is (after all) directly defined when $\dot{\lambda}$ becomes zero for the first time (after it was already strictly positive), and since $\dot{\lambda} = 1/(\sqrt{(2/3)}\sigma_0)\sqrt{\dot{\varepsilon}_{ij}\dot{\varepsilon}_{ij}}$, then the critical time instant is also defined when $\dot{\varepsilon}_{ij}$ becomes zero for the first time (after being non-zero initially). So, the time when strain rates reach zero is a critical time instant; consequently, the velocity plays a key role. The ultimate effect of watching for the critical time instant and, then, terminating the solution at that instant is to make the total (plastic) strains ε_{ij} never decrease in magnitude irrespective of its sign without application of external work by an external agency (i.e., by external loading that has a reversed effect on the motion).

It is important to explain why when the strain rates reach zero, there will be a critical time instant. It is because strain rates (according to the well-established flow rule) must be normal to the yield surface (since it is proportional to s_{ij} which is normal to the von Mises surface) and pointing towards the exterior of the yield surface (since $\dot{\lambda}$ is non-negative). Hence, if strain rates were initially positive, then decreasing to zero, and then turning negative, they must be normal and pointing to the exterior of the yield surface in the final state (i.e., when they are negative). That means that the stress state must change from the previous state (when the strain rate was positive and decreasing) to a new state for which the associated new strain is normal and pointing to the exterior. Since only the sign of the strain rates has been changed, the new stress state (associated with the new negative strain rate) is the image of the previous state across the yield surface. Recall that it has been discussed earlier that the stress and strain rates, according to the classical flow rule, must have the same sign. In other words, the stress s_{ij} "instantaneously" travelled through the interior of the yield surface (i.e., the elastic domain) to appear on the other side of the yield surface so that to change its sign. This situation is already familiar in the one-dimensional uni-axial stress problem, in which the stress immediately (or instantaneously) changes from $(+\sigma_0)$ when the uni-axial strain rate was positive to $(-\sigma_0)$ as soon as strain rate turns negative.

In summary, it was shown that $\dot{s}_{ij} = 0$ directly implies that $\ddot{\varepsilon}_{ij} = s_{ij}\ddot{\lambda}$. That is, acceleration of strain, $\ddot{\varepsilon}_{ij}$, is normal to the yield surface or, equivalently, is parallel to s_{ij} since $\ddot{\lambda}$ is a scalar. When $\ddot{\lambda}$ is positive, then $\ddot{\varepsilon}_{ij}$ points to the exterior of the yield surface (as is the strain rate, $\dot{\varepsilon}_{ij}$, in terms of direction). In contrast, when $\ddot{\lambda}$ is negative, then $\ddot{\varepsilon}_{ij}$ is still normal to the yield surface but, in the present case, points to the interior of the yield surface (as opposed to the strain rate in terms of direction). In either case, the point on the yield surface (at which one measures and associates these strain quantities) remains the same throughout the evolution of deformation, i.e., $\dot{s}_{ij} \equiv 0$. For both cases, the foregoing

deformation regime is denoted as being progressive yielding at the same point on the yield surface.

From now on, it will be assumed that $\varepsilon_{ij} = \lambda s_{ij}$, see Eq. (3.4.11), holds, and s_{ij} satisfies the yield condition whenever the strains, and hence λ, are non-zero.

3.5 Equilibrium Equation of a Simple Membrane Made of a Rigid-Perfectly Plastic Von Mises Material

It is well-known that a von Mises material is plastically incompressible because one has $\dot{\varepsilon}_{ii} = \dot{\lambda} s_{ii} = 0$ since $s_{ii} \equiv 0$. Similarly, under the conditions mentioned above for which $\varepsilon_{ij} = \lambda s_{ij}$ holds, one also has $\varepsilon_{ii} = \lambda s_{ii} \equiv 0$. There is no volume change during the plastic deformation of a rigid perfectly plastic von Mises material. Hence, the total plastic work, $\sigma_{ij}\varepsilon_{ij}$ is $s_{ij}\varepsilon_{ij}$ (the internal work of a rigid perfectly plastic von Mises material is provided by the deviatoric stresses, s_{ij}, alone).

Hence, the internal (plastic) work (per unit volume of the membrane) is

$$\begin{aligned} W_p &= \sigma_{ij}\varepsilon_{ij} \\ &= s_{ij}\varepsilon_{ij} \\ &= s_{ij}s_{ij}\lambda \\ &= \sqrt{(2/3)}\sigma_0\sqrt{\varepsilon_{ij}\varepsilon_{ij}} \end{aligned} \tag{3.5.1}$$

For later use in the principle of the virtual work, of interest is the variation of the above internal work, i.e., evaluating δW_p, where δ is the virtual (or variational) operator. For this, one has

$$\begin{aligned} \delta W_p &= \delta\left(\sqrt{(2/3)}\sigma_0\sqrt{\varepsilon_{kl}\varepsilon_{kl}}\right) \\ &= \sqrt{(2/3)}\sigma_0\frac{\partial}{\partial\varepsilon_{ij}}\left(\sqrt{\varepsilon_{kl}\varepsilon_{kl}}\right)\delta\varepsilon_{ij} \\ &= \sqrt{(2/3)}\sigma_0\frac{\varepsilon_{ij}}{\sqrt{\varepsilon_{kl}\varepsilon_{kl}}}\delta\varepsilon_{ij} \\ &= \frac{\varepsilon_{ij}}{\lambda}\delta\varepsilon_{ij} \\ &= s_{ij}\delta\varepsilon_{ij} \end{aligned} \tag{3.5.2}$$

Hence, it is found that $s_{ij}\delta\varepsilon_{ij} = \delta W_p$.

In the virtual work, one has, for the internal virtual work, the quantity $\sigma_{ij}\delta\varepsilon_{ij}$ when the strains are independent of each other (they are only required to be compatible with the displacements using the usual strain-displacement relations). So, if one replaces $\sigma_{ij}\delta\varepsilon_{ij}$ with $s_{ij}\delta\varepsilon_{ij}$, there is a side condition that implies that the three normal strains ε_x, ε_y, and

ε_z are related so that the incompressibility holds, i.e., their sum is zero, or $\varepsilon_{ii} = 0$. Thus, one can let ε_z depend on the other normal strains, ε_x and ε_y, to enforce the incompressibility explicitly. An alternative approach to make these normal strains independent is to multiply the (subsidiary) incompressibility condition, $\varepsilon_{ii} = 0$ by an independent Lagrange multiplier and integrate over the volume (note that this multiplier will eventually appear as the internal pressure), and then it is added to the virtual work (using s_{ij} instead of σ_{ij}) expression. However, this will not be done.

Instead, the incompressibility will be enforced explicitly, using $\varepsilon_z = -(\varepsilon_x + \varepsilon_y)$. If this is done, then the internal virtual work becomes $s_{ij}\delta\varepsilon_{ij}$, which has been shown earlier to be equivalent to $\delta W_p = \sqrt{(2/3)}\sigma_0\delta\left(\sqrt{\varepsilon_{ij}\varepsilon_{ij}}\right)$.

Therefore, in addition to the in-plane strains ε_x, ε_y, and ε_{xy} as given in Eq. (3.3.3), one has the additional relation that

$$\varepsilon_z = -(\varepsilon_x + \varepsilon_y) \tag{3.5.3}$$

So, since the internal virtual work now is given by δW_p, and that involves the quantity $\sqrt{\varepsilon_{ij}\varepsilon_{ij}}$, focus is now made on evaluating the expression $\varepsilon_{ij}\varepsilon_{ij}$, using the non-zero strains, ε_x, ε_y, ε_{xy}, *and* ε_z. First, note, according to the definitions of the in-plane strains in Eq. (3.3.3), that

$$\frac{\partial w_0}{\partial x} = \sqrt{2\varepsilon_x}$$
$$\frac{\partial w_0}{\partial y} = \sqrt{2\varepsilon_y}$$

and using which, one has, for ε_{xy}^2,

$$\varepsilon_{xy}^2 = \frac{1}{4}\left(\frac{\partial w_0}{\partial x}\right)^2\left(\frac{\partial w_0}{\partial y}\right)^2 = \varepsilon_x\varepsilon_y$$

Next, $\varepsilon_{ij}\varepsilon_{ij}$ can be expanded as

$$\begin{aligned}
\varepsilon_{ij}\varepsilon_{ij} &= \varepsilon_x^2 + 2\varepsilon_{xy}^2 + \varepsilon_y^2 + \varepsilon_z^2 \\
&= \varepsilon_x^2 + 2\varepsilon_x\varepsilon_y + \varepsilon_y^2 + \varepsilon_z^2 \\
&= \left(\varepsilon_x^2 + 2\varepsilon_x\varepsilon_y + \varepsilon_y^2\right) + \varepsilon_z^2 \\
&= (\varepsilon_x + \varepsilon_y)^2 + \varepsilon_z^2 \\
&= (\varepsilon_x + \varepsilon_y)^2 + [-(\varepsilon_x + \varepsilon_y)]^2 \\
&= 2(\varepsilon_x + \varepsilon_y)^2
\end{aligned} \tag{3.5.4}$$

Note that the factor 2 appeared because of the incompressibility, which was enforced explicitly by $\varepsilon_z = -(\varepsilon_x + \varepsilon_y)$.

Using the last relation, $\sqrt{\varepsilon_{ij}\varepsilon_{ij}}$ is found as

$$\sqrt{\varepsilon_{ij}\varepsilon_{ij}} = \sqrt{2}\,(\varepsilon_x + \varepsilon_y) \tag{3.5.5}$$

Finally, the variation of internal work δW_p is found as

$$\delta W_p = \sqrt{(2/3)}\ \sigma_0\ \delta\left(\sqrt{\varepsilon_{ij}\varepsilon_{ij}}\right) = \sqrt{(2/3)}\ \sigma_0\sqrt{2}\,(\delta\varepsilon_x + \delta\varepsilon_y)\,, \tag{3.5.6}$$

in which the factor $\sqrt{(2/3)}$ came from von Mises yield condition and its consequence on the internal plastic work. A further additional factor, $\sqrt{2}$, appeared from the explicit enforcement of the plastic incompressibility. The product of these two factors is $2/\sqrt{3}$, which is the one that will show up in the equilibrium equation.

Now applying the virtual work principle to a membrane under zero in-plane displacements ($u_0 = v_0 = 0$), i.e., to a simple membrane, and using the internal virtual work as δW_p as given by the last expression, Eq. (3.5.6), (with an explicit enforcement of the incompressibility condition, $\varepsilon_x + \varepsilon_y + \varepsilon_z = 0$), one obtains the following equilibrium equation

$$\frac{2}{\sqrt{3}}\sigma_0\left(\frac{\partial^2 w_0}{\partial x^2} + \frac{\partial^2 w_0}{\partial y^2}\right) + \frac{p}{h} = \rho\ddot{w}_0 \tag{3.5.7}$$

In deriving the above equation, the simple membrane is assumed to be restrained along its outer edges. The equation will be used later when the external pressure p is set to zero in describing an impulsively loaded membrane. See Reddy (2002) and Washizu (1975) for excellent step-wise derivations of obtaining the governing equilibrium equation(s) using the virtual work method.

3.5.1 Discussion

In deriving the last equilibrium equation, no assumption has been made on the stress state except that it is and remains on the yield surface (i.e., without specifying a particular point on the yield surface). The strains, ε_{ij}, when non-zero will choose the appropriate point when motion takes place.

By comparing the last equilibrium equation with those developed in Section 3.3.4, in which the stress state was assumed to be free of in-plane shear stress throughout the membrane and in all orientations, it becomes apparent that the contributions of the in-plane shear stress and the incompressibility of the membrane provide extra membrane resistance that amounts to a factor of $2/\sqrt{3}$ compared to unity when they are neglected such that the resistance is provided solely by the normal membrane stresses.

However, this approach is valid when the loading path is monotonic and yielding is progressive. The monotonicity of the deformation path means that the absolute value of the strains is not allowed to decrease without an external agency that reverses the motion (i.e., extra external work is applied); this is because ε_{ij} are plastic strains (which cannot be

allowed to unload freely as elastic strains would). If reversal of motion happens, then there will be non-zero initial conditions for ε_{ij} and λ that must be accounted for. A progressive yielding is defined by the situation that yielding continues to be satisfied at a fixed point on the yield surface, i.e., $\dot{s}_{ij} \equiv 0$, throughout motion for every point on the membrane. The main assumption is that $\varepsilon_{ij} = \lambda s_{ij}$; if it is not valid, then it cannot be guaranteed that the last equilibrium equation is applicable.

3.6 Deriving the Equilibrium Equation Using the Virtual Work

3.6.1 Internal Virtual Work

In the previous section, the steps of deriving the equilibrium equations by the application of the virtual work were omitted for brevity. Herein, the procedure is revisited for the sake of clarity and completeness. The principle of virtual work is the starting point to develop the appropriate equilibrium equation. It is a powerful tool and very general in the sense that it applies to any structure made of any constitutive behaviour. In particular, it is applicable when the structure is a membrane made of rigid-perfectly plastic material. Among the terms of the virtual work statement, focus is made on the form of the internal virtual work as the other terms remain the same as in the general problems.

The internal virtual work is given by $\delta W_{int} = \sigma_{ij}\delta\varepsilon_{ij}$ that is integrated over the volume of the membrane. Herein, both quantities, σ_{ij} and ε_{ij}, are total, i.e., each is the sum of the corresponding deviatoric and volumetric parts. By expanding the stresses in terms of the deviatoric (s_{ij}) and hydrostatic pressure ($\hat{p}\delta_{ij}$) parts, one has, for the internal virtual work, $\delta W_{int} = (s_{ij}\delta\varepsilon_{ij} + \hat{p}\delta\varepsilon_{ii})$. It is important to recall that ε_{ij} is the total strain (i.e., it is not the deviatoric strain alone), whose volumetric part is ε_{ii}. The strains that are given in terms of the derivatives of the displacement are the total strains.

At this point, the form of the internal virtual work will be tailored to the present specific problem, which is a simple membrane that is free of in-plane displacements ($u_0 = v_0 = 0$) and in a state of plane stress. In particular, one has $\sigma_z = \sigma_{xz} = \sigma_{yz} = 0$. From $\sigma_z = 0$, one has $(s_z + \hat{p} = 0)$, and from which one can write $\hat{p} = -s_z$, where s_z is the deviatoric stress in the z direction. Since $\varepsilon_{ii} = \varepsilon_z + \varepsilon_x + \varepsilon_y$, then the internal virtual work of a membrane in a plane-stress is

$$\begin{aligned}
\delta W_{int} &= s_x\delta\varepsilon_x + 2s_{xy}\delta\varepsilon_{xy} + s_y\delta\varepsilon_y + s_z\delta\varepsilon_z + \hat{p}\left(\delta\varepsilon_x + \delta\varepsilon_y + \delta\varepsilon_z\right) \\
&= s_x\delta\varepsilon_x + 2s_{xy}\delta\varepsilon_{xy} + s_y\delta\varepsilon_y + s_z\delta\varepsilon_z - s_z\left(\delta\varepsilon_x + \delta\varepsilon_y + \delta\varepsilon_z\right) \\
&= s_x\delta\varepsilon_x + 2s_{xy}\delta\varepsilon_{xy} + s_y\delta\varepsilon_y - s_z\left(\delta\varepsilon_x + \delta\varepsilon_y\right),
\end{aligned} \tag{3.6.1}$$

where $\hat{p} = -s_z$ (since $\sigma_z = 0$) has been utilised. Now, if one lets the quantity $-(\varepsilon_x + \varepsilon_y)$ be interpreted as the normal strain ε_z so that the membrane is incompressible, i.e.

$$\varepsilon_z + \varepsilon_x + \varepsilon_y = 0, \tag{3.6.2}$$

then one obtains $-(\varepsilon_x + \varepsilon_y) = \varepsilon_z$. Hence, the internal virtual work can be expressed as

$$\begin{aligned} \delta W_{int} &= s_x \delta\varepsilon_x + 2s_{xy}\delta\varepsilon_{xy} + s_y\delta\varepsilon_y + s_z\left[-\left(\delta\varepsilon_x + \delta\varepsilon_y\right)\right] \\ &= s_x \delta\varepsilon_x + 2s_{xy}\delta\varepsilon_{xy} + s_y\delta\varepsilon_y + s_z\delta\varepsilon_z \end{aligned} \tag{3.6.3}$$

where ε_z, which re-appeared in the last equality above, is defined as $-(\varepsilon_x + \varepsilon_y)$, and it is said that the membrane whose internal virtual work as given above is explicitly incompressible. Now, it is important to bear in mind that all the strains appearing in the above internal virtual work expression are the total strains (not the deviatoric). In particular, these strains can be substituted with the relevant derivatives of displacements; the strain ε_z needs to be evaluated in terms of the derivatives of the displacement through its definition, i.e., $\varepsilon_z = -(\varepsilon_x + \varepsilon_y)$ since it appeared from there. Thus, the internal virtual work, as given by the last expression, can be rewritten compactly (in indicial notation), as $\delta W_{int} = s_{ij}\delta\varepsilon_{ij}$, while keeping in mind that the membrane is in a state of plane-stress, hence $s_{xz} = s_{yz} \equiv 0$.

Next, the internal virtual work is further specialised for the rigid-perfectly plastic membrane where its plasticity obeys von Mises's condition. For the conditions under which the total form of the flow rule applies (i.e., $\dot{s}_{ij} = 0$ throughout the (purely plastic) response and with zero initial conditions of ε_{ij} and λ), one has for the (purely plastic) strains: $\varepsilon_{ij} = \lambda s_{ij}$. Also, it was shown that the internal (plastic) work during deformation is given by $W_p = s_{ij}\varepsilon_{ij} = \sqrt{(2/3)}\sigma_0\sqrt{\varepsilon_{ij}\varepsilon_{ij}}$ where σ_0 is the uni-axial yield stress. Furthermore, it has been shown that the variation of this internal work is $\delta W_p = s_{ij}\delta\varepsilon_{ij}$. In summary, the internal virtual work given earlier, δW_{int}, is δW_p. That is,

$$\begin{aligned} \delta W_{int} &= s_{ij}\delta\varepsilon_{ij} \\ &= \delta W_p = \delta\left[\sqrt{(2/3)}\sigma_0\sqrt{\varepsilon_{ij}\varepsilon_{ij}}\right] \\ &= \sqrt{(2/3)}\sigma_0\delta\left(\sqrt{\varepsilon_{ij}\varepsilon_{ij}}\right) \end{aligned} \tag{3.6.4}$$

Recall once again that the strains appearing above are the total strains, and hence they can be expressed in terms of the derivatives of displacements. Now, for the present simple membrane (which is free of in-plane displacements), one has for the in-plane strains, as

presented earlier in Eq. (3.3.3),

$$\begin{aligned} \varepsilon_x &= \frac{1}{2}\left(\frac{\partial w_0}{\partial x}\right)^2 \\ \varepsilon_y &= \frac{1}{2}\left(\frac{\partial w_0}{\partial y}\right)^2 \\ \varepsilon_{xy} &= \frac{1}{2}\frac{\partial w_0}{\partial x}\frac{\partial w_0}{\partial y} \end{aligned} \tag{3.6.5}$$

and in addition, one has for ε_z (due to the incompressibility, Eq. (3.6.2)),

$$\varepsilon_z = -\left(\varepsilon_x + \varepsilon_y\right)$$

From the definitions of the three in-plane strains, $\varepsilon_x, \varepsilon_y, \varepsilon_{xy}$, it can be inferred (by compatibility) that

$$\varepsilon_{xy}^2 = \varepsilon_x \varepsilon_y$$

Therefore, the quantity $\varepsilon_{ij}\varepsilon_{ij}$ is expanded as

$$\begin{aligned} \varepsilon_{ij}\varepsilon_{ij} &= \varepsilon_x^2 + 2\varepsilon_x\varepsilon_y + \varepsilon_y^2 + \left[-\left(\varepsilon_x + \varepsilon_y\right)\right]^2 \\ &= 2\left(\varepsilon_x + \varepsilon_y\right)^2, \end{aligned}$$

where only algebraic operations were performed. Hence, it was found that $\sqrt{\varepsilon_{ij}\varepsilon_{ij}} = \sqrt{2}(\varepsilon_x + \varepsilon_y)$. Consequently, one has for the internal virtual work,

$$\begin{aligned} \delta W_{int} = \delta W_p &= \sqrt{(2/3)}\sigma_0 \delta\left(\sqrt{\varepsilon_{ij}\varepsilon_{ij}}\right) \\ &= \sqrt{(2/3)}\sigma_0\sqrt{2}\left(\delta\varepsilon_x + \delta\varepsilon_y\right) \end{aligned} \tag{3.6.6}$$

Finally, by expressing the normal strains, ε_x and ε_y, in terms of the displacements, one gets

$$\begin{aligned} \delta W_{int} &= 2/(\sqrt{3})\sigma_0\left(\delta\varepsilon_x + \delta\varepsilon_y\right) \\ &= 2/(\sqrt{3})\sigma_0\left(\frac{\partial w_0}{\partial x}\frac{\partial \delta w_0}{\partial x} + \frac{\partial w_0}{\partial y}\frac{\partial \delta w_0}{\partial y}\right) \end{aligned} \tag{3.6.7}$$

since $\delta\varepsilon_x = \frac{\partial w_0}{\partial x}\frac{\partial \delta w_0}{\partial x}$ and $\delta\varepsilon_y = \frac{\partial w_0}{\partial y}\frac{\partial \delta w_0}{\partial y}$.

3.6.2 Total Virtual Work

Now, the virtual work equation for the simple membrane (with $u_0 = v_0 = 0$)

$$\int_V \delta W_{int}\, dv + \int_V \rho\ddot{w}_0\delta w_0\, dv - \int_S p(x,y)\delta w_0\, ds = 0 \tag{3.6.8}$$

can be expanded as

$$2/(\sqrt{3})\sigma_0 h \int_S \left(\frac{\partial w_0}{\partial x}\frac{\partial \delta w_0}{\partial x} + \frac{\partial w_0}{\partial y}\frac{\partial \delta w_0}{\partial y} \right) \, ds + \rho h \int_S \ddot{w}_0 \delta w_0 \, ds - \int_S p(x,y)\delta w_0 \, ds = 0,$$

where h is the (uniform) thickness of the membrane, across which all quantities are uniform, and ρ is its (uniform) mass density (mass per unit volume). The externally applied pressure (in the direction of w_0) is denoted by p. By performing integration by parts, one then obtains

$$\int_S \left[-2/(\sqrt{3})\sigma_0 h \left(\frac{\partial^2 w_0}{\partial x^2} + \frac{\partial^2 w_0}{\partial y^2} \right) - p(x,y) + \rho h \ddot{w}_0 \right] \delta w_0 \, ds = 0, \tag{3.6.9}$$

in which the assumption that w_0 is imposed on the boundary of the membrane requires that $\delta w_0 \equiv 0$ on the boundary, which was utilised in arriving at the above result.

3.6.3 The Equilibrium Equation

The equilibrium equation is then obtained by making δw_0 arbitrary over the interior of the membrane area, S, and hence the integrand in Eq. (3.6.9) is required to vanish for the virtual work to hold for any surface area of the membrane. The equilibrium equation is

$$\frac{2\sigma_0}{\sqrt{3}} \left(\frac{\partial^2 w_0}{\partial x^2} + \frac{\partial^2 w_0}{\partial y^2} \right) + \frac{p}{h} = \rho \ddot{w}_0 \tag{3.6.10}$$

Recall that this equilibrium equation is considered valid for a membrane that is:

(i) Free of in-plane displacements ($u_0 = v_0 = 0$), and the strain energy is due (only) to the transverse displacement w_0 being large;

(ii) Made of a rigid-perfectly plastic von Mises material, with uni-axial tensile stress σ_0, and incompressible;

(iii) Subjected to a monotonic loading path (with the initial condition for ε_{ij} being zero) and experiencing progressive yielding so that $\dot{s}_{ij} = 0$ throughout the response. That is, $\varepsilon_{ij} = \lambda s_{ij}$ holds.

An alternative approach to derive the equilibrium equation of the simple membrane, which is made of a rigid-perfectly plastic von Mises material, is provided in Appendix A. Therein, the general equilibrium equation is chosen as the starting point, then the constitutive relation (i.e., the total flow rule) is utilised to replace the stresses (in the original equilibrium equation) with the deformation measures, i.e., the strains and the gradients of the transverse displacement. The final equation of motion is identical to the plastic wave equation, Eq. (3.6.10), that was derived in the present chapter. That is, the obtained equilibrium equation is not a mere consequence of the variational principle (whether the virtual work

or the extended Hamilton's principles). Although, the application of the variational principle (namely, the virtual work as used in the present chapter) is of convenience to derive the final equilibrium equation systematically and simply. In Section 4.3.2 in Chapter 4, the extended Hamilton's principle will be used to re-derive the same equilibrium equation for the rigid-perfectly plastic von Mises simple membranes. In overall, three different (yet completely equivalent) approaches have been utilised to obtain the same plastic wave equation.

The problem of an axi-symmetric circular simple membrane that is made of a rigid-perfectly plastic von Mises material is addressed in Section B.1.4 of Appendix B. For such problem, the in-plane displacement is the radial displacement which is considered zero, and the transverse equilibrium equation is derived in which the factor $(2/\sqrt{3})\sigma_0$, also, appears.

The effect of the in-plane displacement on the transverse motion of (general) membranes is thoroughly discussed for the axi-symmetric circular case in Cloete and Nurick (2014), in which the authors derive an important result that the in-plane (i.e., the radial) displacement provides a zero total contribution to the total plastic internal work. That is, the externally imparted energy to the membrane is dissipated through the transverse deformation only. In Section B.2.1 of Appendix B, the original problem of Cloete and Nurick is reviewed and analysed in detail to guide the reader and also to derive some important features of the in-plane displacement response, which are direct consequences of the original authors' result. Furthermore, the main idea of Cloete and Nurick that the total plastic work is completely independent of the in-plane displacement for the axi-symmetric circular problem is extended, in Section B.2.2 of Appendix B, to make it applicable to general (e.g., rectangular) membrane problems. The simple membrane kinematics removes the in-plane displacement effect completely, which is found to be of a practical importance in determining the stress state and expressing the transverse equilibrium equation in terms of fixed (or constant) stresses. Again, the simple membrane kinematic's idealisation is based on the result of Cloete and Nurick (2014) and its generalisation, which was mentioned above, as given in Appendix B.1.3.

3.7 Implications of $\varepsilon_{ij} = \lambda s_{ij}$ on the Validity of the Solution

When the total form of the flow rule holds, one has $\varepsilon_{ij} = \lambda s_{ij}$, in the rigid-perfectly plastic von Mises membrane. This relation emerges by integrating the classical "incremental" flow rule from zero initial conditions (for ε_{ij} and λ) and by assuming that $\dot{s}_{ij} = 0$. Whenever the strain rates $\dot{\varepsilon}_{ij}$ are non-zero, the stresses have to satisfy the yield condition in the rigid-plastic membrane. The accumulations (over time) of the non-zero $\dot{\varepsilon}_{ij}$ result in non-zero total strains, ε_{ij}. Hence, the stresses in the total flow rule, $\varepsilon_{ij} = \lambda s_{ij}$, are required to satisfy the yield condition when ε_{ij} are non-zero *and* when they are changing with respect to time, (i.e., the instantaneous strain rates, $\dot{\varepsilon}_{ij}$, are non-zero).

Furthermore, for the condition $\dot{s}_{ij} = 0$ to be valid, the acceleration of the strains, $\ddot{\varepsilon}_{ij}$, must be normal to the yield surface (i.e., aligned with s_{ij}) but can be pointing either toward its exterior or to its interior. The first direction of $\ddot{\varepsilon}_{ij}$ (i.e., to the exterior of the yield surface) implies that the strain rates are increasing in magnitude. In contrast, the other possible direction of $\ddot{\varepsilon}_{ij}$ corresponds to a decreasing strain rate (in magnitude); this is a critical scenario as it signals that the response is approaching a critical time instant when the strain rates reach zero. If strain rates become zero, one cannot require the stresses to satisfy the yield condition. In particular, the total flow rule is not applicable for the subsequent response after the critical time instant. When strain rates reverse their sign (as they pass through zero from the initial phase of response) and continue to become non-zero, the stresses need to satisfy the yield condition at another point on the surface; recall that strain rates $\dot{\varepsilon}_{ij}$ and stresses s_{ij} have to have similar signs (this is direct consequence of the incremental flow rule, $\dot{\varepsilon}_{ij} = \dot{\lambda} s_{ij}$, and by noting that $\dot{\lambda}$ must be non-negative at all times). Hence, the total form of the flow rule must be established for the new phase of response, and at this time it must account for the new initial conditions of ε_{ij} and λ, which are the final values from the initial phase of the response (just before $\dot{\varepsilon}_{ij}$ turned zero for the first time).

Since the strain rates have not been considered explicitly when the total form of flow rule is adopted, it is important to identify another quantity that can signal the occurrence of the critical time instant. One important quantity is the parameter λ, since it is a scalar and is directly related to the strains ε_{ij}. If the value of λ starts to decrease, then there must be a critical time instant. This is because λ is $1/(\sqrt{(2/3)}\sigma_0)\sqrt{\varepsilon_{ij}\varepsilon_{ij}}$, and hence it measures the magnitude of the strains. When the strains, ε_{ij}, just start decreasing, they indicate that the strain rates have just reversed their signs, i.e., they have just passed through zero. This will make λ begin to decrease. Preventing λ from decreasing is the idea of watching for the critical time instant. Furthermore, λ is the time integral of $\dot{\lambda}$, and it is $\dot{\lambda}$ that must be kept non-negative at all times; that is, λ cannot be allowed to decrease, and if it does, then the subsequent motion is not correct.

Therefore, the total flow rule, $\varepsilon_{ij} = \lambda s_{ij}$, is valid until λ starts to decrease, this is the instant of critical time. The response is stopped at this instant, and for the subsequent motion, a new total flow rule is established in the form of $\varepsilon_{ij} = \varepsilon_{ij}^{(0)} + s_{ij}\lambda - s_{ij}^{(0)}\lambda^{(0)}$. The new initial conditions (denoted by the superscript (0)) are the corresponding values just before the critical time instant. However, the real merit of adopting the total form of the flow rule (from the practical point of view) is when the whole response is terminated at the first occurrence of a critical time instant, that is when the entire motion ends at such time instant so that there is no necessity to use the total form of flow rule with non-zero initial conditions. In other words, of interest is the case when there is only one phase of motion that is associated with the total flow rule with zero initial conditions.

For the present problem of the rigid-perfectly plastic simple membrane, it has been shown that $\sqrt{\varepsilon_{ij}\varepsilon_{ij}} = \sqrt{2}(\varepsilon_x + \varepsilon_y)$. Hence, $\lambda = \sqrt{3}/(\sigma_0)(\varepsilon_x + \varepsilon_y)$, and the solution based on the total flow rule is considered valid until this λ starts to decrease. A simplified example of a

simple membrane that is impulsively loaded and in which the initial velocity is proportional to the first mode of vibration will be treated in Section 3.9.3. Due to the wave nature of the equilibrium equation, the (general) solution comprises a combination of (vibrational) modes, and if the loading term, such as the initial velocity field in an impulsive regime, is proportional to the shape of a single mode, then the total solution becomes very simple as the response of this single mode alone. Hence, the notion of the solution termination step can be clarified analytically therein, where it is related to the evolution of kinetic energy and the plastic work rate. Further discussion on the importance of the solution termination step in general and the *influence* of this step on the prediction of the permanent (or plastic) response will be revisited in Chapters 4 and 5, and lastly in Section 6.5.

3.8 Implications of $\varepsilon_{ij} = \lambda s_{ij}$ on the Stress State of the Simple Membrane

There are other implications of the total form of flow rule, $\varepsilon_{ij} = \lambda s_{ij}$, namely on the stress state at yielding of the present simple membrane. It was shown that $s_z = -\hat{p}$, since $\sigma_z = 0$, and $\varepsilon_z = -(\varepsilon_x + \varepsilon_y)$, due to the incompressibility. Hence, by direct application of the total flow rule, the deviatoric stress s_z is found as

$$\begin{aligned} s_z = \frac{\varepsilon_z}{\lambda} &= \sqrt{(2/3)}\sigma_0 \frac{\varepsilon_z}{\sqrt{2}(\varepsilon_x + \varepsilon_y)} \\ &= \sqrt{(2/3)}\sigma_0 \frac{-(\varepsilon_x + \varepsilon_y)}{\sqrt{2}(\varepsilon_x + \varepsilon_y)} \\ &= \frac{-1}{\sqrt{3}}\sigma_0, \end{aligned} \tag{3.8.1}$$

which also gives $\hat{p} = -s_z = 1/(\sqrt{3})\sigma_0$.

Since $\hat{p} = (1/3)(\sigma_x + \sigma_y)$, the following result is obtained

$$\begin{aligned} \sigma_x + \sigma_y &= 3\hat{p} \\ &= \frac{3}{\sqrt{3}}\sigma_0 \\ &= \sqrt{3}\sigma_0 \end{aligned}$$

From the total flow rule, one also has

$$\begin{aligned} s_x = \frac{\varepsilon_x}{\lambda} &= \sqrt{(2/3)}\sigma_0 \frac{\varepsilon_x}{\sqrt{2}(\varepsilon_x + \varepsilon_y)} \\ &= \frac{\varepsilon_x}{(\varepsilon_x + \varepsilon_y)} \frac{1}{\sqrt{3}} \sigma_0 \\ s_y = \frac{\varepsilon_y}{\lambda} &= \frac{\varepsilon_y}{(\varepsilon_x + \varepsilon_y)} \frac{1}{\sqrt{3}} \sigma_0 \\ s_{xy} = \frac{\varepsilon_{xy}}{\lambda} &= \frac{\varepsilon_{xy}}{(\varepsilon_x + \varepsilon_y)} \frac{1}{\sqrt{3}} \sigma_0 \end{aligned} \tag{3.8.2}$$

so that, using $\sigma_x = s_x + \hat{p}$ and $\sigma_y = s_y + \hat{p}$, one can find that

$$\begin{aligned} \sigma_x &= s_x + \hat{p} \\ &= \frac{\varepsilon_x}{(\varepsilon_x + \varepsilon_y)} \frac{1}{\sqrt{3}} \sigma_0 + \frac{1}{\sqrt{3}} \sigma_0 \\ &= \frac{2\varepsilon_x + \varepsilon_y}{(\varepsilon_x + \varepsilon_y)} \frac{1}{\sqrt{3}} \sigma_0 \\ \sigma_y &= s_y + \hat{p} \\ &= \frac{2\varepsilon_y + \varepsilon_x}{(\varepsilon_x + \varepsilon_y)} \frac{1}{\sqrt{3}} \sigma_0 \\ \sigma_x + \sigma_y &= \frac{3\varepsilon_x + 3\varepsilon_y}{(\varepsilon_x + \varepsilon_y)} \frac{1}{\sqrt{3}} \sigma_0 \\ &= \sqrt{3}\sigma_0 \end{aligned} \tag{3.8.3}$$

By the definition of the in-plane strains, it might be written that $\varepsilon_{xy}^2 = \varepsilon_x \varepsilon_y$, which, in fact, was used in deriving $\sqrt{\varepsilon_{ij}\varepsilon_{ij}} = \sqrt{2}(\varepsilon_x + \varepsilon_y)$. Hence, one also has the following relation for the shear stress $s_{xy} = \sigma_{xy}$,

$$\sigma_{xy}^2 = \left(\frac{\varepsilon_{xy}}{(\varepsilon_x + \varepsilon_y)} \frac{1}{\sqrt{3}} \sigma_0 \right)^2 = \frac{\varepsilon_x \varepsilon_y}{(\varepsilon_x + \varepsilon_y)^2} \frac{1}{3} \sigma_0^2$$

from which one can write

$$\sigma_{xy} = \frac{\pm\sqrt{\varepsilon_x \varepsilon_y}}{(\varepsilon_x + \varepsilon_y)} \frac{1}{\sqrt{3}} \sigma_0, \tag{3.8.4}$$

where one has two (equally valid) solutions for the σ_{xy}.

From the above, it is seen that the stress state is completely determined by the values of the in-plane normal strains, ε_x and ε_y. These strains are given by the derivatives of the transverse displacement w_0, i.e., by $\varepsilon_x = (1/2)\left(\frac{\partial w_0}{\partial x}\right)^2$ and $\varepsilon_y = (1/2)\left(\frac{\partial w_0}{\partial y}\right)^2$. Since these normal strains are always non-negative, then the sum $\varepsilon_x + \varepsilon_y$ will not be zero unless

both of these strains are identically zero, i.e., when the membrane is rigid. Hence, the stress state can be determined whenever the membrane is not rigid, i.e., whenever either or both of ε_x and ε_y are non-zero.

3.8.1 Determination of Stress States for Special Cases of the In-Plane Strains

3.8.1.1 In-Plane Stresses

According to the above relations, Eqs. (3.8.3) and (3.8.4), important special cases of the stress states can be studied based on the values of the in-plane normal strains:

Case (A): $\varepsilon_y = 0$ and $\varepsilon_x \neq 0$.

For this case, one obtains

$$\varepsilon_{xy} = \pm\sqrt{\varepsilon_x \varepsilon_y} = 0$$

$$\sigma_{xy} = 0$$

$$\sigma_x = \frac{2}{\sqrt{3}}\sigma_0$$

$$\sigma_y = \frac{1}{\sqrt{3}}\sigma_0 = \frac{1}{2}\sigma_x$$

$$\sigma_x + \sigma_y = \frac{3}{\sqrt{3}}\sigma_0 \equiv 3\hat{p} = \sqrt{3}\sigma_0$$

Case (B): $\varepsilon_x = 0$ and $\varepsilon_y \neq 0$.

For this case, one obtains

$$\varepsilon_{xy} = \pm\sqrt{\varepsilon_x \varepsilon_y} = 0$$

$$\sigma_{xy} = 0$$

$$\sigma_x = \frac{1}{\sqrt{3}}\sigma_0$$

$$\sigma_y = \frac{2}{\sqrt{3}}\sigma_0 = 2\sigma_x$$

$$\sigma_x + \sigma_y = \frac{3}{\sqrt{3}}\sigma_0 \equiv 3\hat{p} = \sqrt{3}\sigma_0$$

Case (C): $\varepsilon_x = \varepsilon_y \neq 0$.

For this case, one obtains

$$\varepsilon_{xy} = \pm\varepsilon_x = \pm\varepsilon_y$$

$$\sigma_{xy} = \frac{\pm\varepsilon_x}{(2\varepsilon_x)}\frac{1}{\sqrt{3}}\sigma_0 = \frac{\pm 1}{2}\left(\frac{1}{\sqrt{3}}\sigma_0\right)$$

$$\sigma_x = \frac{3}{2\sqrt{3}}\sigma_0 = \frac{\sqrt{3}}{2}\sigma_0$$

$$\sigma_y = \sigma_x = \frac{3}{2\sqrt{3}}\sigma_0 = \frac{\sqrt{3}}{2}\sigma_0$$

$$\sigma_x + \sigma_y = \left(\frac{\sqrt{3}}{2}\sigma_0 + \frac{\sqrt{3}}{2}\sigma_0\right) \equiv 3\hat{p} = \sqrt{3}\sigma_0$$

It should be pointed out that the stress state can not be determined when ε_x and ε_y are both zero because the structure is rigid in this case. As soon as either or both of these in-plane normal strains deviate from zero, then one says that the membrane is yielding and hence its stress state (which has to be satisfying the yield condition) can be determined, as it has been shown for the special cases above and also by the general relations in terms of the arbitrary (but non-zero) values of these normal strains. Recall, again, that these strains are non-negative (from their dependence on the square of the derivates of w_0), and hence their sum, which appears in the denominator of the above relations, can not be zero unless the membrane is rigid.

3.8.1.2 Principal In-Plane Stresses

As it was shown, above, the stress state $(\sigma_x, \sigma_y, \sigma_{xy})$ can be determined once at least one of the normal strains is non-zero. Then, use can be made of Mohr's circle to further determine the values of the principal stresses and the orientations of the principal axes. In particular, one can do so for the above important special cases, A, B, and C, for which the stress states, i.e., the triplets $(\sigma_x, \sigma_y, \sigma_{xy})$, are fixed values that are proportional to the uni-axial tensile yield stress σ_0 (the dependency of the in-plane stresses on the normal strains disappear for those special cases).

The largest (in-plane) principal stresses will be denoted by σ_1 and the other by σ_2, and thus one has $\sigma_1 \geq \sigma_2$ as a convention. Then, recall that for a plane-stress problem, a Mohr circle is drawn in the space of normal stress σ and shearing stress τ, where the horizontal axis is the normal stress, and the vertical axis is the shearing stress, see Fig. 3.2. The procedure of principal stress analysis for plane-stress problems can be found in any standard engineering textbook on the mechanics of materials.

Furthermore, the centre of the circle always lies on the horizontal axis. An arbitrary stress state, characterised by the triplet $(\sigma_x, \sigma_y, \sigma_{xy})$, is a point on the Mohr's circle. The in-plane principal stresses are the abscissas of the (two) special points on the circle where

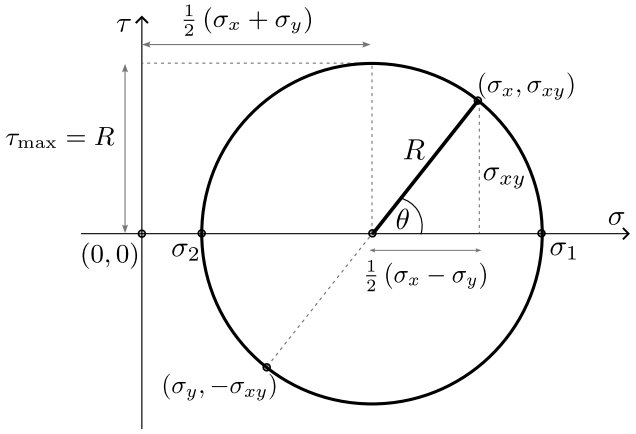

Fig. 3.2. A generic Mohr's circle for plane-stress. The important parameters defining the stress state are shown. A general plane-stress state, i.e., with arbitrary triplet $\sigma_x, \sigma_y, \sigma_{xy}$, completely defines the centre of the Mohr's circle $\left(\frac{1}{2}[\sigma_x + \sigma_y], 0\right)$, its radius $\left(R = \sqrt{[\frac{1}{2}(\sigma_x - \sigma_y)]^2 + \sigma_{xy}^2}\right)$, and an angle (2θ); by geometry, $\tan(2\theta) = \sigma_{xy}/[\frac{1}{2}(\sigma_x - \sigma_y)]$. The principal stresses σ_1 and σ_2 are also determined, as the abscissas of two extreme points of the circle as it intersects the horizontal axis. The angle (2θ) determines the inclination of the largest principal stress σ_1 axis with the x-axis. Note that, in this figure, it is implied that $\sigma_x \geq \sigma_y$.

there are no shearing stresses. The principal stress states are, thus, the two extreme points on the circle where the circle intersects the horizontal axis since this axis is the line of zero shear stress. Hence, by geometry, σ_1 equals the abscissa of the coordinate of the circle's centre *plus* the radius of the circle. Also, σ_2 equals the abscissa of the circle's centre *minus* the radius of the circle.

The abscissa of the centre is the average of σ_x and σ_y, or $(1/2)(\sigma_x + \sigma_y)$. The radius of the circle is $\sqrt{[(\sigma_x - \sigma_y)/2]^2 + \sigma_{xy}^2}$. So, once σ_x, σ_y and σ_{xy} are known, one can find the abscissa of the centre and the radius of the Mohr circle, and, in turn, the values of the principal stresses σ_1 and σ_2. Note that since the present problem is a plane-stress, then the abscissa of the centre, $(1/2)(\sigma_x + \sigma_y)$, is always given by $(1/2)(\sigma_x + \sigma_y) = (3/2)\hat{p}$, which for the present rigid-perfectly plastic membrane corresponds to $3/(2\sqrt{3})\sigma_0 = \sqrt{3}/(2)\sigma_0$.

Therefore, the principal stresses for the three special cases, A, B, and C, are:

Case (A): $\varepsilon_y = 0$ and $\varepsilon_x \neq 0$.

It was shown that

$$\sigma_{xy} = 0$$

$$\sigma_x = \frac{2}{\sqrt{3}}\sigma_0$$

$$\sigma_y = \frac{1}{\sqrt{3}}\sigma_0 = \frac{1}{2}\sigma_x$$

Thus, the abscissa of the centre of Mohr's circle is $(1/2)(\sigma_x + \sigma_y) = \sqrt{3}/(2)\sigma_0$. And, the radius of the circle is $\sqrt{\left[1/(2\sqrt{3})\sigma_0\right]^2} = 1/(2\sqrt{3})\sigma_0$. Therefore, the

principal stresses are

$$\sigma_1 = \sqrt{3}/(2)\sigma_0 + 1/(2\sqrt{3})\sigma_0 = 2/\sqrt{3}\sigma_0 = \sigma_x$$
$$\sigma_2 = \sqrt{3}/(2)\sigma_0 - 1/(2\sqrt{3})\sigma_0 = 1/\sqrt{3}\sigma_0 = \sigma_y$$

Furthermore, the principal shear stress is $\tau_{max} = \pm 1/(2\sqrt{3})\sigma_0$. Note that since $\sigma_{xy} = 0$ for the present case, then $\sigma_1 = \sigma_x$ and $\sigma_2 = \sigma_y$. The geometric axes x and y *are* the principal stress axes. The principal shear direction is at 45° degrees with respect to principal stress σ_1 axis, which is the x axis in this case.

Case (B): $\varepsilon_x = 0$ and $\varepsilon_y \neq 0$.

It was shown that

$$\sigma_{xy} = 0$$
$$\sigma_x = \frac{1}{\sqrt{3}}\sigma_0$$
$$\sigma_y = \frac{2}{\sqrt{3}}\sigma_0 = 2\sigma_x$$

Again, the abscissa of the centre is $\sqrt{3}/(2)\sigma_0$, and the radius of Mohr's circle for the present case is $\sqrt{\left[-1/(2\sqrt{3})\sigma_0\right]^2} = 1/(2\sqrt{3})\sigma_0$. From these, one obtains, for the principal stresses, the following

$$\sigma_1 = \sqrt{3}/(2)\sigma_0 + 1/(2\sqrt{3})\sigma_0 = 2/\sqrt{3}\sigma_0 = \sigma_y$$
$$\sigma_2 = \sqrt{3}/(2)\sigma_0 - 1/(2\sqrt{3})\sigma_0 = 1/\sqrt{3}\sigma_0 = \sigma_x$$

where have retained our convention that $\sigma_1 \geq \sigma_2$. According to the above, it is seen that $\sigma_1 = \sigma_y$ and $\sigma_2 = \sigma_x$. The direction of the largest principal stress σ_1 is the geometric y axis, and the second principal axis coincides with the x axis. The principal shear stress is again $\tau_{max} = \pm 1/(2\sqrt{3})\sigma_0$, as in the previous case A. The direction of principal shear stress is at 45° degrees with respect to the principal stress σ_1 axis, which is the y axis in the present case.

Case (C): $\varepsilon_x = \varepsilon_y \neq 0$.

It was shown that

$$\sigma_{xy} = \frac{\pm 1}{2}\left(\frac{1}{\sqrt{3}}\sigma_0\right)$$

$$\sigma_x = \frac{\sqrt{3}}{2}\sigma_0$$

$$\sigma_y = \sigma_x = \frac{\sqrt{3}}{2}\sigma_0$$

The abscissa of the centre is as before, i.e., $\sqrt{3}/(2)\sigma_0$. For the present case, the radius of the circle is simply the absolute value of σ_{xy}, since $\sigma_x = \sigma_y$. That is, the radius is $1/(2\sqrt{3})\sigma_0$. Since $\sigma_x = \sigma_y = \sqrt{3}/(2)\sigma_0$, which is the abscissa of the centre, then for the present case, the stress state is the principal shear stress state, the points on the circle that is directly above its centre. Thus, τ_{max} is simply the absolute value of σ_{xy}. Furthermore, the principal normal stresses, σ_1 and σ_2 are found as

$$\sigma_1 = \sqrt{3}/(2)\sigma_0 + 1/(2\sqrt{3})\sigma_0 = 2/\sqrt{3}\sigma_0$$

$$\sigma_2 = \sqrt{3}/(2)\sigma_0 - 1/(2\sqrt{3})\sigma_0 = 1/\sqrt{3}\sigma_0,$$

which are numerically the same as in all the previous cases, A and B. However, the direction of the principal (normal) stress, σ_1, the axis is rotated at 45^o to the x axis. The direction of the second principal stress, σ_2, makes $90^o + 45^o$ angle with respect to the x axis. Note that for the present case, the geometric axes x and y are the directions of principal shear stresses.

From the above considerations, it is seen that the numerical values of the principal stresses are all the same. However, the directions of the principal stresses σ_1 and σ_2 vary in each of these cases. The largest principal stress, σ_1, axis is the x-axis when $\varepsilon_y = 0$; it is the y-axis when $\varepsilon_x = 0$; and it makes equal (45^o degrees) angles with the x and y-axes when $\varepsilon_x = \varepsilon_y$.

3.8.2 Principal Stresses for the General Strain Case

Based on the observation that the numerical values of the principal stresses are fixed for the three special cases discussed in the previous subsection, focus in the following is on their values for the general case when the normal strains ε_x and ε_y are arbitrary (but not both zero simultaneously). By the definition of the principal stresses in plane-stress, one

has

$$\begin{aligned} \sigma_1 &= \frac{1}{2}(\sigma_x + \sigma_y) + R \\ &= \frac{3}{2}\hat{p} + R, \\ \sigma_2 &= \frac{1}{2}(\sigma_x + \sigma_y) - R \\ &= \frac{3}{2}\hat{p} - R, \end{aligned} \tag{3.8.5}$$

where R is the radius of Mohr's circle, and the common first term in both equations is the abscissa of the centre of the circle. It was already found that $\hat{p} = 1/(\sqrt{3})\sigma_0$. Thus, to determine the principal stresses, one needs to evaluate R. From the geometry of the Mohr's circle, R is

$$R = \sqrt{\left(\frac{\sigma_x - \sigma_y}{2}\right)^2 + \sigma_{xy}^2}, \tag{3.8.6}$$

where it is seen that the signs of both $(\sigma_x - \sigma_y)$ and σ_{xy} are not important, since each term will be squared. From the earlier relations for the three in-plane stresses, σ_x, σ_y, and σ_{xy}, in terms of the normal strains ε_x and ε_y, namely

$$\begin{aligned} \sigma_x &= \frac{2\varepsilon_x + \varepsilon_y}{\varepsilon_x + \varepsilon_y}\frac{1}{\sqrt{3}}\sigma_0 \\ \sigma_y &= \frac{2\varepsilon_y + \varepsilon_x}{\varepsilon_x + \varepsilon_y}\frac{1}{\sqrt{3}}\sigma_0 \\ \sigma_{xy} &= \frac{\pm\sqrt{\varepsilon_x\varepsilon_y}}{\varepsilon_x + \varepsilon_y}\frac{1}{\sqrt{3}}\sigma_0 \end{aligned}$$

one finds that

$$\begin{aligned} \left(\frac{\sigma_x - \sigma_y}{2}\right)^2 &= \frac{(1/4)(\varepsilon_x - \varepsilon_y)^2}{(\varepsilon_x + \varepsilon_y)^2}\left(\frac{1}{\sqrt{3}}\sigma_0\right)^2 \\ \sigma_{xy}^2 &= \frac{\varepsilon_x\varepsilon_y}{(\varepsilon_x + \varepsilon_y)^2}\left(\frac{1}{\sqrt{3}}\sigma_0\right)^2 \end{aligned}$$

and, hence,

$$\begin{aligned} \left(\frac{\sigma_x - \sigma_y}{2}\right)^2 + \sigma_{xy}^2 &= \frac{(1/4)(\varepsilon_x + \varepsilon_y)^2}{(\varepsilon_x + \varepsilon_y)^2}\left(\frac{1}{\sqrt{3}}\sigma_0\right)^2 \\ &= \left(\frac{1}{2\sqrt{3}}\sigma_0\right)^2 \end{aligned} \tag{3.8.7}$$

Therefore, one has for the radius of Mohr's circle, (for arbitrary ε_x and ε_y),

$$\begin{aligned} R &= \sqrt{\left(\frac{\sigma_x - \sigma_y}{2}\right)^2 + \sigma_{xy}^2} \\ &= \frac{1}{2\sqrt{3}}\sigma_0 \end{aligned} \tag{3.8.8}$$

Finally, the principal stresses, σ_1 and σ_2, are

$$\begin{aligned} \sigma_1 &= \frac{3}{2}\hat{p} + R \\ &= \frac{3}{2\sqrt{3}}\sigma_0 + \frac{1}{2\sqrt{3}}\sigma_0 \\ &= \frac{2}{\sqrt{3}}\sigma_0 \\ \sigma_2 &= \frac{3}{2}\hat{p} - R \\ &= \frac{3}{2\sqrt{3}}\sigma_0 - \frac{1}{2\sqrt{3}}\sigma_0 \\ &= \frac{1}{\sqrt{3}}\sigma_0 \end{aligned} \tag{3.8.9}$$

where σ_1 is (by convention) the largest principal stress, i.e., $\sigma_1 > \sigma_2$. The above general solution agrees with all the special cases. Thus, it is shown that σ_1 is always $2/(\sqrt{3})\sigma_0$ and $\sigma_2 = 1/(\sqrt{3})\sigma_0 = (1/2)\sigma_1 = \hat{p}$. The numerical values of the two principal stresses are fixed irrespective of the amount of the normal strains ε_x and ε_y, provided that these strains are not both zero; the membrane is rigid if one has $\varepsilon_x = \varepsilon_y = 0$, and hence there is no requirement that the yield condition is satisfied, which in turn means that the stress state cannot be determined.

In summary, in the two-dimensional σ_1-σ_2 space, the membrane (if yielding) is at a fixed point on the yield curve, namely the point $(\sigma_1, \sigma_2) = (2/\sqrt{3}\sigma_0, 1/\sqrt{3}\sigma_0)$, during the whole response. This is in agreement with the earlier assumption that the membrane is yielding at the same yield point on the yield surface so that $\dot{s}_{ij} = 0$, which led to the total form of flow rule, $\varepsilon_{ij} = \lambda s_{ij}$.

From the above analysis, a further observation is noted. By the definition of the principal stresses, the shearing stress in the principal orientation is zero; an element of the membrane is subjected to the two normal principal stresses, σ_1 and σ_2, which are purely normal stresses. From the flow rule, there is no shear strain (because there is no shear stress) in the principal orientation. Furthermore, it can be verified that the yield curve in the σ_1-σ_2 has a normal that is parallel to the σ_1 axis at the point $(2/\sqrt{3}\sigma_0, 1/\sqrt{3}\sigma_0)$ (on the curve). To illustrate this, recall that the equation of von Mises yield condition (see Fig. 3.3) in

terms of the in-plane principal stresses is

$$\frac{1}{2}\left[(\sigma_1 - \sigma_2)^2 + \sigma_1^2 + \sigma_2^2\right] - \sigma_0^2 = f(\sigma_1, \sigma_2) = 0 \tag{3.8.10}$$

then, the normal to the yield curve, $f(\sigma_1, \sigma_2) = 0$, has the components

$$n_1 = \frac{\partial f}{\partial \sigma_1} = 2\sigma_1 - \sigma_2$$

$$n_2 = \frac{\partial f}{\partial \sigma_2} = 2\sigma_2 - \sigma_1$$

So, at the stress point (σ_1, σ_2) where $\sigma_1 = 2/\sqrt{3}\sigma_0$ and $\sigma_2 = 1/\sqrt{3}\sigma_0 = (1/2)\sigma_1$, the normal has the components $n_1 = (3/2)\sigma_1 = \sqrt{3}\sigma_0$ and $n_2 = 0$. Therefore, the component of the normal along σ_2 is $n_2 = 0$; hence, the normal vector is parallel to σ_1 at the point given by $\sigma_1 = 2/\sqrt{3}\sigma_0$ and $\sigma_2 = 1/\sqrt{3}\sigma_0$. The von Mises yield curve, corresponding to the equation $f(\sigma_1, \sigma_2) = 0$, is shown in Fig. 3.3, where the point $(\sigma_1, \sigma_2) = \left(\frac{2}{\sqrt{3}}\sigma_0, \frac{1}{\sqrt{3}}\sigma_0\right)$ and the outward normal (to the curve) at it are shown. The reader is referred to Chen and Han (1988) for derivation of the equation of von Mises yield condition in the principal space.

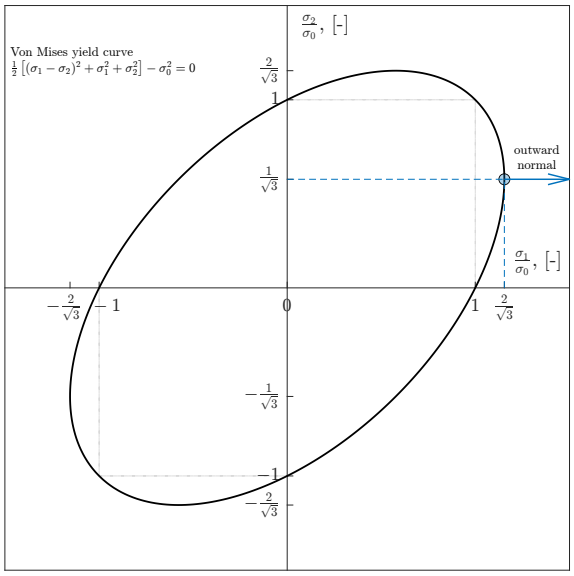

Fig. 3.3. Von Mises yield curve in the in-plane principal stress σ_1-σ_2 space. The outward normal to the curve at the point $(2/\sqrt{3}\sigma_0, 1/\sqrt{3}\sigma_0)$, which is shown as the small blue circle, is drawn. This indicates that the normal is identically *parallel* to the σ_1 axis. The principal stress state of the membrane is the point shown here, i.e., the blue circle. The equation displayed in the figure is the von Mises condition for the plane-stress case and is expressed in terms of the principal stresses σ_1 and σ_2. σ_0 is the uni-axial yield stress in tension.

Then, from the flow rule, the normal strain along the direction of σ_2 must be zero, because the strains must be normal to the yield curve but the component of the normal to the curve along σ_2 is zero as demonstrated above. In other words, the element of the material is under a state of uni-axial stretch (uni-axial strain) in the direction of the σ_1 stress, i.e.,

along the first (or largest) principal axis.

However, from the computational perspective, determining the orientation of the first principal axis (with respect to the Cartesian axis x) requires evaluating the Cartesian stresses σ_x, σ_y, and σ_{xy} (through the relative values of the normal strains ε_x and ε_y; it is the ratio ε_x to ε_y, or its inverse, that matters). Nevertheless, from the material behaviour point of view, the membrane is subjected to a uni-axial stretch along its first principal (stress) axis at every point on the membrane during the whole response whenever the membrane is subjected to progressive yielding, and the stress state is $\sigma_1 = 2/(\sqrt{3})\sigma_0$ and $\sigma_2 = (1/2)\sigma_1$.

3.8.3 Principal Directions for the General Strain Case

By the geometry of the Mohr's circle, given an arbitrary (plane-) stress state characterised by the triplet $(\sigma_x, \sigma_y, \sigma_{xy})$, the directions of the principal axes can be determined. Denoting the angle of the largest principal stress σ_1 with respect to the Cartesian x axis by θ, and the radius of the Mohr' circle by R, as given earlier, one can determine θ by one of the following equivalent relations

$$\begin{aligned}
\tan(2\theta) &= \frac{\sigma_{xy}}{(\sigma_x - \sigma_y)/2} \\
&= \frac{2\varepsilon_{xy}}{\varepsilon_x - \varepsilon_y} \\
\sin(2\theta) &= \frac{\sigma_{xy}}{R} \\
&= \frac{\varepsilon_{xy}}{\varepsilon_x + \varepsilon_y} \\
\cos(2\theta) &= \frac{(\sigma_x - \sigma_y)/2}{R} \\
&= \frac{\varepsilon_x - \varepsilon_y}{\varepsilon_x + \varepsilon_y},
\end{aligned} \tag{3.8.11}$$

where substitutions have been made of the expressions of the stress quantities in terms of the normal strains ε_x and ε_y according to the total form of the flow rule, which was given earlier. The direction of the second principal stress σ_2 is obtained as $\theta + (\pi/2)$ (in radians). The direction of principal shear stress $\pm\tau_{max}$ is obtained as $\theta \pm (\pi/4)$. Herein, θ is the angle of σ_1 axis, as defined above. Therefore, once the normal strains ε_x and ε_y are given, the directions of principal stresses axes can be determined.

Note that although the above expressions for θ should give identical results. However, due to the periodicity of the trigonometric functions, the signs of the values of θ might be different. Thus, it is recommended that the angle is determined by the *tangent* relation, i.e., by $\tan(2\theta)$, as it preserves the sign of the angle so that it covers the range $[-\pi/2 - \pi/2]$ for θ. Hence, in practice, one should use $\tan(2\theta)$ to calculate θ.

Now, from the definition of the in-plane strains, ε_x, ε_y, and ε_{xy}, in terms of the derivatives of the transverse displacement w_0, one can write

$$\begin{aligned}\tan(2\theta) &= \frac{2\varepsilon_{xy}}{\varepsilon_x - \varepsilon_y} \\ &= \frac{2\left[(1/2)\frac{\partial w_0}{\partial x}\frac{\partial w_0}{\partial y}\right]}{(1/2)\left[\left(\frac{\partial w_0}{\partial x}\right)^2 - \left(\frac{\partial w_0}{\partial y}\right)^2\right]} \\ &= \frac{2e}{1-e^2}\end{aligned} \tag{3.8.12}$$

where it has been defined that

$$e = \left(\frac{\partial w_0}{\partial y}\right) / \left(\frac{\partial w_0}{\partial x}\right) \tag{3.8.13}$$

The quantity e is the ratio $(\varepsilon_{xy}/\varepsilon_x)$, and its square is $e^2 = (\varepsilon_y/\varepsilon_x)$. Therefore, it is seen that the direction of the first principal stress, σ_1, depends only on the ratio of the in-plane strains, i.e., through e and e^2, but not their actual magnitudes. It is worth mentioning that the case when both $\frac{\partial w_0}{\partial x}$ and $\frac{\partial w_0}{\partial y}$ are simultaneously zero should be excluded since it implies that ε_x and ε_y are both zero and hence the membrane is rigid (so its stress state can not be determined).

From the practical point of view, it can be observed that the angle θ can also be determined by considering a right triangle, with hypotenuse's length of $(1 + e^2)$, an adjacent side's length of $(1 - e^2)$, an opposite side's length of $(2e)$, and the angle between the adjacent side and the hypotenuse being (2θ).

According to the relation, $\tan(2\theta) = (2e)/(1 - e^2)$, some observations can be made: (i) when $(2e)$ and $(1 - e^2)$ are both positive, one has $0 \leq 2\theta \leq \pi/2$; (ii) when these are both negative, then one has $\pi \leq 2\theta \leq 3\pi/2$; (iii) when $2e$ is positive while $(1 - e^2)$ negative, then $\pi/2 \leq 2\theta \leq \pi$; (iv) and lastly when $2e$ is negative while $(1 - e^2)$ positive, then $3\pi/2 \leq 2\theta \leq 2\pi$.

By letting e varies over the entire range $[-\infty, +\infty]$, θ can be obtained from

$$\theta = \frac{1}{2}\tan^{-1}\left(\frac{2e}{1-e^2}\right), \tag{3.8.14}$$

the graph of which is depicted in Fig. 3.4.

The expression for θ can be simplified further as follows. Since $\tan(2\theta)$ can be expressed as

$$\tan(2\theta) = \frac{2\tan(\theta)}{1 - \tan^2(\theta)}$$

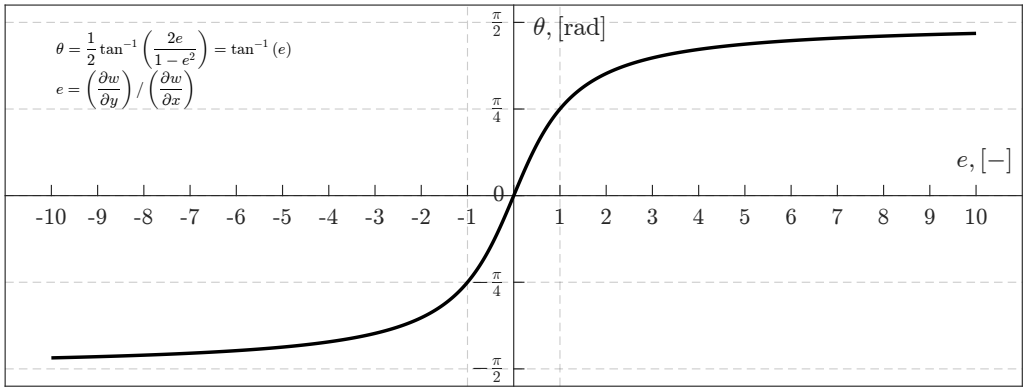

Fig. 3.4. Orientation, θ, of the first principal stress σ_1 (with respect to the x-axis) as a function of the ratio e of the in-plane strains, $e = \varepsilon_{xy}/\varepsilon_x$, and $e^2 = \varepsilon_y/\varepsilon_x$. As $e \to \pm\infty$ implies $\varepsilon_x \to 0$, but ε_y must be finite (and hence σ_1 is aligned with the y axis); $\theta \to \pm\pi/2$ as $e \to \pm\infty$. As $e \to 0$ implies $\varepsilon_y \to 0$, but ε_x is finite (and hence σ_1 is aligned with the x axis). As $e = \pm 1$ implies $\varepsilon_x = \varepsilon_y$ (and hence σ_1 makes equal angles (of $\pi/4$ or 45^o) with the two axes x and y). The value of σ_1 is fixed at $2/\sqrt{3}\sigma_0$, and only its direction varies from point to point on the membrane (and this variation of orientation is controlled solely by the relative magnitude of the actual in-plane strains, as indicated by the dependence of θ on e. The strains must be normal to the yield surface (from the material point of view) and must be compatible with each other and with the derivatives of the displacement. So the orientation of the first principal stress varies to make all these conditions satisfied throughout the response.)

for any θ, then one can infer from

$$\frac{2\tan(\theta)}{1-\tan^2(\theta)} \equiv \tan(2\theta) = \frac{2e}{1-e^2}$$

the following practical relation

$$\tan(\theta) = e \tag{3.8.15}$$

Therefore, one has

$$\theta = \tan^{-1}(e)$$

This last relation clearly gives the values of θ for the following special cases: when $e = -\infty$, then $\theta = -\pi/2$; when $e = \infty$, one has $\theta = \pi/2$; when $e = 0$, one has $\theta = 0$ (or $\theta = \pi$); when $e = 1$, then $\theta = \pi/4$; and when $e = -1$, then $\theta = -\pi/4$.

Recall that the case when both ε_x (or $\frac{\partial w_0}{\partial x}$) and ε_y (or $\frac{\partial w_0}{\partial y}$) are zero represents a rigid material and, hence, the determination of the stress state can not be made (since the yield condition can not be said to be satisfied). So the fact that the ratio $e = (\frac{\partial w_0}{\partial y})/(\frac{\partial w_0}{\partial x})$ can not be evaluated when both the denominator and numerator are zero is associated with the membrane being rigid and its yield condition needs not be satisfied (and hence the stress state, including the direction of the principal axis, can not be predicted).

The trajectories of first principal stress, σ_1, are defined by the (differential) equation $dy_1/dx = \tan(\theta)$, and those of the second principal stress, σ_2, are given by $dy_2/dx = \tan(\theta + \pi/2)$. It was derived that $\tan(\theta) = e$, and $\tan(\theta + \pi/2) = -1/\tan(\theta) = -1/e$. Therefore, the two families of trajectories (of σ_1 and σ_2) are mutually orthogonal because

their dot product is zero (note that $dy_1 = e\ dx$ and $dy_2 = -1/(e)\ dx$) as shown below

$$\begin{aligned} dx^2 + dy_1 dy_2 &= dx^2 + (e\ dx)\ [-1/(e)\ dx] \\ &= \left(1 - \frac{e}{e}\right)\ dx^2 \\ &= 0 \end{aligned}$$

3.8.4 Remarks on the Determination of the Stress States

When the equilibrium equation was derived, in previous sections, the starting point was the principle of virtual work, then it was specialised for the case when the yield condition of von Mises is satisfied, and then the compatibility of strains and incompressibility of the material were utilised. Furthermore, use has been made of the assumption that the total strains are associated with the deviatoric stresses that satisfy the yield condition, and hence the strains obey the normality rule; this was made by assuming the total form of flow rule to hold. Thus, the obtained equilibrium equation already includes the satisfaction of the yield condition (namely $s_{ij}s_{ij} = (2/3)\sigma_0$), the normality of the total strains (namely $\varepsilon_{ij} = \lambda s_{ij}$), and compatibility of the in-plane strains (namely $\varepsilon_{xy} = \pm\sqrt{\varepsilon_x \varepsilon_y}$), and the incompressibility (namely $\varepsilon_z = -(\varepsilon_x + \varepsilon_y)$). Therefore, the obtained equilibrium equation accounts for all the aspects of the response as long as the yielding of the material is taking place. Once yielding stops, the equilibrium equation becomes not applicable. That is, when the material is actively yielding (or under progressive yielding), one only needs to solve the obtained equilibrium equation without the need to determine the stress state in the Cartesian x and y axes. The foregoing discussion of evaluating the principal stresses and the orientations of their axes only provides additional information that is important when needed. It does not affect the form of the equilibrium equation that one needs to solve to obtain the response, the transverse displacement w_0 of the membrane.

When the solution w_0 is obtained (by solving the equilibrium equation), one can determine the ratio $e = \left(\frac{\partial w_0}{\partial y}\right) / \left(\frac{\partial w_0}{\partial x}\right)$. Thus, the principal directions θ (of σ_1) and $\theta + 90^{\text{o}}$ (of σ_2) become available. Note that since w_0 is a function of (x, y, t), then so are the strains, ε_x and ε_y, and the angles θ and $\theta + 90^{\text{o}}$. That is, in general, the directions of the principal stresses are time-dependent, i.e., dynamic.

However, once again, the solution w_0 of the equilibrium equation is valid as long as the material is under active yielding. It has been discussed earlier that there is a critical time instant at which the equilibrium equation becomes invalid because the already assumed form of the total flow rule is not correct. It also was discussed that the critical time instant can be identified when λ starts to decrease. For our (rigid-perfectly plastic) simple membrane problem, $\lambda = \sqrt{3}/(\sigma_0)(\varepsilon_x + \varepsilon_y)$, so that it is proportional to $(\varepsilon_x + \varepsilon_y)$. So, the response w_0 that is obtained by solving the equilibrium equation is valid until the instant of time when $(\varepsilon_x + \varepsilon_y)$ just starts to decrease. The strain rates are temporarily zero at that instant, and the membrane is instantaneously rigid. Thus, the total strains can not

decrease in magnitude. So, for the next phase of response, the additional total strains are zero (only the initial strains from the end of the last phase are finite). When the strain rates reverse their signs, all the active stresses must reverse their signs. The new reversed stresses cancel out the initial stresses (that are associated with the total strains by the end of the first phase), and hence the membrane is forced to remain in a permanent deformed state, provided that there are no external forces that lead to imbalance in the established equilibrium between the two opposing stresses. In summary, in the absence of external forces, whenever λ starts to decrease, the membrane has reached its final deformation state, and the entire motion will end at the first occurrence of this specific (critical) time instant.

3.9 A Simplified Example of an Impulsively Loaded Simple Membrane

3.9.1 General

In this section, a simple example is considered as a rectangular simple membrane under an impulsive loading. The equilibrium equation then takes the following form

$$c_p^2 \left(\frac{\partial^2 w_0}{\partial x^2} + \frac{\partial^2 w_0}{\partial y^2} \right) = \ddot{w}_0 \tag{3.9.1}$$

where

$$c_p^2 = \frac{2\sigma_0}{\sqrt{3}\rho} \tag{3.9.2}$$

It is assumed that the membrane is fixed at its outer edges and its initial displacement is zero, $w_0(x, y, 0) = 0$. The lengths of the membrane are L_x and L_y along x and y, and one corner of the membrane is taken as the origin of the x and y axes. Then, the boundary conditions are $w_0(0, y, t) = w_0(L_x, y, t) = w_0(x, 0, t) = w_0(x, L_y, t) = 0$.

As stated above, the membrane is impulsively loaded so that its initial velocity is given by

$$\dot{w}_0(x, y) = \frac{i(x, y)}{\rho h}, \tag{3.9.3}$$

where $i(x, y)$ is the specific impulse (as would be generated from a blast), and h is the membrane's thickness. This dynamic initial condition model, Eq. (3.9.3), and its basis will be discussed in Chapter 4.

The response w_0 is the one that solves the above equilibrium equation as long as λ is increasing. Since the equilibrium equation is initially linear in w_0, and it is a wave equation, the general solution (with zero initial displacement) is used, which is given in terms of the

well-familiar Fourier expansion. This solution is given by

$$w_0(x,y,t) = \frac{1}{\rho h}\sum_{m=1}^{\infty}\sum_{n=1}^{\infty}\frac{I_{mn}}{\omega_{mn}\|\phi_{mn}(x,y)\|^2}\phi_{mn}(x,y)\sin(\omega_{mn}t) \tag{3.9.4}$$

where

$$\begin{aligned}
\phi_{mn}(x,y) &= \sin\left(\frac{m\pi x}{L_x}\right)\sin\left(\frac{n\pi y}{L_y}\right)\\
\omega_{mn} &= c_p\sqrt{(m\pi/L_x)^2+(n\pi/L_y)^2}\\
I_{mn} &= \int_0^{L_y}\int_0^{L_x} i(x,y)\phi_{mn}(x,y)\;dx\;dy\\
\|\phi_{mn}(x,y)\|^2 &= \frac{L_xL_y}{4}
\end{aligned} \tag{3.9.5}$$

The method of obtaining the solution and discussion of the various parameters will be given in great detail later in Chapter 4.

For our present purpose of investigating the response of a simple example, the simplest form of a specific impulse $i(x,y)$ is used such that it is proportional to the first mode shape, i.e., $\phi_{mn}(x,y)$ with $m=n=1$. The first mode shape is denoted by $\phi_{1,1}(x,y)$ by $\phi_1(x,y)$ for simplicity. That is, $i(x,y)$ is taken to be

$$i(x,y) = a_0\phi_1(x,y) = a_0\sin\left(\frac{\pi x}{L_x}\right)\sin\left(\frac{\pi y}{L_y}\right),$$

where a_0 is some non-zero constant that gives the central amplitude of the specific impulse.

For this particular choice of $i(x,y)$, one then have

$$I_{mn} = \begin{cases} a_0\,(L_xL_y/4) \equiv a_0\|\phi_{mn}(x,y)\|^2, & \text{when } m=n=1\\ 0, \qquad \text{otherwise} \end{cases}$$

Note, as seen in the above, that all modal contributions will vanish except one single mode which is the first (since the forcing function, i.e., the specific impulse, spatially matches the first mode). Thus, the exact solution will be the first mode solution, and thus it is the simplest solution for the present simple investigation.

3.9.2 Membrane's Response Under Specific Impulse That Is Proportional to the First Mode Shape

Hence, the solution w_0, when $i(x,y) = a_0\phi_1(x,y)$, takes the following simple form

$$\begin{aligned} w_0(x,y,t) &= \frac{a_0}{\rho h\omega}\phi_1(x,y)\sin(\omega t) \\ &= \frac{a_0}{\rho h\omega}\sin(k_x x)\sin(k_y y)\sin(\omega t) \end{aligned} \tag{3.9.6}$$

where it has been defined that

$$\begin{aligned} \phi_1(x,y) &= \sin(k_x x)\sin(k_y y), \\ k_x &= \pi/L_x, \\ k_y &= \pi/L_y, \\ \omega &= c_p\sqrt{k_x^2+k_y^2} = c_p\sqrt{(\pi/L_x)^2+(\pi/L_y)^2}, \end{aligned}$$

and it is emphasised that this is the exact solution of an impulsively loaded membrane when $i(x,y) = a_0\sin(k_x x)\sin(k_y y) = a_0\phi_1(x,y)$, as assumed earlier, and it is valid until λ starts to decrease, or equivalently when $(\varepsilon_x+\varepsilon_y)$ starts to decrease as time evolves.

3.9.3 Determination of the Critical Time Instant

From the solution of our simple example, the normal strains, $\varepsilon_x = (1/2)\left[\frac{\partial w_0}{\partial x}\right]^2$ and $\varepsilon_y = (1/2)\left[\frac{\partial w_0}{\partial y}\right]^2$, can be found (by direct differentiation) as

$$\begin{aligned} \varepsilon_x &= \frac{1}{2}\left(\frac{\partial w_0}{\partial x}\right)^2 = \frac{1}{2}\left(\frac{k_x a_0}{\rho h\omega}\right)^2\cos^2(k_x x)\sin^2(k_y y)\sin^2(\omega t) \\ \varepsilon_y &= \frac{1}{2}\left(\frac{\partial w_0}{\partial y}\right)^2 = \frac{1}{2}\left(\frac{k_y a_0}{\rho h\omega}\right)^2\sin^2(k_x x)\cos^2(k_y y)\sin^2(\omega t) \end{aligned}$$

and, hence, their sum is

$$\varepsilon_x+\varepsilon_y = \frac{1}{2}\left(\frac{a_0}{\rho h\omega}\right)^2\left[k_x^2\cos^2(k_x x)\sin^2(k_y y)+k_y^2\sin^2(k_x x)\cos^2(k_y y)\right]\sin^2(\omega t)$$

Taking the derivative of the above relation, i.e., for the sum of ε_x and ε_y, with respect to time t, one then has

$$\frac{\partial}{\partial t}(\varepsilon_x+\varepsilon_y) = \frac{1}{\omega}\left(\frac{a_0}{\rho h}\right)^2\left[k_x^2\cos^2(k_x x)\sin^2(k_y y)+k_y^2\sin^2(k_x x)\cos^2(k_y y)\right]\sin(\omega t)\cos(\omega t)$$

Thus, it can be seen that $(\varepsilon_x + \varepsilon_y)$ will start to decrease (for the first time) when $[\sin(\omega t)\cos(\omega t)]$ turns negative for the first time. This latter condition is reached when $\cos(\omega t)$ becomes zero for the first time since the cosine becomes negative thereafter while the sine is still positive. Hence, the solution is terminated at the critical time instant t^*, which now is defined by

$$\cos(\omega t^*) = 0,$$

which gives

$$t^* = \frac{\pi}{2\omega}, \tag{3.9.7}$$

since this corresponds to the instant just before the first occurrence when $\cos(\omega t)$ turns negative, and hence $\varepsilon_x + \varepsilon_y$ will start to decrease. Note that ω is a structural constant, $\omega = c_p\sqrt{(\pi/L_x)^2 + (\pi/L_y)^2}$, as given earlier, i.e., it is independent of the loading.

From the above, it is noted that the solution is terminated at one-quarter of the membrane's fundamental period, T, which is defined as $T = 2\pi/\omega$. That is,

$$t^* = \frac{T}{4} \tag{3.9.8}$$

Since t^*, as defined, is the termination time at which the (transient) solution is terminated, then the membrane is allowed to complete only one-fourth of the modal cycle.

It might be more practical to redefine the critical time instant discussed above. For this purpose, it is noted that the condition when λ (and hence $\varepsilon_x + \varepsilon_y$) stops increasing is equivalent to the condition that the kinetic energy stops decreasing. This is because $(2/3)\sigma_0^2\lambda = \sqrt{(2/3)}\sigma_0\sqrt{\varepsilon_{ij}\varepsilon_{ij}}$ is the internal work (due to plastic deformation), which then must balance with the kinetic energy (in the absence of external work due to external forces). Hence, the time instant when λ starts to decrease is the time instant when the kinetic energy starts to increase after having reached zero. Therefore, the critical time instant can be (equivalently) defined to be when the kinetic energy reaches zero and its time rate is instantaneously zero. Now, for the current simple example, the local kinetic energy is

$$E_k = (1/2)\rho\dot{w}_0^2$$

and its time derivative is

$$\dot{E}_k = \frac{\partial E_k}{\partial t} = \rho\dot{w}_0\ddot{w}_0$$

From the solution of the present example, namely $w_0 = a_0/(\rho h)\phi_1(x,y)\sin(\omega t)$, it can be shown that E_k is proportional to $\cos^2(\omega t)$, and $\dot{E}_k$ is proportional to $[\sin(\omega t)\cos(\omega t)]$. So, when the critical time instant, t^* is defined to be when both E_k *and* its time rate $\dot{E}_k$ are both zero, then one should have $\cos(\omega t^*) = 0$ as the condition of the occurrence of the critical time instant t^*. This directly leads to $t^* = \pi/(2\omega)$, which agrees with the earlier (equivalent) definition based on λ (and hence $\varepsilon_x + \varepsilon_y$) attaining its maximum. Note that when $\cos(\omega t) = 0$ means the velocity, $\dot{w}$, is zero. For the present simple example,

the response is represented by a single mode response, which is the first mode, and hence when the $\cos(\omega t^*)$ becomes zero, then all points on the membrane have zero velocities simultaneously; thus, t^* is the time when the whole membrane reaches its final permanent deformed shape.

3.9.4 Directions of the Principal Stresses

The determination of the principal stress direction is to be discussed next. Letting θ be the angle that the axis of the principal stress makes with the Cartesian x axis, it is given by

$$\begin{aligned}\tan(2\theta) &= \frac{2\varepsilon_{xy}}{\varepsilon_x - \varepsilon_y} \\ &= \frac{2\left[(1/2)\frac{\partial w_0}{\partial x}\frac{\partial w_0}{\partial y}\right]}{(1/2)\left[\left(\frac{\partial w_0}{\partial x}\right)^2 - \left(\frac{\partial w_0}{\partial y}\right)^2\right]} \\ &= \frac{2e}{1-e^2}\end{aligned}$$

where it was defined

$$e = \left(\frac{\partial w_0}{\partial y}\right) / \left(\frac{\partial w_0}{\partial x}\right),$$

where $\varepsilon_{xy}/\varepsilon_x$, and its square is $e^2 = \varepsilon_y/\varepsilon_x$. Before e is evaluated, it is convenient to re-write the solution w_0 as

$$w_0(x, y, t) = \alpha(t)\sin(k_x x)\sin(k_y y)$$

where

$$\alpha(t) \equiv \frac{a_0}{\rho h \omega}\sin(\omega t)$$

Hence, one can evaluate the first derivatives $\frac{\partial w_0}{\partial x}$ and $\frac{\partial w_0}{\partial y}$ as

$$\frac{\partial w_0}{\partial x} = \alpha k_x \cos(k_x x)\sin(k_y y)$$

$$\frac{\partial w_0}{\partial y} = \alpha k_y \sin(k_x x)\cos(k_y y)$$

and from which

$$\begin{aligned} e &= \frac{\frac{\partial w_0}{\partial y}}{\frac{\partial w_0}{\partial x}} \\ &= \frac{\alpha k_y \sin(k_x x)\cos(k_y y)}{\alpha k_x \cos(k_x x)\sin(k_y y)} \end{aligned}$$

or,

$$\begin{aligned} e &= \frac{(1/k_x)\tan(k_x x)}{(1/k_y)\tan(k_y y)} \\ &= \frac{L_x \tan(k_x x)}{L_y \tan(k_y y)} \end{aligned}$$

Thus, the direction of the largest principal stress σ_1 can be found from

$$\tan(2\theta) = \frac{2e}{1-e^2}$$

However, as was discussed in the previous sections, since $\tan(2\theta) = 2e/(1-e^2)$ and also $\tan(2\theta) \equiv 2\tan(\theta)/(1-\tan^2(\theta))$ for any θ, then one simply has $\tan(\theta) = e$. That is,

$$\begin{aligned} \tan(\theta) &= e \\ &= \frac{(1/k_x)\tan(k_x x)}{(1/k_y)\tan(k_y y)} \end{aligned} \tag{3.9.9}$$

From the above, θ can be determined at every point (x, y) on the membrane. Note that e is not a function of time t since the dependence on t of ε_x, ε_y, and ε_{xy} are identical, and θ depends on the relative values of the in-plane normal strains (or their ratios given by e and e^2). For the same reason, θ does not depend on the amplitude of the specific impulse, a_0, either; it depends on the spatial shape of $i(x, y)$. It is helpful to recognise that when the specific impulse matches one of the mode shapes of the membrane (as it was made, in this example, to match the first mode in particular), then the solution is a *standing* wave solution, in which the deformed shape is time-invariant and given by the modal shape. In other words, the spatial variation is fixed as time evolves, and only the amplitude depends on time. Hence, the strains are temporally similar. Consequently, the field of θ is fixed as time changes. Again, this is due to the assumption of making the specific impulse as one of the modes, i.e., when the response is a standing wave.

The angle of the direction of the second principal stress σ_2 is simply $\theta + \pi/2$, in radians. From the previous section, it was established that $\sigma_1 = 2/(\sqrt{3})\sigma_0$ and $\sigma_2 = 1/(\sqrt{3})\sigma_0$, where σ_0 is the uni-axial yield stress. That is, the two principal stresses are constants; only their orientations vary over the membrane area. As can be seen from the above expression for θ, the orientation of the principal stress axis purely depends on the planar geometry

of the membrane (not on its material nor the thickness of the membrane).

3.9.4.1 First Principal Stress σ_1 Direction

Next, when the first principal stress axis is denoted by x_1. So, since x_1 makes angle θ with the Cartesian x axis, one can write

$$dx = dx_1 \cos(\theta)$$

$$dy = dx_1 \sin(\theta)$$

$$\frac{dy}{dx} = \tan(\theta) = e$$

To plot the trajectory of the first principal stress, a numerical method can be used. First, one can evaluate θ at many points (x, y) on the membrane. Then, one chooses an arbitrary but small length for dx_1, say 0.05 (or so), and use it for all points; the arbitrary length dx_1 can be adjusted based on the density (or spacing) of the points (x, y). Then, dx and dy are calculated at these points according to $dx = dx_1 \cos(\theta)$, and $dy = dx_1 \sin(\theta)$. Finally, one can plot (at every point (x, y)) the small straight lines (which can be made with start and end markings), the run of each of which is dx and the rise dy. This will result in a vector plot, known as *quiver* in MATALB. Thus, one has (an approximate and discrete) graphical representation of the directions of the principal stress σ_1. With refinement, i.e., increasing the number of points (x, y), the resulting graph would become closer to matching the continuous curves that solve the ordinary non-linear differential equation, $\frac{dy}{dx} = \tan(\theta) = e$, in which $\theta = \theta(x, y)$ is known function of x and y, as given previously for our simple example.

Knowing the direction of the first principal stress can be of direct interest as it is the direction along which the largest stress $2/\sqrt{3}\sigma_0$ is applied and along which the membrane experiences uni-axial stretch. Hence, it is the direction where the membrane may need additional strengthening; that is, along θ, the membrane needs most of its resistance.

From $\tan(\theta) = e$, and since $\frac{dy}{dx} = \tan(\theta) = e$, one can, then, write

$$\frac{dy}{dx} = \frac{(1/k_x)\tan(k_x x)}{(1/k_y)\tan(k_y y)}$$

and from which one obtains

$$\frac{\sin(k_y y)dy}{k_y \cos(k_y y)} = \frac{\sin(k_x x)dx}{k_x \cos(k_x x)}$$

The last equation can be manipulated slightly to make it of a familiar form,

$$\frac{-k_y \sin(k_y y)dy}{k_y^2 \cos(k_y y)} = \frac{-k_x \sin(k_x x)dx}{k_x^2 \cos(k_x x)}$$

Hence, by letting $v = \cos(k_y y)$ (and $v_0 = \cos(k_y y_0)$), and $u = \cos(k_x x)$ (and $u_0 = \cos(k_x x_0)$), one has

$$\frac{1}{k_y^2}\frac{dv}{v} = \frac{1}{k_x^2}\frac{du}{u}$$

The solution of the above separable differential equation is

$$\frac{1}{k_y^2}\ln\left(\frac{v}{v_0}\right) = \frac{1}{k_x^2}\ln\left(\frac{u}{u_0}\right),$$

where the initial conditions u_0 and v_0 were given above. This solution can be simplified further by

$$\ln\left[\left(\frac{v}{v_0}\right)^{(-k_y^2)}\right] = \ln\left[\left(\frac{u}{u_0}\right)^{(-k_x^2)}\right]$$

and, hence, by exponentiating both sides (to remove the natural logarithms), one finds

$$\left(\frac{v}{v_0}\right)^{(-k_y^2)} = \left(\frac{u}{u_0}\right)^{(-k_x^2)},$$

where $v = \cos(k_y y)$, $v_0 = \cos(k_y y_0)$, $u = \cos(k_x x)$, and $u_0 = \cos(k_x x_0)$. The point (x_0, y_0) is any arbitrary point on the membrane through which a curve $y = y(x)$ passes. For every point (x_0, y_0), there is a unique curve; hence, overall one has a family of such curves. These are the trajectories (or locus) of the principal stress σ_1 axis.

By substituting the expressions for u and v (and their initial values) in terms of x and y (and their initial values x_0 and y_0), an explicit expression for $y(x)$ that passes through (x_0, y_0) is obtained

$$\frac{\cos(k_y y)}{\cos(k_y y_0)} = \left[\frac{\cos(k_x x)}{\cos(k_x x_0)}\right]^{\left(\frac{k_y}{k_x}\right)^2} \tag{3.9.10}$$

which leads to

$$y(x; x_0, y_0) = \pm\frac{1}{k_y}\cos^{-1}\left[\cos(k_y y_0)\left[\frac{\cos(k_x x)}{\cos(k_x x_0)}\right]^{\left(\frac{k_y}{k_x}\right)^2}\right],$$

where the notation $y(x; x_0, y_0)$ implies that y is function of x with (x_0, y_0) as parameters.

Fig. 3.5 shows the trajectories of σ_1 for a square simple membrane, $k_y/k_x = L_x/L_y = 1$ by plotting the *implicit* relation between $\cos(k_y y)$ and $\cos(k_x x)$ given earlier. It can be seen that the direction of σ_1 makes right angles with the edges of the square membrane except near the four corner regions where its direction is aligned with the diagonals of the square. The plot was obtained using several initial points (x_0, y_0) lying on the membrane edges. Continuous lines of σ_1 traverse the entire membrane (from one edge to the corresponding opposite edge) and pass through the membrane's centre.

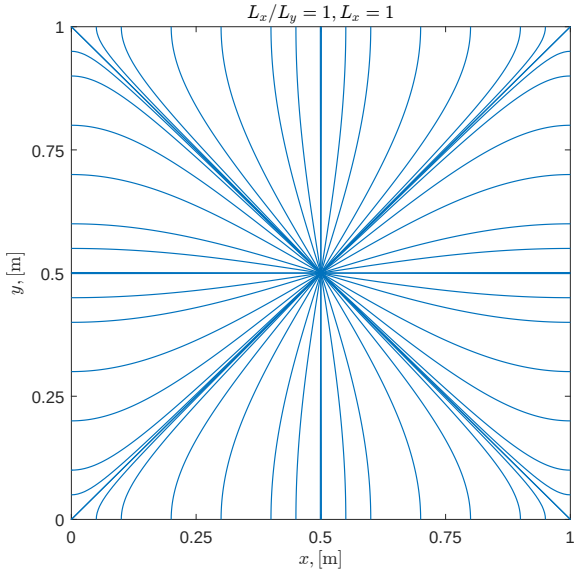

Fig. 3.5. Trajectories of the first principal stress $\sigma_1 = 2/(\sqrt{3})\sigma_0$. The membrane is square, $k_y/k_x = L_x/L_y = 1$, of side length $L_x = 1$. The membrane displacement w_0 is due to the first mode since the specific impulse was chosen to be that mode in particular. The graph of σ_1 trajectory was obtained by plotting the implicit equation relating $\cos(k_y y)$ and $\cos(k_x x)$ for a variety of initial conditions (x_0, y_0) that were chosen to be points on the four edges of the membrane. Although the direction of σ_1 varies as can be seen in this graph, its value is fixed at $2/(\sqrt{3})\sigma_0$. The trajectory of the second principal stress σ_2 can be inferred from this graph as it must be perpendicular to every and all curves of σ_1 shown here.

3.9.4.2 Second Principal Stress σ_2 Direction

The direction of the second principal stress σ_2 makes an angle of $\pi/2$ with the direction of σ_1, whose orientation was denoted with θ. Thus, the angle of σ_2 makes an angle of $\theta + \pi/2$ with the Cartesian x axis. Thus, if one lets $dy/dx = \tan(\theta + \pi/2)$ to find the trajectories $y(x)$ of the axis of σ_2. Since $\tan(\theta + \pi/2)$ is

$$\begin{aligned}
\tan(\theta + \pi/2) &= \frac{\sin(\theta + \pi/2)}{\cos(\theta + \pi/2)} \\
&= \frac{\sin(\theta)\cos(\pi/2) + \cos(\theta)\sin(\pi/2)}{\cos(\theta)\cos(\pi/2) - \sin(\theta)\sin(\pi/2)} \\
&= -\frac{\cos(\theta)}{\sin(\theta)} \\
&= \frac{-1}{\tan(\theta)}
\end{aligned}$$

Then, one can write

$$\begin{aligned}\frac{dy}{dx} &= \tan(\theta + \pi/2) \\ &= \frac{-1}{\tan(\theta)} \\ &= \frac{-1}{e}\end{aligned}$$

and using $e = [(1/k_x)\tan(k_x x)] \,/\, [(1/k_y)\tan(k_y y)]$, the above becomes

$$\frac{k_y \cos(k_y y)dy}{\sin(k_y y)} = \frac{-k_x \cos(k_x x)dx}{\sin(k_x x)}$$

Then, the substitutions $v = \sin(k_y y)$ (along with $v_0 = \sin(k_y y_0)$) and $u = \sin(k_x x)$ (along with $u_0 = \sin(k_x x_0)$) are made to re-write the last equation into the following (separable) familiar form

$$\frac{dv}{v} = -\frac{du}{u}$$

which once integrated (using the initial conditions u_0 and v_0) gives

$$\ln\left(\frac{v}{v_0}\right) = -\ln\left(\frac{u}{u_0}\right) = \ln\left(\frac{u_0}{u}\right)$$

By exponentiating both sides (to remove the logarithms), one then obtains

$$\frac{v}{v_0} = \frac{u_0}{u}$$

which can be transformed back to x and y, using the definitions of u and v (and their initial conditions) given earlier,

$$\frac{\sin(k_y y)}{\sin(k_y y_0)} = \frac{\sin(k_x x_0)}{\sin(k_x x)}$$

This relation gives (in implicit form) the trajectories of the second principal stress σ_2.

An interesting observation can be made from the last implicit relation. By re-arranging the terms so that the variables x and y are on one side while the constants x_0 and y_0 in the other side, one obtains the following

$$\sin(k_x x)\sin(k_y y) = \sin(k_x x_0)\sin(k_y y_0) \tag{3.9.11}$$

Now, it is seen that the left-hand side is precisely the mode shape of the solution, $\phi_1(x, y) = \sin(k_x x)\sin(k_y y)$. The right-hand side represents constant modal displacements of the mode under consideration (which is the first mode for our simple example), $\phi_1(x_0, y_0) =$

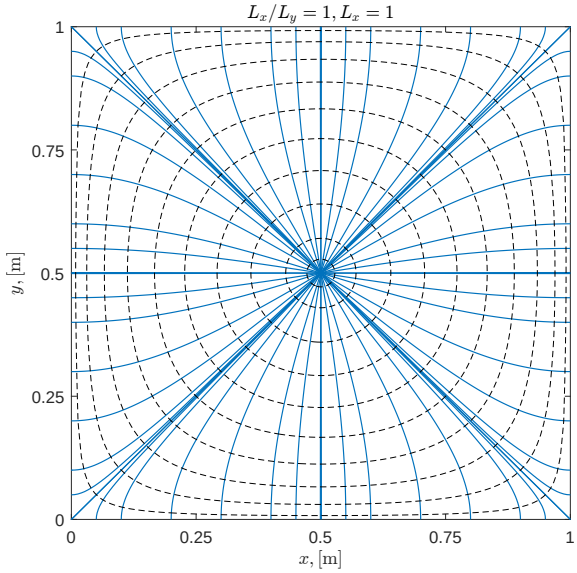

Fig. 3.6. Combined trajectories (curves) of the first principal stress $\sigma_1 = 2/(\sqrt{3})\sigma_0$ (blue solid lines) and the second principal stress $\sigma_2 = (1/2)\sigma_1$ (black dashed lines). It is seen that the curves of σ_1 axis are orthogonal to those of σ_2. Moreover, the trajectories of the σ_2 axis are themselves the iso-lines of the first mode shape $\phi_1(x, y)$.

$\sin(k_x x_0)\sin(k_y y_0)$. Thus, the trajectories (or curves) of σ_2 are the iso-lines of the mode shape $\phi_1(x, y)$, and each curve corresponds to a constant value $\phi_1(x_0, y_0)$, for any (x_0, y_0) in the membrane's area.

Thus, the contours of the constant modal displacements are themselves the curves defining the direction of the second principal stress σ_2 axis. That is, the trajectories of the σ_2 axis are obtained immediately as the curves of intersections when slicing the mode shape by horizontal planes passing through any point on the membrane. The stress σ_2 is constant throughout the membrane, and its value was established in the previous section and given as $\sigma_2 = 1/(\sqrt{3})\sigma_0$. Moreover, since the direction of σ_2 makes a perpendicular angle with the direction of the first principal stress σ_1, then the direction of σ_1 is the normal (orthogonal or perpendicular) direction to the contours of the modal displacement at constant amplitudes. Fig. 3.6 shows the trajectories of both the first principal stress σ_1, as was shown in Fig. 3.5, and the second principal stress σ_2.

As was demonstrated in Section 3.8.3, the two families of the trajectories of σ_1 and σ_2 are mutually orthogonal since the dot product of the vectors (dx, dy_1) and (dx, dy_2) is zero

$$dx^2 + dy_1 dy_2 = dx^2 + (e\ dx)\ (-1/(e)\ dx) = \left(1 - \frac{e}{e}\right) dx^2 = 0$$

where dy_1 and dy_2 are the differentials (or increments) along the y-axis of the trajectories of σ_1 and σ_2, respectively. This general property can be verified in Fig. 3.6 as the two trajectories of σ_1 (the solid blue lines) and of σ_2 (in dashed black lines) intersect perpendicularly.

3.9.4.3 Principal Shear Stresses $\pm\tau_{\max}$ Directions

Having determined the direction of the first principal stress σ_1, which makes angle θ with the x axis, the directions of principal shear stresses, $\tau_{max} = \pm(\sigma_1 - \sigma_2)/2 = \pm(1/2\sqrt{3})\sigma_0$, can be obtained. These are given by $\theta \pm \pi/4$, i.e., as pairs of orthogonal directions. Thus, the trajectories of the principal shear solves the following differential equation, $dy/dx = \tan(\theta \pm \pi/4)$. Instead of solving this non-linear equation, resort is made to the numerical method. One can let $dy = dx_s \sin(\theta_s) = dx_s \sin(\theta \pm \pi/4)$, and likewise $dx = dx_s \cos(\theta_s) = dx_s \cos(\theta \pm \pi/4)$, where θ is the direction of first principal stress σ_1, and is assumed to be already determined (using $\theta = \tan^{-1}(e)$, with $e = (1/k_x)\tan(k_x x)/\left[(1/k_y)\tan(k_y y)\right]$). In the expressions for both dy and dx, one makes dx_s to be arbitrary but small enough, e.g., $dx_s = 0.01$ or so. Then, θ is evaluated at sufficiently many points (x, y) on the membrane. For each point, dy and dx are numerically calculated using the above expressions. Note that there will be two pairs of dy and dx at each point, corresponding to the $(\pm\pi/4)$. Finally, a plot of the sets of short vectors (dx, dy) at every point is obtained as the discrete representation of the trajectories of the principal shear stresses.

Fig. 3.7 shows the numerical representation of the directions of principal shear stresses, $\tau_{max} = \pm 1/(2\sqrt{3})\sigma_0$, for the present simple example for the case of square membrane. Although it is not visually evident from the figure, the trajectories of the principal shear stress axes form two pairs of spirals that are orthogonal to each other, with the vortices of the spirals centred at the membrane's centre, and they happen to impinge on the four sides (or outer edges) of the membrane at angles of identically $\pm 45^{\circ}$. As one approaches the membrane's centre, the spacing between the spirals (belonging to one pair) becomes increasingly small; the same is true for the spirals of the other pair. The two spiral families appear to rotate in opposite directions.

An attempt was made to provide smoother graph of the trajectories of maximum shear stresses, $\pm\tau_{\max}$, by solving the non-linear first-order differential equation,

$$\frac{dy}{dx} = \tan(\theta \pm \pi/4),$$

numerically. This was achieved using the `ode45()` in MATALB, and two equations were solved separately for each of the positive and negative signs. The coordinates of multiple points on the four sides of the membrane are used as the initial conditions. A square membrane is used. Although, at the membrane centre, i.e., $x = L_x/2$ and $y = L_y/2$, solutions could not be found due to the singularity of the differential equation when expressed as above (i.e., when it is assumed that y is a function of x, or $y = y(x)$). Thus, the domain was split into four (equal) quadrants, by dividing the membrane into four segments formed by the membrane's centre lines. The solutions, as collections of (x, y) pairs, are then combined to produce the overall trajectories of the two mutually orthogonal principal shear axes. This is presented in Fig. 3.8. Although, the figure does not provide precise information near the membrane's centre, it can be shown that the (already drawn) principal shear trajectories bisect the trajectories of the principal normal stresses σ_1 and σ_2, which

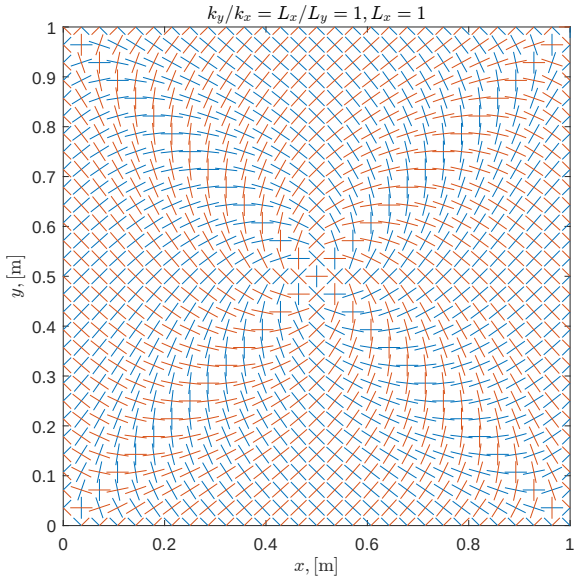

Fig. 3.7. A numerical representation of the directions of principal shear stresses, $\tau_{max} = \pm 1/(2\sqrt{3})\sigma_0$. At sufficiently many points (x, y) on the membrane, two pairs (as shown in blue and red) of directions that are mutually orthogonal are constructed.

were presented early in Fig. 3.7. In line with this, the trajectories of shear stresses can be noted to strike on the four (exterior) edges of the membrane at $\pm 45^{\text{o}}$ degrees (or $\pi/4$ radians); note that the axes of σ_1 and σ_2 are perpendicular and parallel, respectively, to the membrane's edges.

3.9.5 Comparison of the First Mode Analytical Solution to a Numerical Solution Using LS-DYNA

In this section, the solution of the simple example membrane (given in the previous subsection) is compared to an LS-DYNA simulation. Since the first mode solves the equilibrium equation when the spatial distribution of specific impulse, $i(x, y)$, matches the first mode shape, $\phi_{1,1}(x, y)$, the specific impulse distribution was assumed to be of the form

$$i(x, y) = a_0 \phi_{1,1}(x, y) = a_0 \sin(k_x x) \sin(k_y y),$$

where a_0 is the central amplitude of the specific impulse.

A square membrane that is fixed along all its outer edges is considered. The membrane material is assumed to be mild steel, and the Johnson-Cook (JC) material model in LS-DYNA was utilised. Hence, the current (or dynamic) yield stress $\sigma_{d,y}$ takes the form

$$\sigma_{d,y} = (A + B\varepsilon_{\text{eff}}^n) \left[1 + \frac{\dot{\varepsilon}_{\text{eff}}}{\dot{\varepsilon}_0}\right]^c,$$

where ε_{eff} is the effective plastic strain, and $\dot{\varepsilon}_{\text{eff}}$ being its rate. $\dot{\varepsilon}_0$ is strain rate threshold above which the material becomes strain-rate sensitive. The JC model will be discussed

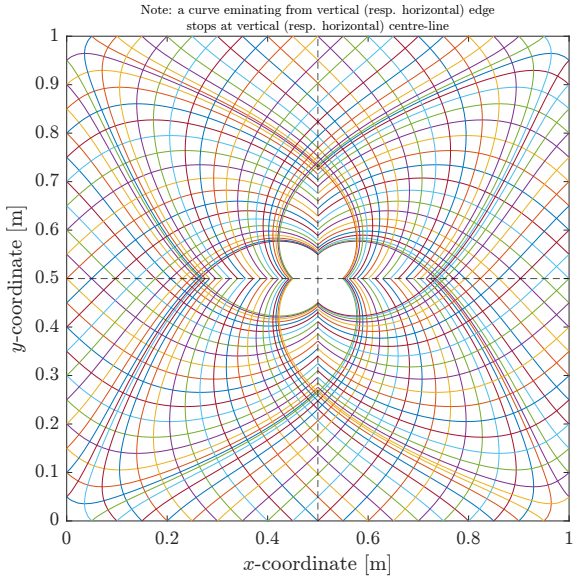

Fig. 3.8. Trajectories of the principal shear stresses, $\pm\tau_{\max}$, which were obtained by solving the differential equation $dy/dx = \tan(\theta \pm \pi/4)$, where θ is the direction of the principal normal stress σ_1. Problems were encountered at the membrane's centre (the intersection of the dashed black lines), due to the singularity of the differential equation, as given above, at that point. This is because $\tan(\theta \pm \pi/4) = [\tan(\theta) \pm 1]/[1 \mp \tan(\theta)]$ and $\tan(\theta) = e$ cannot be determined at the membrane's centre. However, the trajectories of $\pm\tau_{\max}$ are well-defined as shown in the regions away from the centre; the trajectories are the two sets of mutually orthogonal maximum shear axes as seen in the figure. Also, it is seen that the trajectories make angle of $\pm 45^{\circ}$ at the four sides of the square membrane.

in detail in Section 5.3.4.

However, the material parameters controlling strain-hardening (B) and strain-rate sensitivity ($\dot{\varepsilon}_0$) were set so that the material behaviour approaches perfect plasticity during yielding; namely, very small B and relatively high $\dot{\varepsilon}_0$ were used. The actual values are $\dot{\varepsilon}_0 = 14$ [1/s], and $B = 642 \times 10^3$ [Pa]. Note that the used values, for $\dot{\varepsilon}_0$ and B respectively, correspond to 10^4 and 10^{-3} times the typical values for a Domex-355 steel as suggested by Curry (2017); the remaining parameters in JC model, namely, n and c, are 0.5597 and 0.0320, respectively, which are directly adopted from Curry (2017). Realistic values were used for the elastic parameters, in particular the elastic modulus and Poisson's ratio are $E = 205 \times 10^9$ [Pa] and $\nu = 0.29$, respectively, and for the (quasi-static) yield stress. For simplicity, thermal and damage-based softening were neglected. Essentially, $\sigma_{d,y} \approx A = \sigma_0$, where σ_0 is the uni-axial yield stress.

The following values of the parameters, length L_x, width L_y, density ρ, thickness h, uni-axial yield stress σ_0, and specific impulse's maximum amplitude a_0, were chosen as given in Table. 3.1. A negative value for a_0 indicates an impulsive action in the negative (z) direction.

The membrane is set into motion by a prescribed initial velocity field, $\dot{w}_0$, according to

$$\dot{w}_0(x,y) = \frac{i(x,y)}{\rho h} = \frac{a_0}{\rho h}\phi_{1,1}(x,y)$$

In the LS-DYNA simulation, the outer nodes of the membrane are fixed for all degrees of freedom. The membrane was modelled using thin shell elements with five (5) through-thickness integration points, and a value of (5/6) was adopted for the coefficient of transverse shear. Note that the membrane behaviour in the simulation includes all components of displacement and bending and transverse shear effects, in addition to the membrane's elasticity.

From the LS-DYNA results, the membrane response is analysed to verify some aspects of the accuracy of the analytical solution. Namely, the displacement shape predicted by LS-DYNA was compared to the first mode shape predicted by the present model. For this purpose, the intensity of the first mode, which will be denoted by I_{M1}, is defined to measure the presence of the first mode (as predicted by the present model) in LS-DYNA response, according to

$$I_{\mathrm{M1}}(t) = \frac{\int_A w(x,y,t)\phi_{1,1}(x,y)\ dA}{\|w(x,y,t)\| \times \|\phi_{1,1}(x,y)\|} \tag{3.9.12}$$

where

$$\|w(x,y,t)\| = \sqrt{\int_A w^2(x,y,t)\ dA}$$

$$\|\phi_{1,1}(x,y)\| = \sqrt{\int_A \phi_{1,1}^2(x,y)\ dA},$$

and A is the whole area of the membrane. In the above, $w(x,y,t)$ is the one from LS-DYNA simulation.

The value of I_{M1}, thus, can be viewed as a direct metric to measure the spatial similarity of displacement field given from LS-DYNA simulation and the mode shape under consideration, which is $\phi_{1,1}(x,y)$, that solves the equilibrium equation predicted by the present model. The value of $I_{\mathrm{M1}}(t)$ approaches unity when $w(x,y,t)$ is a scalar multiple of the mode shape $\phi_{1,1}(x,y)$; the scalar multiplier disappears due to the normalisation as given by the norm of $w(x,y,t)$ in the denominator, $\|w(x,y,t)\|$. The basis of choosing this quantity, I_{M1}, is due to the standard Fourier analysis. It can be seen that if $w = \alpha\phi_{1,1}$, for any non-zero α, then one will have $|I_{\mathrm{M1}}| \equiv +1$. Since $w(x,y,t)$ is a function of time, then so is I_{M1}. On the other hand, $|I_{\mathrm{M1}}|$ will have a value less than 1 when $w(x,y,t)$ is spatially different from $\phi_{1,1}$; in general $|I_{\mathrm{M1}}| \leq 1$. The difference of $|I_{\mathrm{M1}}|$ from unity reflects that w and $\phi_{1,1}$ are less related.

Evaluations of $I_{\mathrm{M1}}(t)$ associated with the transverse displacement, w, response from LS-DYNA are made, for the range in time from $t = 0$ up to the time instant, denoted $t_{\max}$, when the central displacement attained its peak value. The result is given in Fig. 3.9, which interestingly shows that the (transverse) displacement profile from LS-DYNA is practically the first mode $\phi_{1,1}(x,y)$ predicted by the present model as $I_{\mathrm{M1}}(t)$ is 1 in the considered time interval, $t = (0, t_{\max}]$.

Table 3.1. Used parameters' values for validating the first mode solution against numerical results from a simplified LS-DYNA analysis

Parameter	Value	Unit
a_0	-2000	Pa.s
L_x	0.35	m
L_y	0.35	m
σ_0	352 $\times 10^6$	Pa
ρ	7830	kg/m^3
h	0.002	m

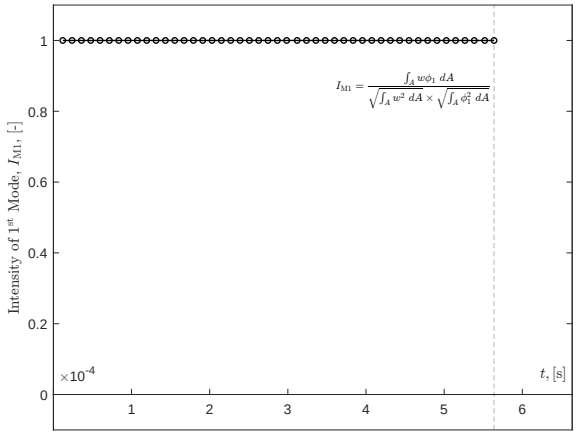

Fig. 3.9. Measuring the resemblance of the transverse displacement profile, $w(x, y, t)$, as predicted by LS-DYNA and the shape of the first mode, $\phi_{1,1}(x, y) = \phi_1(x, y)$, which solves the equilibrium equation predicted by the analytical model. It is shown that $I_{\mathrm{M1}}(t) = 1$ for the considered time interval, $t = [0, t_{\max}]$, where $t_{\max}$ (shown as dashed vertical line) is the time when the peak displacement is reached at the membrane's centre. Consequently, w from LS-DYNA is practically the first mode of the present model.

As an additional assessment of the accuracy of the present model, the transverse displacement history at the square membrane's centre, $w_c(t)$, is used to compare the predictions of the model against that from LS-DYNA. Recall that the time-dependent solution given by the model is valid until the critical time instant t^* is reached, where $t^* = \pi/(2\omega)$, as was given in the previous subsection. The analytical solution thus is terminated at t^*, and the subsequent displacement is taken to be $w(x, y, t = t^*)$, which is considered as the permanent displacement. The result of the present validation is given in Fig. 3.10.

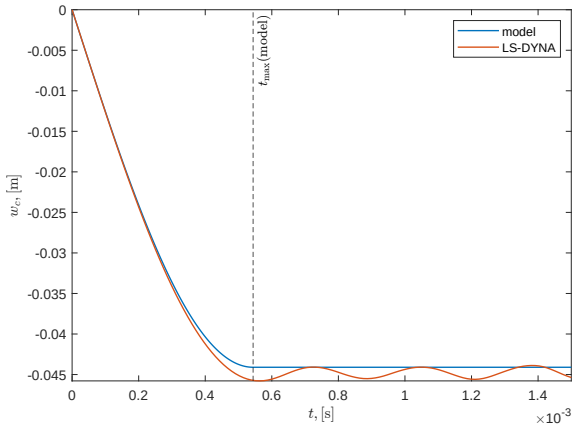

Fig. 3.10. Transient central displacement $w_c \equiv w(L_x/2, L_y/2, t)$ as predicted by the present model and LS-DYNA associated with the first mode solution. A vertical dashed line is drawn at the critical time instant t^*, beyond which the analytical solution is held constant. It is seen that (i) the variation of the central displacement from the model and LS-DYNA are correlated well before $t = t^*$; (ii) the peak displacements from the model and LS-DYNA are very close from each other; (iii) the time of maximum displacement occurrence from the model and LS-DYNA are comparable; (iv) the model can predict the velocity at the membrane's centre (as can be inferred from the slope of the curves) when compared to LS-DYNA, before the critical time is reached.

From Fig. 3.10, the time to peak central displacement from LS-DYNA compares well with the model, and the slopes of the displacement's time histories (i.e., the central velocity) from the LS-DYNA and the model match, from the initial time up to the time of peak response. Hence, this suggests that the angular frequency, ω, predicted by the model is practically the same as that in LS-DYNA response. Furthermore, from Fig. 3.9, it can be concluded that LS-DYNA response, w, is the first mode of the present model, from time zero up to the peak time. Now, since ω is directly related to the model's plastic wave speed, c_p, and the magnitude of the first mode's wavenumber, $\left(\sqrt{k_x^2 + k_y^2}\right)$, then it can be said that c_p is also (implicitly) present in LS-DYNA response, which, in turns, implies that the functional form of c_p is accurate, namely, its dependence on $\left(2/\sqrt{3}\right)\sigma_0$. Thus, it can ultimately be inferred that the response w from LS-DYNA solves the wave equation, $c_p^2\left(\frac{\partial^2 w}{\partial x^2} + \frac{\partial^2 w}{\partial y^2}\right) = \ddot{w}$, where c_p is as given by the present model, i.e., $c_p^2 = 2\sigma_0/(\sqrt{3}\rho)$.

The foregoing validation example, then, shows that the equilibrium equation predicted by the model is also valid when the specific impulse is non-uniform, since $i(x, y)$ considered therein is spatially non-uniform and has the spatial shape that is proportional to the first mode, $\phi_{1,1}(x, y)$. Also, the modal solution is adequate and accurate for this non-uniform specific impulse case when compared to LS-DYNA results. It should be re-emphasised that the specific impulse is non-uniform, and the model is reasonably accurate for this

loading distribution.

Lastly, the present validation study successfully tested the applicability of the simple membrane kinematics and the rigid-plastic (i.e., negligible elasticity) idealisations to accurately reproduce the transverse motion of the impulsively loaded thin plate where the impulse intensity is high (which corresponds to typical blast impulse amplitudes) and the in-plane membrane strains are attributed merely to the transverse displacement being large. Note that the impulsive regime and the perfect plasticity assumptions are not investigated as the validation data (from LS-DYNA results) incorporate these assumptions as well.

Chapter 4

Validation of the Uniform Model

4.1 Note

The content of this chapter is, subject to minor re-structuring, the manuscript of the paper by Alotaibi et al. (2023) that has been published in the International Journal of Impact Engineering, and as such, the word(s) "authors" or "present authors" refer to the authors of the paper, including the author of the present thesis. The full bibliography record of the paper is given below:

> S. A. Alotaibi et al. (2023). "Rigid-plastic membrane response of thin plates under impulsive blast loads using the extended Hamilton principle". In: *Int. J. Impact Eng.* 178, p. 104624. ISSN: 0734743X. DOI: 10.1016/J.IJIMPENG.2023.104624

4.2 Overview

The present work aims to develop an analytical model to predict the response of thin ductile plates under impulsive blast loads. To this end, the current knowledge about the physical problem, see Section 2.2, is utilised while attempting to minimise the complexity of the problem.

First, the load is assumed to be perfectly impulsive and, thus, specified in terms of an initial velocity field derived from the prescribed blast-induced specific impulse. According to the UFC 3-340-02 design manual (U.S. Army, 2008), the impulsive regime applies when the time to maximum response to load duration ratio exceeds three, see Figure 1-7 of the manual. Secondly, the material is idealised as rigid-perfectly plastic, which obeys von Mises's yield function and its associated flow rule. Finally, the plate, which is restrained along its outer periphery, is assumed to deform in membrane mode without in-plane displacements; hence, flexural effects are ignored.

The first assumption, due to Rigby et al. (2019a), is fundamental to the present analysis (the absence of externally applied forces ensures a monotonic deformation path in a rigid-plastic structure, as will be discussed in Section 4.3). The last assumption is based on the

membrane thinness and loading intensity.

The well-known extended Hamilton's principle, see, e.g., Reddy (2002) and Washizu (1975), is applied to the above described problem to obtain the appropriate equation of motion governing the transverse displacement of the thin membrane. The equation is found as a two-dimensional linear wave equation. Therefore, it is solved by the modal decomposition technique while enforcing Drucker's (1957; 1956) postulate of the plastic work non-negativity. Analytical solutions are provided for rectangular membranes subjected to arbitrary distribution of specific impulse and for axi-symmetric circular membranes.

The closed-form solutions for rectangular and circular membranes loaded by uniform impulses are compared to experimental data found in Nurick et al. (1985), Gharababaei and Darvizeh (2010), and Nurick et al. (1996). In addition, the analytical solution is compared to results from LS-DYNA simulations, where the loads are prescribed through the initial velocity field according to Rigby et al. (2019a) and using experimentally validated parameters for the plate's material that are adopted from Rigby et al. (2019a), Curry (2017), and Curry and Langdon (2017). Finally, the present model is compared to an existing model proposed by Chung Kim Yuen et al. (2016) as a modification to Nurick and Martin (1989b) model. The uniform and non-uniform impulse solutions are found to be reasonably accurate with very low computational expense.

4.3 Theory

4.3.1 Problem Definition

Consider a thin membrane made of a rigid-perfectly plastic metal that is subjected to a prescribed initial velocity field obtained from a specific impulse distribution according to Tyas and Pope (2003) and Rigby et al. (2019a).

The membrane can be of a rectangular or circular geometry, and it is supported along its outer periphery. For the rectangular geometry, L_x and L_y are the sides' lengths, as indicated in Fig. 4.1, and R is the radius of the circular membrane. The specific impulse is denoted by $i(x, y)$ or $i(r)$, where x and y are the rectangular undeformed coordinates for rectangular geometry, whereas r is the radial undeformed coordinate for the circular membrane. Let t denotes time, and ρ, h, and σ_0 denote, respectively, density, thickness, and characteristic yield strength of the membrane.

The membrane is assumed to respond in pure membrane mode. Further, it is assumed that the components of displacement along the undeformed in-plane coordinates are negligible. That is, the only non-zero displacement is the one along the original out-of-plane coordinate, which is denoted by w. In other words, every particle of the membrane displaces only vertically. Note that even though in-plane displacements are absent, there will be membrane (or stretching) action due to the large transverse displacement; for the sake of completeness, the reader is reminded that such membrane action is the one responsible

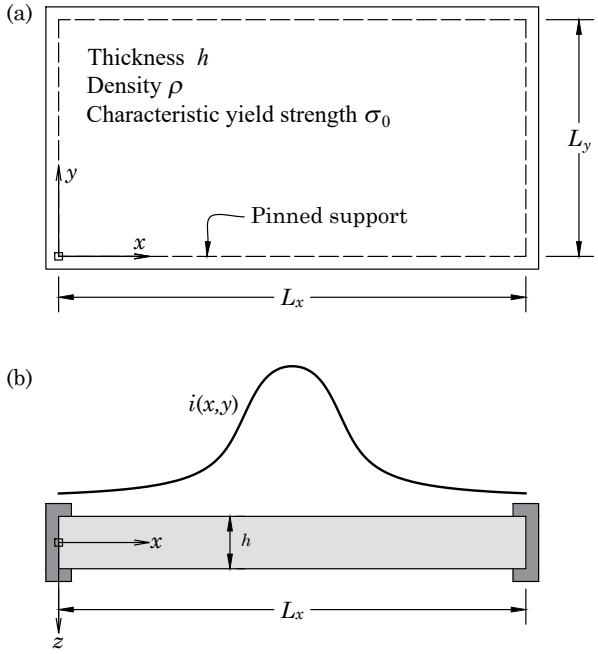

Fig. 4.1. Problem definitions for the rectangular membrane: (a) plan view showing undeformed geometry and (b) side view showing a typical spatial distribution of specific impulse i.

for the well-known (non-linear) flexural-membrane coupling in large displacement analysis of materially linear elastic thin plates and beams, see, e.g., Reddy (2007).

In line with the perfect plasticity assumption, the characteristic yield strength σ_0 is assumed constant. Thus, for materials exhibiting substantial work-hardening, see, e.g., Elveli et al. (2022) and Granum et al. (2019), σ_0 could be defined such that a rectangular stress-plastic strain curve preserves the total area under the actual uni-axial stress-plastic strain curve. This approach is adopted in the UFC 3-340-02 (2008) manual.

4.3.2 Development of the Equation of Motion

Note A thorough derivation of the equation of motion (the rigid-plastic membrane's equilibrium equation) was given and extensively discussed earlier in Chapter 3 of the thesis. The present section summarises the derivation as given in the published paper that is referenced at the beginning of the present chapter.

The extended Hamilton's principle is applied to the present problem to systematically derive the equation of motion. In applying the principle, treatment of kinetic energy and external work (if any) terms are not new and will not be shown for brevity. However, the internal energy term needs special consideration. First, there is no elastic strain energy in the system, and the only allowed internal energy (arising from the accumulation of plastic deformation) is dissipative in nature. To obey such irreversible behaviour, the rate of plastic work must always be non-negative (Drucker, 1956; Drucker, 1957). That is, when strain rate tends to change sign, stress must instantly do so in a rigid-perfectly plastic

structure.

In Hamilton's principle, the *total* internal energy is the one that should be included, not the *rate* of energy. The total energy is the time integral of the energy rate. However, the time integration can be carried out beforehand (i.e., explicitly) when the total plastic strain is monotonic since the stress would be constant in terms of sign (recall that its magnitude is already constant from the perfect plasticity). Now, since there are no external forces, the total plastic strain is guaranteed to be monotonic (i.e., the sign of strain rate is fixed) when the transverse velocity is monotonic.

In the following, σ_{ij}, s_{ij}, ε_{ij}, and λ are the stress, deviatoric stress, (Green-Lagrange) strain, and the plastic multiplier, respectively. A dot $(\dot{\cdot})$ over a symbol denotes time differentiation, a repeated subscript implies summation, and a superscript $(^p)$ denotes the plastic part.

With reference to the von Mises's yield function, $f(\sigma_{ij}) = \frac{1}{2}s_{ij}s_{ij}$, yielding of the material occurs when $f(\sigma_{ij}) = \frac{1}{3}\sigma_0^2$. Associated with such a yielding condition, the incremental flow rule reads

$$\dot{\varepsilon}^p_{ij} = \dot{\lambda}\frac{\partial f}{\partial \sigma_{ij}} = \dot{\lambda}s_{ij} \qquad \dot{\varepsilon}^p_{ij} \equiv 0 \text{ if } f(\sigma_{ij}) < \frac{1}{3}\sigma_0^2 \tag{4.3.1}$$

Now, if the material has actually yielded, i.e., $\dot{s}_{ij} \equiv 0$, then under a monotonic deformation regime, the flow rule can be integrated by parts (while taking advantage of $\dot{s}_{ij} = 0$ and assuming $\lambda|_{t=0} = 0$) to obtain

$$\varepsilon^p_{ij} = \int \dot{\varepsilon}^p_{ij}\, dt = \int \dot{\lambda}s_{ij}\, dt = \lambda s_{ij} - \int \lambda \dot{s}_{ij}\, dt = \lambda s_{ij}. \tag{4.3.2}$$

Eq. (4.3.2) allowed a transition from the flow- to the total-theories of plasticity, and it holds only when the path is monotonic. In fact, Drucker (1956) argues that when loading is monotonic, the two plasticity theories are identical.

Using Eq. (4.3.2), it can be shown that $\lambda = \left(\sqrt{3/2\ \varepsilon^p_{ij}\varepsilon^p_{ij}}\right)/\sigma_0$, and the total plastic work, which is

$$W_p = \int_V \sigma_{ij}\varepsilon^p_{ij}\, dV, \tag{4.3.3}$$

can be expanded as $W_p = \int_V s_{ij}\varepsilon^p_{ij}\, dV = \int_V \lambda s_{ij}s_{ij}\, dV = \int_V \lambda\left(\frac{2}{3}\sigma_0^2\right)\, dV$, or

$$W_p = \int_V \sigma_0\sqrt{2/3\ \varepsilon^p_{ij}\varepsilon^p_{ij}}\, dV, \tag{4.3.4}$$

where the plastic incompressibility, $\varepsilon^p_{ii} = \lambda s_{ii} = 0$, of the von Mises material was utilised.

From now on, the superscript p will be omitted as total strain and plastic strain are identical in line with the rigid-plastic assumption. To evaluate the quantity $\varepsilon_{ij}\varepsilon_{ij}$, the four non-vanishing strain components as functions of the transverse displacement, $w(x, y, t)$,

will be utilised. These are

$$\varepsilon_x = \frac{1}{2}\left(\frac{\partial w}{\partial x}\right)^2, \quad \varepsilon_y = \frac{1}{2}\left(\frac{\partial w}{\partial y}\right)^2,$$
$$\gamma_{xy} = \frac{\partial w}{\partial x}\frac{\partial w}{\partial y} = 2\sqrt{\varepsilon_x \varepsilon_y}\,, \tag{4.3.5}$$

and from the incompressibility condition, one has

$$\varepsilon_z = -(\varepsilon_x + \varepsilon_y). \tag{4.3.6}$$

Then, through some algebra simplifications, it can be shown that

$$\varepsilon_{ij}\varepsilon_{ij} = 2(\varepsilon_x + \varepsilon_y)^2. \tag{4.3.7}$$

Therefore, the total plastic work under a monotonic deformation path becomes

$$\begin{aligned} W_p &= \int_V \frac{2}{\sqrt{3}}\sigma_0(\varepsilon_x + \varepsilon_y)\, dV \\ &= \int_V \frac{2}{\sqrt{3}}\sigma_0 \left[\frac{1}{2}\left(\frac{\partial w}{\partial x}\right)^2 + \frac{1}{2}\left(\frac{\partial w}{\partial y}\right)^2\right] dV. \end{aligned} \tag{4.3.8}$$

It should be noted that the stress σ_{ij}, appearing in Eq. (4.3.3), is the second Piola-Kirchhoff stress since it is the work-conjugate to Green-Lagrange strain. However, for consistency of the formulation, the small strain assumption implies that this mentioned stress can be replaced with the true Cauchy stress. Hence, we refer to σ_{ij} throughout as the Cauchy stress.

Then, the extended Hamilton's principle is applied, which reads

$$\delta\left(\int_{t_1}^{t_2} H\, dt\right) = 0, \tag{4.3.9}$$

where δ is the variational operator, and t_1 and t_2 are arbitrary times. In Eq. (4.3.9), the Hamiltonian, H, of the system (in absence of external work and elastic strain energy) is given by

$$H = [K - W_p]\,. \tag{4.3.10}$$

in which K is the total kinetic energy of the membrane, which is $K = \int_V \frac{1}{2}\rho \dot{w}^2\, dV$, and W_p was given in Eq. (4.3.8). Notice that H becomes a functional of w only.

Finally, by (i) applying δ on w, (ii) carrying out spatial and temporal integration by parts, (iii) imposing constraints on w at the membrane edges and anywhere at times t_1 and t_2 where δw vanishes identically, and (iv) requiring δw to be otherwise arbitrary, then one obtains the (Euler-Lagrange) equation of motion governing the response of the

rigid-perfectly plastic membrane as

$$\frac{2}{\sqrt{3}}\sigma_0\left[\frac{\partial^2 w}{\partial x^2}+\frac{\partial^2 w}{\partial y^2}\right]=\rho\ddot{w}. \tag{4.3.11}$$

Eq. (4.3.11) is a two-dimensional scalar (plastic) wave equation in $w(x,y,t)$ in a rectangular coordinate system and with a wave speed $\left[2\sigma_0/(\sqrt{3}\,\rho)\right]^{1/2}$. Note that Eq. (4.3.11) is a field equation so that it applies to any membrane geometry with restrained edges.

Later, the equation is solved for a rectangular membrane, as defined in Fig. 4.1, under the following kinematic conditions

$$\begin{aligned} &w(0,y,t)=w(L_x,y,t)=w(x,0,t)=w(x,L_y,t)=0,\\ &w(x,y,0)=0, \end{aligned} \tag{4.3.12}$$

and the dynamic condition

$$\dot{w}(x,y,0)=\frac{i(x,y)}{\rho h}. \tag{4.3.13}$$

Eq. (4.3.13) is experimentally shown to hold for thin plates under non-uniform specific impulse by Rigby et al. (2019a), Rigby et al. (2019b), and Tyas and Pope (2003), which was derived from the balance of linear momentum of shear non-rigid thin plates.

For a circular membrane and under axi-symmetric conditions (which will be assumed throughout), it can be shown, through the standard transformation from rectangular to polar coordinates, that the equation of motion is given as

$$\frac{2}{\sqrt{3}}\sigma_0\left[\frac{\partial^2 w}{\partial r^2}+\frac{1}{r}\frac{\partial w}{\partial r}\right]=\rho\ddot{w}. \tag{4.3.14}$$

where a term within the brackets on the left-hand side $(1/r^2)\,\partial^2 w/\partial\theta^2$ has been omitted due to the axi-symmetric assumption. Eq. (4.3.14) will be solved under the following conditions

$$w(R,t)\;=\;w(r,0)\;=\;0,\quad \dot{w}(r,0)=\frac{i(r)}{\rho h}. \tag{4.3.15}$$

Although the actual problem involves plastic deformations, the obtained equations of motion are linear. Hence, they can be solved by Fourier's decomposition, which is based on the principle of superposition. The Fourier decomposition technique is a type of the eigen-expansion method, where the eigen-functions are the components of the Fourier series in the rectangular membrane case, whereas the eigen-functions are the classical Bessel's functions of the first kind for the circular membranes. Wierzbicki discusses the possibility to extend and apply the eigen-expansion (i.e., the superposition) method to structural plasticity problems.

It should be recalled that the above equations of motion are valid as long as the deformation

path remains monotonic so that Eq. (4.3.2) is not violated. Hence, the solutions (to be presented later) of Eq. (4.3.11) and Eq. (4.3.14) are valid up to the instant of time when the transverse velocity, $\dot{w}$, tends to change sign, or simply when velocity reaches zero. In other words, a component of the solution must terminate whenever the velocity associated with it reaches zero for the first time. Otherwise, plastic work would decrease and thereby violating its irreversibility or dissipating nature, and thus the solution becomes non-physical.

Many textbooks, e.g., references that treat the elastic free vibration of pre-tensioned membranes under small displacements, such as Rayleigh (1894, Ch. IX) and Timoshenko and Young (1955, Sec. 69), show how equations similar to Eqs. (4.3.11) and (4.3.14) can be solved. Excellent stepwise derivations are presented in Rao (2019b), which is open-access. Hence, the derivation steps of the solution will be omitted for brevity. Instead, the solutions themselves are given.

4.4 Rectangular Membranes

4.4.1 Response of Rectangular Membranes

The rectangular membrane equation of motion, Eq. (4.3.11), was solved by the modal decomposition technique under the prescribed geometric conditions, Eqs. (4.3.12) and (4.3.13). The solution is

$$w(x,y,t) = \frac{4}{\rho h L_x L_y} \sum_{m,n=1}^{\infty} \frac{I_{mn}}{\omega_{mn}} \phi_{mn}(x,y) \sin(\omega_{mn} t), \tag{4.4.1}$$

with the wave speed c, mode shape $\phi_{mn}(x,y)$, modal angular frequency ω_{mn}, and total modal impulse I_{mn} given by

$$c = \sqrt{\frac{2}{\sqrt{3}} \frac{\sigma_0}{\rho}} \tag{4.4.2}$$

$$\phi_{mn}(x,y) = \sin\left(\frac{m\pi x}{L_x}\right) \sin\left(\frac{n\pi y}{L_y}\right)$$

$$\omega_{mn} = \frac{\pi c}{L_x L_y} \sqrt{(L_y m)^2 + (L_x n)^2} \tag{4.4.3}$$

$$I_{mn} = \int_0^{L_x} \int_0^{L_y} i(x,y) \sin\left(\frac{m\pi x}{L_x}\right) \sin\left(\frac{n\pi y}{L_y}\right) dy\, dx. \tag{4.4.4}$$

The pair (m,n) defines a particular mode with mode shape $\phi_{mn}(x,y)$. It is known that the modes are orthogonal over the membrane domain, and hence they are independent. Therefore, the requirement of a monotonic deformation path enforces the termination of a

particular mode when the associated (modal) velocity reaches zero for the first time, i.e., when

$$t = t_{m,n} = \frac{\pi}{2\omega_{mn}}. \tag{4.4.5}$$

From ω_{mn}, see Eq. (4.4.3), it is clear that the sequence of turning off the modal contributions is ordered from highest to lowest modes in terms of frequency. The notion of sequential terminations of the modes was previously used in Jones (1967) and Wierzbicki and Nurick (1996). The last contributing mode is the first, i.e., with $(m = n = 1)$. Thus, the whole membrane ceases motion at no later than $t = t_{1,1}$, which is given by

$$t_{1,1} = \frac{L^*}{2c} \tag{4.4.6}$$

where L^*, defined for convenience, is the ratio of the membrane area to the length of its diagonal and given by

$$L^* \equiv \frac{L_x L_y}{\sqrt{L_x^2 + L_y^2}}. \tag{4.4.7}$$

Note that if $t_{1,1}$ is less than three times the duration of blast load, the global response is less likely to be impulsive, based on U.S. Army (2008), since $t_{1,1}$ is an upper bound on the response time. The actual time of maximum response is the modal time $t_{m,n}$ of the dominant mode (whose total modal impulse is I_{mn}) of the membrane under a particular distribution of specific impulse i. If there are several dominant modes, then the maximum time is the largest $t_{m,n}$ among these modes.

The permanent shape, $w_p(x, y)$, of the membrane is given by $w(x, y, t)$ when $t \geq t_{1,1}$, or

$$w_p(x, y) = \frac{4}{\pi\rho c h} \sum_{m,n=1}^{\infty} \frac{I_{mn}}{\sqrt{(L_x n)^2 + (L_y m)^2}} \phi_{mn}(x, y). \tag{4.4.8}$$

For all cases in which the specific impulse distribution is symmetric about the membrane's centre, the peak displacement is located at the centre. The central permanent displacement, $w_c \equiv w_p(L_x/2, L_y/2)$, is

$$w_c = \frac{4}{\pi\rho c h} \sum_{m,n=1}^{\infty} \frac{I_{mn}}{\sqrt{(L_x n)^2 + (L_y m)^2}} \sin\left(\frac{m\pi}{2}\right) \sin\left(\frac{n\pi}{2}\right). \tag{4.4.9}$$

According to Pannell et al. (2021), the specific impulse distribution from a near-field spherical charge blast is of a Gaussian form as a function of the angle of incidence. However, it was not possible to evaluate I_{mn} symbolically for a specific impulse distribution, $i(x, y)$, as predicted by Pannell et al. Hence, numerical integration is needed. A practical MATLAB code for calculating I_{mn} using the Fast Fourier Transform (FFT) is given in D.

Fig. 4.2 shows the normalised permanent displacement, w_p, profiles along $y = L_y/2$ due to three impulse distributions with constant amplitudes applied over varying central areas

of a rectangular membrane. In the figure, the legends indicate the ratios of the loaded to total areas. It is, thus, evident that a localised impulse induces localised displacement shape, i.e., with central dishing, while the case of uniform impulse applied over the whole area of the membrane results in global uniform dishing. In practice, a finite number of

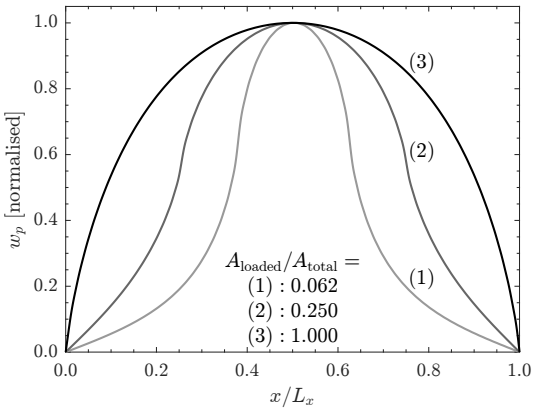

Fig. 4.2. Permanent displacement profile for rectangular membrane under three sets of impulses of constant amplitudes applied over central rectangular regions with loaded-to-total area ratios of (1) 0.062, (2) 0.25, and (3) 1.0. Curve (1) is associated with localised impulse, and (3) results from a uniform impulse over the entire membrane.

modes is used to numerically evaluate the permanent, $w_p(x, y)$, and permanent central, w_c, displacements. To maintain sufficient accuracy while truncating the infinite series in Eqs. (4.4.8) and (4.4.9), the error estimate given in C can be used. The error relates the sum of modal impulses (included in the approximation) to the energy-equivalent total impulse, I_k, that is due to Rigby et al. (2019a) and Tyas and Pope (2003) and given by

$$I_k = \sqrt{A \int_A i^2 \, dA},$$

in which A is the loaded area of the membrane. The absolute importance of a particular mode is shown to be indicated by the measure $0 \leq (2I_{mn}/I_k)^2 \leq 1$, which can also be used to identify the dominant mode(s); dominant modes have values closer to unity.

4.4.2 Uniform Specific Impulse Case (Rectangular Membrane)

For the case where the specific impulse has a constant distribution, i.e., $i(x, y) = i_0$, the modal impulse, I_{mn}, simplifies to

$$I_{mn} = \begin{cases} \frac{4i_0 L_x L_y}{\pi^2 mn} & \text{when } (m, n) \text{ are odd} \\ 0 & \text{otherwise,} \end{cases}$$

which suggests that the first mode is the most dominant.

The peak displacement is located at the plate's centre and is given by

$$w_c = \frac{16 i_0 L_y}{\pi^3 \rho c h} \sum_{m,n=1,3,5}^{\infty} \frac{\sin\left(\frac{m\pi}{2}\right) \sin\left(\frac{n\pi}{2}\right)}{mn\sqrt{n^2 + m^2 (L_y/L_x)^2}}. \tag{4.4.10}$$

In Eq. (4.4.10), the summand depends solely on the membrane's aspect ratio L_y/L_x. Denoting the sum by S_0, it was observed to converge. The value of S_0 for any aspect ratio in the range $[0.1 - 1.0]$ can be read from Fig. 4.3, in which $L_y \leq L_x$.

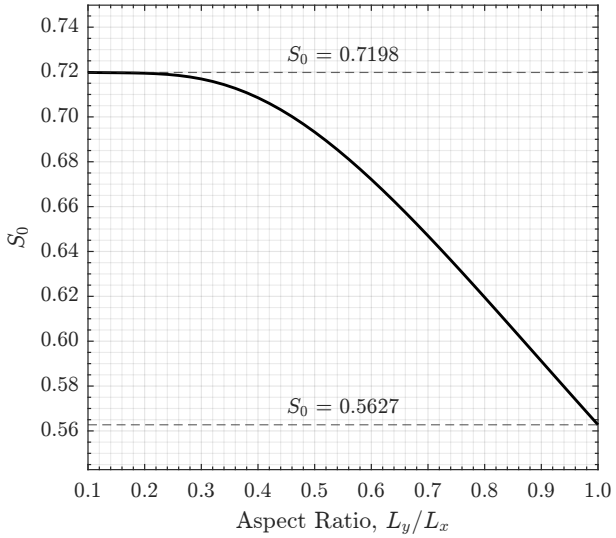

Fig. 4.3. The converged value of truncated sum, S_0, for the rectangular membrane associated with uniform impulse case as a function of the membrane aspect ratio, L_y/L_x, where $L_y \leq L_x$.

With S_0 known, the central displacement of a membrane due to a uniform impulse (with intensity i_0) is given by

$$w_c = \frac{16 i_0 L_y}{\pi^3 \rho c h} S_0. \tag{4.4.11}$$

Or, using the total impulse $I_0 = \int_A i(x, y)\, dA = A\, i_0$, the last expression becomes

$$w_c = \frac{16 S_0}{\pi^3 \rho c h L_x} I_0 \equiv k_0 I_0, \tag{4.4.12}$$

where a structural parameter k_0 was introduced and defined as

$$k_0 = \frac{16 S_0}{\pi^3 \rho c h L_x}. \tag{4.4.13}$$

It should be re-emphasised that L_y is the shorter side's length, i.e., $L_y/L_x \leq 1$, when S_0 is estimated from Fig. 4.3.

4.5 Circular Membranes

4.5.1 Response of Circular Membranes

As stated in Section 4.3, axi-symmetric conditions are assumed for the circular membrane problem. Eq. (4.3.14) was solved by the modal decomposition technique. The solution is presented below, Eq. (4.5.1), which gives the displacement of a circular rigid-perfectly plastic membrane of radius R, mass density ρ, characteristic yield strength σ_0, and thickness h, due to a specific impulse (impulse per unit area), $i(r)$.

$$w(r,t) = \frac{2}{\rho c R h} \sum_{m=1}^{\infty} \frac{I_m}{j_{0,m} J_1(j_{0,m})^2} \phi_m(r) \ \sin(\omega_m t), \tag{4.5.1}$$

where

$$\phi_m(r) = J_0\left(\frac{j_{0,m}}{R}\ r\right), \tag{4.5.2}$$

$$\omega_m = \frac{c j_{0,m}}{R}, \tag{4.5.3}$$

$$I_m = \int_0^R i(r)\, J_0\left(\frac{j_{0,m}}{R}\ r\right) r dr \tag{4.5.4}$$

I_m is the total modal impulse per unit radian, c is the wave speed given in Eq. (4.4.3), $\phi_m(r)$ is the m^{th} mode shape, and ω_m is the corresponding frequency. In above, $J_0(x)$ and $J_1(x)$, respectively, are Bessel *functions* of the first kind of order zero and one, while the *scalar* value $j_{0,m}$ is the m^{th} root of $J_0(x) = 0$, i.e., $J_0(j_{0,m}) \equiv 0$. The solution does not involve Bessel functions of the second kind to avoid infinite (non-physical) response at the origin (plate's centre). Furthermore, the modal solution depends only on the zeroth order Bessel function due to the axi-symmetry of the problem. Again, the m^{th} mode shape is $J_0(j_{0,m}r/R)$, and the square of its norm (per unit radian) is $(1/2)R^2\left[J_1(j_{0,m})\right]^2$. The modes, $\phi_m(r)$, are orthogonal to each other, and thus they are independent.

Similar to the rectangular case, the contribution from a given mode in the solution is valid until the corresponding modal velocity reaches zero when $t \geq t_m$, where $t_m = \pi R/(2cj_{0,m})$. Thus, the modes will be switched off sequentially in descending order with respect to frequency. Thus, the whole membrane motion terminates at or before $t = t_1 = \pi R/(2cj_{0,1})$, where $j_{0,1} = 2.405$.

The permanent membrane profile, $w_p(r)$, is obtained from Eq. (4.5.1) for $t \geq t_1$ and is given by

$$w_p(r) = \frac{2}{\rho c R h} \sum_{m=1}^{\infty} \frac{I_m}{j_{0,m} J_1(j_{0,m})^2} \phi_m(r). \tag{4.5.5}$$

Since the problem is axi-symmetric, the central displacement is the peak. Using the fact

Table 4.1. The first seven roots of the zeroth order Bessel function $J_0(x)$ and their related quantities, which were computed using a MATALB function developed by Nicholson (2022).

m	1	2	3	4	5	6	7
$j_{0,m}$	2.4048	5.5201	8.6537	11.7915	14.9309	18.0711	21.2116
$J_1(j_{0,m})^2$	0.2695	0.1158	0.0737	0.0540	0.0427	0.0352	0.0300
$J_1(j_{0,m})/j_{0,m}$	0.2159	-0.0616	0.0314	-0.0197	0.0138	-0.0104	0.0082

that $J_0(0) = 1$, the central permanent displacement, $w_c \equiv w_p(r = 0)$, is

$$w_c = \frac{2}{\rho c R h} \sum_{m=1}^{\infty} \frac{I_m}{j_{0,m} J_1(j_{0,m})^2}. \tag{4.5.6}$$

Some available tools, e.g., MATLAB native function `besselj()` and the user-built MATLAB function in Nicholson (2022), can be utilised to evaluate Bessel quantities appearing in the above expressions. Table 4.1 is provided for convenience.

Similar to the rectangular case, it was not possible to evaluate the integral I_m for a specific impulse distribution, $i(r)$, of the type predicted by Pannell et al. (2021) model. Thus, I_m needs to be computed numerically.

Experiments indicate that when a circular membrane is subjected to localised impulse, say, over the membrane's central region, then central dishing results, see Curry and Langdon (2017). Thus, to qualitatively test the developed solution, such a loading case was simulated that results in the permanent shape depicted in Fig. 4.4 by curve (1), in which a central bulging can be seen.

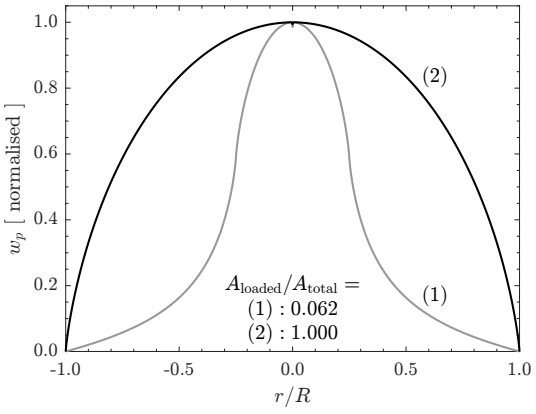

Fig. 4.4. Permanent displacement profile of an axi-symmetric circular membrane subjected to a uniform impulse which is applied over a localised region (1) with a loaded-to-total area ratio of 0.062 and over the whole area (2) of the membrane as predicted by the present solution.

4.5.2 Uniform Specific Impulse Case (Circular Membrane)

When the specific impulse (impulse per unit area) is spatially uniform with intensity i_0, the total modal impulse I_m simplifies to $I_m = [i_0 R^2 J_1(j_{0,m})]/j_{0,m}$.

In this case, the permanent central displacement of a circular membrane is

$$w_c = \frac{2Ri_0}{\rho ch} \sum_{m=1}^{\infty} \left[j_{0,m}^2 J_1(j_{0,m}) \right]^{-1}$$
$$= \frac{2Ri_0}{\rho ch} \, S_0, \tag{4.5.7}$$

in which the numerical value of the infinite sum is denoted with S_0 and evaluates to 0.2674. Hence, the central permanent displacement of a circular membrane due to a uniform specific impulse (of intensity i_0) is

$$w_c = \frac{2Ri_0}{\rho ch} \times 0.2674. \tag{4.5.8}$$

Alternatively, in terms of total impulse $I_0 = \pi R^2 i_0$, the central displacement becomes

$$w_c = \frac{2 \times 0.2674}{\pi R \rho ch} \, I_0 \equiv k_0 \times I_0 \tag{4.5.9}$$

with the circular structural parameter k_0 defined as

$$k_0 = \frac{2 \times 0.2674}{\pi R \rho ch}. \tag{4.5.10}$$

The model predicts the normalised permanent membrane profile for the uniform specific impulse case as shown by curve (2) in Fig. 4.4, presented earlier.

4.6 Uniform Model Verification

4.6.1 Rectangular Membrane

4.6.1.1 Results

The solution w_c for the uniform impulse case, as given by Eq. (4.4.12), is validated using experimental data obtained from Nurick, Martin, and Pearce (1985). In the tests, 82 experiments were conducted using rectangular and square thin plates made of steel, and the specimens were loaded impulsively by distributed sheets of explosives. The authors suggest that the impulse distributions are uniform over the specimens' exposed surfaces. The sides measured 113 mm and 70 mm for the rectangular plates, and a side length of 89 mm was given for the square plates. The thickness and static yield strength were given as 1.6 mm and 296 MPa, respectively; the mass density is assumed to be 7830 kg/m^3. In the tests, the amounts of explosives were varied, resulting in different values of total impulses measured using a ballistic pendulum. The permanent central displacements were measured and given in the paper, and further details can be found there.

Nurick et al. (1985) data is used to validate the solution, Eq. (4.4.12). The static yield strength reported in the experiments is taken as σ_0 in the model. The results of the comparisons are shown in Figs. 4.5 and 4.6.

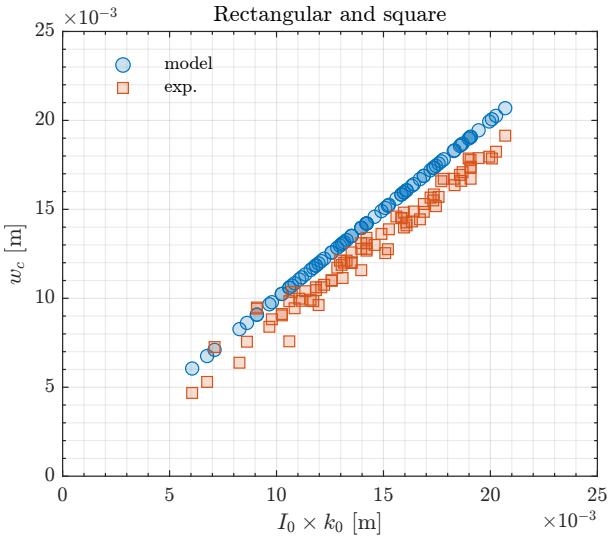

Fig. 4.5. Comparison of model predictions to experimental data (Nurick et al., 1985) in terms of central residual displacement w_c of rectangular and square membranes under uniform impulse of total magnitude of I_0; k_0 is the membrane's parameter defined in Eq. (4.4.13).

Nurick et al.'s experiments were simulated numerically using LS-DYNA, in which the plates were subjected to uniform initial velocity fields. The steel material was modelled using the `*Mat_Simplified_Johnson_Cook` model, available in LS-DYNA (LST, 2021b), which accounts for strain-hardening and strain-rate effect on the current yield stress. Thermal softening and strain-based failure were neglected in the analyses. The material parameters, except the static yield strength, were taken from Curry (2017) and Rigby et al. (2019a). Description of the material model will be given in Section 5.3.4. The rectangular plates were modelled as fully integrated shell elements using `*Element_Shell` and `*Section_Shell` keywords with `Elform`=16 (free of hourglass modes) and 3 through-thickness integration points, `NIP`=3, (to incorporate flexural effects). The uniform initial velocities were prescribed using the `*Initial_Velocity_Node` keyword. Nodes on the plates' peripheries were restrained in all (including the rotational) degrees of freedom.

The peak displacement at the plate's centre was used to determine an appropriate element mesh density, which was then held fixed in subsequent analyses; results of similar analysis will be presented in Section 5.3.2. The permanent displacement was determined by averaging (through time integration) the displacement time history beyond the first peak over a small number of vibration cycles.

LS-DYNA results are compared to the experiments and the analytical predictions for the rectangular and square tests (separately) as shown in Fig. 4.6.

From the team at SIMLab, Aune et al. (2016) and Aune et al. (2017) and Spranghers et al. (2012b) and Spranghers et al. (2013) presented experimental and numerical studies on the response of thin plates under free-air blasts, and further studies on the response

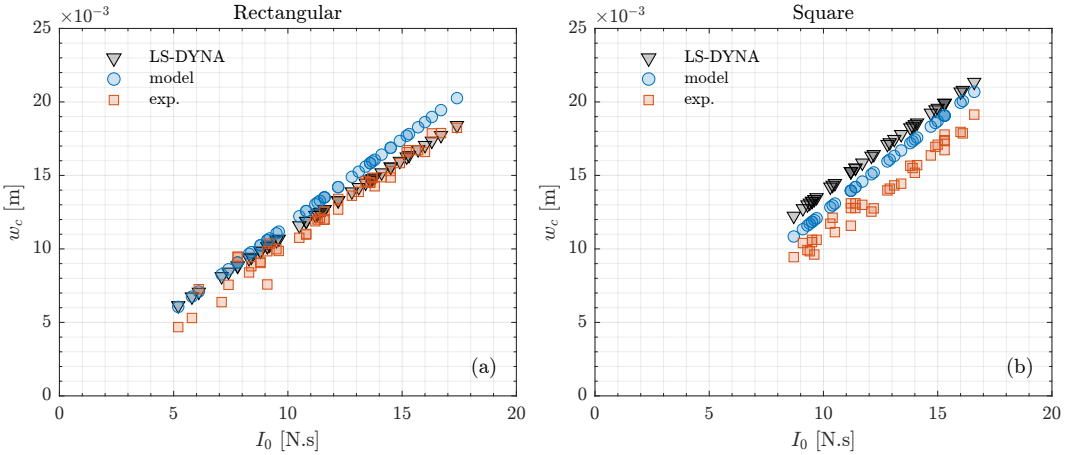

Fig. 4.6. Comparison of model predictions to experimental data (Nurick et al., 1985) and LS-DYNA numerical results in terms of central residual displacement w_c of (a) rectangular and (b) square membranes under uniform impulse of total magnitude of I_0. LS-DYNA data are for permanent displacements. The data was separated for visual convenience.

of similar structures due to blasts produced in a shock tube facility are given by Elveli et al. (2022). The rectangular plates are made of ductile materials (structural steel and aluminium). Some specimens are seen to respond impulsively and plastically. From the span-to-thickness ratios of some experiments and the intensity of the generated blast loads, the targets are thought to respond in membrane mode. Therefore, their experiments can, in general, be used to further assess the accuracy of the present model. However, few tests should be excluded from the validation analysis in which the plates: (1) experienced complete fractures, (2) had pre-formed cracks or holes, or (3) experienced a (counterintuitive) bifurcation or rebound buckling due to their ultra thinness when combined with low blast intensity. The validation of the model against the above experiments is not presented herein because the original works, cited above, did not provide quantitative information about the distribution of the blast-generated specific impulses, which the present model requires.

4.6.1.2 Discussion and Limitations

Fig. 4.5 and Fig. 4.6 exhibit a reasonable accuracy of the analytical model, Eq. (4.4.12), although the model accounts only for membrane behaviour, rigid-perfectly plastic material model, and idealised impulsive load.

However, as can be seen in the figures, the analytical model appears to be vertically offset when compared to the data. The offset is attributed to the fact that the model equation passes through the origin of w_c versus I_0, which is a shortcoming of the model since one expects a negative intercept on the w_c-axis (note that w_c is a plastic displacement).

From the other hand, it should be noted that Nurick et al. (1985) measured (indirectly) the total impulse, and the actual specific impulse distribution (which is assumed uniform herein) was not reported. The slight discrepancy between the present model prediction

and the experimental data could then be attributed to the implied lack of precise data.

Furthermore, the slight discrepancy can also be linked to the perfect plasticity assumption on the material behaviour. The model excludes strain-hardening and strain-rate effects, and for simplicity the static yield strength is taken as the perfectly plastic limit. However, many practical ductile materials exhibit various levels of yield enhancement due to these plastic effects. Heat-treated metals, e.g., typically possess substantial work-hardening where the current yield strength progresses gradually from the (less distinct) initial yield stress up to the ultimate strength that could be as twice as the initial yield strength (Granum et al., 2019). A certain class of steel, which has been used in blast environments, exhibits different hardening-ductility characteristics depending on the material composition, heat-treatment, and manufacturing processes (Elveli et al., 2022). Idealising plates made of hardening materials as perfectly plastic would then result in overestimations of the responses under large dynamic loads. Therefore, it is important that such plastic characteristics are incorporated in computer numerical analyses since mathematical complexity is not a barrier.

The perfect plasticity assumption is adopted in the present work to obtain a "first-order approximation" model. Addition of the two mentioned effects into the model was found, by the authors, to lead to a non-linear equation of motion. Therefore, the solution given by the present perfectly plastic model should be regarded as an upper-bound solution for structures made of materials that (in practice) deviate from the perfect plasticity behaviour.

If desirable, we propose that the yield strength to be used in the model might be adjusted (e.g., amplified) to compensate for large strain-hardening strengthening. For example, the *actual* area under the plastic part of the engineering stress-strain curve could be converted to a *rectangular* area, and by maintaining the ultimate strain, the characteristic (or effective) yield strength can then be determined. This procedure should give better predictions while maintain the upper-bound sense. However, in the foregoing validation work, the model is evaluated using the "static" yield strength because it was found to agree with the data.

A simplified study to assess the effect of work-hardening on the response of a single-degree-of-freedom (SDOF) due to blast-type loading is presented in E. Few representative numerical cases are given in which the ratios of the constant hardening moduli to elastic stiffness are in a range of practical values. Furthermore, a numerical parametric study using LS-DYNA of the effect of strain-hardening on the residual response of thin plates is also given in E; in addition, the corresponding predictions by the present analytical model are compared to LS-DYNA results.

The experiments in Aune et al. (2016), Aune et al. (2017), Elveli et al. (2022), Spranghers et al. (2012b), and Spranghers et al. (2013), discussed earlier, can be used to quantify the effect of neglecting the work-hardening in the model as some uni-axial tensile specimens show a significant presence of strain-hardening.

Finally, it should be re-emphasised that values of the material parameters, except the static yield strength, used in the LS-DYNA simulations are assumed. The source papers reported neither the Johnson-Cook (JC) parameters nor re-usable stress-strain data to enable identifications of the constitutive plastic parameters. For example, Nurick et al. (1985) present the engineering stress-strain data at different strain rates. Using their data, it was attempted to obtain digitally converted true stress-strain curves and determine the material parameters by curve-fitting the data to JC model. However, this was not possible due to precision issues associated with the strain axis resolution. Thus, practical JC parameters (except the static yield strength) were adopted from Rigby et al. (2019a) and Curry (2017), as mentioned already. Curry point out that when quasi-static stress-strain data are fitted to JC model, the resulting static yield stress (A_{JC}) underestimates the value observed experimentally, due to the hardening power-law in JC model. Although, the used material parameters were found to give reasonable predictions when compared to the experiments. Example techniques to determine such parameters are explained by Spranghers et al. (2012a) and Curry (2017). Validated JC material parameters for commonly used ductile materials and their justifications can be found in Rigby et al. (2019a), Lomazzi et al. (2021), Spranghers et al. (2013), Aune et al. (2017), and Mehreganian et al. (2018b).

4.6.2 Circular Membrane

4.6.2.1 Results

In this section, we compare the predictions of the model for uniform specific impulse, as given by Eq. (4.5.9), to experimental data and numerical LS-DYNA predictions. Nurick et al. (1985), discussed in Section 4.6.1.1, also report experimental data for the permanent displacements of circular membranes of fixed diameters of 100 mm when subjected to uniform impulses of varying amplitudes. The membrane material properties and thickness are as described for the rectangular membrane, see Section 4.6.1.1. The data are compared to predictions from the model for the uniformly loaded circular membranes, Eq. (4.5.9). The characteristic yield strength σ_0 is taken as the static yield strength in Nurick et al. (1985). The results are shown in Fig. 4.7.

In addition, LS-DYNA was used to replicate the tests of Nurick et al. (1985) for the circular membrane case. Axi-symmetric conditions were assumed in the simulations, and hence the problems were solved using beam elements along the radial axis of the plates using `*Element_Beam` and `*Section_Beam` keywords with `Elform`=8 and 3 through-thickness integration points `IR/QR`=3. With this set-up, it is unnecessary to specify the conditions at the axis of symmetry. Because the axi-symmetric solver was utilised, the `*Mat_Modified_Johnson_Cook` model was used; it should be noted that the "modified" and "simplified" Johnson-Cook models differ in describing the strain-rate sensitivity. Again, applicable material parameters (except the static yield strength) were adopted from Rigby et al. (2019a) and Curry (2017). Motion is induced by a uniform initial velocity field calculated

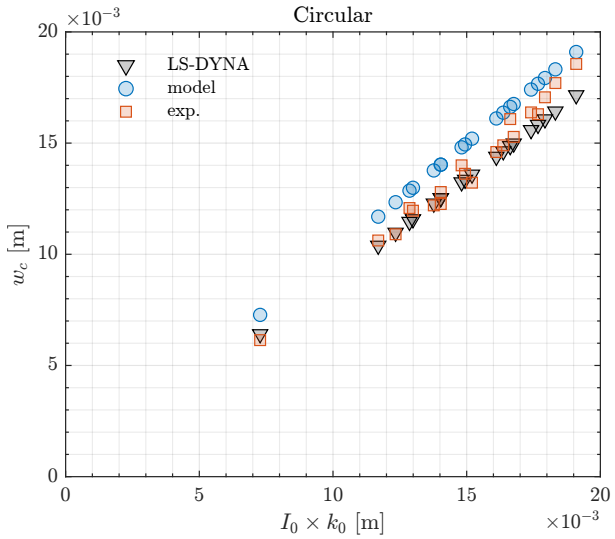

Fig. 4.7. Comparison of model predictions to experimental data (Nurick et al., 1985) and LS-DYNA results in terms of central residual displacement w_c of circular membranes under uniform impulse of total magnitude of I_0; k_0 is the circular structural parameter defined in Eq. (4.5.10).

from the uniform specific impulse. The periphery node was fully restrained. Finally, the central displacement was chosen to carry out mesh convergence study to determine the appropriate mesh density, which was then maintained throughout.

The finite element results for the permanent displacement are compared to the present analytical model and the experimental data of Nurick et al. (1985), as shown in Fig. 4.7.

Gharababaei and Darvizeh (2010) report results from 86 experiments on circular plates. The authors measured the central permanent displacements of steel, copper, and aluminium thin plates and the total impulses they were subjected to using a ballistic pendulum. All specimens had circular exposed areas with a fixed diameter of 100 mm. Among the experiments, 42 tests are assumed to generate spatially uniform specific impulse based on the following. The blast loads were generated by detonating thin (cylindrical) disks of C4 explosives located at a stand-off distance of 300 mm from the plates' centres for the 42 tests. The smallest scaled distance was Z=1.12 m/kg$^{1/3}$, and a 9.5° angle of incidence at the plates' periphery was held constant for the tests. Furthermore, the authors used a rigid circular tube of equal diameter as that of the specimens to guide the propagation of the shock waves along its axis. Further details can be found in the original paper.

The predictions from the present model, Eq. (4.5.9), and LS-DYNA simulations are compared to the experimental data of Gharababaei and Darvizeh. Again, the static yield strengths reported in experiments are taken as the characteristic yield strengths in the model calculations. The data for the aluminium plates were excluded due to numerical difficulties in simulating their behaviour as the material is not strain-rate sensitive, and there is no available material data given in Gharababaei and Darvizeh (2010) regarding its strain-hardening parameters. The results are given in Fig. 4.8.

As shown in Fig. 4.8, the model does not accurately predict the experimental outcomes

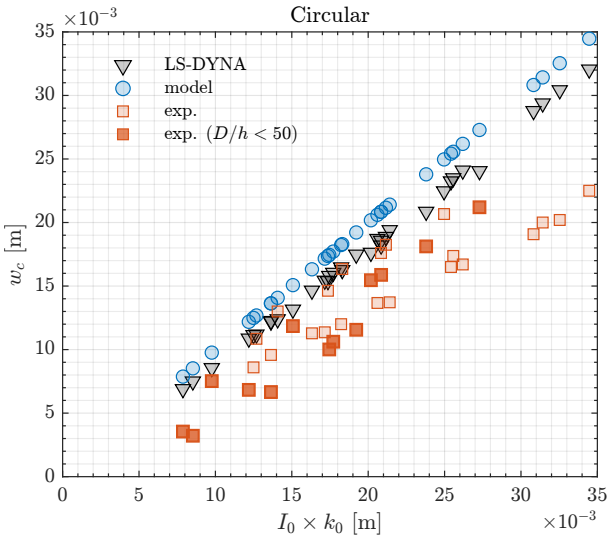

Fig. 4.8. Comparison of model predictions to experimental data (Gharababaei and Darvizeh, 2010) and LS-DYNA results in terms of central residual displacement w_c of circular membranes under uniform impulse. In Gharababaei and Darvizeh (2010), the total impulse I_0 was measured by ballistic pendulum; however, it was generated from thin disks of explosives with charge-to-target radius ratios of 0.2 and 0.30, but with a stand-off distance to plate's diameter ratio of 3.0. Experimental data for specimens with diameter-to-thickness ratio, (D/h), less than 50 are highlighted with filled red markers. k_0 is the circular structural parameter defined in Eq. (4.5.10).

of Gharababaei and Darvizeh (2010), in particular for $k_0 \times I_0$ larger than 0.03 m. The model overpredicts the permanent displacement by at most a factor of two.

Fig. 4.9 compares the model to data from LS-DYNA alone, which combines data already shown in Fig. 4.7 and Fig. 4.8. In the validation data in Fig 4.9, yield strength, plate thickness and density are variables in addition to the total impulse. As the model properly captures the trend of LS-DYNA predictions, it is concluded that the functional form of w_c in terms of these structural parameters is accurate.

Nurick et al. (1996) present additional 162 experiments on circular steel plates, of varying diameters, loaded with uniform impulses. All had 1.6 mm thickness and assumed density of 7850 kg/m^3. For plates with diameters 60, 80, 100, 120 mm, the corresponding static yield strengths were given as 251, 220, 270, 220 MPa, respectively. These specimens were clamped with sharp edges. Two additional sets of specimens with filleted clamping supports had diameters of 100 mm and yield strength of 251 MPa each. All data, including the total impulses and central residual displacements, are tabulated in Nurick et al. (1996), and further details can be found there. Their data, excluding five tests for which displacements are not reported, are used to verify the circular membrane solution, Eq. (4.5.9), as shown in Fig. 4.10.

So far, the experimental tests used for the validation involve limited ranges of plates' thickness. To further assess the performance of the model under combined variations of total impulse and plate thickness in broader ranges, the input data presented in Rigby et al. (2019a) was used in additional LS-DYNA simulations. The set-ups are similar to those described earlier. From a sample simulation run, the central displacement time history is

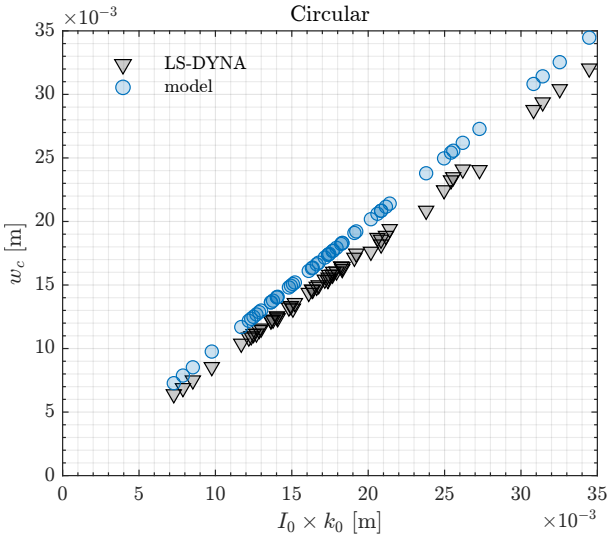

Fig. 4.9. Comparison of model predictions to results from LS-DYNA simulations corresponding to the experimental set-ups in Gharababaei and Darvizeh (2010) and Nurick et al. (1985) in terms of central residual displacement w_c of circular membranes under uniform impulse of total magnitude of I_0. Numerical material parameters (except the static yield strength) were taken from Rigby et al. (2019a) for the steel plates. Notice that LS-DYNA simulations account for elasticity, strain-hardening, strain-rate sensitivity, bending and shear effects, which the present analytical model completely ignores. k_0 is the circular structural parameter defined in Eq. (4.5.10).

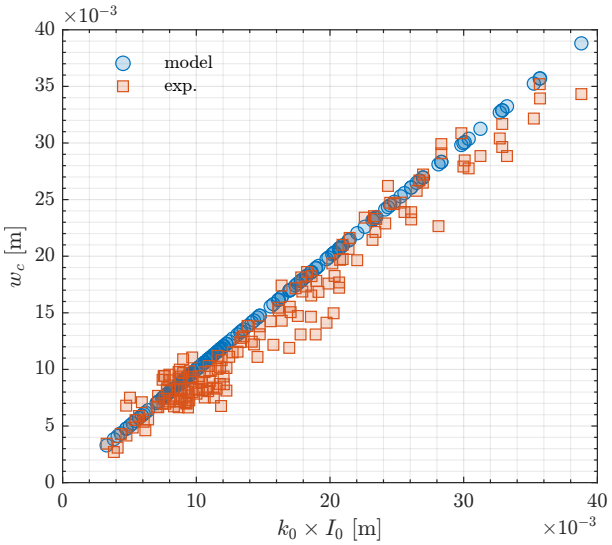

Fig. 4.10. Comparison of model predictions to experimental data (Nurick et al., 1996) in terms of central residual displacement w_c of circular membranes under uniform impulse of total magnitude of I_0. k_0 is the circular structural parameter defined in Eq. (4.5.10).

shown in Fig. 4.11. The results of the latter investigation are depicted in Fig. 4.12, which demonstrates the accuracy of the present model under varying plate thickness.

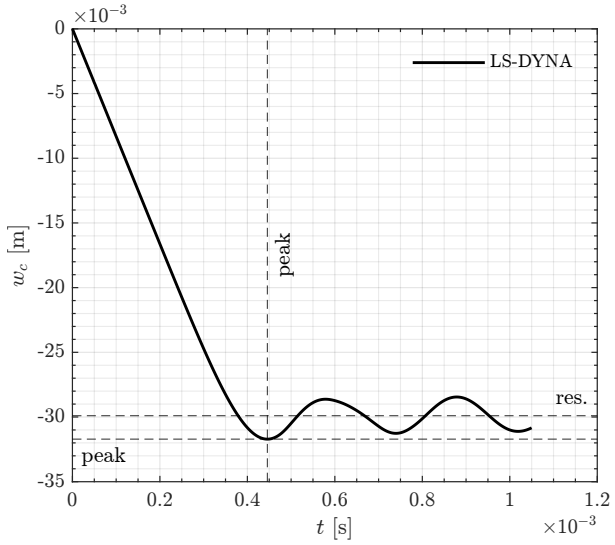

Fig. 4.11. Time history of the central displacement w_c from LS-DYNA simulation for a sample problem using input parameters given in Rigby et al. (2019a). Negative values on the ordinate y-axis correspond to downward displacements. It is seen that the resulting displacement is mainly plastic.

4.6.2.2 Discussion and Limitations

The discussion and limitations presented in Section 4.6.1.2 for the rectangular case are also applicable to the validation of the uniform circular model against the experiments of Nurick et al. (1985) and Nurick et al. (1996). In general, the model slightly deviates from the experimentally observed measurements.

However, there is a pronounced discrepancy when comparing the uniform model to Gharababaei and Darvizeh data. This required a reappraisal of the model, the input data, and the testing set-up to trace the source of discrepancy. As previously discussed, the authors used a rigid tube as a blast wave guide that (when combined with the moderate stand-off distance) could produce wave reflection effects due to the interaction near the tube's wall. However, the assumption of uniformity of the impulse is ruled out. If the resulting specific impulse was indeed non-uniform, then according to Rigby et al. (2019a) and Tyas and Pope (2003), the displacement would then be even larger than that induced by a uniform impulse.

Although the model is built to predict membrane behaviour of thin plates, it performs better for the relatively thicker plates in Gharababaei and Darvizeh (2010) than it does for specimens with diameter-to-thickness ratios greater than 50. This can be seen in Fig 4.8, in which the markers for thicker specimens are filled in red to highlight such observation. Furthermore, the trend of the experimental data deviates from the expected behaviour that moderately thicker plates are stiffer. This is because: (1) extra resisting modes are involved, i.e., bending and shear, that also contribute to absorb (or dissipate) the initial

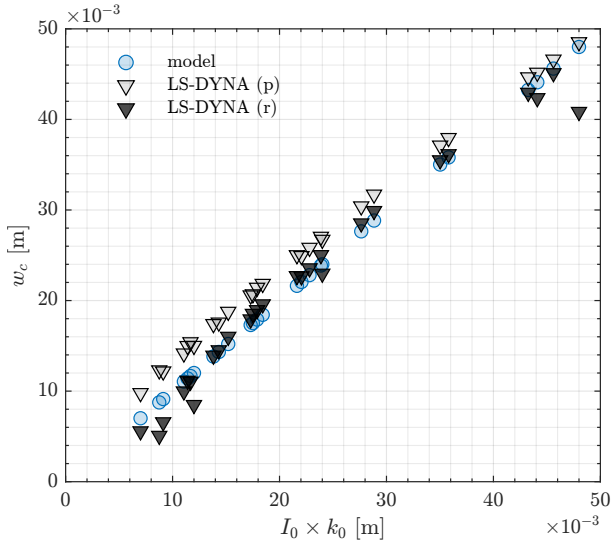

Fig. 4.12. Comparison of model predictions to LS-DYNA results in terms of central residual displacement w_c of circular membranes under uniform impulse of total magnitude of I_0. In the numerical simulations, input parameters were obtained from the parametric study in Rigby et al. (2019a) to investigate the model performance for a wide range of plate's thickness. Peak (p) and residual (r) displacements from LS-DYNA analyses are shown.

kinetic energy; and (2) due to increased mass per unit area, thicker plates attenuate the initial velocity generated by the (externally) imparted impulse according to Rigby et al. (2019a).

However, since an increase in the impulse leads to increase in initial velocity (for a given plate), the dynamic yield stress increases (due to strain-rate effects), which in turn would reduce the permanent displacement. Thus, the discrepancy between the model predictions and the experimental displacements for the range of larger impulses can be partly attributed to neglecting the strain-rate sensitivity of the yield strength and possibly, as discussed in Section 4.6.1.2, the work-hardening of the specimens (in particular made of copper).

Furthermore, similar to the discussion in Section 4.6.1.2, the authors in Gharababaei and Darvizeh (2010) measured the total impulse indirectly using a ballistic pendulum. Rigby et al. (2019b) pointed out that targets typically experience $\sim 67\%$ of the total impulses calculated from the ballistic pendulum measurements. Their conclusion can explain the observed discrepancy between the model predictions and Gharababaei and Darvizeh (2010) data.

4.6.3 Comparison of the Uniform Models to the Modified Nurick and Martin's Model

Yuen et al. (2016) proposed modifications to Nurick and Martin's (1989) model. In their model, the normalised permanent displacement (i.e., displacement-thickness ratio), w_c/h, of circular or rectangular thin plates with exposed areas A is linearly related to the non-

Table 4.2. Comparison of the present model against the modified Nurick and Martin's model proposed by Chung Kim Yuen et al. (2016)

	α		β	
Geometry:	Yuen et al.	Present	Yuen et al.	Present
Circular	0.241	0.281	0.298	0.0
Rectangular	0.253	$0.480 \times S_0(L_y/L_x)^{1/2}$	−0.158	0.0
Square	0.253	0.270	−0.158	0.0

dimensional impulse, $\hat{\phi}_0$,

$$\hat{\phi}_0 = \frac{I_0}{h^2\sqrt{\rho\sigma_0 A}},$$

by the following empirical relation,

$$\frac{w_c}{h} = \alpha\hat{\phi}_0 + \beta,$$

where α and β are correlation coefficients given in Chung Kim Yuen et al. (2016) and presented in Table 4.2 for convenience. Note that α (reported in Yuen et al. Chung Kim Yuen et al. (2016)) is divided herein by $\sqrt{\pi}$ and 2 for the circular and rectangular models, respectively, to unify the form of $\hat{\phi}_0$ for the two geometries, as given above.

Their empirical models were shown to reasonably predict the response of the thin plates compared to 699 (circular) and 356 (rectangular) experiments. Thus, it is of interest to compare the present model, developed herein, to their findings. For the present model, the corresponding coefficients α and β are obtained from the previously developed solutions (for the uniform impulse case) by rewriting them in terms of the normalised impulse, $\hat{\phi}_0$. The comparisons are summarised in Table 4.2.

While Yuen et al.'s α and β are identical for the rectangular and square plates, the present model's α depends on the aspect ratio, L_y/L_x, (the parameter S_0 also depends on the aspect ratio). The values $S_0 = 0.5627$ and $\sqrt{L_y/L_x} = 1$ were used to calculate α for the square geometry using the expression of α for the rectangular model, given in Table. 4.2. Note that β is zero for all cases of the membrane geometry in the present model.

Since the value of β from Yuen et al. is small and will be multiplied by the plate's thickness to give a fraction of w_c, β can be neglected for the present comparison. Overall, the present model overestimates the displacement by around $7 \backsim 17\%$ (based on α) compared to the predictions of Chung Kim Yuen et al. (2016).

From the comparisons of the present model against data from experiments and LS-DYNA simulations, presented in Sections 4.6.1.1 and 4.6.2.1, it is concluded in overall that the model is reasonably accurate in predicting the permanent displacements of rectangular and circular membranes under uniformly distributed specific impulses. The comparison of the uniform model to the already validated predictions of Nurick and Martin (1989a) and Chung Kim Yuen et al. (2016), presented in this section, also supports this conclusion.

4.7 Overall Limitations and the Theory Drawbacks

Despite the relative accuracy of the present model, it has several shortcomings.

First, during the development of the equation of motions, the membrane is assumed to be already yielding as long as there is motion. That is, there is no rigid body motion. The whole membrane experiences (non-uniformly) distributed plasticity.

Second, "plastic" motion is assumed to be initiated by initial velocity, which is directly given by the imposed specific impulse. Hence, the model cannot determine the amount of impulse to be elastically absorbed. Therefore, any amount of given impulse leads immediately to an onset of "plastic" deformation. The model indicates that kinetic energy is at maximum at the initial time state, which gradually and monotonically decays as plasticity evolves. The model assumes complete removal of the external load (that induced the specific impulse) before motion, and hence the decreasing rate of kinetic energy is identical to the increasing rate of plastic work; the time history of plastic work is of an inverted form of the kinetic energy history.

Third, the yield strength is independent of the evolution of the membrane's motion. That is, enhancement (or hardening) of the yield stress due to strain-hardening and/or strain-rate sensitivity are not (correctly) incorporated. This is due to the perfect plasticity assumption. Detailed discussion was given earlier in Section 4.6.1.2.

Fourth, the displacement components along the in-plane coordinates of the undeformed membrane are assumed negligible as compared to the out-of-plane component of displacement. In fact, the in-plane components are set identically to zero throughout. Hence, the longitudinal Green-Lagrange strains are merely due to the quadratic terms of the gradient of the out-of-plane displacement. This, in turn, leads to zero membrane strains at points where zero gradients occur, such as at the centre of a symmetrically loaded membrane. Experiments often show that this is not true; in fact, the peak membrane strains in uniformly and impulsively loaded membranes could be located near their central regions. Despite this shortcoming, the model can predict thinning (or necking) of the membrane near its restraints (i.e., where it is supported). This is directly due to the plastic incompressibility, which necessarily gives the transverse longitudinal strain as the negative of the sum of the other two longitudinal strains (which are always non-negative); thus, thickness shortens.

4.8 Summary and Conclusions

Analytical solutions were developed to predict the profile and peak permanent displacement of thin plates under impulsive blast loads. The plates' materials were assumed rigid-perfectly plastic, obeying von Mises's yield criterion, and their motions were initiated from the blast-induced specific impulse. This problem set-up led to a monotonic deformation path, which was exploited in deriving the governing equation of motion systematically through the application of the extended Hamilton's principle. The equations of motion

apply to thin plates deforming mainly in membrane modes and plastically. Although the obtained equations are general, solutions were given for two membrane geometries, rectangular and circular, by the modal decomposition technique. The modal decomposition was supplemented with sequential mode terminations, a strategy that is justified herein by Drucker's requirement of plastic work non-negativity.

The rectangular solution applies to any spatial distribution of specific impulses. A practical MATLAB code is proposed to efficiently compute the total modal impulses involved in the general solutions for non-uniform impulses. Moreover, a procedure to estimate the errors from truncating the infinite series in the solutions was discussed in connection to the concept of the upper bound kinetic energy of Rigby et al. (2019a) and Tyas and Pope (2003). The circular solution is restricted to axi-symmetric specific impulses.

However, it was possible to provide simple closed-form solutions for the case of uniform specific impulse. The uniform solutions of the rectangular and circular thin plates were verified against experimental data in the literature and results from LS-DYNA simulations performed by the authors.

The present models for the rectangular and circular membranes were shown to be reasonably accurate in comparison to the experimental and numerical results. It should be emphasised that the models account only for simplified idealisations: an *impulsive* blast load, a *rigid-perfectly plastic* material behaviour, and a *membrane* mode of deformation. As a result, the obtained models are believed to be (already validated) simple and fast-running tools. Thus, they can be used by structural blast engineers for probabilistic-based analyses. Although the analytical models were compared against cases with uniform imparted impulsive loads, the relations derived herein are of a general form and can readily model non-uniform impulsive loads. The validation of the main analytical model against the non-uniform impulse case will be covered in detail in the next chapter.

Chapter 5

Validation of the Non-Uniform Model

5.1 Background and Preamble

The equilibrium equation governing the response of a rigid-perfectly plastic membrane under impulsive loading, which is characterised by the specific impulse $i(x, y)$ distribution, was derived in Chapters 3 and 4 and given as

$$c_p^2 \left(\frac{\partial^2 w}{\partial x^2} + \frac{\partial^2 w}{\partial y^2} \right) = \ddot{w},$$

where c_p is the plastic wave speed that is defined by $c_p^2 = 2\sigma_0/(\sqrt{3}\rho)$, in which σ_0 is the uni-axial tensile yield stress of the membrane and ρ its mass density. As stated above, the motion of the membrane is assumed to be initiated by the specific impulse-induced initial velocity $\dot{w}_0$ according to Tyas and Pope (2003) and Rigby's et al. (2019) hypothesis

$$\dot{w}_0 = \frac{i}{\rho h},$$

where i is the specific impulse, and h is the membrane's thickness.

This equilibrium equation was derived on the assumption that the von Mises yield condition is satisfied whenever the membrane undergoes active straining, i.e., when it is under progressive yielding. This is because the stress state satisfies the yield condition only when the (plastic) strain rate is non-zero. When this condition is violated, then the equation of motion given above becomes not applicable. Thus, the solution (that solves the above equation of motion) must be terminated as soon as the instantaneous strain rates tend to reverse in sign. This latter condition is equivalent to the instant of time when the total strain starts to decrease. This is a requirement to avoid the occurrence of a negative rate of plastic work as this would lead to a reduction in the total "plastic" work in the absence of work done by external forces. Now, since the membrane is assumed to be loaded

impulsively (i.e., external forces are absent), the reduction of total plastic work can be prevented by stopping the solution when the kinetic energy attains a zero value for the first time (after being non-zero initially).

In solving the membrane response under uniform specific impulse (in Chapter 4), a strategy was proposed to define the instant of time when the solution should be terminated. The strategy was to terminate every mode in an independent manner based on the velocities of the individual modes; the velocity was chosen since the kinetic energy is the criterion for terminating the solution. This was described as a sequential mode termination strategy, and its basis was the orthogonality of the modes with respect to each other, as the modes are mutually independent as already known. It is a sequential process since the times for zero modal velocities differ from mode to mode based on the modal frequencies, and these frequencies are monotonically increasing as the mode number increases. The termination sequence follows a descending order of the mode numbers. It was shown, (in Chapter 4), that the strategy leads to very accurate predictions for membranes under uniform specific impulses when the model (that incorporates such termination strategy) was validated against experiments and detailed LS-DYNA analyses, Section 4.6.

However, when the general case of non-uniform specific impulse was considered, it was found that the model overpredicts the membrane's displacement when compared to LS-DYNA predictions of similar problems. In the LS-DYNA simulations, the membrane was loaded by non-uniform specific impulses, which were obtained from earlier MM-ALE explosive simulations. It should be kept in mind that non-uniform impulses are, in practice, typically associated with extremely high amplitudes in highly localised regions. Hence, initially it was thought that the model overestimates the structural response (compared to LS-DYNA) due to the neglect of the material's strain-rate sensitivity (which is incorporated in the LS-DYNA structural analyses) as the model is limited to a perfectly plastic behaviour. Nevertheless, the model was seen to account for significant structural parameters correctly according to the functional form of the model.

On the other hand, it was observed that the model accuracy can be substantially improved by introducing another strategy to terminate the solution that is predicted by the model. The new strategy defines the critical time instant, at which the solution is terminated, to be the one when the total velocity (the sum of all active, or dominant, modes) reaches zero after being non-zero initially; this means that the solution is terminated at a specified time for all modes instead of multiple times for each mode independently. Using this new strategy, the model is found to give consistent and reasonably accurate predictions when compared to experiments and LS-DYNA simulations when the specific impulse distribution is non-uniform.

The present chapter aims to provide results of validating the membrane model (using the new solution termination strategy) for the case of membranes under non-uniform specific impulses when the model is compared to LS-DYNA simulations and the experiments of Curry and Langdon (2017). The content of the following sections was written to be a standalone manuscript for publication in the near future.

5.2 Introduction

In Chapter 4, the rigid-perfectly plastic membrane solution of a thin plate response is given as a function of the blast-induced specific impulse, and use has been made of a sequential mode termination strategy to obtain a closed-form model that was validated against uniform impulse experiments and LS-DYNA results. However, validation of the model against non-uniform impulse data was not given. The following work aims to provide such validation.

Preliminary investigation indicated that the solution based on the sequential modal termination approach overestimates the displacements when compared to the validation data (to be discussed in the next sections) from experiments and LS-DYNA simulations for the non-uniform specific impulse case. Thus, the general solutions given in Sections 4.4-4.5, i.e., in their temporal forms, are adopted without switching the modes off. Herein, the plastic-work non-negativity is enforced on the total velocity (i.e., the sum of significant modes) rather than on the individual modal velocities in an independent manner.

For example, the displacement response of a rectangular target, which is of length L_x, width L_y, thickness h, density ρ, and characteristic yield strength σ_0, and subjected to non-uniform specific impulse $i(x,y)$, was given in Section 4.4 by

$$w(x,y,t) = \frac{4}{h\rho c_p L_x L_y} \sum_m \sum_n B_{mn}(x,y) \sin(\omega_{mn} t), \tag{5.2.1}$$

where

$$B_{mn}(x,y) = \frac{I_{mn}\phi_{mn}(x,y)}{\omega_{mn}},$$

$$I_{mn} = \int_0^{L_y} \int_0^{L_x} i(x,y)\phi_{mn}(x,y)\, dx\, dy,$$

and $\phi_{mn}(x,y)$ and ω_{mn} are the (spatial) modal shape and frequency of the $(m,n)^{\text{th}}$ mode, and $c_p = \sqrt{(2\sigma_0)/(\sqrt{3}\rho)}$ is the wave speed. The expressions for all variables are as given in Section 4.4.

It is considered herein that the above solution, Eq. (5.2.1), is valid up to the instant of time when the total velocity reaches zero for the first time. In particular, the solution $w(x,y,t)$ at a given spatial coordinate (x,y) is terminated whenever the total velocity $\dot{w}(x,y,t)$ reaches zero for the first time, and the velocity is held at zero thereafter. In this manner, the kinetic energy can only decrease, and hence the plastic work will be monotonically increasing. Therefore, the deformation path is, thus, monotonic as assumed in deriving the general equation of motion (whose solution is given above for a rectangular membrane).

It is instructive to note that in Section 4.4, the temporal term, $\sin(\omega_{mn} t)$, was ultimately replaced with a value of unity due to the sequential mode termination strategy, which will not be adopted herein as discussed above. Similar modifications will be applied to the

solution of circular membranes.

For the sake of definiteness, the present model is exactly the model proposed in Chapter 4 except that the strategy to terminate the modal solution is modified to be based on the total velocity rather than on the individual modes separately.

In the next sections, the central residual displacements, w_c, are reported as functions of the energy-equivalent total impulse, I_k, due to Rigby et al. (2019), which is defined as

$$I_k = \sqrt{A \int_A i^2(x, y)\, dA}$$

in which, A is the exposed area of the membrane. The energy-equivalent total impulse, I_k, is found by Rigby et al. (2019) to be the significant loading parameter in the response of thin plates under non-uniform specific impulse. In the present model, I_k appears to be significant as well according to the well-known important property of Fourier's decomposed solutions (see Appendix C for details), which, for a rectangular membrane problem, takes the form

$$\sum_{m=1}^{\infty} \sum_{n=1}^{\infty} I_{mn}^2 = \left(\frac{I_k}{2} \right)^2,$$

which states that the sum of the squares of the total modal impulses, I_{mn}, is the square of one-half the energy-equivalent total impulse. This also states that $I_k/2$ is the upper bound of the sum of the modal components of the specific impulse that directly influences the response of the membrane.

5.3 Description of LS-DYNA Models

5.3.1 MM-ALE Set-Up

Following the approach in Rigby et al. (2018), the Multi-Material Arbitrary Lagrangian-Eulerian (MM-ALE) technique, available in LS-DYNA, is used to simulate the air-blast event and calculate the generated reflected pressures and the corresponding specific impulses which a nearby target experiences. An overview of the ALE method will be discussed in Section 5.3.3. Throughout, axi-symmetric conditions and a perfectly rigid target are utilised to reduce computational times. Spherical and cylindrical shapes of the high explosive (HE) charge are considered, and the explosive is assumed as PE4 (Plastic Explosive, Composition 4).

The HE is modelled using the `*Mat_High_Explosive_Burn` material and the `*Eos_Jwl` equation of state (EOS). The detonation of the HE was triggered using the `*Initial_Detonation` keyword. The surrounding medium, which is taken as air, is treated as an ideal gas of a specific heat ratio of 1.4 and modelled with the `*Mat_Null` and `*Eos_Linear_Polynomial` models. The material and EOS parameters for the PE4 explosive and air are taken from Rigby et al. (2019) and Curry (2017). The material models for the air and HE will be

described in Section 5.3.4. The domain is represented with `*Section_ALE2D` and `*Element_Shell`, and the `*Initial_Volume_Fraction_Geometry` keyword was utilised to specify the domain's initial configuration such that it is initially filled with air and the HE is confined in a spherical or cylindrical container representing the physical charge. The ALE reference mesh is allowed to shrink (in a Lagrangian manner) near the blast wave's front (by setting `Prtyp=8` and `Efac=0.1` in `*ALE_Reference_System_Group`), and the second-order accurate `van Leer+HIS` advection logic was chosen, in `*Control_ALE`, with one advection cycle (`Nadv=1`) per one (Lagrangian) time step and without smoothing.

In LS-DYNA, there are three methods to set the interaction between ALE fluids and a rigid body. The first two require explicit modelling of the rigid body's geometry (i.e., using a unique part, section, and `*Mat_Rigid` keywords), and its interaction with the ALE fluids is then modelled using either `*Constrained_Lagrange_In_Solid` or `*ALE_Coupling_Rigid_Body`. However, we adopted the third (simplest) method that does not require an explicit presence of the rigid body. That is, the rigid target was modelled using the `*Rigidwall_Planar` keyword that automatically creates the rigid wall, constrains its motion, and prevents penetration by the surrounding entities (i.e., air and detonation products). The domain boundaries, except the axis of symmetry, are treated as transmitting (using `*Boundary_Non_Reflecting_2D`). The domain extents were deliberately enlarged to provide additional offsets from the nearest transmitting boundaries in order to reduce unwanted boundary effects.

The `*Database_Sensor` keyword is used to define the positions of adequately spaced pressure sensors, which were placed slightly off the rigid wall and towards the blast source's side. The output of these sensors is requested using the `*Database_Trhist` keyword. When the blast simulations were completed, LS-DYNA data were read in Matalb using a user function developed by the author, described in Appendix F and to be published. The overpressure data were subsequently time-integrated to obtain the specific impulses.

The results from a preliminary study to validate the specific impulse predictions using the MM-ALE method in LS-DYNA are shown in Fig. 5.1. In this figure, the specific impulse due to a spherical PE4 charge of mass 100 [g] and at clear stand-off distance of 44.5 [mm] is compared to the corresponding experimental values measured by Rigby et al. (2019).

5.3.2 Lagrangian Only Set-Up

The structural response of the target is modelled using the pure-Lagrangian approach, in which the target is explicitly modelled as a deformable plate that is subjected to blast load in the form of a specific impulse-induced initial velocity. That is, the plate's motion is driven by the prescribed initial velocity without any externally applied pressures. The specific impulse is obtained from the post-processed results of the previous MM-ALE simulations as discussed in the previous section. The specific impulse i is converted into initial velocity profile $\dot{w}_0$ according to Rigby et al. (2019) and Tyas and Pope (2003) models, i.e., $\dot{w}_0 = i/(\rho h)$, where ρ and h are the plate's density and thickness.

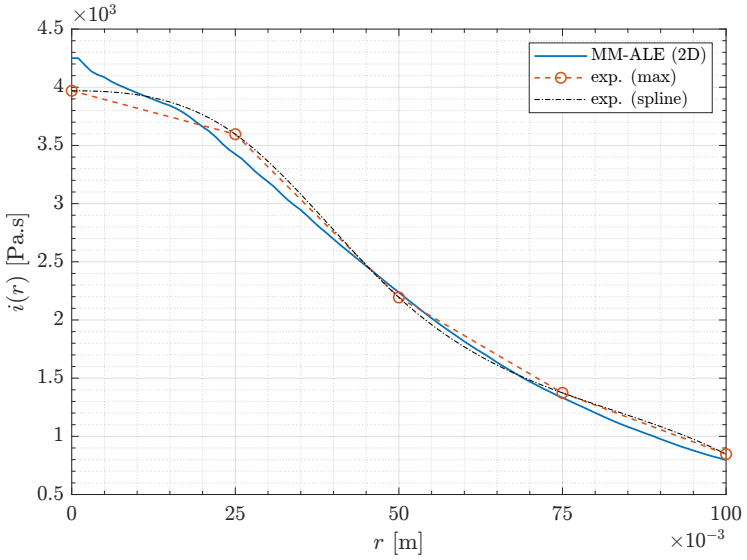

Fig. 5.1. Validation results for the prediction of specific impulse distribution, $i(r)$, using the MM-ALE method in LS-DYNA for a spherical PE4 charge of mass 100 [g] and clear stand-off distance of 55.4 [mm]. The numerical specific impulse (MM-ALE (2D)) is compared to the experimentally measured specific impulse by Rigby et al. (2019). The dashed red line (exp. (max)) connects the maximum experimental data, shown as circular markers, reported in Rigby et al. (2019b). The (exp. (spline)) line is constructed for splined smooth experimental distribution of specific impulse which is constrained to have a zero slope at the membrane's centre, $r = 0$.

Rectangular and circular plate geometries were considered. In the rectangular model, the plate is represented by `*Element_Shell` and `*Section_Shell` with five through-thickness integration points, fully-integrated shell formulation (`Elform = 16`), and the commonly suggested transverse shear factor (`Shrf=5/6`). The nodes on the outer sides of the plate are restrained in all translational and rotational degrees of freedom. The used element formulation is based on the constant transverse shear shell theory, i.e., an extension of the Mindlin plate to include membrane effects; the shear factor scales the traverse shear stresses.

The circular model is considered as axi-symmetric, in which the plate is modelled using `*Element_Beam` and `*Section_Beam` with five through-thickness integration points, `Elform=8`, and default shear factor. The periphery node is fully clamped.

In both models, the plate's material is assumed as Domex-355 steel and described using the `*Mat_Modified_Johnson_Cook` (JC) material model, in which the supplemented material parameters are taken from Curry (2017); the JC model will be described in Section 5.3.4. The rectangular plates had equal sides of length 260 mm, and the diameter of the circular plates is taken as 300 mm. For both models, the plate's thickness is 3 mm.

A preliminary mesh sensitivity study, see Fig. 5.2, was performed for the rectangular plates to determine the appropriate mesh, which was then held fixed in subsequent analyses, and the peak displacement at the plate's centre was chosen as the basis of convergence, Fig. 5.2(c).

The global mechanical energies and all nodal displacements were requested in binary

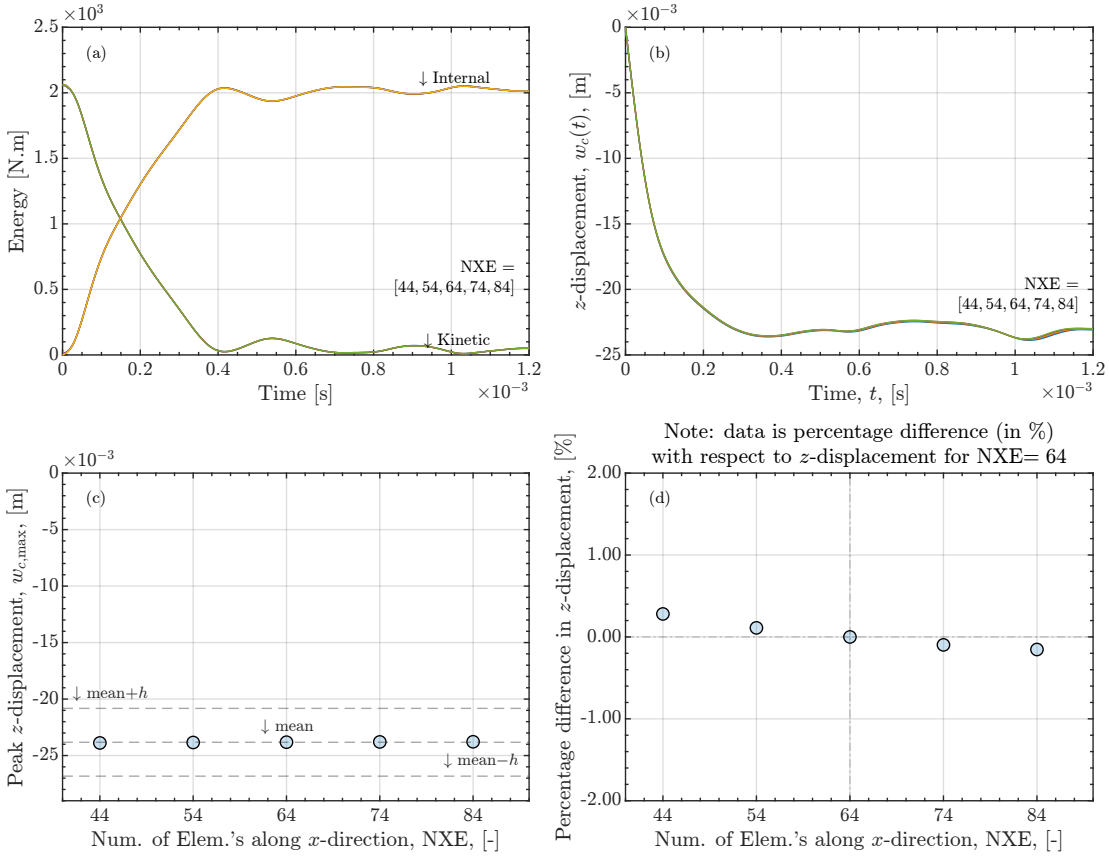

Fig. 5.2. Preliminary mesh convergence analysis for a rectangular membrane problem. A mesh of 64 elements along each direction was chosen based on this analysis. In the two sub-plots at the top, (the time-history) results from all meshes are plotted together, i.e., there are multiple curves and each curve corresponds to one mesh density; some curves are less visible as they are almost identical. In (a), the total kinetic and internal energies are plotted. In (b), the time-history of the transverse displacements at the plate's centre are shown. In (c) and (d), the peak central displacements versus the mesh density, in terms of the number of elements along the x-direction (NXE), are provided; h is the plate's thickness. It is seen that all results are practically identical, and the mesh with NXE = 64 provides the desired convergence. The plate is loaded impulsively by a specific impulse generated by a spherical PE4 explosive charge of mass 50 [g] and clear stand-off of 25 [mm].

format using the `*Database_Glstat` and `*Database_Nodout` keywords. Again, LS-DYNA data were subsequently post-processed in MATALB, after they were read by the MATALB function described in Appendix F. The residual displacements at the plates' centres were calculated by averaging the transient displacement histories over one-half cycles beyond the first peak occurrences. That is, the residual displacement $w_{c,r}$ is defined as

$$w_{c,r} = \frac{1}{t_2 - t_{max}} \int_{t_{max}}^{t_2} w_c(t)\ dt,$$

where t_{max} is the first peak time, i.e., at which the peak central displacement, $w_{c,max}$, is attained, and t_2 is a subsequent time instant at which the velocity is zero for the first time, i.e., $\dot{w}_c(t = t_2) = 0$ where $t_2 > t_{max}$. Note that, by definition, we also have $\dot{w}_{c,max} = 0$.

Additionally, stresses and effective plastic strains in all elements were requested by the `*Database_Elout` keyword. The time histories of von Mises stresses, σ_{vm}, (computed in MATALB) and of the (von Mises) effective plastic strains, $\varepsilon^p_{\text{vm}}$, were used to produce the corresponding stress-strain curves. These are defined as

$$\sigma_{\text{vm}} = \sigma_{\text{eff}} = \sqrt{3/2}\sqrt{s_{ij}s_{ij}},$$

$$\varepsilon_{\text{vm}} = \varepsilon_{\text{eff}} = \sqrt{2/3}\sqrt{\varepsilon^p_{ij}\varepsilon^p_{ij}},$$

where s_{ij} is the deviatoric stress and given by $s_{ij} = \sigma_{ij} - \hat{p}\delta_{ij}$, in which $\hat{p}$ is the hydrostatic pressure (positive in tension), and ε^p_{ij} is the total plastic strain. Note that σ_{vm}, in general, does not need to be at the yielding point. The effective plastic strain rate is $\dot{\varepsilon}^p_{\text{eff}} = \dot{\varepsilon}^p_{\text{vm}}$. Note that the rate of plastic work (per unit volume) at a given time t is $\sigma_{ij}\dot{\varepsilon}^p_{ij} \equiv s_{ij}\dot{\varepsilon}^p_{ij} = \sigma_{\text{vm}}\dot{\varepsilon}_{\text{vm}}$, and the total plastic work is $\int_0^t \sigma_{\text{vm}}\dot{\varepsilon}_{\text{vm}}\ dt$.

This was done to better observe the combined effects of strain-hardening and strain-rate sensitivity on the current yield stresses, which are incorporated in LS-DYNA analyses through the JC model. The average von Mises stresses for each element are calculated (using the above curves) as the characteristic yield stress parameter, and using which a 2D fringe plot is produced over the plate's area, to additionally study the effect of the specific impulse profile on the spatial distribution of plastic work (i.e., how the input kinetic energy has been absorbed internally).

5.3.3 Summary of the ALE Method

As mentioned in the previous subsections, the explosive analyses to simulate the blast event utilise the Multi-Material Arbitrary Lagrangian-Eulerian (MM-ALE) formulation. The high explosive (HE) charge is initially modelled as a solid placed in a volume that is assumed to be air (gas) at ambient conditions. Upon detonation (of the HE), the charge

gradually is converted to hot gases (the detonation products), and when this very rapid process is completed, the domain becomes entirely composed of two interacting gaseous materials (air and the detonation products). Therefore, since these are fluids, and hence their (subsequent) deformations and distortions are substantially large, the appropriate kinematic description is the Eulerian instead of the Lagrangian description.

However, the present problem involves (i) development of shock waves, (ii) interaction of more than one fluid where each fluid has its unique material interface, and (iii) possible presence of Lagrangian solid structures with which the fluids can interact. Thus, use will be made of the Arbitrary Lagrangian-Eulerian formulation instead of the purely Eulerian one.

Using the Lagrangian description, the mesh exactly follows the material, and hence the relative velocity of a material particle to mesh is zero; therefore, there are no convection terms. Note that the mesh motion is not arbitrary as it is exactly the material motion. In the Eulerian description, the mesh is fixed in space, and the material flows with respect to this fixed mesh; thus the relative velocity of a material particle (with respect to the mesh) is the absolute material velocity. Note that mesh motion is not arbitrary as it is not moving at all. However, in the ALE description, the mesh is allowed to move arbitrarily, and its motion is not entirely fixed in space nor follows the material's motion exactly. In this ALE description, the relative velocity of a material particle (with respect to the mesh) is the difference between the velocity of the material particle and the local velocity of the mesh. In both purely Eulerian and ALE formulations, convective terms appear and should be accounted for due to the (generally non-zero) relative velocity of a material point with respect to the corresponding mesh; again, this relative velocity is exactly the material particle's velocity for the Eulerian mesh, while it is the difference between the material particle velocity and the local mesh velocity for the ALE mesh. Therefore, the ALE generalises the description of motion from which the purely Eulerian or purely Lagrangian can be retrieved.

All conservation laws (mass, momentum, and energy) involve the material time derivatives in both the local (differential) and global (integral) forms. The material time derivative depends on the formulation being used to describe the motion. To illustrate the idea, consider a scalar quantity $\phi(x,t)$. The time derivative of ϕ is given as

$$\dot{\phi}(x,t) = \frac{\partial \phi}{\partial t} + c\frac{\partial \phi}{\partial x}$$

in which the second term is the convective term, and c is the velocity of the material particle relative to the mesh; that is,

$$c = v - \hat{v},$$

where v is the material particle's velocity and $\hat{v}$ is the velocity of the mesh. Note that when $v = \hat{v}$ (and hence $c \equiv 0$) corresponds to the purely Lagrangian description since the mesh

is adhered to the material (i.e., a mesh point is made identical to the material point itself). On the other hand, if $\hat{v} = 0$ (and hence $c = v$), the purely Eulerian description is obtained since the mesh is held stationary and fixed. The mesh is made to move arbitrarily in the ALE description, and hence $\hat{v}$ is arbitrary, and associated with such arbitrary motion is the arbitrary relative velocity c.

If the quantity $\phi(x,t)$ is to be conserved over time-changing volume, then we require that $\frac{\partial}{\partial t}\int_V \phi(x,t)\ dv = 0$,

$$0 = \frac{\partial}{\partial t}\int_V \phi(x,t)\ dv = \int_V \dot{\phi} + \phi\frac{\partial v}{\partial x}dv,$$

by Reynold's transport theorem. Thus, substituting for $\dot{\phi}$ by the given-earlier expression, the ALE statement of the conservation of ϕ takes the form

$$\int_V \frac{\partial \phi}{\partial t} + c\frac{\partial \phi}{\partial x} + \phi\frac{\partial v}{\partial x}dv = 0$$

which, since the above holds for any volume V and thus the integrand itself must vanish, is equivalent to the following differential form

$$\frac{\partial \phi}{\partial t} + c\frac{\partial \phi}{\partial x} + \phi\frac{\partial v}{\partial x} = 0$$

The mass conservation (or the continuity) equation, as an example, is obtained by replacing ϕ with the density ρ, that is, $\left(\frac{\partial \rho}{\partial t} + c\frac{\partial \rho}{\partial x} + \rho\frac{\partial v}{\partial x} = 0\right)$. This differential (strong form) equation is then converted into a weighted integral (weak form) equation, which then is discretised using the ALE mesh, associated with which is the convective velocity c. Unlike purely Lagrangian procedures, in which the Galerkin method is used, in the ALE weak form development, typically, the Petrov-Galerkin method is adopted, where the test (virtual variable) and trial (approximation of an actual variable) are different. This latter method has been proven to be stable and adequate to model advection (or convection) phenomena, e.g., as when motion is described by an ALE or purely Eulerian descriptions (as convective terms appear naturally) (Belytschko et al., 2014, Chapter 7).

For all other conservation equations (i.e., momentum and energy), the ALE differential equations can be readily obtained from the corresponding purely Eulerian counterparts by merely replacing all material time derivatives with the ALE material time derivatives as given above for the quantity ϕ which involves the relative convective velocity c. However, it should be noted that the partial time derivatives (i.e., the ones denoted above by $\frac{\partial}{\partial t}$) in the ALE description need to be performed while holding a given ALE coordinate fixed instead of holding the Eulerian coordinate fixed.

For non-zero c (i.e., $v \neq \hat{v}$), convective effects are present and must be accounted for. Since there is a relative motion between the material and the mesh, the material movement is accompanied by transport of physical variables from one element (in the mesh) to an adjacent element. In other words, across an interface joining two elements, the flow of

physical parameters occurs. Such flows must be taken into account in order to correctly guarantee the satisfaction of conservation laws, which require the conservation of the fundamental quantities (i.e., mass, momentum, and energy), in the problem.

Note that the arbitrariness of the mesh motion in the ALE description does not mean that its motion is unknown but rather is controlled such that the individual advantages of the purely Lagrangian and purely Eulerian approaches are combined to obtain a mesh that suits a given problem. In the implementation of the ALE formulation in LS-DYNA, the mesh is made to first follow the material as if it were purely Lagrangian. Typically, this is done for some small number of consecutive time steps. Thus, the mesh will distort as the material deforms. Then, to avoid further unwanted distortion of the so far distorted mesh, the mesh is adjusted by relocating the nodes (to relieve or eliminate the distortion), which is the process where the mesh moves relative to the material. Such relocation of the nodes can be (but is not required to be) optimised by implementing some smoothing procedures (e.g., by averaging a node coordinates based on the coordinates of the neighbouring nodes); in essence, this can be viewed as local and light re-meshing. Now, since there is a relative motion (with or without smoothing) between the material and the mesh, a required step needs to be done next; this is called the advection step since physical quantities are being transported from element to adjacent element and from nodes to neighbouring nodes as the mesh is being moved relative to the material; for this reason, the advection step is also called a re-mapping step as the values of physical quantities in an element (before the mesh motion) are mapped to set of elements that will occupy that element's position (after mesh motion). Note that in the definition of the ALE description, we stated that the material moves with respect to the mesh; however, in the above discussion of ALE implementation, the opposite process is what happens where the mesh initially follows the material and then subsequently the mesh moves (or detaches) from the material. The numerical scheme in which the overall (ALE) computation is subdivided into a first purely Lagrangian step and a subsequent advection (re-mapping) step is known as the operator split technique. Note that all physical time stepping are performed in the first Lagrangian step, whereas the advection/re-mapping is purely computational (the physical time is held fixed during such latter step).

Therefore, in summary, the computation using the ALE formulation consists of three steps: first, a purely Lagrangian step in which the mesh and material move together; then, the independent motion of the mesh relative to the material (with or without smoothing); finally, applying the advection algorithm to account for the relative motion of the mesh and the material. Again, the first step may actually consist of multiple purely Lagrangian increments, say three time increments, before the second and last steps are invoked.

The advection step is critical and generally expensive. There are several advection algorithms available in LS-DYNA, among which is the van Leer algorithm in combination with the half-index shift (HIS) method (Hallquist, 2006). The van Leer-HIS method is second-order accurate (as long as the elements are not heavily distorted) and capable of ensuring monotonicity and conservation of the parameters being advected (transported).

The HIS method is used as a practical treatment of parameters that are defined at nodes (e.g., velocity) rather than at an element's integration points (e.g., stresses, internal energy, etc) so that the nodal variables can be advected (using the van Leer method) as element-based variables. The accuracy of advection algorithms depends significantly on the amount of material being advected (or swept during the movement of the mesh relative to the material). For this reason, the ALE formulation becomes very superior to the purely Eulerian formulation since the ALE mesh is (in part) moving with the material and its re-positioning does not need to exactly bring the elements back to their initial location, and hence there is less material transported in comparison to the fixed purely Eulerian mesh.

The advection algorithm is said to be conservative if it ensures the conservation of an advected parameter, say ϕ, in the sense that $\int_V \phi_{\text{after}}\, dv = \int_V \phi_{\text{before}}\, dv$, where the field of ϕ before and after the advection step is denoted by ϕ_{before} and ϕ_{before} respectively. The requirement of monotonicity ensures that during the advection, the values of the various physical quantities (e.g., density and/or energy) do not fall outside permissible ranges (e.g., occurrence of negative density which is not physical) since the local values will change by such advection process. Achievement of monotonicity and second-order accuracy requires additional iterative computations and verifications where the iterations can be thought of to take place over artificial time. Thus, the performing of this required step increases the computational cost. Therefore, it is typically practical to make the mesh follow the material for several physical time steps before the independent mesh motion and advection steps are applied. In other words, the computations are kept Lagrangian until there is a need or necessity to move the mesh (alone without the material) and hence do the advection step.

In comparison to purely Eulerian formulation, the ALE description better suits explosive simulations for the following reasons

- The boundaries of the fluid can be made purely Lagrangian, i.e., the mesh nodes on the boundary follow (or deform) with the material. This permits proper specification of boundary conditions;
- The fluid particles in the vicinity of solid structures (rigid or deformable) can be made purely Lagrangian so that the fluid-structure interaction (FSI) can be modelled more accurately.
- When a shock wave develops, the area of the fluid under shock, can be represented as nearly Lagrangian. So, the very thin nature of the shock front can be modelled as the elements are allowed to be heavily compressed (i.e., shrunk) and hence making nodes dense around such zone and facilitating the capture of steep gradients of some important physical variables (e.g., the pressure); across the thin layer (front), jumps in the properties can then be simulated.
- Elements can accommodate more than one physical material and their interfaces can

be tracked more better.

- Adverse (unwanted) effects associated with the advection process can be minimised due to the motion of the mesh (since less material is being transported per one advection cycle).
- Account of material's path dependence is improved due to the following of the mesh to the material because of the partly Lagrangian nature of the mesh (Lagrangian elements store all needed information about the history of the material).
- The initial mesh does not need to be oversized to account for future (unknown) movement of the exterior fluid materials (i.e., to avoid complexities arising from the possibility that the material out-flows from the initial domain without a priori specification of the required boundary conditions). If the material tends to move outside the boundaries of the initial domain, those domain boundaries can themselves be made moving (i.e., in a Lagrangian way).

On the other hand, in comparison to purely Lagrangian description, The ALE mesh is significantly less affected by the large distortion (deformation) of the material as the essence of making the mesh in part independent of the material means that the mesh can be regularised (healed) at any point during the simulation; moreover, such partial or total mesh's re-construction can be optimised when smoothing is performed. Accumulated mesh distortion after several pure Lagrangian increments can be judicially removed or alleviated to some extent, especially in most of the computational domain where the nearly Lagrangian behaviour is not needed. Hence, the restrictions imposed on the critical time step (associated with very small element sizes) are alleviated in the majority of the domain; also, the accuracy of the solution is improved due to the healing of the mesh distortions. Furthermore, an ALE mesh is less prone to unwanted hour-glassing effects since the hour-glassing mechanism can be prevented by healing the mesh. This additionally suggests that lower hourglass coefficients should be used to avoid applications of unnecessary forces to counter-act against hour-glassing modes; note that these forces can be very detrimental, especially if they are not needed at all. It should be noted that the ALE is not limited to fluid-like materials, and indeed it is an attractive formulation to model solids undergoing large deformations, i.e., where the limitations of purely Lagrangian formulation prohibit accurate modelling.

Further discussions on the underlying theory of the ALE technique and its practical aspects can be found in Belytschko et al. (2014), Rigby (2014), Curry (2017), and Livermore Software Technology Corporation (2019), from which the foregoing material are taken, and additional references are available in Donea et al. (2004).

In LS-DYNA, the ALE mesh will be purely Eulerian *unless* an important command is invoked; this is the ALE reference system group, namely the `*ALE_Reference_System_Group`. In this command, some important parameters concerning explosive simulations are: `Prtyp` which when set to 8 allows the ALE mesh to distort near the shock wave's front, and

Efac which ranges from 0 (corresponding to purely Lagrangian) to 1 (purely Eulerian); the mesh tends to more resemble a Lagrangian motion (and hence distort) when Efac gets smaller. In this study, we set Prtyp=8 and Efac=0.1. According to LS-DYNA user's manual, as the shock front moves away from an element, the element tends to behave in an Eulerian way as time progresses, but the element was nearly Lagrangian when it was in the shock zone. Also, using this ALE reference system command, the initial ALE mesh is set by identifying the part (or part set) IDs associated with which a usual finite element mesh (elements, nodes, sections) is assigned.

LS-DYNA lumps most of the controls that affect the ALE implementation in another important command, which is the *Control_ALE. Among the very many parameters available through this keyword are: Meth to specify the advection algorithm, Nadv to set the number of (Lagrangian) calculation cycles before one advection step is performed. In this present explosive simulations, Meth =2 (or -2) for the van Leer-HIS with monotonicity being strongly enforced (or relaxed, when -2 is used), and Nadv=[1-3] to speed up the calculations (when it is greater than 1) but without increasing the amount of material being advected (as the values are not far from 1).

The blast simulations considered in the present study are axi-symmetric. That is, the domain is two-dimensional (2D), and the ALE mesh is modelled using Element_Shell and using the special command *Section_ALE2D, with ALEform=11 (for MM-ALE formulation) and Elform=14 (for axi-symmetric solid formulation). Furthermore, the practical keyword *Initial_Volume_Fraction_Geometry was utilised in all the simulations to facilitate the specifications of the initial configurations of the different (air and HE) ALE materials; namely, to define the initial mesh as filled entirely of air except the volume that the solid HE charge initially occupies. The precise assignments of the different materials in the different regions (in the originally empty mesh) are done automatically by LS-DYNA according to this latter command.

5.3.4 Material and Equation of State (EOS) Models in LS-DYNA

The explosive simulations using the multi-material arbitrary Lagrangian-Eulerian (MM-ALE) method are essentially supersonic fluid dynamics, in which a shock wave propagates through the initially ambient air. The shock wave in the air is produced by the expansion of the detonation products, which were generated from the detonation of a solid high explosive. The detonation products are high-energy, temperature, and pressure gases. By their extreme thermodynamic state, the hot gases expand rapidly and hence compress the surrounding air such that a sharp increase in air pressure occurs. Since the levels of the resulting pressures are extremely high, the pressure wave is supersonic, i.e., it is a shock wave. The thus-established shock wave then propagates (or travels) towards the ambient region (i.e., away from the source of shock wave formation, or away from the explosive centre, in all outward directions).

In the explosive analyses, the domain physically consists of two materials: the surround-

ing medium and the solid charge prior to detonation. The surrounding medium is assumed as air in standard atmospheric conditions. The bare charge is taken as a plastic explosive–composition 4, (PE4), which is thermodynamically equivalent to C4 (Bogosian et al., 2016), another common type of plastic explosive. Once the explosive experiment is completed, the blast-generated reflected pressures and the associated reflected specific impulses are obtained. Subsequently, the reflected specific impulses are converted into initial velocity fields, according to Rigby et al. (2019a) and Tyas and Pope (2003), in purely Lagrangian analyses to study the (structural) responses of the Domex-355 steel plates. Note that in the Lagrangian analyses, there are no externally applied pressures, i.e., the loadings are perfectly impulsive. Hence, the Lagrangian domain consists only of the steel plate. In the following, the material and equation of state (EOS) models, which were used in the uncoupled explosive and purely Lagrangian analyses, are described, and the numerical values (and their sources) of the various parameters are given.

Air. The air is modelled using its equation of state (EOS) and its ambient properties. The EOS relates the current pressure in terms of the current density and current internal energy. In practice, the air is modelled as an ideal (and calorically perfect) gas so that its EOS is the ideal gas law

$$p = (\gamma - 1)\rho e,$$

where p, ρ, and e are the current pressure, density, and internal energy (energy per unit mass), and γ is the specific heat ratio (c_p/c_v), which has a (constant) value of 1.4 for diatomic gases, such as air. In LS-DYNA, the ideal gas EOS is implemented by using the `*Eos_Linear_Polynomial` model,

$$p = \sum_{n=0}^{3} c_n \mu^n + \left(c_4 + c_5\mu + c_6\mu^2\right)\rho_0 e,$$

where $\mu = \rho/\rho_0 - 1$, and then setting $c_0 = c_1 = c_2 = c_3 = c_6 = 0$ and $c_4 = c_5 = \gamma - 1$. In addition, the null material model is used to define the initial density of air. The quantity $(\rho_0 e)$ is denoted by E and defined as the internal energy per unit initial volume. The values of the parameters of air that were used in the simulations are listed in Table. 5.1. In the table, the value of E_0 was obtained from $E_0 = \rho_0 e_0 = p_0/(\gamma - 1)$ (see the ideal gas law, given earlier), when the standard air's ambient pressure, p_0, is taken as 101.32×10^3 [Pa], and $\gamma = 1.4$.

LS-DYNA allows controlling the transient behaviour of bulk material, e.g., air, when it is subjected to sudden loading such that unreasonable spikes (or high-frequency oscillations) in pressure can be regulated (or reduced) by means of artificial damping, namely by introducing a bulk viscosity that depends on the current strain rate along the direction of load application (or in the direction of the wave propagation that loads the material). Note that this is meant to regulate post-peak pressure oscillation; although, excessive damping could smear out the initial (and physically important) jump in the pressure by the shock

Table 5.1. Air parameters used in `*Eos_Linear_Polynomial` and `*Mat_Null`

Parameter	Value	Units
`*Eos_Linear_Polynomial`:		
$c_0 - c_3, c_6$	0	[-]
c_4	0.4	[-]
c_5	0.4	[-]
E_0	253.3×10^3	[N.m/m^3]
`*Mat_Null`:		
ρ_0	1.18	[kg/m^3]

Subscript 0 (in E_0 and ρ_0) refers to initial (ambient) values

arrival (Rigby, 2014). This is described as the bulk viscosity feature in (Livermore Software Technology Corporation, 2019).

High explosive, PE4. PE4 is modelled in LS-DYNA by (i) specifying the physical geometry of the charge and its density (as a solid); (ii) specifying the point (within the charge) of initial detonation and the time of detonation; (iii) prescribing its Chapman-Jouguet's (CJ) detonation characteristics to model the transient detonation process as the solid explosive burns and thereby generates the detonation products (the hot-gases); and (iv) defining the EOS governing the thermodynamic state of the high-pressure and high-temperature detonation products as they expand and interact with the surrounding medium, which is air.

That is, the explosive is first modelled as an inert solid occupying a certain volume, then at a particular point within the explosive, detonation starts at a prescribed time. Then, detonation progresses through the rest of the unexploded material with a speed called the CJ detonation velocity. The detonation front, as it travels, brings the inert solid explosive into the state of decomposed (fully detonated) explosive (or detonation products). The pressure at the fully detonated state is called the CJ pressure; knowledge of CJ detonation velocity and the CJ pressure determines other properties of the fully detonated explosive. The CJ state of the fully detonated explosive is the initial state of the detonation products. Further behaviour of the detonation products is then described by their EOS starting from the CJ state. The high pressures and temperatures of the already detonated explosive drive (from behind) the detonation wave towards the remaining inert solid explosive. Once the detonation front has passed through the whole inert explosive, the detonation process ends, and the detonation products are modelled by the EOS as gaseous material. The detonation products interact with all surrounding media from the moment of their formation as they (i.e., the hot detonation products) expand. This eventually results in compressing and heating the surrounding air and thereby creating a shock wave in the air.

LS-DYNA provides a feature in modelling the detonation process such that the explosive transitions from the initial inert state to the fully detonated state in a finite time interval. For this, a burning fraction parameter is defined that ramps linearly from zero (inert) to unity (fully-detonated); this burning fraction is linear in time t measured with respect

to the lighting time, t_L, (the time at which the detonation front has just reached the element in question, which is the distance from the initial detonation point divided by the detonation velocity). Therefore, the inert explosive does not turn into fully detonated products instantaneously but requires some time (or delay) to do so. The value of the burning fraction is capped (from above) at the value of 1. Then, the instantaneous pressure in one element (for which $t \geq t_L$) is taken as the burning fraction times the current pressure calculated from the EOS of the fully detonated explosive. This is called the "programmed burning" scheme in LS-DYNA and is used in the present simulations as a representation of initiating detonation deliberately by a detonator.

For PE4, the detonation products are modelled by the Jones-Wilkins-Lee (JWL) EOS, `*Eos_Jwl`, which gives the current pressure p, in terms of the current specific volume change v and internal energy e, as

$$p = A\left(1 - \frac{\omega}{r_1 v}\right)\exp\left(-r_1 v\right) + B\left(1 - \frac{\omega}{r_2 v}\right)\exp\left(-r_2 v\right) + \frac{\omega}{v}e,$$

in which A, B, r_1, r_2, and ω are material constants. As the detonation products expand significantly (i.e., as v becomes large), the first two terms can be neglected, and the overall gas approaches the ideal gas behaviour where ω can be interpreted as $(\gamma - 1)$; note that $1/v \equiv \rho$.

In LS-DYNA, the high explosive characteristics controlling its detonation (or burning) are the Chapman-Jouget's (CJ) pressure, p_{CJ}, and the detonation velocity (the speed with which the reaction (or detonation) front progresses through the unreacted explosive material), D_{CJ}. These parameters, in addition to the charge's mass density, are defined in `*Mat_High_Explosive_Burn`. The initial detonation point (within the solid explosive) and time instant are supplied using the `*Initial_Detonation` keyword. The values of the various parameters for the PE4 explosive as used in the simulations are provided in Table 5.2. The parameter `beta` when set to 2 disables the feature that the explosive may detonate (on its own) depending on the (mechanical) state of the inert (or unreacted) solid explosive so that it cannot be detonated except by explicitly invoking the initial detonation command (keyword) in LS-DYNA, discussed earlier.

Domex-355 steel In the structural response of the membrane, in a purely Lagrangian setting, the material behaviour is modelled using the modified Johnson-Cook (1985) (JC) constitutive relation, through the keyword `*Mat_Modified_Johnson_Cook`. The model is initially linear elastic up to the current yield limit. On yielding of the material, plasticity develops and is represented as an extension of von Mises plasticity such that the current yield stress depends on the current total plastic strain (strain-hardening), the instantaneous plastic strain rate (strain-rate sensitivity), the current temperature (thermal softening). The model allows for softening due to the accumulation of damage, which is directly related to the maximum value of the total plastic strain. This is achieved in LS-DYNA by scaling the stresses based on the damage value. As the model is based on von Mises

Table 5.2. PE4 parameters used in `*Eos_Jwl` and `*Mat_High_Explosive_Burn`. All values are adopted from Curry (2017) and Rigby et al. (2019a).

Parameter	Value	Units
`*Eos_Jwl`:		
A	609.77×10^9	[Pa]
B	12.95×10^9	[Pa]
r_1	4.50	[-]
r_2	1.40	[-]
ω	0.25	[-]
e_0	9.00×10^9	[N.m/m^3]
`*Mat_High_Explosive_Burn`:		
ρ_0	1616.0	[kg/m^3]
D_{CJ}	8193.0	[m/s]
p_{CJ}	29.0×10^9	[Pa]
β	2	[-]

Subscript 0 refers to initial (ambient) values.
Subscript CJ refers to Chapman-Jouguet's detonation condition.

criterion, the yielding of the material depends on the state of the deviatoric stress, s_{ij}, only and, thus, is independent of the hydrostatic pressure. Therefore, any volume change is purely elastic.

According to JC model, an element of the material yields when the following (yield) condition is satisfied

$$\sqrt{(3/2)}\sqrt{s_{ij}s_{ij}} = \sigma_{y,d}$$

where $\sigma_{y,d}$ is the current (or dynamic) yield stress (yield limit), and s_{ij} is the usual deviatoric stress; that is, $s_{ij} = \sigma_{ij} - \hat{p}\delta_{ij}$, where the internal hydrostatic pressure is $\hat{p} = (1/3)\sigma_{kk}$, which is positive in tension, and δ_{ij} is the Kronecker's delta. The quantity $\sqrt{(3/2)}\sqrt{s_{ij}s_{ij}}$ is called the effective (von Mises) stress, σ_{eff}.

Whenever the yield condition is satisfied, a material element can undergo *plastic shearing* deformation, in addition to possible further elastic (shearing and volumetric) deformations. Thermal softening in the material might be achieved through a reduction in the current yield limit, $\sigma_{y,d}$ as temperature, T, increases. On the other hand, hardening (or strengthening) is achieved by increases in $\sigma_{y,d}$ as the total plastic strain and/or plastic strain-rate increase; there is a critical strain-rate threshold below which strain-rate sensitivity is deactivated. The quasi-static initial yield stress is $\sigma_{y,d}$ without any of the above increases or reductions.

The current yield stress $\sigma_{y,d}$, according to JC model, is given by

$$\sigma_{y,d} = \left(A + B\varepsilon_{\mathrm{p,eff}}^{n}\right)\left[1 + \left(\frac{\dot{\varepsilon}_{\mathrm{p,eff}}}{\dot{\varepsilon}_0}\right)\right]^{c}\left[1 - \left(\frac{\Delta T}{\Delta T_m}\right)^{m}\right],$$

where $\varepsilon_{\mathrm{p,eff}}$ is the effective plastic strain and $\dot{\varepsilon}_{\mathrm{p,eff}}$ is its rate. In the above, A, B, n, c, and m are material constants. A is the initial yield stress, B and n control strain-hardening, c

and $\dot{\varepsilon}_0$ control strain-rate effects ($\dot{\varepsilon}_0$ is the quasi-static strain-rate threshold). According to LS-DYNA user's manual (LST, 2021b), $\dot{\varepsilon}_{\mathrm{p,eff}}/\dot{\varepsilon}_0 = 0$ when $\dot{\varepsilon}_{\mathrm{p,eff}}/\dot{\varepsilon}_0 < 1$.

$\Delta T = T - T_0$ and $\Delta T_m = T_m - T_0$, where T, T_m, and T_0 are the current, melting, and the room (absolute) temperatures. The model allows the conversion of plastic work to heat, and this feature requires the specification of the Taylor-Quinney ratio, χ, and the specific heat at constant pressure, c_p. The plasticity-induced (adiabatic) heating is given by $\rho c_p \dot{T} = \chi \sigma_{\mathrm{eff}} \dot{\varepsilon}_{\mathrm{p,eff}}$, where the plastic work rate is $\dot{W}_p = \sigma_{\mathrm{eff}} \dot{\varepsilon}_{\mathrm{p,eff}}$, and χ is the fraction of plastic work that is converted into heat.

As mentioned earlier, the modified JC model in LS-DYNA allows material softening due to the accumulation of damage based on the largest attained total plastic strain. The damage is stored as the damage variable D. When this feature is enabled, the effective deviatoric stress and effective plastic strains are factored based on the value of D according to

$$\sigma^*_{\mathrm{eff}} = \frac{\sigma_{\mathrm{eff}}}{1 - \beta D},$$

$$\varepsilon^*_{\mathrm{p,eff}} = (1 - \beta D)\varepsilon_{\mathrm{p,eff}},$$

where the star refers to the scaled quantities, according to the current damage value, D, and $\beta = 1$ when the damage-induced softening is activated. However, in the present study, this behaviour is neglected, $\beta = 0$, and the starred and unstarred quantities are identical. It should be mentioned that the modified JC model in LS-DYNA includes a modification to the power-hardening law that would cause an additional reduction of the current yield limit $\sigma_{y,d}$; however, this is also neglected in the present study following Curry's (2017) work.

The various JC material parameters for the Domex-355 steel material as used in the present simulation analyses are given in Table. 5.3.

The adopted values of various parameters are taken from Richard Curry's (2017) thesis. Curry derived the values by advanced curve-fitting (through LS-OPT (2019)) the JC model to experimental data from dynamic and static material testing on Domex-355 steel specimens. High strain-rates and different temperatures were varied in the author's work. Finally, the author demonstrated the validity of his derived values when compared to experiments on the response of shells to explosive loading. In addition, Rigby et al. (2019) show the excellent agreement of numerical models, in which Curry's data are utilised, when compared to experimental measurements of near-field blast-loaded thin plates.

Documentations of the material models, their underlying theories, and recommendations on the values of some parameters (not given herein) are available in LS-DYNA keyword manuals (LST, 2021b; LST, 2021a).

Table 5.3. Domex-355 steel parameters in `*Mat_Modified_Johnson_Cook` which are adopted from Curry (2017) and Rigby et al. (2019a).

Parameter	Value	Units
ρ	7830	[kg/m^3]
E	200×10^9	[Pa]
ν	0.29	[-]
A	352×10^6	[Pa]
B	642×10^6	[Pa]
n	0.5597	[-]
c	0.032	[-]
$\dot{\varepsilon}_0$	0.0014	[-]
χ	0.9	[-]
c_p	452	[N.m/(Kg.K)]
m	0.81	[-]

5.4 The Non-Uniform Model Versus LS-DYNA

The present model is first evaluated by comparing it to numerical results from LS-DYNA analyses performed by the author, which are outlined as follows. First, the MM-ALE technique in LS-DYNA was utilised to generate physically relevant specific impulses that are imparted onto rigid targets due to the detonations of close-in PE4 spherical charges. The technique was experimentally validated by Rigby et al. (2018) using near-field blast experiments (Rigby et al., 2015). Subsequently, in a separate purely Lagrangian set-up, the responses of rectangular and circular thin (Domex-355) steel plates were simulated, in which the plates are set into motion by prescribed initial velocities $\dot{w}_0$ obtained by converting the specific impulses i from the earlier MM-ALE analyses. According to Rigby et al. (2019), $\dot{w}_0$ is given by

$$\dot{w}_0 = \frac{i}{\rho h},$$

where ρ and h are the plate's density and thickness, respectively; both $\dot{w}_0$ and i are dependent on the spatial coordinates of the target, i.e., non-uniform.

The energy-equivalent total impulses, I_k, are taken as representative for both the amplitudes and non-uniformities of the non-uniform specific impulses, and hence for the near-field blast threats. The values of I_k corresponding to the considered masses and clear stand-off distances of the spherical PE4 charges are summarised in Table. 5.4.

In the Lagrangian analyses, the Domex-355 steel material is described using the modified Johnson-Cook (JC) model and for which the material parameters are adopted from Curry (2017). It is important to highlight that in the Lagrangian LS-DYNA simulations, the plates' behaviours incorporate flexural and membrane modes and strain-hardening and strain-rate sensitivity effects; in addition, the membranes' elasticity is accounted for. Further details of the MM-ALE and pure Lagrangian models were provided earlier, see Section 5.3.

In the model predictions, the peak displacement occurring when the total velocity reaches

Table 5.4. Input parameters for the MM-ALE explosive analyses and the corresponding energy-equivalent total impulses (Tyas and Pope, 2003; Rigby et al., 2019a), I_k, and area-integrated total impulses I_0. The total impulses are computed over the circular (cir.) and rectangular (rec.) plates. The Hopkinson-Cranz scaled distance Z are shown.

ID	Charge mass [g]	clear SOD [mm]	SOD [mm]	Z [m/kg$^{1/3}$]	I_0 (rec.) [N.s]	I_k (rec.) [N.s]	I_0 (cir.) [N.s]	I_k (cir.) [N.s]
1	50.0	25.0	44.5	0.12	51.62	104.15	53.10	111.15
2	75.0	25.0	47.4	0.11	73.63	146.66	76.53	156.42
3	100.0	25.0	49.6	0.11	95.96	186.40	99.41	198.66
4	125.0	25.0	51.5	0.10	117.20	224.17	121.99	238.90
5	150.0	25.0	53.2	0.10	141.07	260.80	144.36	277.67
6	175.0	25.0	54.7	0.10	161.28	295.48	166.32	314.69
7	200.0	25.0	56.0	0.10	181.33	329.43	188.14	350.95
8	225.0	25.0	57.3	0.09	201.66	362.25	209.93	385.98
9	50.0	35.0	54.5	0.15	49.83	87.32	52.34	93.43
10	75.0	35.0	57.4	0.14	72.09	123.94	74.86	132.28
11	100.0	35.0	59.6	0.13	93.49	158.44	96.79	168.96
12	125.0	35.0	61.5	0.12	115.65	191.73	118.46	204.19
13	150.0	35.0	63.2	0.12	134.48	223.39	139.70	238.16
14	175.0	35.0	64.7	0.12	155.88	254.33	160.82	270.97
15	200.0	35.0	66.0	0.11	175.33	284.41	181.60	303.10

zero is identified herein as the residual (or permanent) displacement at a given spatial coordinate on the membrane. Throughout, the specific impulses are symmetric with respect to the membranes' centres, and hence the peak residual displacements are located at the plates' centres and are denoted by w_c. In evaluating the analytical solutions for the rectangular membrane, the FFT procedure described in Appendix D is utilised for computational efficiency.

The model predictions are compared to LS-DYNA results for rectangular membranes under non-uniform specific impulses, and the results are shown in Fig. 5.3 using the permanent central displacement, w_c, as a function of the energy-equivalent total impulse, I_k.

Similar model validation is provided for the circular membranes under non-uniform specific impulse, and the results are shown in Fig. 5.4.

From the two validation analyses, it is shown that the model compares excellently with the predictions from the LS-DYNA structural analyses. Furthermore, it can be seen that both the model and LS-DYNA predictions exhibit the linear dependence of the central peak plastic displacements with the energy-equivalent total impulse, I_k, in agreement with the findings of the original authors who derived this important load parameter (Rigby et al., 2019a; Tyas and Pope, 2003). This demonstrates the accuracy of the present analytical model and, also, indicates that the functional form of the membrane model is correct when applied to non-uniform specific impulse cases. Additionally, it is evident, from Figs. 5.3 and 5.4, that the peak and residual displacements are almost coincident, such that the resulting membranes' responses are mainly plastic. In Section 5.6, the precise specific impulse profiles, as predicted from the foregoing explosive analyses in LS-DYNA, will be given, which are highly non-uniform (as the case from typical near-field blast scenarios).

It should be emphasised that the analytical model predictions compare well with the cor-

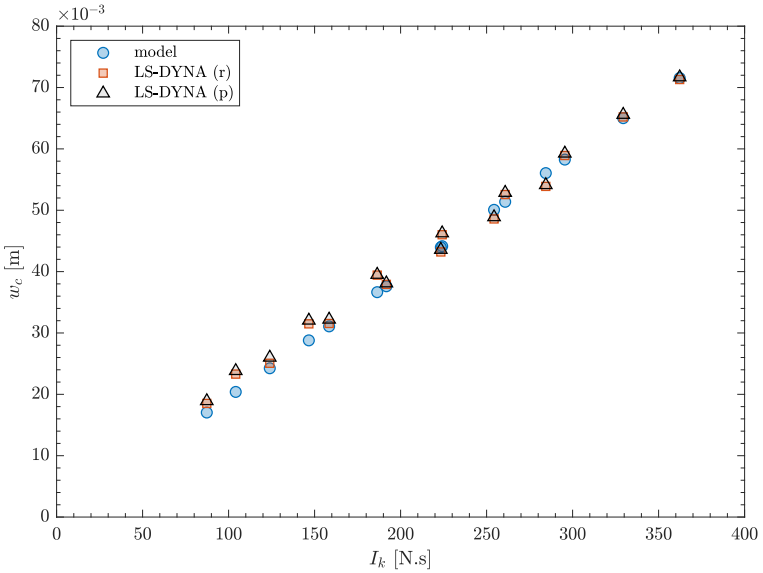

Fig. 5.3. Comparisons of the model predictions to LS-DYNA results for rectangular membranes in terms of the central displacements, w_c, versus the energy-equivalent total impulse, I_k. Residual (r) and peak (p) displacements are shown from LS-DYNA simulations. I_k values correspond to specific impulses generated by explosive simulations using the MM-ALE technique in LS-DYNA.

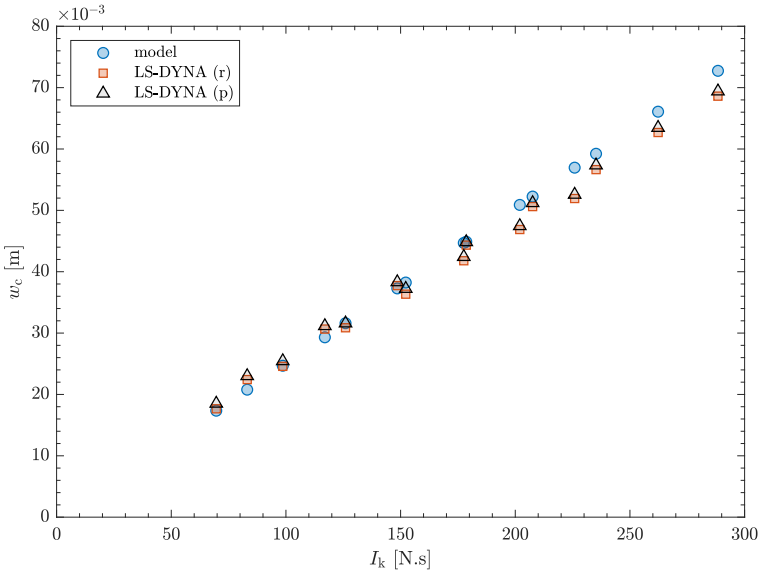

Fig. 5.4. Comparisons of the model predictions to LS-DYNA results for circular membranes in terms of the central displacements, w_c, versus the energy-equivalent total impulse, I_k. Residual (r) and peak (p) displacements are shown from LS-DYNA simulations. I_k values correspond to specific impulses generated by explosive simulations using the MM-ALE technique in LS-DYNA.

responding numerical results from the Lagrangian LS-DYNA analyses, even though the input specific impulses in both approaches are based on the MM-ALE calculations. That is, given a non-uniform specific impulse (without associating it with an actual explosive event), the analytical model and the purely Lagrangian simulations give comparable results. Although, the MM-ALE technique was utilised to base the comparisons on physically relevant specific impulse characteristics (i.e., reasonable amplitudes and distributions) as would be encountered in real situations.

5.5 The Non-Uniform Model and LS-DYNA Predictions Versus Explosive Plate Experiments

As already mentioned, in the above validation work, the specific impulses used in both the model predictions and the LS-DYNA Lagrangian simulations are based on results from the earlier LS-DYNA MM-ALE analyses. In this section, experimental results (discussed below) are used to validate both predictions from LS-DYNA and the present model.

Curry (2017) and Curry and Langdon (2017) performed 26 air-blast experiments on thin circular Domex-355 steel plates of constant diameter of 300 mm and thickness of 3 mm, and the specimens were loaded by near-field blasts generated by detonating cylindrical PE4 explosive charges. In the tests, the charges had various masses and were located at two clear stand-off distances. The authors measured the transient and residual displacements of the plates and outlined the blast configuration in detail.

However, in Curry and Langdon (2017), only measurements of the total impulses are reported, whereas the actual specific impulse distributions are not quantitatively available. In addition, the total impulses are inferred by their effects on the early oscillatory motion of a ballistic pendulum housing the target specimens and the explosive charge, as described in the authors' work. Thus, in order to apply the analytical model, MM-ALE simulations using LS-DYNA were performed by the present author to numerically reproduce the blast-induced specific impulses according to the experimental blast set-ups in Curry and Langdon (2017), as was described in Section 5.3.1.

Fig. 5.5 shows the test matrix of the explosive experiments of Curry and Langdon (2017) in terms of the masses and clear stand-off distances of the explosives. The left sub-figure gives the values of the energy-equivalent total impulses, I_k as predicted by the MM-ALE analyses, and the right sub-figure provides the average (among replicates) values of the experimental total impulses. This figure is meant to relate the values of I_k, discussed herein, to the input explosive experiments of Curry and Langdon (2017).

The MM-ALE results were then validated using the measured total impulses in Curry and Langdon (2017), as shown in Fig. 5.6. It should be pointed out that total impulses from the MM-ALE simulations correspond to areas of circular targets of radius 0.15 [m], as this is the radius of *exposed* (or unsupported) areas of the plate specimens (i.e., portions of impulse transferred by the clamping frame are omitted). The total area of the front surface

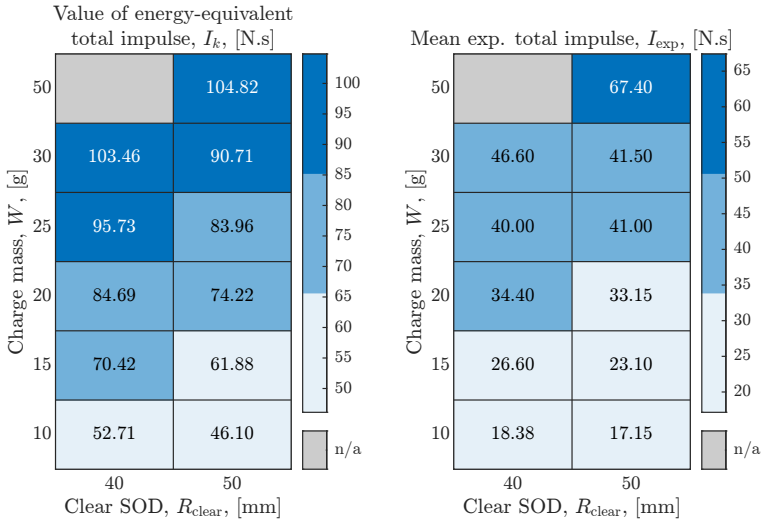

Fig. 5.5. Explosive testing matrix of Curry and Langdon (2017) and their associated energy-equivalent total impulses (as predicted by the MM-ALE analyses in LS-DYNA) (left) and the average values of the experimentally measured total impulses (right).

of the pendulum (consisting of the unsupported area of the specimens *and* the front area of the clamping frame) is 0.4^2 or 0.16 [m^2], whereas the surface area of the unsupported area of the plate specimens is (π 0.15^2) or $\sim$ 0.07 [m^2]. Thus, the area considered in the impulse calculations comprises 0.44 of the total area (exposed to the explosive charge). The part of impulse transferred through the clamping frame is thought to *not* influence the plate's response, as will be explained later. The red data points indicate that these explosive tests are excluded from the subsequent Lagrangian analyses of the specimens' responses.

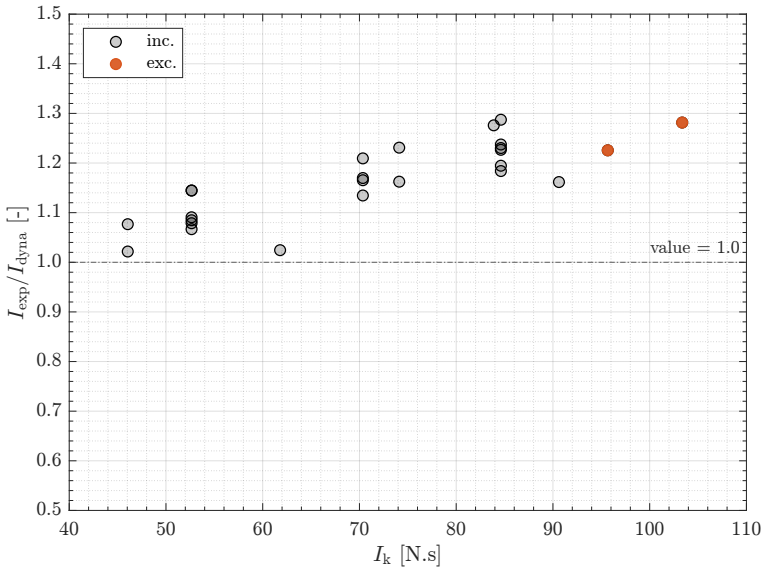

Fig. 5.6. Area-integrated total impulses from LS-DYNA MM-ALE simulations (I_{dyna}) and Curry and Langdon's (2017) experiments (I_{exp}) versus the equivalent impulses, I_k. Red markers indicate that experiments were excluded from the subsequent Lagrangian analyses.

It is seen in Fig. 5.6 that the MM-ALE model underestimates the total impulses compared

to the experiments. This is in agreement with the findings of Rigby et al. (2019a) that the total impulse inferred from the ballistic pendulum readings is generally larger than what the actual target specimens (mounted on the pendulum's front) experience. The experimental impulses, shown in Fig. 5.6, are based on ballistic pendulum measurements, as discussed earlier. Furthermore, the contributions of the total impulse associated with the exposed area of the clamping frame (which is neglected in the impulse calculations from the MM-ALE results) appear to be accounted for in the experimental readings (shown in Fig. 5.6 as I_{exp}) in Curry and Langdon (2017), see the authors' Section 2.3. However, since the specific impulses are highly non-uniform due to the near-field nature of the blast experiments, the majority of the specific impulse is concentrated in a partial region of unsupported area of the circular plate specimen. Thus, the total impulse contribution associated with the clamping frame is not directly related to the ratio of the omitted area to total area, which is $(1 - 0.44) = 0.56$.

The numerically obtained specific impulses are subsequently used in the analytical model to calculate the predicted residual displacements at the plates' centres, which are then compared to the corresponding experimentally measured displacements of Curry and Langdon (2017) as shown in Fig. 5.7.

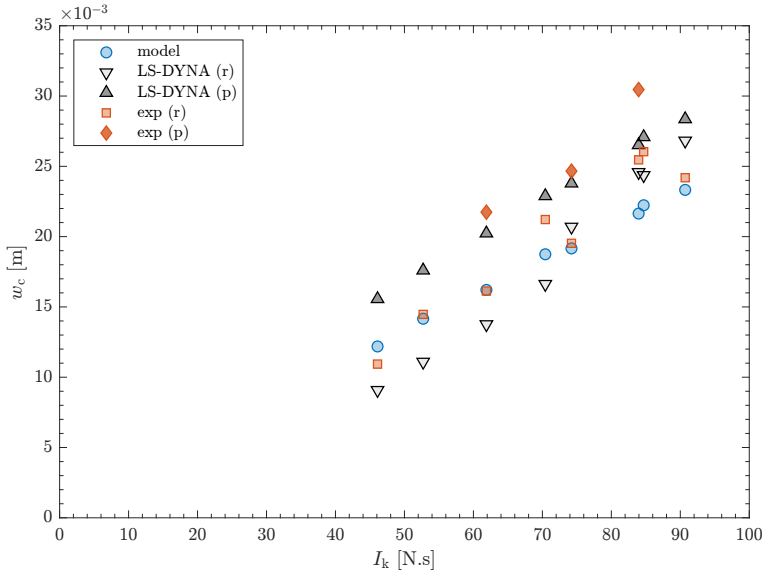

Fig. 5.7. Experimental validation of the model predictions for circular membranes in terms of the central displacements, w_c, versus equivalent impulse, I_k. The Model and LS-DYNA predictions are compared to the experimental data of Curry and Langdon (2017). Residual (r) and peak (p) displacements are given from LS-DYNA simulations and experiments (exp).

Furthermore, purely Lagrangian LS-DYNA analyses (using the modified JC model) were also performed to predict the structural response of the plates, as was described in Section 5.3.2, and the results are compared to both the model predictions and the experimental data of Curry and Langdon as already shown in Fig. 5.7. Two testing arrangements in Curry and Langdon (2017), as indicated by the red markers in Fig 5.6, were excluded from the structural analyses of the steel plates. This is because the peak transverse displacements from the Lagrangian LS-DYNA simulations that are associated with these

explosive tests were found to be less than the experimentally measured residual displacements, and experimental data were not provided for the peak displacements. Hence, the two tests were eliminated from the validation work.

As can be seen in Fig. 5.7, since the maximum displacements from the experiments and the Lagrangian LS-DYNA analyses are in reasonable agreement, it is concluded that the specific impulses from the MM-ALE models are accurate as well, despite the deviations of numerical total impulses from the experimentally reported ones. The maximum displacement is the quantity that is least affected by the method of determination in both the experiments and the post-processing of LS-DYNA results. The model predictions, as discussed earlier, are based on the MM-ALE specific impulses. Therefore, the model predictions in terms of the central plastic displacements, as depicted in Fig. 5.7, compare excellently with the experimental findings of Curry and Langdon (2017). The results in the present and previous sections both exhibit that the model is accurate when compared to LS-DYNA results.

5.6 Additional Analysis Results from LS-DYNA Simulations

As mentioned in the previous sections, the purpose of performing LS-DYNA analyses is to validate the analytical model for the non-uniform specific impulse case. Furthermore, the model was also validated against real experiments conducted by Curry and Langdon (2017) using explosive charges (made of PE4) detonated at very small stand-off distances. However, the experimental measurements did not provide quantitative data on the spatial profile of the specific impulses impinged onto targets. Therefore, explosive analyses using the MM-ALE method in LS-DYNA were performed to numerically reproduce the specific impulses, where the explosive set-up used in Curry and Langdon is replicated. The obtained specific impulse profiles were then used in the analytical model to predict the structural response of the membranes. In addition, these numerically generated impulse profiles were used as input in subsequent purely Lagrangian analyses to predict the membrane response in LS-DYNA.

The aim of the present section is to provide additional results that were not shown in the previous sections. Herein, the structural responses of the target are associated with the specific impulses and the explosive input parameters, namely, in terms of the charge masses and the stand-off distances. The following graphs are referred to the various explosive experiments using the following (naming) convention: Mx-Sy, where "M" stands for mass and "S" stands for stand-off distance, and x is the mass in [g] and y is the stand-off distance in [mm], measured from the target's centre to the nearest edge of the charge. For all analyses, the charge is placed directly above the target's centre, and the target is assumed rigid.

Fig. 5.8 shows the specific impulse profiles, $i(r)$ where r is the radial coordinate from the centre of the circular targets, corresponding to the explosive experiments, as designated

Table 5.5. Blast input parameters in explosive MM-ALE simulations

Experiment ID	Range of x [g]	Range of y [mm]	Charge shape
Mx-Sy x: mass of charge [g] y stand-off distance [mm]	$[10-50]$	$[40-50]$	Cylindrical

by the earlier-defined naming convention Mx-Sy. First, the profiles remarkably follow the Gaussian distribution predicted by Pannell et al. (2021), and the high non-uniformity of the specific impulse is obvious. This is attributed to two facts, the variations of (i) the actual stand-off distances and (ii) the angles of incidence of the various points on the target's surface are highly variable as the explosive charge is very close to the target. The actual distances and the angle of incidence near the target's centre are by far small compared to points that are further away. These two blast parameters directly lead to high increases in the reflected pressure from the explosive blast. Although the positive phase duration is generally much shorter for smaller stand-off distances, the positive specific impulse (which is the time integral of the reflected pressure over the positive phase) is much larger in the central region of the target, thus giving a highly localised profile. Moreover, the figure also shows that the specific impulse is highly dependent on both the stand-off (from the target's centre), R, and the cylindrical charge's mass W, or the scaled distance $Z = R/(W)^{(1/3)}$; smaller Z leads to larger specific impulses in the central regions.

Fig. 5.9 shows the resulting permanent displacement profiles $w_p(r)$ when deformable thin membranes are subjected to the specific impulses (through prescribed initial velocity fields $\dot{w}_0(r) = i(r)/[\rho h]$), where the specific impulses are as shown in Fig. 5.8, presented earlier. In this figure, we also used the earlier-defined experiments' designations. The permanently deformed profiles are given for each considered charge's mass and stand-off distance. Note that the membrane responses were obtained from axi-symmetric LS-DYNA analyses, and the deformed profiles $w_p(r)$ were extended (in the negative radial direction), i.e., by reflection about the axis of symmetry, for visual convenience. It can be seen that the target displacement profiles, $w_p(r)$, exhibit spatial non-uniformity in direct correspondence with the imparted specific impulse distributions $i(r)$. In particular, localised dishing (or bulging) can be seen near the central region of the circular target where the specific impulse has greater amplitude, which is in agreement with experiments, see Curry and Langdon.

In order to provide valuable insights, the results obtained from LS-DYNA were subsequently post-processed in MATALB. In particular, the von Mises stresses, σ_{vm}, were computed for every element and were related to the effective plastic strains ε_{eff}. It was noted that plasticity (as indicated by ε_{eff}) developed very rapidly (in terms of time) and propagated (in terms of space) through most of the membrane's area. The average von Mises stresses for all elements were also computed by time integration. Also, the average von Mises stress and effective plastic strains were computed through integration over the membrane surface area.

Fig. 5.10 shows the von Mises stress versus effective plastic strain curves for the most-

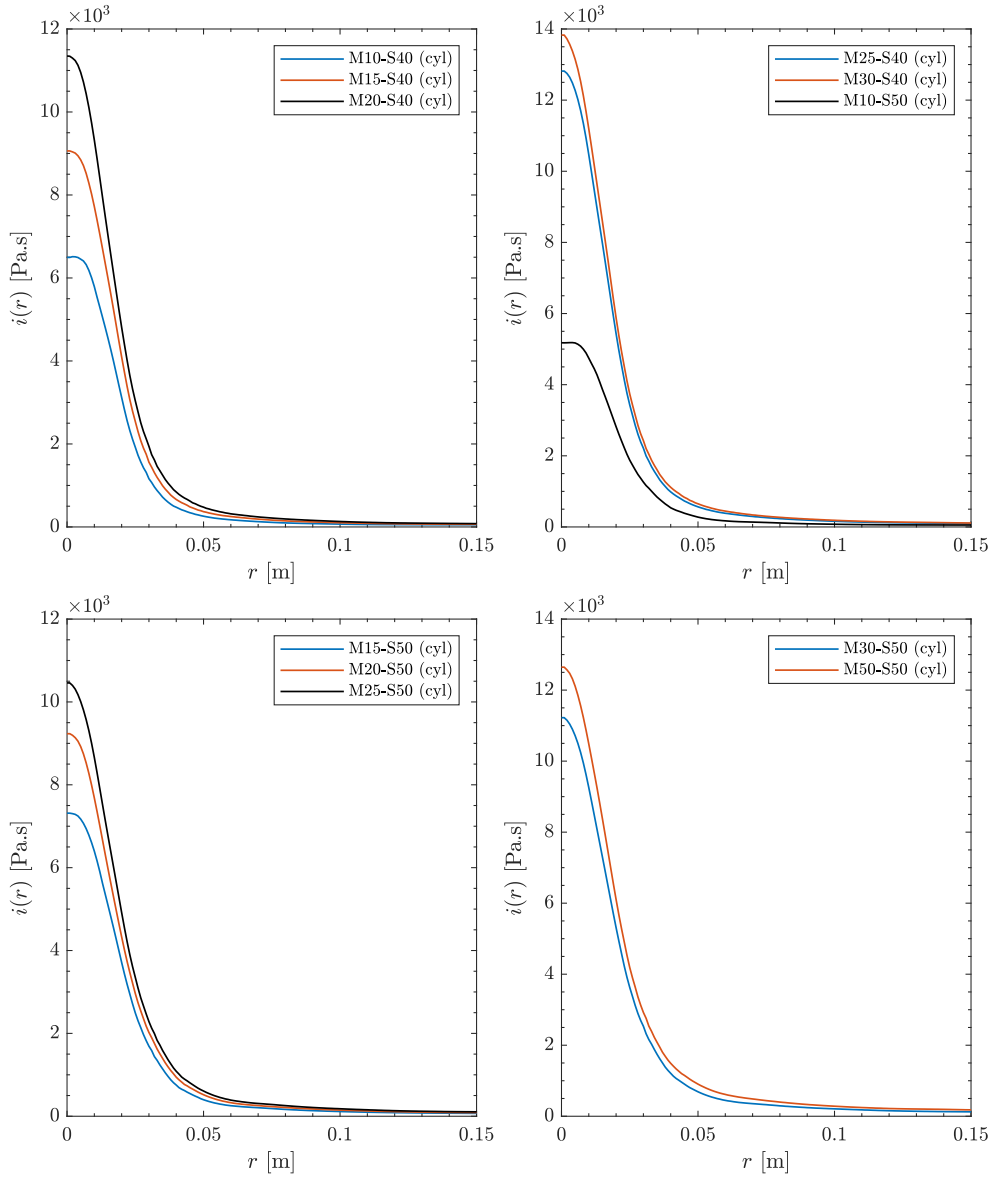

Fig. 5.8. Numerically predicted (from MM-ALE LS-DYNA) specific impulse profiles that were generated from the detonations of cylindrical explosive charges. The designation Mx-Sy gives the charge's mass x in [g] and the *clear* stand-off distance y in [mm]. The charge is directly located above the centre of the rigid target.

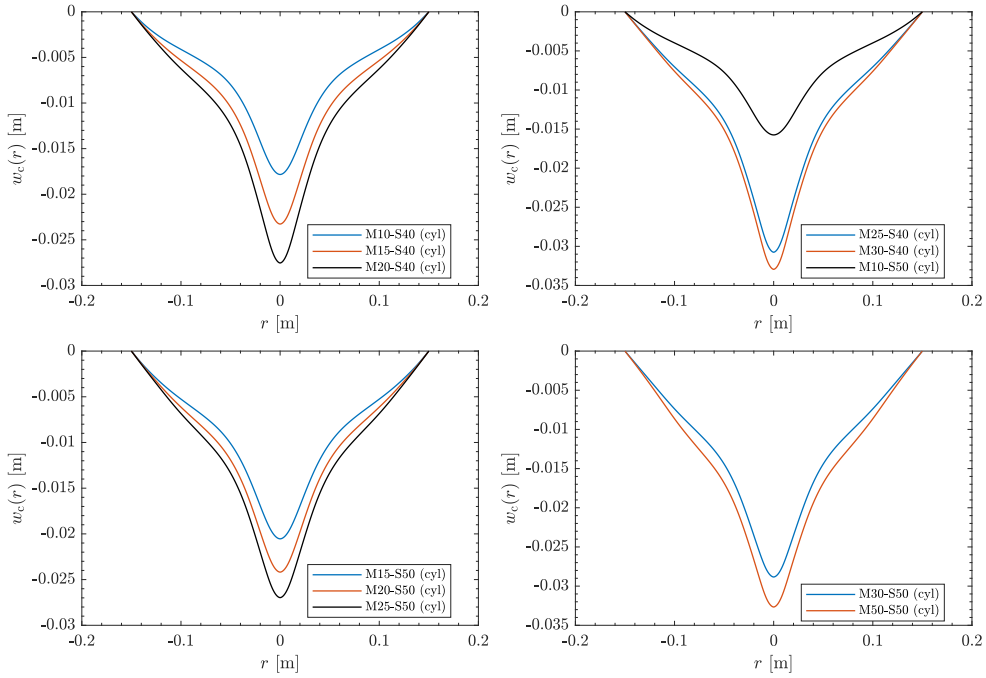

Fig. 5.9. Residual (or permanent) deformed profiles, $w_p(r)$, of impulsively loaded circular targets as predicted by purely Lagrangian structural analyses in LS-DYNA. The targets were loaded by near-field blasts associated with non-uniform specific impulses. In the legends, the designation Mx-Sy refers to the explosive charge's mass x in [g] and the clear stand-off distance y in [mm], as the specific impulses were obtained from separate MM-ALE explosive analyses, as shown in Fig. 5.8. It can be inferred that there is a direct correspondence between the specific impulse profiles (shown in Fig. 5.8) and the permanent displacement profiles, shown in this figure. Note that $r = 0$ is the centre of the circular membrane, and the profile $w(r)$ in the negative r range is simply the image of the profile in the positive r range; this was made for visual convenience, and the actual analyses were all axi-symmetric.

stressed element for each blast experiment. This curve comprises the time histories of the von Mises stress and the effective plastic strain at the same integration point of a single element. As can be seen, strain-hardening and strain-rate effects are present as the stress levels (corresponding to non-zero effective plastic strains) exceed the initial yield stress, σ_0, which is the parameter A in the JC model. In addition, the figure shows that maximum effective strains are within physically reasonable range; that is, it can be said that the neglect of strain-based material failure are practically justified (recall that the present figure correspond to the most-stressed element in each of the numerical explosive experiments).

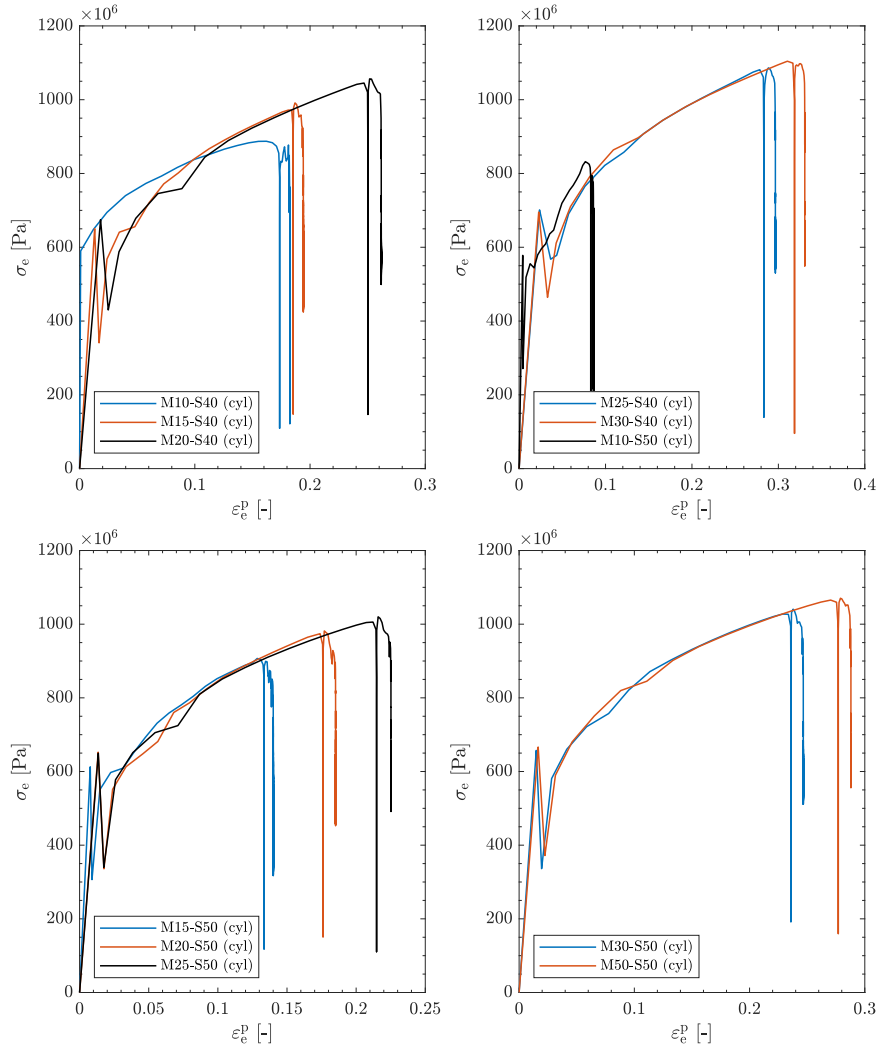

Fig. 5.10. Von Mises stress, σ_e, versus effective plastic strain, ε_e^p, curves as deduced from the results of circular membrane responses under non-uniform specific impulses. The von Mises stresses and effective plastic strains correspond to the most stressed elements for each blast experiment. Time was used to directly map the stresses to the strains. The nearly vertical lines in the curves are due to purely elastic unloading and/or reloading, i.e., phases during which no change of plastic strain takes place. The quasi-static yield stress, i.e., Johnson-Cook's A, of the material, was 352×10^6 [Pa]; thus, strain rate sensitivity and strain hardening are seen to play a substantial role as the current stresses exceed the mentioned quasi-static yield value.

For each element, the von Mises stress time history was determined, and then the time-

average stress was calculated by time integration (per element). Then, the profile of such time-averaged von Mises stress over the entire membrane domain is obtained. Fig. 5.11 shows these profiles for each experiment designated by the charge's mass and stand-off distance, i.e., Mx-Sy defined previously; note that every experiment corresponds to a particular specific impulse distribution as present earlier in Fig. 5.8.

In the plate response LS-DYNA simulation, recall that the material of the membrane was described by Johnson-Cook (JC) model, and the quasi-static yield stress, i.e., A in JC model, was 352×10^6 [Pa]. Thus, it can be seen that the dynamic yield stress is significantly affected by strain-hardening and strain-rate sensitivity. The effective (or von Mises) stress profiles are area-averaged and the mean effective stresses are shown in the figure by the horizontal dashed lines labelled "mean". It can be seen that the mean stresses are in order of the initial yield stress σ_0 (which is taken as the parameter A in JC model). Therefore, the initial yield stress in the analytical model, which is taken as σ_0, can be viewed to reflect the global (or overall) yield stress in an average sense. This is believed to explain the reasonable agreement between the model and LS-DYNA predictions of the plastic displacements of the plates despite the actual differences of the yield stress values in the two approaches.

Further numerical blast experiments were performed in LS-DYNA for impulsively loaded circular membranes. The specific impulses were generated from earlier axi-symmetric explosive simulations using the MM-ALE technique, in which the explosive charges are spherical and were detonated at small stand-off distances from rigid targets. The specific impulses were then converted into initial velocity fields that drive the motion of the purely-Lagrangian circular membranes. Certain combinations of the explosive charge masses and clear stand-off distances (from the closest outer edge of the charge to the centre of the target) were considered. Again, we designate the numerical blast experiments using the code Mx-Sy, where x is the mass in [g] and y is the stand-off distance in [mm]. The blast-induced specific impulses were all non-uniform and followed Pannell et al.'s Gaussian profile. Herein, we will present the time histories of the central points of the circular membranes for each blast experiment, as shown in Fig. 5.12. The figure suggests that for all explosive scenarios, the response of the target is mainly plastic as the central points are practically held at the permanent displacement values, which are attained very early through the response. Thus, it can be said that most of the input (kinetic) energy has already been entirely dissipated as soon as the peak central displacement is attained, for all the numerical experiments. This is also verified by examining the time histories of global (kinetic and internal) energies (although these graphs are not shown herein for brevity).

As the present model is based on the simplifying assumption that the in-plane strains of the thin target are associated with membrane action and without in-plane displacement effects, hence the local variation of the (purely plastic) strains does not accurately capture the corresponding observations from experiments and well-detailed numerical simulations. In particular, expected deviations of the model predictions regarding the distribution of the effective plastic strains exist, which are attributed to the additional membrane action

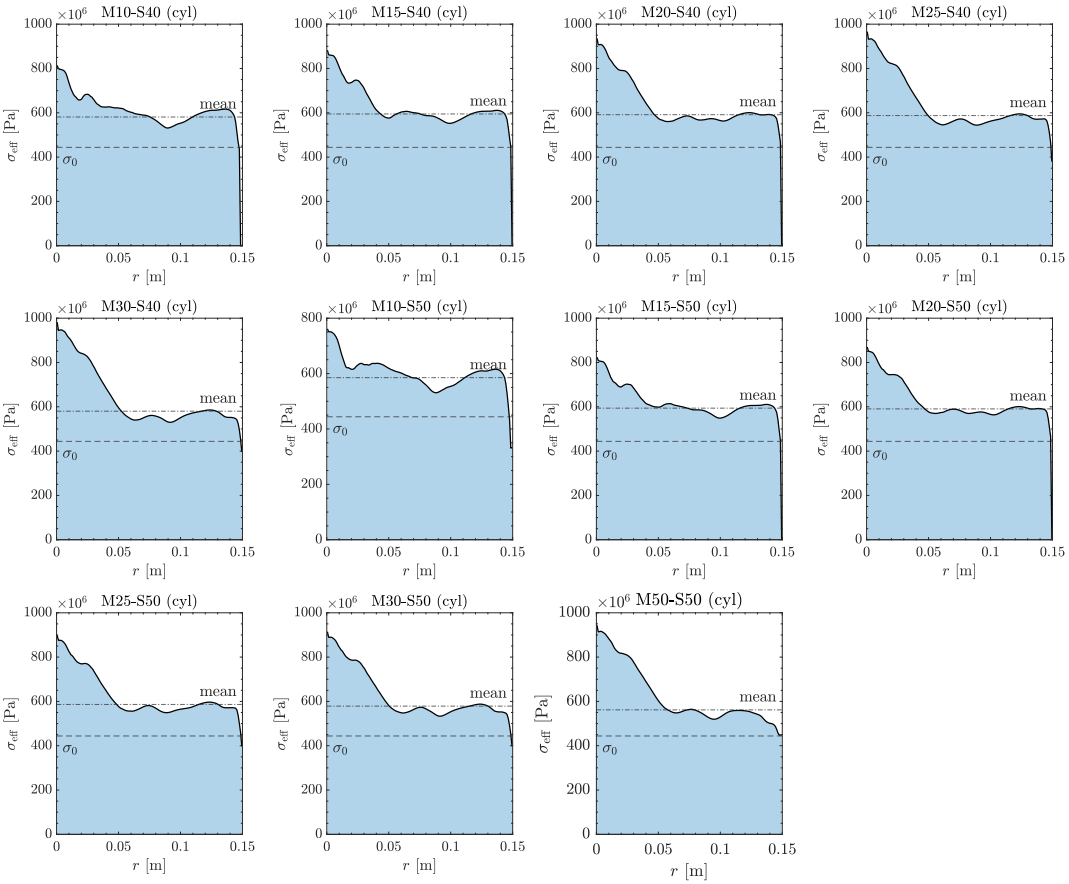

Fig. 5.11. Profiles of the von Mises stress, σ_{e}, versus the radial coordinate, r, of the circular membranes. The von Mises stress at a given point, r, is the average of the corresponding von Mises versus time curve at that point; the averaging is performed by time integration. The quasi-static yield stress, σ_0, of the membrane's material is taken as 444×10^6 [Pa], which corresponds to the corresponding experimental value in Curry and Langdon (2017). Dashed horizontal lines in the sub-plots represent the quasi-static yield stress, σ_0, and the area-averaged, labelled "mean", of the profiles (obtained by integration over the membrane's circular area).

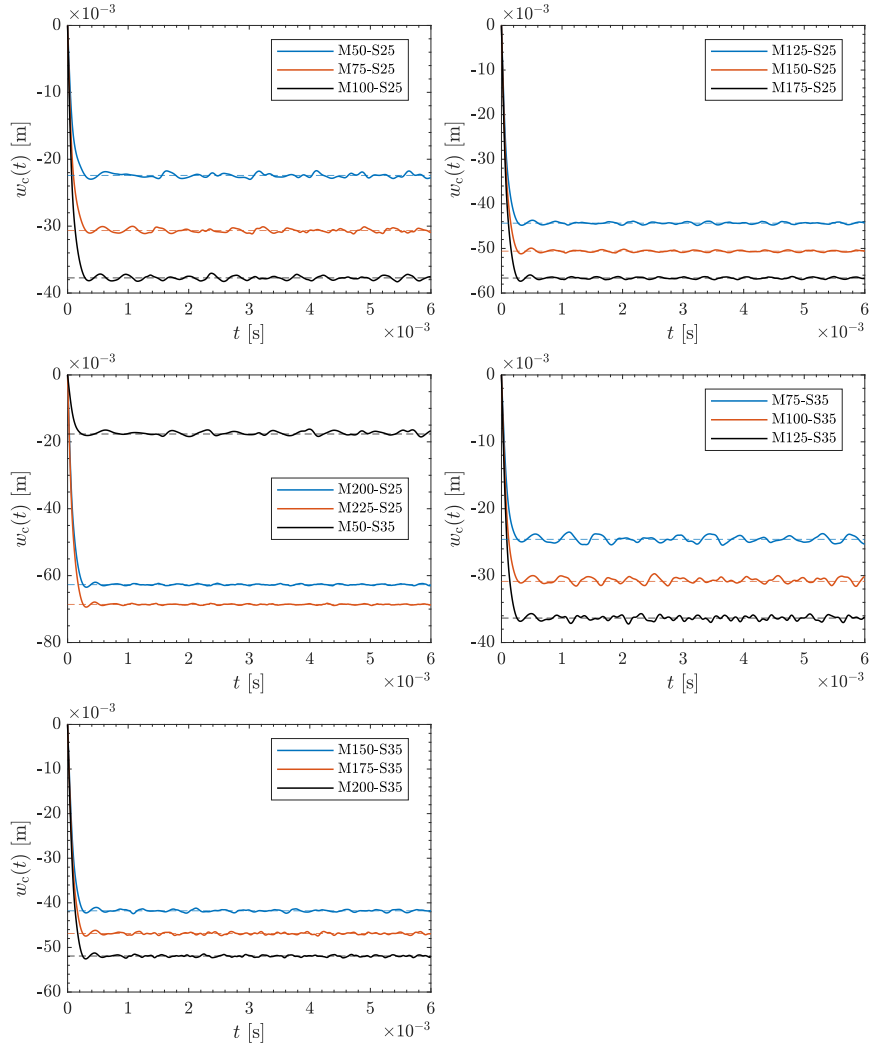

Fig. 5.12. Time histories of the central transverse displacements, $w_c(t)$, of circular membranes loaded by non-uniform specific impulses. The impulses were generated from earlier explosive MM-ALE experiments in LS-DYNA, and the experiments are labelled using the naming code Mx-Sy, where x is the explosive's mass in [g] and y is the stand-off distance in [mm]. The charges are located directly above the target's centres. It can be recognised that the response is mainly plastic and that the peak response is attained in the early phase of the response.

due to the in-plane displacements and possibly to flexural effects near the top and bottom surfaces of the thin plate. Moreover, the analytical model is expected to deviate from the real local distribution of the effective plastic strain field due to the neglect of the strain-hardening and/or strain-rate sensitivity effects, which are experimentally observed in the real behaviour of some typical ductile materials (e.g., Domex-355 steel). These plastic characteristics, to some extent, prohibit plastic flow as the yield stress increases during the evolution of deformation.

It should be re-emphasised that the present model can only predict the plastic strain contribution that is associated with the large transverse displacements. That is, the predicted plastic strain is a lower-bound geometrically (or kinematically) due to the neglect of the in-plane displacement contribution. In contrast, the predicted strain is an upper-bound materially (or constitutively) due to the perfect-plasticity assumption. The overall effect can be identified as an explanation for the reasonably accurate prediction of the transverse displacement's spatial profile (both transient and permanent deformed shapes). Fig. 5.13 shows the deformed shapes of a circular plate that is impulsively loaded by a near-field blast (corresponding to a PE4 spherical charge with mass $m = 75$ [g] and clear stand-off distance of $R_{\text{clear}} = 35$ [mm]). In this figure, the model-predicted profile (solid blue) is compared to a set of deformed profiles from the LS-DYNA simulation corresponding to different time instants (solid red curves). In addition, the permanent deformed profile, $w_p(r)$, from LS-DYNA is represented by the dashed red curve; the remaining dashed black curves provide offsets (using the plate's thickness, h) of LS-DYNA permanent profile.

It is seen, in Fig. 5.13, that the predicted profile is reasonably accurate compared to the numerical results; the conservative deviation is within the order of one plate's thickness, h. For the same blast problem, the time history of the total (or global) kinetic energy as predicted by the present theory when compared to the corresponding LS-DYNA result is shown in Fig. 5.14. From the latter figure, it can be seen that the model's prediction exhibits reasonable agreement with the numerical prediction, in particular with respect to the time interval during which the plate as a whole dissipates the blast input kinetic energy. For example, the model predicts that beyond time $t = 0.5$ [ms], the plate is completely rigid, which can be regarded as a reasonable approximation to the global predictions from the LS-DYNA simulation.

The combined contributions of in-plane displacement, strain-rate sensitivity, and strain-hardening, in addition to the large transverse displacement, on the effective plastic (membrane) strains at the mid-plane of circular thin plates that are subjected to non-uniform impulsive loading, due to near-field blast, were studied numerically using LS-DYNA. Namely, the results from Lagrangian LS-DYNA analyses are post-processed to determine the spatial profiles of the mid-plane effective plastic strain, strain-rate, dynamic yield (von Mises) stress. Elveli et al. (2022) suggested that the influence of work-hardening on the distribution of effective plastic strains in blast-loaded plates can be studied numerically due to expected difficulties in the experimental approach. The near-field blasts are characterised by the (non-uniform) specific impulses, which are shown in Fig. 5.15, as obtained by the

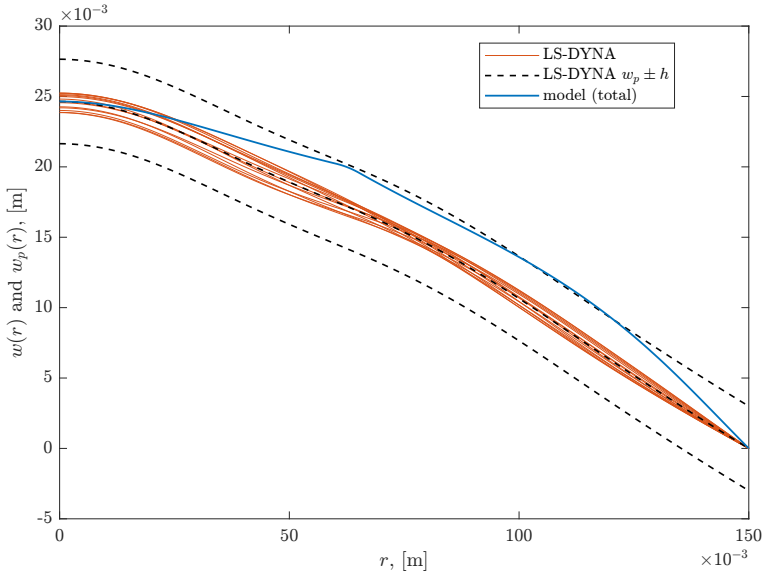

Fig. 5.13. Deformed profiles of a circular thin plate due to an impulsive near-field blast corresponding to a spherical PE4 explosive with a mass of 75 [g] and detonated at a clear stand-off distance (measured from the plate's centre) of 35 [mm]. Shown are the profiles predicted by the analytical model (based on the total solution termination strategy) and the corresponding ones from a purely Lagrangian LS-DYNA simulation. The plate thickness, ($h = 3$ [mm]), is used to offset the permanent deformed profile, w_p, that is determined from LS-DYNA results, and the model predicted profile is shown to be within one plate thickness with respect to the corresponding numerical prediction.

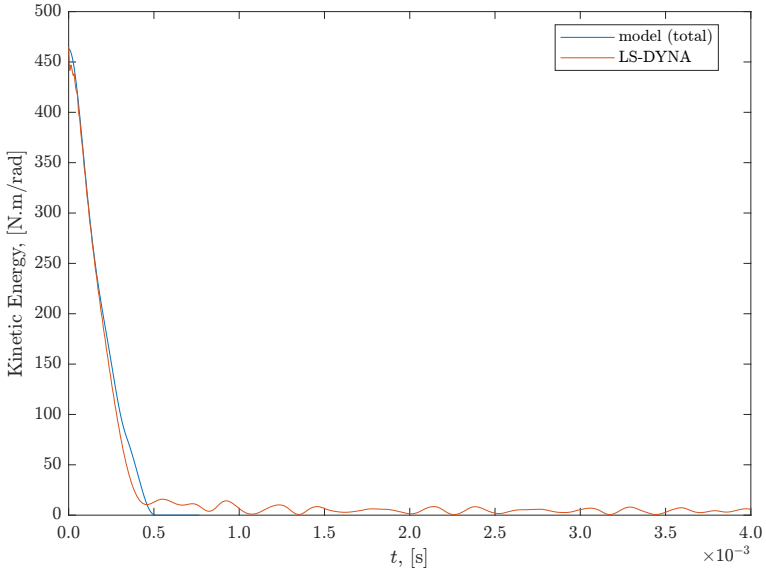

Fig. 5.14. Evolution of total kinetic energy of a circular thin plate due to an impulsive near-field blast corresponding to a spherical PE4 explosive with a mass of 75 [g] and a clear stand-off distance (measured from the plate's centre) of 35 [mm]. The kinetic energy as predicted by the analytical model (based on the total solution termination strategy) is compared to the corresponding one from a purely Lagrangian LS-DYNA simulation. There appears slight deviation among the initial kinetic energies, i.e., at $t = 0$, which can be attributed to small numerical error, in LS-DYNA, associated with the linear interpolation of the initial velocity profile. The exact kinetic energy (per unit radian) is $1/(2\rho h)\int_R i^2 r dr$, where the specific impulse, $i(r)$, is as will be given by the curve (M75-S35) in Fig. 5.15.

priorly performed MM-ALE explosive analyses. The actual input parameters of the blast configurations are shown in the various graphs with reference to the mass of the spherical PE4 explosives and the clear stand-off distance. The naming convention Mx-Sy is adopted where x is the charge's mass in [g], and y is the clear stand-off distance in [mm].

Representative profiles of effective plastic strain and the effective plastic strain-rate are shown in Figs. 5.16 and 5.17, respectively. Note that the plastic strain and plastic strain-rate at a spatial point (in the corresponding profiles) are the maximum values of the respective time histories. Since the circular plates were impulsively loaded, and the results correspond to the mid-plane of the plates, the obtained profile of maximum plastic strain is the final distribution of the plastic strain. The maximum strain-rate profiles were smoothed using the moving average method with a span (or moving width) of 8 (out of 150) data points; this due to observed spikes in the raw data.

As well-known, evolution of plastic strains and high strain-rates lead to enhancement in the dynamic yield stress, which is accounted for by the utilisation of Johnson-Cook model in the present numerical study. To obtain suitable representation of the dynamic yield stress, LS-DYNA results were initially processed to determine the effective (or von Mises) stress (which is not necessarily the yielding stress) versus effective plastic strain curve for each element (using the integration point at the mid-plane of the plate). These curves, then, are averaged by integration over the plastic strain. Hence, elastic rebounds are eliminated automatically since the plastic strain is held fixed during such events. This averaging process is performed for all elements, and hence a spatial profile is obtained for the dynamic yield stress (again, a point on the profile is the average estimate of the dynamic yield stress over the entire course of plastic deformation). Such representation of the dynamic effective yield stress, in the described average sense, is presented in Fig 5.18.

Since the targets are impulsively loaded and their material is strain-hardening and strain-rate dependent, the increase in the dynamic yield stress provides extra resistance to further plasticity, i.e., the material strain-hardens. As such, subsequent plastic strains evolve more slowly, and, hence, the magnitudes of strain-rates are expected to diminish. That is, the profiles of strain-rates based on the maximum values are not entirely representative of the whole deformation path. Nevertheless, the maximum profiles were shown earlier, in Fig. 5.16, to obtain a quantitative sense of the order of high strain-rates that could arise in the impulsive loading regime. For the present problems, the maximum strain-rates are in the range of 10^6 times the quasi-static threshold of strain-rate (which is $\dot{\varepsilon}_0 = 0.0014$ [1/s] for the Domex-355 steel material (Curry, 2017)); the extreme yield enhancement in the foregoing analysis due to the strain-rate effect alone amounts to 263%.

When the profiles of the average dynamic stresses, as given in Fig. 5.18, are averaged further over the circular area of the plates (by spatial integration), a measure of the global dynamic stress is obtained for each numerical experiment. For clarity, the global dynamic stress is averaged twice (first over the plastic deformation cycle at a particular spatial coordinate, then over the circular area of the plate). The ratio of the global dynamic stress to the experimentally measured quasi-static (or initial) yield stress is, then, related

to the total impulse from a given specific impulse distribution for the same numerical experiment. This is shown in Fig. 5.19, which shows a (nearly) linear dependence of the increase in the global yield stress of the plates on the imparted total impulse from the blast loading.

The aim of the foregoing presentation of additional results from the numerical simulations using LS-DYNA is to provide the reader with accurate representation of the more realistic effects of near-field blast loadings on the response of thin plates, especially in areas where the present analytical model (the main work of the thesis) exhibits deficiencies. The foregoing discussion, also, highlight that further research is, indeed, required to improve the developed model, such as by addressing the effects of in-plane displacements on the membrane strains and the strain-hardening and/or strain-rate sensitivity of the material on the dynamic increase in the yield stress and the corresponding local distribution of the effective plastic strains. This can be essential as the basis of design against material failure is typically based on the maximum plastic strains (just before fracture) and the regions of severe plasticity in the target's area, i.e., where failure is likely to initiate.

Although the near-field blast loading is highly localised, as seen in Fig. 5.15 in terms of the blast-generated specific impulses, the target's plasticity appears to spread laterally in some numerical experiments, e.g., see Fig. 5.17 for effective plastic strain profile in the M200-S35 experiment. This is attributed to the smoothing effect of the work-hardening of the material. Elveli et al. (2022) and Granum et al. (2019) point out that low hardening plates under blast loadings exhibit pointed (or distinct localisation of) plasticity patters in the permanent deformed profiles, while plates with considerable work-hardening result in smeared (or smooth) distribution of plastic strains and permanent deformed configuration.

Finally, the present numerical analysis quantitatively demonstrate that the thin plate's membrane action is a primary mechanism to dissipate the blast-imparted initial kinetic energy in a distributed manner, e.g., see the lateral spread of the average dynamic yield stress profiles shown in Figs. 5.18 and 5.11, and the profiles of final effective plastic membrane strain in Fig. 5.17. A structure's ability to distribute plasticity even though it was subjected to intense localised loading offers practical advantage such that the material is more efficiently exploited; the whole structure is being actively utilised to dissipate the inputted kinetic energy, and the (ductile) membrane, due to its thinness, can be relatively light in weight. The set-ups of the numerical analyses and the values of the parameters in the material and equation of state models are as given in Section 5.3.

5.7 Summary and Conclusions

The primary aim of this chapter was to assess the accuracy of the analytical model for the general case of non-uniform specific impulse. Such distribution of the specific impulse is the actual case encountered in typical near-field blasts. Thus, investigating the model performance for the considered case is of significant practical importance. To accomplish

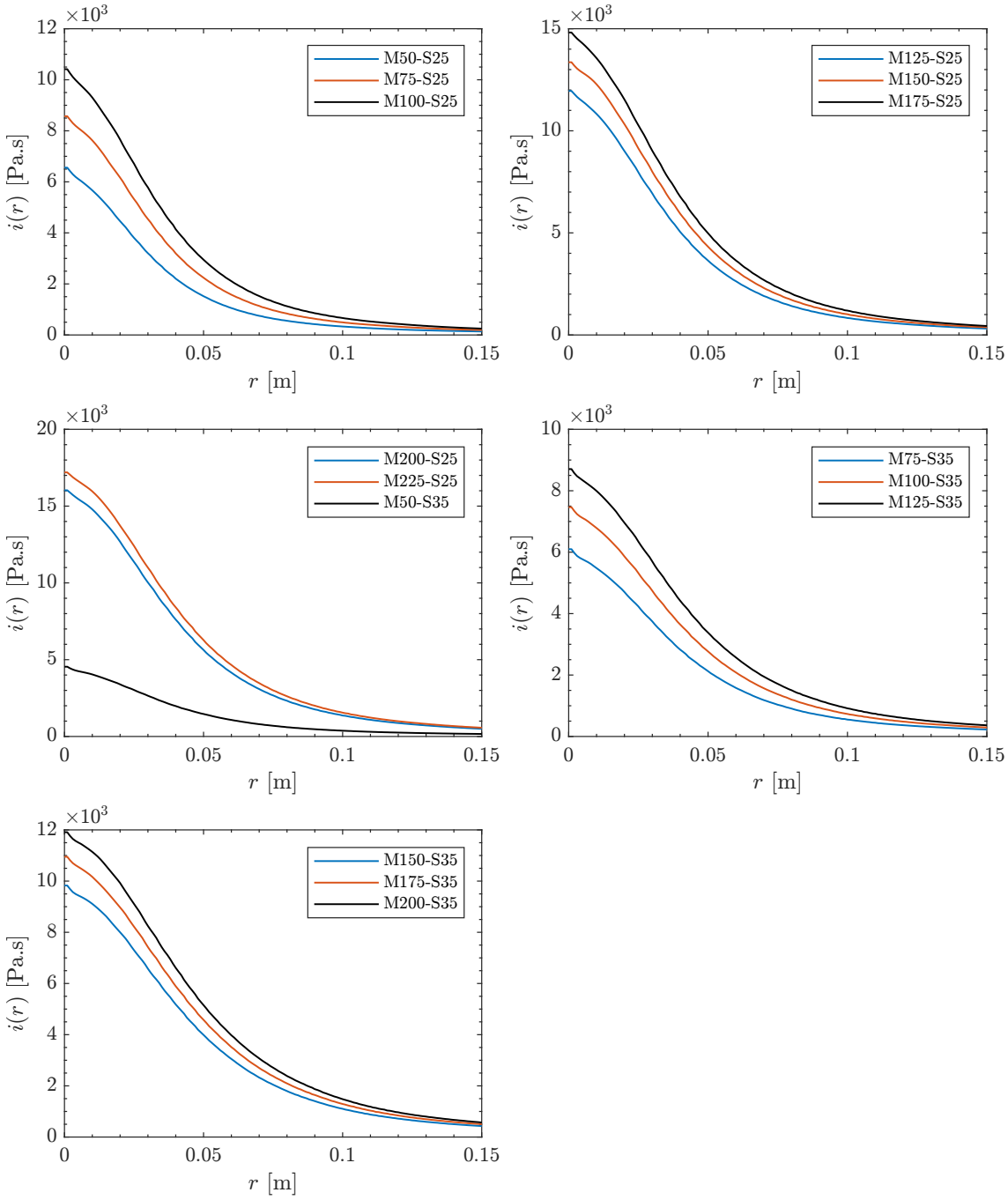

Fig. 5.15. Specific impulse distributions from near-field blasts that are labelled by Mx-Sy where x is the mass in [g] of the spherical PE4 explosive, and y is the clear stand-off distance (measured from the plate's centre) in [mm].

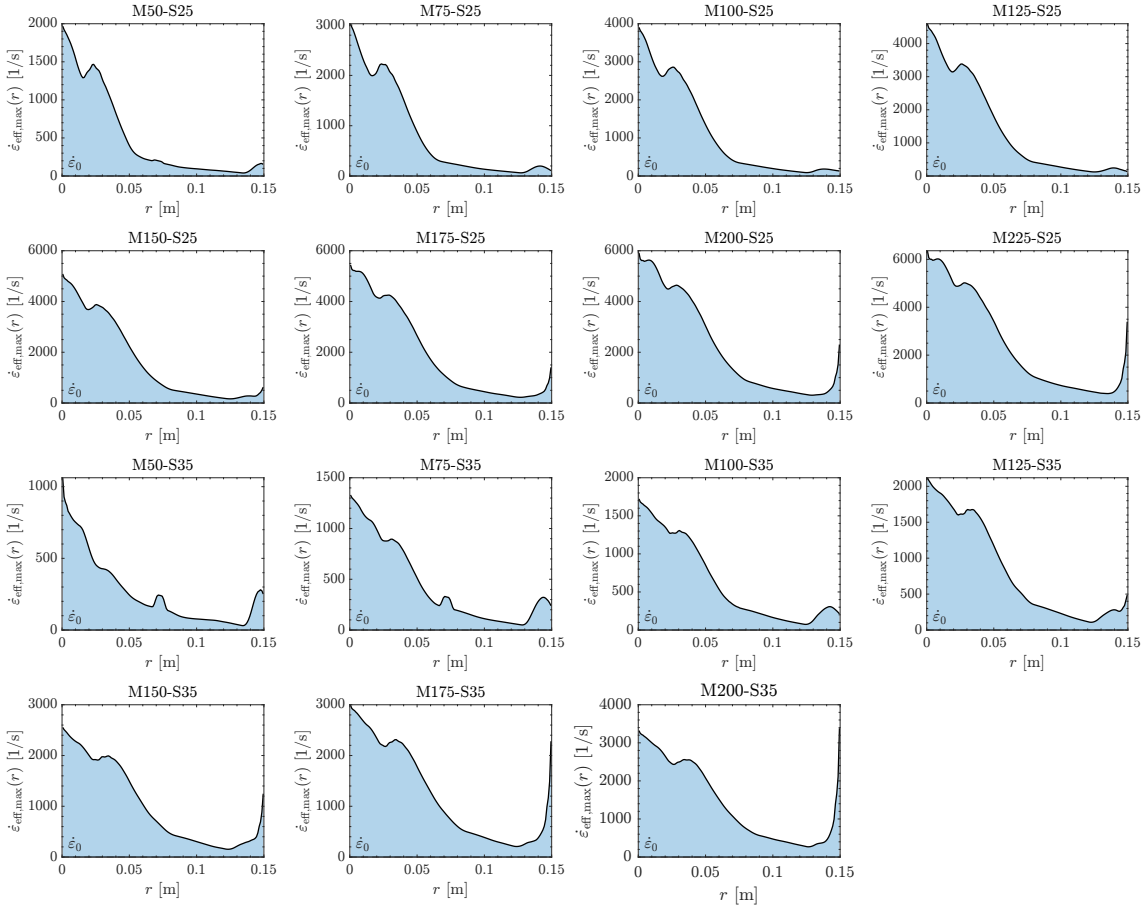

Fig. 5.16. Maximum plastic strain-rate distributions in circular thin plates when subjected to near-field blasts. The blasts are labelled by Mx-Sy where x is the mass in [g] of the spherical PE4 explosive, and y is the clear stand-off distance (measured from the plate's centre) in [mm]. The corresponding specific impulses were given in Fig. 5.15. The plastic strain-rate at a point (in the profiles) is the maximum strain-rate in the corresponding time history at that point. Shown by the dashed horizontal line in each sub-graph is the value of the quasi-static threshold of strain-rate, $\dot{\varepsilon}_0$; notice that these lines are hardly distinguishable from the zero axis line due to the relatively small value of $\dot{\varepsilon}_0 = 0.0041$ [1/s].

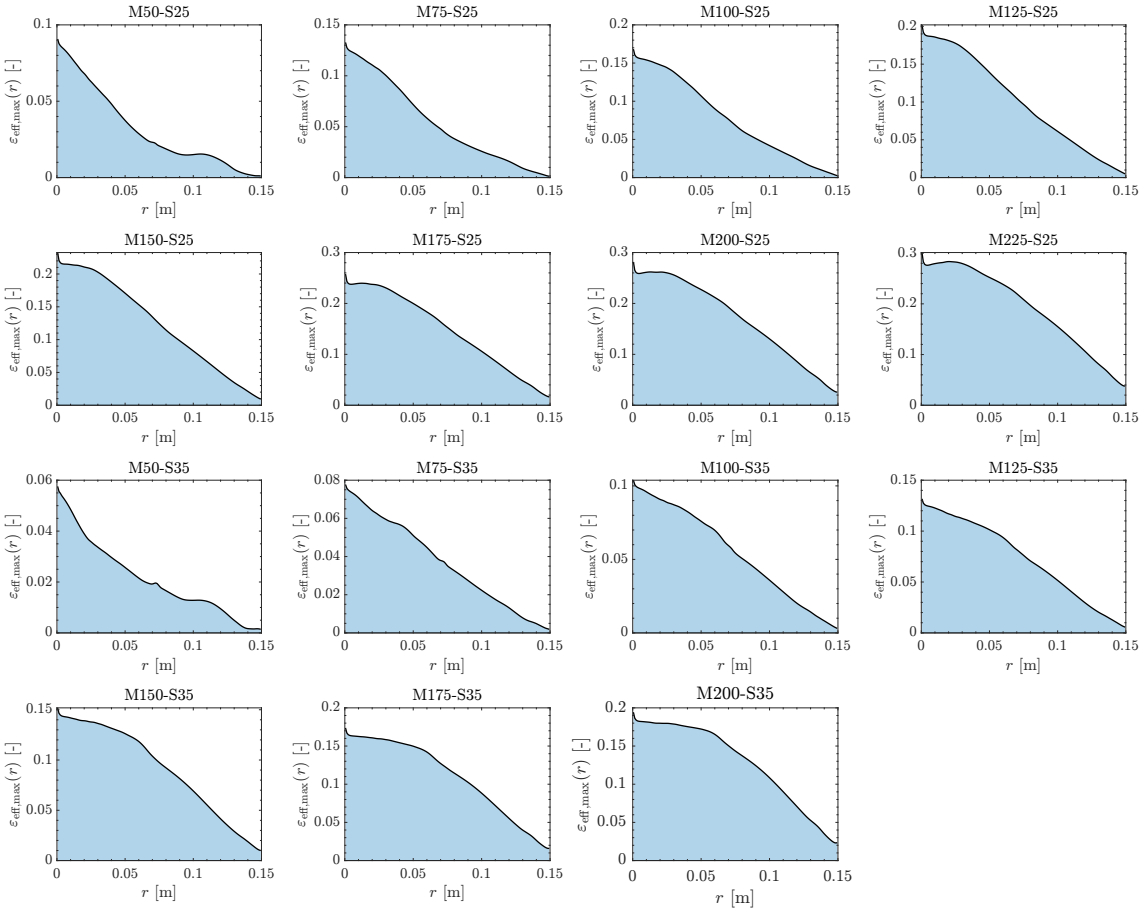

Fig. 5.17. Maximum (effective) plastic strain distributions in circular thin plates when subjected to near-field blasts. The blasts are labelled by Mx-Sy where x is the mass in [g] of the spherical PE4 explosive, and y is the clear stand-off distance (measured from the plate's centre) in [mm]. The corresponding specific impulses were given in Fig. 5.15. The plastic strain at a point (in the profiles) is the maximum plastic strain in the corresponding time history at that point. Observe that the region of large plastic strains are near the plates' centres; the analytical model incorrectly predict zero plastic strains near the central part of the plates. This limitation is attributed by the presence of in-plane displacements despite their insignificance in the determination of the plate's permanent profile of the transverse displacement.

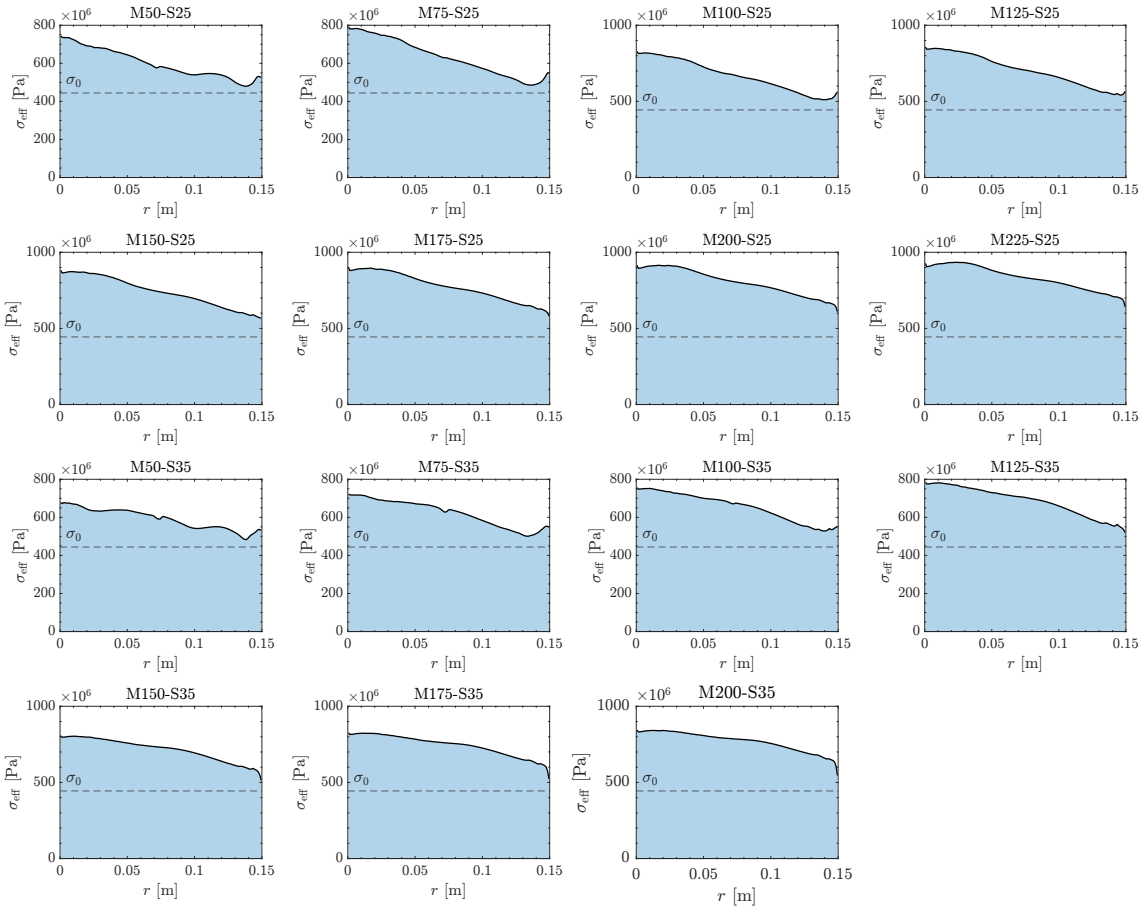

Fig. 5.18. Average effective (or von Mises) yield stress distributions in circular thin plates when subjected to near-field blasts. The blasts are labelled by Mx-Sy where x is the mass in [g] of the spherical PE4 explosive, and y is the clear stand-off distance (measured from the plate's centre) in [mm]. The corresponding specific impulses were given in Fig. 5.15. The effective yield stress at a point (in the profiles) is the average stress that is determined by integrating the von Mises stress versus effective plastic strain curve at that point. The plate's material assumed as Domex-355 steel and is modelled by the JC material model in LS-DYNA. It is seen that the effective dynamic stress is well above the quasi-static (or initial) yield stress, $\sigma_0 = 444\times10^6$ [Pa], (represented by the dashed horizontal lines). This is explained by the large magnitudes of the effective plastic strains and strain rates experienced during the deformation regime of the near-field blast-loaded plates. Figs. 5.16 and 5.17 provide graphical representations of the profiles of effective plastic strain-rate and effective plastic strain, respectively.

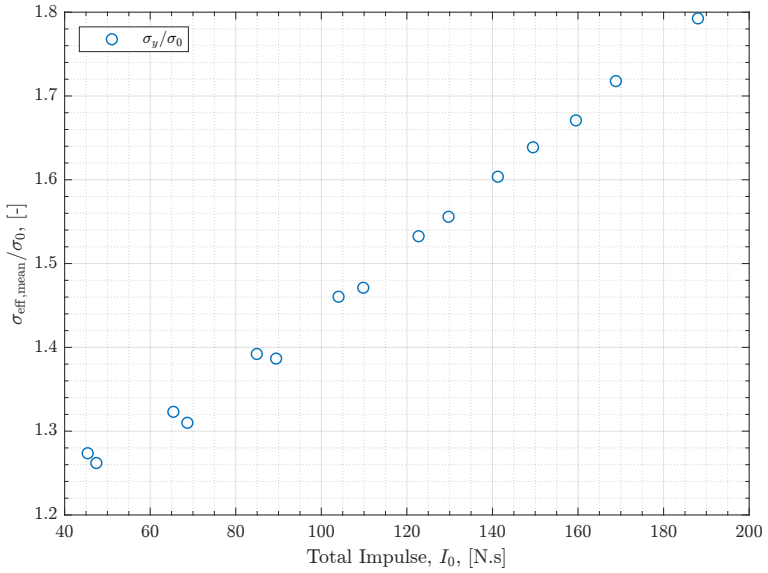

Fig. 5.19. Ratio of global dynamic yield stress to quasi-static yield stress versus total impulse. The global dynamic yield stress is the spatial average of the profiles shown in Fig. 5.18. The total impulses, I_0, are the spatial integrals of the specific impulse profiles shown in Fig. 5.15. The quasi-static yield stress is taken as 444 [MPa], which corresponds to the experimental value in Curry (2017) for the Domex-355 steel.

this, validation data were obtained from relevant experiments, performed by others, and high-fidelity numerical predictions from LS-DYNA. Concerning the loading parameter, the used experiments reported only the total impulses instead of the actual specific impulses imparted on the structural plates. Hence, it was necessary to carry out numerical explosive blast analyses, using the MM-ALE technique in LS-DYNA, to replicate the explosive events, using the blast configuration detailed in the experimental source, and thus reproduce the specific impulse fields. The numerically obtained specific impulse is eventually used in the analytical model to provide predictions of the structural target response. In addition, these calculated specific impulses are inputted in subsequent purely Lagrangian structural simulations, in LS-DYNA, to obtain the target response. The analytical model was then compared to the experimental and LS-DYNA results.

Additional LS-DYNA simulations, both explosive and structural, were performed to investigate and present the effects of the near-field blasts, in terms of specific impulse distributions, on the structural responses of thin Domex-355 steel plates. The utilised material models and their underlying theories as well as an overview and considerations of relevant best practices of the ALE technique were discussed. Due to the large size of the numerical analyses, and the associated post-processing, a highly practical MATLAB function was developed to automate reading the binary outputs from LS-DYNA, the source code of which will be made public.

The main conclusions, drawn from the work presented in this chapter, are:

- The sequential termination strategy, which is adopted for the response of plates under uniform specific impulse, is found to overestimate the plastic response when the specific impulse is highly non-uniform;

- A new solution termination strategy is introduced and greatly improves the accuracy of the membrane model for the non-uniform specific impulse (i.e., that arises from an actual near-field blast event). The new strategy requires the termination of the solution (of the plastic wave equation) when the local kinetic energy (i.e., the kinetic energy at a particular point) reaches zero for the first time after it was initially non-zero. Thus, the solution is terminated when the total velocity (the sum of dominant modes) reaches zero;

- The membrane model (based on the new termination strategy) is found to agree well with the used validation data, from experiments performed by Curry (2017) and Curry and Langdon (2017) and results from LS-DYNA simulations performed as part of the present work;

- The numerical simulations of near-field blast events using the MM-ALE in LS-DYNA are shown to provide reliable predictions of the near-field blast-generated reflected positive specific impulse distributions. The profiles of the specific impulse appear to capture the important features of near-field blasts, such as the high sensitivity to variations of stand-off distances and angles of incidence. These profiles follow the Gaussian spatial distribution as predicted by Pannell et al. (2021). The total impulse (obtained by spatial integration of the specific impulse) compares reasonably with the corresponding experimental measurements in Curry and Langdon (2017), when the findings of Rigby et al. (2019b) and Rigby et al. (2019a) are taken into account;

- In the structural LS-DYNA analyses, where thin steel plates are subjected to non-uniform specific impulse, it is found that plasticity (as measured by the effective total plastic strains) of the plates develops and progresses through the majority of the domain (the planar areas of the plates), in the early phase of the response. The responses of the targets are, hence, mainly plastic. Furthermore, the peak displacements are attained in the early phase.

- The model predictions and LS-DYNA numerical results on the plastic responses of the thin targets both show linear dependence on the energy-equivalent total impulse, as first developed and discussed in Rigby et al. (2019a) and Tyas and Pope (2003).

Chapter 6

Discussion

6.1 Overview of the Work

The work contributes to the engineering field through the fast-running engineering models (FREMs) framework (Dennis and Rigby, 2023). In particular, the present research provides a FREM tool by adopting a set of idealising assumptions in an attempt to reasonably reformulate and simplify the physical problem such that only the most dominant mechanical features are retained while achieving accurate fast-running predictions. The model should be able to predict the response of thin targets under a near-field blast loading. This can be explained by noting, as informed by experiments and past analytical studies in the literature, that real plated structures would respond to the near-field blast loading impulsively, by undergoing considerable plasticity, and through dominantly membrane mode of deformation. These mechanical features are those that are retained in the mathematical formulation of the problem to be solved. The main outcomes of the present work are: (i) the development and derivation of the equation of motion that applies to the transverse motion of impulsively blast-loaded rigid-perfectly plastic membrane in the absence of in-plane displacement; (ii) the identification of the conditions defining the applicability of the derived equation of motion and their implications on the solution; and (iii) the solution of the equation of motion, i.e., the wave equation, and a strategy to terminate the solution to respect the conditions of physical applicability of the mathematical model. Since the equation of motion of the membrane is valid only conditionally, and it is very important to identify the conditions of its validity, this topic has been given a full treatment in a separate chapter, Chapter 3, of the present thesis.

The fundamental limitations of the present work are primarily due to the adopted assumptions in the model's development. These are the inabilities to account for (i) the in-plane displacements on the membrane (plastic) strains; and (ii) the realistic plastic effects of strain-hardening and strain-rate sensitivity when the plate's material exhibit such features, as the case for common ductile materials in practice. Associated with these drawbacks, the accuracy of the model is confirmed to be only reasonable for the prediction of the *global* response of the blast-loaded thin plate, i.e., the transient and permanent

transverse deformed configuration. At the local level, the profiles of effective plastic strains are incorrectly predicted by the model as these profiles qualitatively deviate from those observed experimentally, as emphasised in Cloete and Nurick (2014), and obtained by numerical simulations using LS-DYNA by the author. In the local sense, other deviations are expected due to flexure, particularly near the clamping edges of the membrane, and due to elasticity of the material. There is an additional limitation of the model that is explained as follows. The model assumes that when the blast imparts specific impulse on the target, the target picks up an initial velocity, according to Rigby et al. (2019a) and Tyas and Pope (2003), which triggers the motion of the membrane (i.e., the target). Then, the membrane's motion induces deformation, and its material is assumed under active yielding (i.e., the yield condition is assumed to be satisfied). As such, the present analytical treatment cannot identify the level of imparted impulse below which no plasticity would develop. For clarity, the model assumes the onset of plasticity regardless of the magnitude of the impulse (and, hence, the initial velocity), provided that it is non-zero. The main reason of this (arguably inevitable) drawback is the non-linear nature of the membrane problem in the pre-plastic regime; note that membranes (or strings in the one-dimensional case) would not sustain lateral loadings without being transversely deflected (i.e., the transverse equilibrium of the structure is displacement-dependent, hence, geometrically non-linear) unless the structure is initially under large pre-tension (Rao, 2019a).

Despite the above limitations, the model is shown to be reasonably accurate for predicting the gross (or global) effects of the impulsive blast loading on the response of the targets. During the model's validation, predictions are compared to realistic observations from both experiments and high-fidelity numerical simulations. The specimens in the validating experiments are thin plates with finite thickness, and some of their materials have realistic plastic characteristics (i.e., strain-hardening and visco-plasticity, or strain-rate sensitivity). Furthermore, the impulses are associated with real blasts generated by detonations of high explosives. Related to the existing knowledge, the present work provided the novel contributions that the impulsive blast loading can be arbitrary in terms of spatial distribution, and the ductile material obeys the von Mises yielding criterion, which is the most widely adopted criterion of initial yielding in the current practice of metal plasticity. Furthermore, the present work jointly contributes to engineering research where the complexity of the original mechanical problem is reduced to obtain practical first-order approximation of the solution. The adopted assumptions are informed by existing knowledge that is credited to others.

6.2 Notes on the Model's Applicability

As the aim of the work is to provide practising engineers with simple and fast-running model to analyse near-field blast-loaded thin plates, it is vital to discuss some preliminary guidelines on when the model should be used with confidence. Although, thorough and extensive treatment is beyond the scope of the undertaken study, and, as such, further

research is deemed necessary as will be highlighted in the following.

The model, in overall, is applicable when:

(1) The blast load is impulsive such that the actual duration of the positive phase duration is considerably less than the time of maximum response of the given target. In the current practice of simplified blast analysis of structures based on the UFC (2008) manual, the loading-response domain is impulsive when the ratio of load duration to the time of maximum response is less than one-third. However, this practical definition is based on the initial elastic response of an elastic SDOF structure. That is, the time of maximum response of the SDOF system is related to its frequency, which is related to the elastic stiffness and, in turn, the appropriate elastic modulus. However, when the structure experiences elastic-perfectly plastic deformation, the calculation of the maximum time response depends additionally on the plastic characteristics (namely, associated with the change in stiffness and mass factors based on the assumed deformed shape in the plastic range). The manual, see Section 3.17-4 in U.S. Army (2008), suggests that the calculation of the maximum response time can be based on plastic response alone when the structure undergoes large plastic deformations.

The present model concerns the purely plastic response of the structure that is governed by the developed plastic wave equation. In particular, the time of maximum response is derived to be related to the plastic wave speed that, in turn, is related to the tensile yield stress of the membrane. Thus, as the yield stress is typically substantially smaller than common elastic moduli of ductile materials, the time of maximum response of a purely plastic membrane is much longer than that of an elastic counterpart structure. In other words, when there is confidence that a given blast loading acts impulsively on a relevant elastic thin plate, then the plastic membrane response of the thin target would be much more impulsive.

As a preliminary guideline, the same rationale on defining the practical threshold on the impulsive regime in the SDOF analysis can be extended to the present problem of a rigid-perfectly plastic membrane. Although, it should be emphasised that this conclusion is theoretical, and elaborate investigation is needed to address the issue. The basis of the above guideline is that the impulsive regime, which is an idealisation, tends to be justifiable when the displacement (in the direction of the applied external load) at the end of the load duration is small so that the external work is effectively absent. Therefore, the input energy is due only to the kinetic energy that is built up during the load application. The transition from perfectly impulsive to completely quasi-static regimes is gradual, as can be understood from an SDOF analysis. The practical thresholds, in Biggs (1964) and the U.S. Army (2008), to define the "nearly" impulsive regime appear to be based on the (analytically based) observation that when the load duration to maximum response time ratio is less than (1/3), the load's magnitude and temporal variation are irrelevant, and the response is, mainly, driven

by the imparted impulse.

The reader should be aware that the condition of impulsive response based on merely the elastic characteristics of the target can be more restrictive. This condition would be relaxed if the purely plastic response is concerned; that is, a blast loading with a longer positive phase duration could be considered impulsive in the purely plastic domain, even though it is not for a purely elastic response.

Again, note that the impulse that is discussed herein is due, completely, to the blast loading. Namely, it is not associated with the *excess* force (blast force minus plastic resistance force). Thus, the impulse estimate is conservative in the above discussed sense. As will be discussed later in this section, the present theory is incapable of determining the plastic resistance pressure (i.e., the one below which the target would be completely elastic).

Lastly, the impulsive regime implies that the initial velocity of a point on the target is associated with the amplitude of specific impulse at that point, $\dot{w}_0 = i/(\rho h)$, where $\dot{w}_0$ and i are the initial velocity and specific impulse at the same coordinate on the target. That is, the initial velocity is not affected by the specific impulse at neighbouring points. This has been called the upper bound kinetic energy hypothesis in Rigby et al. (2019a) and Tyas and Pope (2003), in which the wave speed, during the application of the blast pressure, is zero due to the zero shear (stiffness) modulus of infinitely thin targets. It should be mentioned that the findings of the above-cited authors are the main basis of the adopted assumption that the thin plate responds to the near-field blast impulsively. Namely, as discussed in Section 2.2.5, Rigby et al. (2019a) and Rigby et al. (2019b) provided experimental and numerical evidence that the response of a thin plate to a near-field blast is impulsive, i.e., it is mainly driven by the specific impulse alone which gives rise to a proportional initial velocity field.

In the present work, the (plastic) wave speed of transverse motion of the membrane is derived as a function of the tensile yield stress. Mechanical information propagates laterally with this speed. Hence, by the end of finite durations of reflected blast waves, partial specific impulses from neighbouring points could affect the accumulated initial velocity at a given point since the wave speed is finite (i.e., non-zero); mechanical information is likely to be arrived from different points to the point under consideration. Although, since near-field blasts are typically associated with extremely short durations, and the plastic wave speed is dependent on the yield stress (and, hence, practically small when compared to the speeds associated with elastic shear moduli), then, the "perfect" impulsive regime can reasonably be assumed to hold. Equivalently, the mechanical information, practically, has no time to propagate laterally. That is, $\dot{w} = i/(\rho h)$ is valid, and accordingly the blast loading is fully characterised by the specific impulse alone.

(2) The structure is a thin plate that responds in a pure membrane mode of deformation. As such, the target should be thin in the sense that the ratio of loading span to

thickness is high. From existing knowledge, one can define the target to be thin plate (i.e., without presence of transverse shear effects) when this ratio exceeds 20 according to Reddy (2007) for elastic plate responses. Although, in Mehreganian et al. (2019b) and Blaauwendraad (2010), the thin-plane response domain is dominant when the span to thickness ratio is greater than or equal to five (5) for rigid-plastic plates. The corresponding ratios for the specimens used in the validation data (with which the model was shown to give accurate predictions) are in the order of 30 or more. Thus, this is a safe preliminary value to recommend; a higher value is suggested to practically ensure the applicability of the large displacement regime in the thin plate response. The flexural resistance can be negligible, in comparison to that due to the membrane action, for very thin plates. However, the membrane resistance additionally depends on the magnitude of the transverse displacement. When the displacement is large, the membrane resistance (or geometric stiffening) can dominate the overall response.

The criterion to determine the domain of pure membrane action is more well-defined. In his excellent book, Jones (2012) defines the membrane threshold of response when the ratio of maximum transverse displacement to thickness is equal to 1 for fully clamped rectangular plates or (1/2) for simply supported plates. Additional helpful classification is provided by Cloete and Nurick (2014), in which a ratio of about 2.5 is proposed. These are the suggested thresholds of maximum transverse displacement to thickness ratios at which the response transition from the initial flexural-membrane to the eventual pure membrane mechanisms.

However, the model treats the thin target as a pure membrane from the onset of motion (i.e., as soon as deformation starts). Hence, the analyst is advised to treat the target as a membrane then verify the validity of the membrane-only assumption by computing the ratio of the maximum displacement to the target's thickness; the calculations are deemed satisfactory when Jones's condition, i.e., the ratio is at least one, is met. In summary, the model is applicable when the plate is thin (so that transverse shear is not an issue), and the transverse displacements are large (so that flexure can be neglected). To ensure the validity of this statement, the above criteria can be utilised as practical guidelines.

(3) The transverse response is primarily dominated by the plastic deformations of the blast-loaded target. This is crucial as the model assumes the target to be rigid-perfectly plastic. Hence, the model is applicable when the elastic deformations can be deemed negligible. Note, as briefly mentioned in Section 6.1, that if elasticity of the membrane is retained, the problem will be geometrically non-linear, regardless of the linearity in the constitutive (or material) behaviour, which could make it difficult to be solved analytically. Since stresses are constant for a rigid-perfectly plastic membrane, a linear equation of motion has been found.

There is a general agreement in the literature that elasticity can be neglected whenever the blast-induced initial (or input) kinetic energy (i.e., in an impulsive regime)

is several orders of magnitude, e.g., ten times, larger than the maximum elastic energy associated with the actual target response; the reader is referred to Section 3.10 in Jones (2012) for a discussion on the validity of the rigid-plastic assumption; in addition, see Sections E.1 and E.2 in Appendix E. However, determination of the maximum elastic energy of a membrane is non-trivial as the elastic response is non-linear, as mentioned earlier. Therefore, a practical approach would be to subject the membrane to small impulsive loading and obtain predictions of the elasto-plastic response and compare them with the model predictions. The deviation (or inaccuracy) of the model predictions from the obtained results can be used to define a practical threshold defining the insignificance of the elastic portion of the overall response. It is instructive to note that for the initiation of plastic deformation of a thin plate, the transverse displacement is initially small, and hence plastic bending (which is assumed negligible herein) predominates membrane action (Hopkins and Prager, 1953).

The same applies to the validity of neglecting the additional resistance provided by strain-hardening and strain-rate sensitivity, when applicable, beyond the material's initial yielding. As the model assumes perfect plasticity, the model can be regarded as conservative when applied to targets made of strain-hardening and strain-rate sensitive ductile materials. However, the model predictions can be improved when the initial yield stress of the material is reasonably amplified to grossly account for the extra (or the increased dynamic) strength, as discussed in Section 4.6.1.2 to address the contribution of strain-hardening; in Appendix E, the work-hardening effect on the global response is discussed and compared to the corresponding rigid-perfectly plastic solution.

The increase in dynamic yield stress due to merely the strain-hardening is bounded as can be observed from quasi-static tensile testing of the material, and noting that plastic strain is limited by the material's failure (or ultimate) strain. However, the corresponding increase associated with high strain-rates appear to be unbounded, and there can be a situation where a priorly assumed amplification can be overconservative if it is based on unrealistically high strain-rates. The reader is referred to Gharababaei and Darvizeh (2010) for an approximate treatment to account for the dynamic increase of yield stress in the analytical treatment of blast-loaded circular thin plates responding in a single mode (which coincides with the first mode predicted by the present theory for circular membranes). However, it is found herein that it is more balanced to neglect the strain-rate sensitivity until a reliable predictive technique is developed to estimate the likely order of magnitude of strain rates associated with a given impulsive blast load amplitude and non-uniformity; the important parameter of the energy-equivalent total impulse due to Rigby et al. (2019a) is envisaged to be critical, in addition to the area-integrated total impulse. The proposed treatment, in above, of accounting for the dynamic increase in the yield stress are empirical in nature, and it is justified according to the findings of the

present study that the inclusion of the aforementioned plastic characteristics in the mathematical formulations would lead to a non-linear equation of motion. The above discussion concerns the "global" effect of strain-hardening and the visco-plasticity; the corresponding effect of these plastic characteristics on the local response, e.g., in terms of effective plastic strain field, will be addressed later in Section 6.6.

Nevertheless, it should be re-emphasised that the overall aim of the present work is to balance the problem's accuracy-and-simplicity and achieve a fast-running and practical solution. As has been discussed herein and throughout the thesis, the developed model attempts to idealise the actual problem and provide solution of the simplified version of the problem. The model is found to have inherent limitations that are imposed by the adopted assumptions. The limitations are fully acknowledged, the bases of which are identified, and the need for further research is appropriately highlighted.

(4) The blast loading is monotonic, and the target is strain-free initially. An impulsive blast load is monotonic in the sense that there is no loading reversal, and its spatial distribution is invariant. However, the (plastic) deformation regime should be progressive in terms of yielding since the model is based on the total (or integral form of the incremental) flow rule. This means that the model is applicable as long as there is no decrease of the plastic work, and the solution of the response is valid until this statement is violated. The subsequent response is taken to be the state of the target just prior to the terminated solution (i.e., the last valid state). The author believes that the impulsive nature of blast loading and a solution termination strategy can be taken as an approximation to fulfil the above statement. To guide the reader and explain the basis of the importance of the solution termination, further material is provided in Appendix G describing a relevant and simple problem of a rigid-perfectly plastic SDOF model so that the important physical concepts can be described in full detail without being hidden by the mathematical complexity. There are two solution termination strategies, which are proposed in the present work, as will be discussed later in Section 6.5.

6.3 On the Definition of the Near-Field Blast Loading and Its Non-Uniformity

The thesis discussed two alternative methods to define the practical limit for the classification of the blast loading as near-field blast. First, Tyas (2019) defines the near-field blast according to the scaled distance, namely when it is less than or equal to 2; the reader should be aware that shock fronts' irregularities, i.e., Rayleigh-Taylor instabilities, are present, which might influence the local spatial distribution of the near-field blast loading, when the scaled distance is between 0.5 and 2 (Tyas, 2018). Additionally, Gel'fand et al. (2004) proposes an alternative definition for the near-field blast domain that is based on

the characteristic size of the blast wave (when it reaches the structure) in comparison to a multiple times the nominal size (e.g., radius) of the explosive charge. The reader is referred to Section 2.1.8 for further details.

The model of Pannell et al. (2021) provides a mathematical characterisation of the spatial distribution of the specific impulse from near-field blasts associated with spherical explosive charges. According to their model, the specific impulse, due to typical near-field blasts, assumes a Gaussian spatial profile, i.e., generally non-uniform. The practical parameter of the impulse-enhancement factor that is derived by Rigby et al. (2019a) can be utilised as appropriate measure to quantify the non-uniformity of any specific impulse distribution. When the factor is 1, the distribution is perfectly uniform. The specific impulse's non-uniformity increases as the factor increases above 1. The impulse-enhancement factor can be readily computed once the specific impulse distribution is obtained (Rigby et al., 2019a).

The blast analyses, presented in Chapter 5 for the validation of the model against non-uniform loadings, correspond to values of 1.4 or greater for the impulse-enhancement factor. The specific impulses distributions agree with the Gaussian model of Pannell et al.; furthermore, the blasts are associated with clear scaled distances of less than 0.15 [m/kg$^{1/3}$], see Table. 5.4, and, hence, the explosive events correspond to near-field blasts according to Tyas's definition.

6.4 Solutions for Irregularly Shaped Targets

In the development of the present model, the membrane geometry is arbitrary provided that the membrane is pin-supported along its outer edges. Thus, the derived plastic wave equation should be applicable for arbitrary shapes of the membrane. This is supported by the fact that the circular membrane equation of motion was achieved by, simply, transforming the wave equation in rectangular coordinates, and the circular and rectangular models were shown to be of equal performance when compared to their corresponding validation data. Hence, the wave equation should apply to any membrane's shape. Although, as discussed in Chapter 4, analytical solutions were given only for the rectangular and circular geometries, which are the most common shapes in practice, as they are simple to derive. In addition, the given circular solution is limited to axi-symmetric specific impulse distributions.

Thus, when the target is of irregular or complex shape, it is vital to provide preliminary guidelines on how to predict the solution using the present theory. The suggested procedure, in the following, is numerical and consists of two steps: solving the conditionally valid wave equation and adaptation of a solution termination strategy to respect the applicability of the wave equation. Thus, in the first step, one might start with the plastic wave equation of the present theory and solve it numerically to obtain the transverse displacement of the target. Example techniques to numerically solve the plastic wave equation

can be any method of choice that is applicable for a hyperbolic scalar partial differential equation (PDE) in two dimensions (2D) for bounded domains, e.g., the finite element (FE) method, the finite difference method, or the spectral method; the reader is referred, e.g., to the recommendations in Marfurt (1984) and Komatitsch et al. (1999). Although, it should be mentioned that when the spatial domain is arbitrary (as the case in the foregoing discussion), then the first method can be more effective. The domain's boundary should be treated as reflecting, or non-absorbing, as the given plastic wave equation concerns membranes that are fully pinned (or restrained) along the periphery.

It is believed that the adaptation of the present plastic wave equation, as the starting point, would lead to considerable advantages in terms of the computational cost of the implied numerical approach. In particular, as can be seen in the plastic wave equation, the only variable (or unknown) is the transverse displacement (i.e., the stresses are fixed and the incompressibility of the membrane is inherently taken into account). Furthermore, since the wave speed is related the yield stress (which is substantially smaller than typical elastic moduli), the restrictions on the time step size in an explicit time integration are much more relaxed, i.e., larger time steps can be used without stability issues for a given mesh resolution (or element size). In addition, since the PDE is linear, involves constant coefficients, and homogeneous (i.e., forcing term is zero due to the impulsive loading), then it can be more efficient to utilise the (unconditionally stable) implicit time integration scheme without convergence issues since no iterations are needed per one time step. Nevertheless, it should be re-emphasised that the membrane must be restrained (against transverse displacement) along its entire periphery, as the developed model does not address the presence of stress (or natural) boundary conditions, e.g., free edge(s).

The same (numerical) approach is suggested to the case of circular membranes that are subjected to non-symmetric specific impulse distributions (i.e., when the circular problem is not axi-symmetric). The reader is warned that the main wave equation for the circular problem is only applicable for the axi-symmetric case, as the term depending on the angular coordinate is removed from the equation. That removed term is given in the text following the first presentation of the polar wave equation. For clarity, the equation of motion for circular membranes under non-axi-symmetric impulsive loading is given below

$$\frac{2}{\sqrt{3}}\sigma_0 \left[\frac{\partial^2 w}{\partial r^2} + \frac{1}{r}\frac{\partial w}{\partial r} + \frac{1}{r^2}\frac{\partial^2 w}{\partial \theta^2}\right] = \rho \ddot{w}. \tag{6.4.1}$$

which should be solved under the following conditions

$$w(R,\theta,t) = 0, \qquad w(r,\theta,0) = 0, \qquad \dot{w}(r,\theta,0) = \frac{i(r,\theta)}{\rho h}. \tag{6.4.2}$$

Since the plastic wave equation only holds at a point on the domain when the membrane is under active plastic straining (or yielding), then the solution that is obtained numerically using the above approach needs to be processed; this is the second (and last) step, which is described as follows. The transient response is considered valid, in the point-wise sense,

until the velocity reaches zero for the first time at the considered spatial coordinate. The maximum displacement attained at a given point can be considered as the permanent displacement. The final deformed profile of the membrane is, hence, given by the envelope of the maximum displacements at all points.

The reader should be aware that the above-described rapid practical approach for the solution termination corresponds to the *total* solution termination strategy, which will be discussed in Section 6.5; hence it is applicable for non-uniform specific impulses. Note that for circular plates, the uniform impulse is already an axi-symmetric problem, and, therefore, the circular uniform model in Chapter 4.5 can be utilised.

The remaining case for irregular membrane under uniform specific impulse is suggested to be solved incrementally using a forward-time marching, i.e., in an explicit manner, as described in the following. The stable time step size, Δt_s, can be chosen based on $\Delta x^*/c_p$, where c_p is the plastic wave speed, and Δx^* is a characteristic length of the smallest element. For procedures of solving linear dynamic problems using the finite element method and the explicit time scheme, the reader is referred, among many others, to Bathe (1996) and Hughes (2012). Initially, it is assumed that the plastic wave equation holds. The solution is incremented by time stepping. By the end of a time increment, compute the (total) plastic multiplier. If it is not decreasing, then the last step is valid and the analysis is continued to the next step where the acceleration is specified by the wave equation. On the other hand, if the plastic multiplier decreased, then the previous step is revised by requiring the acceleration to be zero. The initially wrong acceleration would have been non-zero by a deformation event that cannot happen; the event is detected by a decrease in the plastic multiplier which cannot have negative rate at all times during a valid plastic deformation. The total strain can be non-zero, but in a non-monotonic deformation path, the total flow rule does not apply. Hence, the change in plastic work, which is in balance with the change in kinetic energy (and hence giving rise to non-zero acceleration), is zero. Thus, the stresses must be made zero to ensure that no change in plastic work is available for updating the kinetic energy. Since accelerations are evaluated per node in a finite element analysis, and strains and plastic multipliers are evaluated per element, say, e.g., at its centre, then interpolation/extrapolation might be necessary to determine the plastic multiplier at the nodes.

Furthermore, upon first detection of a decrease in the total plastic multiplier, the time step size might be made progressively smaller in a set of consecutive time steps to enhance the accuracy of detecting the critical time instant at which the acceleration is forced to be zero; the magnitude of the decrease in the last plastic multiplier should reflect whether the size of the time step is adequately small. Alternatively, it can be assumed that the acceleration is constant per one time step, and the approximate critical time instant can then be determined by requiring the rate of plastic multiplier at the critical time to be zero using a linear Taylor approximation in time: $\dot{\lambda}(t^*) \approx \dot{\lambda}(t_0) + \ddot{\lambda}(t_0)\Delta t_c$, where $\dot{\lambda}$ and $\ddot{\lambda}$ are the rate and acceleration of the plastic multiplier, λ, see Eq. (3.4.12), and t_0 and Δt_c are the previous time and the unknown critical time step size; t^* is the critical time

instant, $t^* = t_0 + \Delta t_c$. The above equation is solved for Δt_c by requiring $\dot{\lambda}(t^*) = 0$, and note, by assumption, that $\ddot{\lambda}(t_0)$ is negative since the objective is to detect an expected violation of the non-negativity of the rate of plastic multiplier in the next time increment; if the computed critical time step size, Δt_c from above, is greater than the given earlier stable time step size, Δt_s, then one should use the latter, i.e., the smallest, and when $\ddot{\lambda}$ is positive, then one should ignore the critical time step size and use the stable time step size. The notion of detecting the critical time instant is a primary topic in rigid-plastic analysis using the mathematical programming, e.g., linear and quadratic programming, approaches, and the reader is referred to Capurso (1972), Maier and Nappi (1984), and Maier (1968). The constant acceleration method of detecting the critical time instant was originally proposed by Capurso (1972).

It must be mentioned that the described approach has not been validated, and it is simply given as a starting point, which is a consequence of the generality of the present theory.

6.5 The Two Solution Termination Strategies and the Solution Termination Dilemma

There are two distinct solution termination strategies that are proposed to terminate the solution of the plastic wave equation. The wave equation is valid only conditionally; that is, it holds until the condition of non-negative plastic work rate is violated. This is because the developed equation of motion is based on the validity of the *total* flow rule, see Section 3.4.1. Without the total flow rule assumption, the (linear) wave equation could not be arrived at. This rule applies if (i) the loading is monotonic, and (ii) the yielding of the membrane is progressive (or the material is currently under active straining). Under these conditions, the total flow rule gives correctly identical results to the incremental flow rule, the basis of the modern plasticity theory (Prager, 1948; Drucker, 1956).

Clearly, as can be seen from Eq. (4.3.11), the wave equation relates the (point-wise) acceleration of the membrane, i.e., the right-hand side, to the left-hand side that depends on the yield stress and the measure of "total" deformation. When deformation ceases, the yield condition needs not be satisfied, and, hence, the wave equation, as given, does not hold. In this case, the acceleration must be zero, and the velocity is implied to be zero since strain-rate is zero (when the membrane is, locally, not under active straining). That is, motion stops. The total flow rule, in effect, is a tool to linearise the equation of motion, and the linear equation is the plastic wave equation. Again, the linear equation holds conditionally. Thus, when the equation is solved as it is unconditional (i.e., using the modal decomposition and sum of the modes), the solution must be terminated.

In attempt to emphasise the importance of the solution termination step, a simplified material is provided in Appendix G to explain the concept in the simplest level without unneeded mathematical complexity. Therein, it is hypothesised that an initially non-linear equation can be linearised so that it can be solved easily, then the obtained solution

(of the linear problem) is terminated posteriorly such that the linear model is physically acceptable. This is believed to be the same approach that is implemented in solving the rigid-perfectly plastic membrane problem, i.e., the main topic of the thesis. The simple problem in Appendix G will not be discussed any further.

The membrane's time-dependent general solution (of the plastic wave equation when it holds) is the sum of the modes; each of the modes solves the conditional wave equation, and the modes are mutually independent (or orthogonal to each other). In chapter 4, and in Alotaibi et al. (2023), a "sequential" solution strategy is proposed to terminate the solution, in which the modes are switched off sequentially based on the individual modal velocities. It should be emphasised that when a mode is terminated, it does not mean it is removed altogether (or considered absent); rather, the solution contribution by the terminated mode is held fixed at its termination's state. That is, that mode does not contribute to further changes of velocity (and acceleration), though the displacement associated with this mode is, generally, non-zero. This non-zero modal displacement is the final contribution to the total displacement provided by the mode in question, i.e., it is held constant as time evolves. The same applies to all modes.

Since the modal velocities reach zero for the first time at different time instants for the various modes, and these time instants are inversely related to the corresponding angular frequencies of the modes, then the modes are terminated sequentially according to the values of their modal frequencies. The modal frequencies are increasing functions of the modes' numbers, and hence the solution termination is sequential. The last terminated mode is the first mode since its frequency is the smallest. The basis of adopting this sequential strategy is that the (linear) wave equation is the one that is conditional. Therefore, if the total solution is the sum of the modes, then each mode should satisfy the wave equation *and* its condition of validity. Again, the condition is the plastic work rate's non-negativity, and without the satisfaction of which, the wave equation itself does not hold. Hence, the individual modes were forced to satisfy the latter condition.

A mode to be acceptable candidate solution to the complete system, it has to satisfy all conditions, in addition to the differential equation. It is instructive to note the following as an example. The mode's wavenumber, k_x, for the rectangular case in the x direction is $k_x = (m\pi/L_x)$ where m must be an integer so that the boundary condition, at $x = L_x$, is satisfied, i.e., $\sin(k_x L_x) = 0$. The wavenumber appears also in the angular frequency; thus, it affects the spatial and temporal variations of the displacement. Herein, when there is an extra condition, which is the plastic work non-negativity, the modes were altered such that a mode does not violate this condition. The physics of the problem is modelled by the set of all conditions: the equation of motion, boundary and initial conditions, and the plastic work non-negativity. Thus, a mode to be physically valid and hence an independent solution, it was initially proposed to terminate. Since other modes are not linearly dependent, the other modes (as independent solutions in their own) have to be terminated and, then, added together to constitute the total solution.

With the above justification, the model solution was simplified to derive the expression of

the permanent displacement (when all modes were terminated). In mathematical terms, the membrane attains its permanent shape when the value of the temporal (sinusoidal) factor is taken to be one for all the modes when adopting the sequential modal termination strategy. The total plastic work associated with the obtained permanent deformed profile is derived to be in balance with the initial kinetic energy, see Eq. (C.3) in Appendix C. This simplification led to the derivation of a closed-form solution for the *uniform* specific impulse case of loading.

The uniform model (which is based on the sequential modal termination) was shown to reasonably agree with the validation data that corresponds to uniform impulsive blast loadings, see Section 4.6. Therefore, it is concluded that a fast-running and reasonably accurate model is achieved for the uniform specific impulse case, and the sequential modal termination strategy is shown to be appropriate from the practical perspective. Furthermore, the uniform model excellently agrees in functional form with the well-performing model of Nurick and Martin (1989a) and its modified version by Chung Kim Yuen et al. (2016), see Section 4.6.3. The functional form of the closed-form solution of the present uniform model is a primary consequence of the sequential modal termination strategy. Therefore, it can be said that the present model, for the uniform impulse case, along with its sequential termination strategy theoretically explains the model of Nurick and Martin, including, within a reasonable accuracy, the values of their experimentally-based calibration coefficients.

However, when the performance of the model that is based on the sequential strategy is assessed against numerical predictions for *non-uniform* specific impulses, it was found that the model is significantly overestimating and, hence, inaccurate. Preliminary attempts were made to enhance the model performance. Namely, it was thought that the poor-performance was due to the perfect plasticity assumption such that dynamic increase in the yield stress should be accounted for. Although amplifying the initial yield stress improved the model predictions, the optimal dynamic yield multiplier seemed to be empirical, and it was not verified that the numerical values are not specific to the used validation data. Furthermore, the improvement is only in terms of the peak displacement, and the model predicted deformed profile exhibits deviations when compared to the corresponding profile from the numerical simulations.

It is important to note that even though the amplification of yield stress would result in reduced displacements (as desirable), it would not affect the total plastic work associated with the permanent deformed profile that is based on the sequential (or modal) termination strategy, see Appendix C. Thus, the balance of plastic work and the initial kinetic energy (which is completely independent of the response) is guaranteed. This can be a legitimate subject for further research, and the yield stress amplification can, e.g., be based on the energy-equivalent total impulse, impulse enhancement factor, and/or area-integrated total impulse; the first two parameters are due to Rigby et al. (2019a). The foregoing articulations are provided to inspire new research on this topic. However, the implied approach was not adopted herein as the alternative solution, as given in Chapter 5, has

been proposed as will be discussed below.

On the other hand, it has been observed that excellent overall improvements in the model predictions are achieved when the solution termination strategy is considerably modified for the non-uniform impulsive blast loadings. Thus, a new termination strategy was proposed, as discussed and justified in Sections 5.2 and 5.3.4, that is based on the total velocity of the membrane instead of the individual modal velocities. In the "total" solution termination strategy, the time-dependent displacement at a given spatial point (or coordinate) is terminated (and taken as the permanent displacement) when the total velocity at that point reaches zero for the first time, after it had been non-zero initially. The model based on the total termination strategy (i.e., the new one) reasonably compares well with the validation data from experiments and LS-DYNA predictions for the non-uniform specific impulse case of loading, as already demonstrated in Sections 5.5 and 5.6.

However, the new termination strategy has been found to lead to inaccurate predictions when applied to the *uniform* specific impulse case. In particular, the model based on the total termination strategy highly overpredicts the response of uniformly loaded membranes as compared to the predictions based on the sequential modal termination strategy.

That is, there are *two* distinct termination strategies: the sequential termination and the total termination strategies. One strategy is confirmed to provide accurate predictions for one of two cases of impulsive loading distributions, whereas the other strategy is the appropriate one for the other case of loading distribution. Clear guidance will be given later. It must be mentioned that a unified strategy is not reached yet, and such dilemma is acknowledged as a serious limitation of the present analytical work. Although, it has been carefully observed that the appropriate termination strategy (among the sequential and the total solution terminations) always leads to the least peak transverse displacements (in magnitude). The recommendations to be given next are merely based on clear observations, namely the corresponding accuracies with respect to the transverse motion of the membranes, when validating the uniform and non-uniform models.

Note that the two solution termination strategies will lead to identical results when the specific impulse distribution coincides with one of the mode shapes. In Section 3.9, a simple example was studied for a specific impulse profile that is proportional to the first mode shape in a rectangular target. This simple problem was investigated, in purpose, to test the main model (the plastic wave equation and transient transverse deformed profile) without the issues introduced by the choice of the termination strategy. Note that for this single mode response, the total velocity is the modal velocity of the considered mode, i.e., the sequential and total termination strategies are identical. For other non-modal specific impulse distributions, the choice of the termination strategy affects the temporal variation of the total velocities, and, hence, the magnitude of the transverse displacements. That is, two responses will be obtained from the two termination strategies if the specific impulse is not proportional to, precisely, one mode shape, which is generally the case for real impulsive blast loadings.

Hence, for practical reasons, the author suggests that the two different termination strategies need to be implemented to obtain the predictions of the transverse displacements. The appropriate termination strategy is taken as the one corresponding to the least peak displacement. This is recommended when there is an ambiguity on classifying the impulsive loading distribution, i.e., whether nearly uniform or slightly non-uniform.

On the other hand, when the impulsive loading is uniform, then it is confirmed that the sequential modal termination strategy is appropriate, and the uniform model in Chapter 4 is applicable. In contrast, when the impulsive loading is non-uniform, the model as described in Chapter 5, with the total termination strategy, is applicable. The excellent parameter, due to Rigby et al. (2019a), of the impulse-enhancement factor, defined as the ratio of energy-equivalent total impulse to area-integrated total impulse, can be used to determine how "non-uniform" an impulsive blast loading is; the load is identically uniform when the factor is one, and the non-uniformity increases as the factor increases above one (Rigby et al., 2019a). The non-uniform specific impulses that were used during the validation of the non-uniform model, in Sections 5.5 and 5.6, correspond to impulse enhancement factors of 1.4 and larger, and the specific impulse distributions obey the general Gaussian profile as proposed and predicted by Pannell et al. (2021), which is the mathematical characterisation of real (spherical) near-field blast-generated specific impulses.

In overall, the equation of motion (i.e., the plastic wave equation) is applicable conditionally. The solution of which must be terminated before the equation becomes invalid. Thus, the solution termination step is required as part of the overall solution. Without the solution termination strategy, completely false predictions could be obtained. The solution can be terminated based on the modal velocities or the total velocity. In the modal termination procedure, a given mode is terminated at a specific time; all points on the membrane are treated simultaneously since the modal velocity is shared by all points for the mode under consideration. The procedure is completed by repeating the procedure for all other modes. Different modes are terminated at different (and sequential) time instants. As such, the procedure is called modal or sequential termination. On the other hand, the total termination strategy is based on the total velocities. At one point on the target, the total velocity is the sum of all modes. The solution at this point is terminated based on this total velocity. The procedure is completed by doing the same for all points on the membrane. This latter strategy is called the total solution termination. It might be more instructive to call this strategy as the *point-wise* termination because it contrasts to the mode-wise termination of the modal termination strategy. In the two strategies, the kinetic energy of the membrane is forced to not increase after it had been decreasing. The plastic work increases identically by the decrease in kinetic energy. Thus, in both terminations strategies, the plastic work is monotonically increasing. Maximum plastic work is reached when the kinetic energy is zero.

The balance of energy has been confirmed with the two termination strategies. The energy balance for a circular membrane associated with the solution termination strategies for non-uniform and equivalent uniform specific impulses is depicted in Figs. 6.1 and 6.2. In

these figures, additional curves are plotted that correspond to the solutions without any termination, which clearly reflect that the termination strategy is an important step for the solution to be physically valid. The difference between the predictions based on the two termination strategies is on the magnitude and distribution of transverse displacement. The reader is referred to the above practical recommendations on the choice of the appropriate termination strategy based on the distribution of the specific impulse.

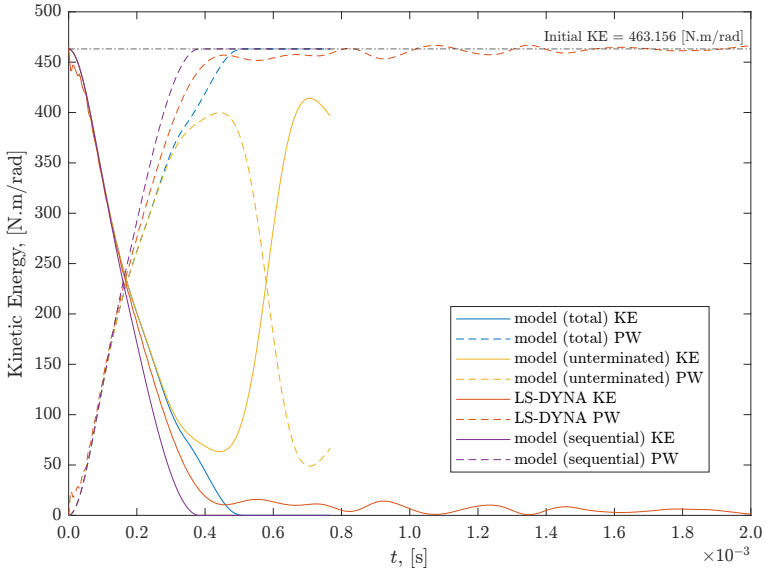

Fig. 6.1. Kinetic (KE) energy and plastic work (PW) balance for a circular membrane under non-uniform specific impulse corresponding to the two solution termination strategies. The time histories of energies are given as predicted using the (total) solution termination strategy and the (sequential) termination strategy. The corresponding time histories from purely Lagrangian LS-DYNA simulation of the same input impulsive loading are given for reference. The dashed horizontal line is the initial kinetic energy. The global energies are given per unit radian. The actual used specific impulse distribution correspond to a spherical PE4 charge of mass 75 [g] and at clear stand-off distance of 35 [mm] from the centre of the circular membrane. The profile of the specific impulse was given by the curve labelled "M75-S35" in Fig. 5.15. The yellow curves correspond to the solution without any termination, which clearly reflect that the termination strategy is an important step for the solution to be physically valid; note that internal work oscillates, namely, it decreases, which is unacceptable.

The user of the model is kindly advised to be aware of the above limitation (i.e., existence of two termination strategies for the uniform and non-uniform distributions), and further research is highly needed to alleviate or eliminate this dilemma. The reader is kindly reminded that the present approach of the analytical modelling is to provide fast-running reasonable predictions of the target response under generic impulsive blast loadings. The starting problem is already an idealised (or simplified) version of the actual problem. Thus, the above practical workaround could be acceptable until a more rigorous solution is obtained.

6.6 On the Local Plastic Strain Distribution

The model, throughout the thesis, is only shown to provide accurate predictions on the global level. Namely, the transient and permanent deformed transverse profile and the

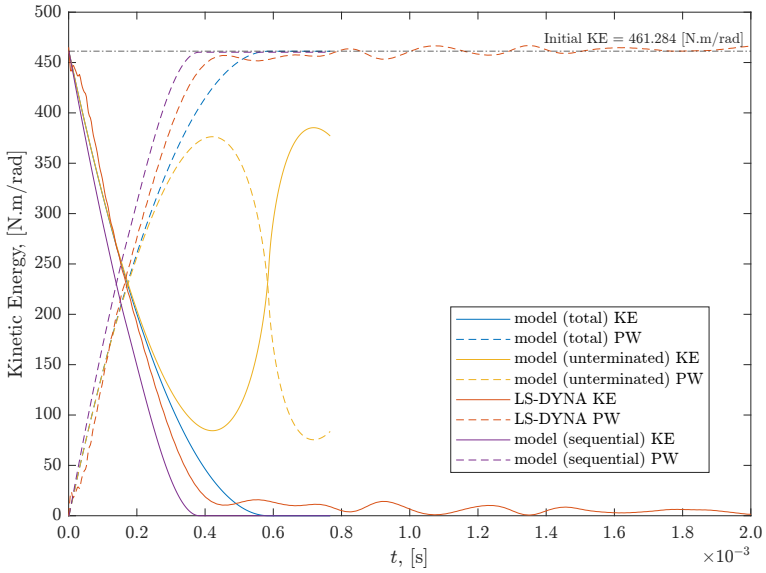

Fig. 6.2. Kinetic (KE) energy and plastic work (PW) balance for a circular membrane under uniform specific impulse corresponding to the two solution termination strategies. The specific impulse is uniform and energy-equivalent, according to Rigby et al. (2019a), to the non-uniform specific impulse that was used in Fig. 6.1. The time histories of energies are given as predicted using the (total) solution termination strategy and the (sequential) termination strategy. The dashed horizontal line is the initial kinetic energy. The global energies are given per unit radian. Note that the curves corresponding to LS-DYNA predictions are not relevant for the present case of equivalent uniform specific impulse. The yellow curves correspond to the solution without any termination, which clearly reflect that the termination strategy is an important step for the solution to be physically valid; note that internal work oscillates, namely, it decreases, which is unacceptable.

global (kinetic and plastic) energies time histories as predicted by the model show relatively excellent agreement with the (experimental and numerical) testing data. However, in the local level, namely in terms of effective stresses and plastic strains, the model exhibit deficiencies when compared to experiments and numerical (LS-DYNA) results. These limitations are discussed below.

The model is assumed to apply to ductile thin plates when subjected to large lateral impulsive blast loading. It is hypothesised that the relevant loading intensity is sufficient to produce significant plastic deformation that is responsible for the transverse displacement of the target. The goal of the present analytical modelling was not to exactly replicate the actual physical problem as this would result in increased complexity and, hence, to some extent, prohibit advancing the theoretical development further. Thus, crucial simplifications were adopted in describing the material behaviour of the membrane. In particular, the ductile material was treated as rigid-perfectly plastic. However, real materials in practice could deviate from the perfect plasticity idealisation beyond the initial yielding, namely, by exhibiting appreciable yield enhancement as total plastic strain, plastic strain-rate, or both increase during the deformation path. As such, the perfect plasticity assumption could be conservative in the global sense.

However, there is a possibility that the development of the mentioned yield enhancements (i.e., due to strain-hardening, strain-rate sensitivity, or both) could affect the local response

in terms of an anticipated stress or strain redistribution. The reader is referred to the excellent experimental and numerical investigations of Aune and his team where strain-hardening is associated with the lateral spread of yielded regions in blast-loaded thin plates (Elveli et al., 2022; Granum et al., 2019). Furthermore, it is implied by the authors' work that such a phenomenon is attributed to the scatter of the directions of the principal in-plane plastic strains so that plastic flow is distributed spatially (or flattened out). The profile of the plastic membrane strain as predicted by the model is qualitatively incorrect, due to the neglect of the in-plane displacement contribution that will be discussed later in this section; the effect of the strain-hardening on the local plastic strain distribution can not be studied by direct comparisons between the numerical predictions (which account for strain-hardening) and the predictions of the present rigid-perfectly plastic model. It will be highlighted later that further research is needed to account for the influence of the in-plane displacement on the plastic strains to qualitatively enhance the local model predictions. The assessment of the strain-hardening and strain-rate effects on the local behaviour can then be made possible.

Again, the model has been shown to reasonably re-produce the global effect (i.e., the peak permanent transverse displacement) observed in real experiments, see Sections 4.6, and 5.6. In addition, the time histories of the transverse displacement and the global energies as predicted by the numerical simulations, using LS-DYNA, are closely followed by the model predictions, see Fig. E.5 in Appendix E. Moreover, the permanently deformed profiles predicted by the model agree reasonably with the corresponding profiles obtained from LS-DYNA simulations, as demonstrated in Fig. 5.13. As such, it is concluded that the perfect plasticity is sufficient in practically re-producing the permanent displacement (or the global response) of thin targets when subjected to intense lateral impulsive blast loading.

On the other hand, the model, as presented in the thesis, is incapable of providing a complete and accurate picture of the local distribution of the stresses, especially when the target material exhibits pronounced deviation from the perfect plasticity idealisation. These limitations can be overcome by utilisation of some commercially available finite element programs. The reader is highly suggested to consult Section 5.7 for a realistic and accurate picture, as obtained from Lagrangian LS-DYNA analyses, of the local plastic strain distributions in near-field blast-loaded thin plates.

The influence of the in-plane displacement on the membrane plastic strains is addressed next. Recall that the model assumes a pure membrane mechanism that is merely associated with the transverse displacements being large. That is, the membrane contribution by the in-plane displacements was neglected. Consequently, whenever the slopes of the transverse displacement are zero, the membrane strains are zero. These slopes are always zero at the midpoint of a membrane that is loaded symmetrically. However, experiments, see, e.g., the relevant graph of in-plane strain profile in Cloete and Nurick (2014), and numerical simulations, see Fig. 5.17 in Chapter 5, show that the membrane strains in the central region of symmetrically loaded membranes are non-zero, which are attributed to

the non-zero contributions of the in-plane displacements. Thus, the model is incapable of providing a correct description of the local (plastic) strain field near the central region of symmetrically loaded thin plates; note that the strains that are computed by the model are plastic. This latter limitation is due to the simplifying assumption for the membrane's kinematics (i.e., it is not associated with the perfect plasticity idealisation).

The contribution to the membrane strain by the in-plane displacement is discussed in Cloete and Nurick (2014) for a uniformly loaded thin circular plate. In their work, the authors showed that the transverse response is independent of the in-plane displacement (which is the radial displacement); the main reason is that the terms of the in-plane strains associated with the in-plane (or the radial) displacement provide zero contribution to the total plastic work of the circular membrane. However, the non-zero in-plane displacement will affect the membrane strain. The authors derived a linear differential equation that relates the radial displacement to the transverse displacement using the assumption that the radial and circumferential strains are equal, which followed from the von Mises' associated flow rule and the equality of the corresponding normal in-plane stresses; the normal stresses (i.e., the radial and circumferential) were argued to be equal according to the equilibrium equation in the radial direction. This treatment led the authors to determine the radial displacement (by solving the differential equation), associated with which is the contribution to the membrane (radial) strain by the in-plane (or radial) displacement. The starting transverse solution was taken to be a single mode with a parabolic (spatial) shape. The authors argued that this was the "exact" solution for a uniformly loaded quasi-static membrane.

It is noted that for a circular membrane under axi-symmetric conditions, the principal in-plane stresses are the radial and circumferential stresses, see, e.g., Hopkins and Prager (1953). As such, the results of Cloete and Nurick on the zero contribution of the membrane strains due to the in-plane displacements to the plastic work apply to the principal plane (i.e., in terms of principal in-plane stresses and the corresponding strains). This problem of Cloete and Nurick is covered in detail in Sections B.2.1 and B.2.2 of Appendix B of the present thesis; therein, the independence of the total plastic work on the in-plane displacement is generalised for non-circular problems. It is hoped that the added material in Appendix B would be useful to improve the present theory, in future research, to accommodate the influence of the in-plane displacements on the maximum membrane strains.

Although the Cloete and Nurick's approach is analytically very attractive, it would require careful investigation to be integrated within the present analytical modelling consistently. Note that the model in the present thesis predicts the transverse displacement for arbitrarily non-uniform impulsive loading, and as such it consists of a sum of, generally many, Bessel's modes (for the circular membrane case). However, another crucial issue follows. A consequence of the present theory is that the first and second principal in-plane stresses are $(2/\sqrt{3})\sigma_0$ and $(1/\sqrt{3})\sigma_0$ such that the second principal in-plane strain is zero since the normal to the von Mises yield curve at the point $\left(2\sigma_0/\sqrt{3}, \sigma_0/\sqrt{3}\right)$ has zero compo-

nent along the second principal stress, see Fig. 3.3. Hence, for the axi-symmetric circular problem, when the circumferential stress is the second principal stress, then the circumferential strain is zero, which immediately gives zero radial displacement. This would make it troublesome to equate the radial strain to, this, zero circumferential strain; in fact, the in-plane normal strains, according to the present work, are not required to be equal since the point on the yield curve (in the principal plane) is as given above, namely it not (σ_0, σ_0) associated with which the in-plane strains would have to be equal. It should be mentioned that the results on the stress state of the membrane are direct consequences of the total flow rule where the total strains were assumed to be pure functions of the transverse displacement; that is, the strain contributions by the in-plane displacements were set as zero.

For this reason, among possibly others, the incorporation of the practical method of Cloete and Nurick (2014) in the attempt to rectify the present work limitation on the in-plane displacement effect is a possible research topic. According to the above-cited authors, the in-plane displacements can be added posteriorly without necessary modifications to the predictions of the transverse response. That is, the present model is still valid for the purely transverse motion of the membrane, and the developed transverse response can be used in subsequent future work to incorporate the in-plane displacement effect to enhance the predictions of the membrane's plastic strains. For clarity, according to Cloete and Nurick, the in-plane displacement depends on the solution of the transverse displacement, to which the present model has been shown to provide a reasonably accurate solution.

Despite the mentioned limitations for the localised behaviour, the model can predict the plastic strains due to the pure membrane action without the in-plane displacement effects. This portion of membrane strain is significant as it reflects the dominance of the membrane action due to large displacement; namely, it is the main mechanism where the in-plane strains are non-negative (i.e., non-compressive). Hence, it is the reason why membranes, despite their thinness, are stable structures (i.e., without buckling-related instabilities). It is instructive to note that in-plane strain contribution due to in-plane displacements can be negative in some regions of the membrane, and the added contribution due to the large transverse displacement ensures non-negative total in-plane strains throughout the domain. Furthermore, the model predicts that the principal in-plane stresses are constant in magnitude. The directions of these stresses rotate according to the relative magnitudes of the membrane strains. It was analytically derived that the material of the membrane in the mid-plane is, in fact, under a state of uni-dimensional straining (or stretch), along the directions of the first (i.e., the largest) principal in-plane stress, see Section 3.8. Lastly, the model additionally predicts that the membrane thickness will shrink (or will experience necking) as the transverse normal strain (i.e., along the thickness direction) will be compressive whenever the in-plane normal strains are non-zero. The transverse normal strain is negative since the in-plane strains are always non-negative as they are related to the square of the slope of the transverse displacement. Again, recall that the strains, mentioned above, are associated with large transverse displacements.

6.7 Practical Engineering Applications of the Model

The model can be of important use in the field of structural blast engineering in two main ways. First, the model can provide rapid estimates of the likely response of thin plates that are subjected to near-field blast loading, particularly when the blast loading is of extreme magnitude so that the pure plasticity and pure membrane action are the most dominant mechanisms of resistance (Jones, 2012; Mehreganian et al., 2018a). It is part of the present work to assess the model's ability to reasonably re-produce and explain observations from real experiments and realistic numerical modelling using LS-DYNA. Thus, due to the relatively excellent performance of the model during its validation, and as far as the overall response is concerned, the model can be used with confidence to obtain reasonable first-order predictions when designing very thin targets to resist a set of near-field blast loadings as characterised by the blast-induced specific impulses.

That is, the first application is through the utilisation of the model by practising engineers to investigate the blast-loaded thin plates and obtain the predictions (i.e., blast effects). Thin plates are primary structural elements in the blast engineering industry (Rajendran and Lee, 2009); when these plates are made of ductile materials (e.g., structural steel, copper, aluminium), then the model is hopefully an appropriate candidate to obtain fast-running predictions to inform the designer. Furthermore, as the model is fast-running, it has the great potential to be implemented as a core deterministic engine in a probabilistic analysis, e.g., in a Monte Carlo simulation, that involves large repetitive calculations to obtain initial performance-based designs of blast-loaded thin plates (Tetlow et al., 2023). As discussed in Chapter 2, the blast loading's magnitude and spatial profile can vary significantly (Seisson et al., 2020).

Second, the model can be used to increase confidence on the utilisation of ductile thin plates as protective solution against blasts that are impulsive. This can be achieved once a reliable predictive method (e.g., the present model) is available that characterises the likely effect of the blast loading on the protective structural element. As one reliably knows what the worst-case scenario would be, and that is decided to be safe and acceptable in the event of an anticipated risk, then such knowledge would inform (or support) the decision-making in adopting a viable candidate design. In relation to the present model application, as the designer would know in advance about how a ductile thin plate would respond to an impulsive blast load, he/she might choose to protect an existing critical structural member (i.e., a key column or solid wall) by ductile membranes as the primary means to dissipate the initial (kinetic) energy transferred directly by the impulsive blast loading. That is, the model could serve as a rational basis to utilise ductile thin plates (or membranes) as structural blast protection devices. The membrane-protected structure is responsible to carry out the other (or conventional) loading cases, e.g., dead or earthquake loadings, where stiffness and compressibility are important. Note that the present model is applicable to thin plates that respond primarily as pure membranes (i.e., without in-plane compressive stresses).

Utilisation of membranes for blast protection might come in two forms. The first is already discussed above, i.e., the membrane is installed on the front (or loaded) side to dissipate the blast energy and actively shield the (protected) structure (Ioannou and Gantes, 2021). As the second form, ductile membranes could be erected on the back (or free) side of an existing under-rated structural element as a type of external reinforcement or a passive catcher system; here, the membrane is engaged (i.e., providing reserve resistance) in the event of flexural failure, due to a lateral blast loading, of the priorly unstrengthened structure (Pope, 2002; Ioannou and Gantes, 2021). One of the findings of the present thesis is that the membrane action alone can provide the needed energy dissipation against impulsive blast loadings that are of extreme magnitudes. In the performed analyses, the maximum transverse displacements are in the order of few centimetres; thus, these can be the values for the gap to be maintained when the membrane is installed on the front of an existing planar structure to be protected. Note that the ideal scenario can be achieved by a trade-off of the primary blast effects; for example, limited yield strength and high ductility (i.e., large failure strain) would limit (or cut-off) the reaction forces that are transferred to the structure (supporting the membrane), see, e.g., Ioannou and Gantes (2021), whereas it would result in excessive permanent deflections and larger plastic strains; the reader is referred to Elveli et al. (2022) for the important notion of strength-ductility trade-off in the blast engineering setting.

Chapter 7

Summary and Conclusions

7.1 Conclusions

Note Detailed conclusions were provided by the end of Chapters 3, 4, and 5. The purpose of the present chapter is to provide the most overall summary and conclusions. These are organised by the individual chapters.

- Chapter 3:
  - The problem of a thin plate subjected to a near-field blast loading is investigated analytically. The plate responds impulsively and in a pure membrane mode, and its material is rigid-perfectly plastic according to von Mises's criterion of yielding and its associated flow rule. The in-plane strains are dominated by the gradients of the transverse displacements, and accordingly, the in-plane displacements were neglected. The ultimate kinematic description of the plate is termed the simple membrane motion.
  - Given the impulsive nature of loading (i.e., without externally applied pressures), the incremental plastic flow rule is extended, and the plastic relations were eventually expressed in terms of the total plastic strains. This was called the total flow rule;
  - Through the application of the principle of virtual work, a general equation of motion governing the plastic transverse displacement is derived, and it is recognised as a linear (two-dimensional) wave equation, and called herein as the plastic wave equation, with the wave speed given in terms of the uni-axial yield stress of the membrane;
  - The adoption of the total flow rule introduced restrictions on the solution of the (plastic) wave equation such that the requirement of the plastic work rate's non-negativity is not violated;
  - Certain practical consequences of the developed total flow rule on the stress states of the membranes, the principal in-plane (normal and shear) stresses

and their directions are derived;

- Preliminary results on the first mode solution of a membrane under a particular specific impulse, which is taken to be proportional to the first mode shape, are presented. Closed-form solutions on the principal stresses and their directions (or trajectories) are given.
- The first mode solution was compared with corresponding numerical predictions using LS-DYNA. The analytical solution (of the first mode problem) is shown to compare excellently with LS-DYNA results. The accuracy of the model's performance is measured with respect to the transient and maximum transverse displacements and the corresponding transient and permanent deformed profiles. The results, also, imply the appropriateness of the derived plastic wave equation and the dependence of the wave speed on the factor $2\sigma_0/\sqrt{3}$ in modelling the transverse motion of the impulsively-loaded thin plate. The notion of the solution termination step, which is essential to ensure the applicability of the wave equation, is studied in relation to time at which plastic work rate tends to become negative. Nearly beyond this time, the corresponding time history of the peak displacement from the LS-DYNA results show that only elastic oscillations (i.e., purely elastic loading/unloading cycles) take place without further plasticity;
- The closed-form solution based on the first mode provided an important conclusion that the time to maximum response is one-quarter of the first mode period of the membrane. This period, in turn, is inversely proportional to the uni-axial yield stress. As the yield stress is by far smaller than typical elastic moduli, the plastic response of the membrane would, hence, take longer times to attain its peak value, which in turn means that the membrane response is more likely to be impulsive as assumed when it is loaded by a near-field blast of considerably small duration. Lastly, it was derived that the trajectories of first (i.e., the largest) principal (normal) stress is identically orthogonal to the contours of constant transverse displacements; in other words, the principal stress is always along the directions of the steepest descent of the transverse displacement profile. The contours of constant transverse displacements are, themselves, the trajectories of the second principal stress.

- Chapter 4:
  - The plastic wave equation was solved for rectangular and axi-symmetric circular membranes by using the eigen-expansion, or modal decomposition, technique. For the rectangular membranes, the eigen-functions are the usual (sinusoidal) components of the Fourier series, while the eigen-functions are the first-kind Bessel's functions of order zero (due to the axi-symmetric condition in the circular case) for the circular membranes;
  - A sequential mode termination strategy is proposed, which is based on ter-

minating the individual modes (of the solution of the plastic wave equation) whenever the corresponding modal velocity (of a particular mode) reaches zero for the first time after being non-zero initially. This strategy ensures that the total plastic work does not decrease at any instant during the response of the membrane;

- The obtained solutions of the wave equation when combined with the above termination strategy provide the transient plastic response of the rectangular and circular membranes;
- Closed-form solutions of the maximum plastic displacements associated with uniform specific impulses are derived. The uniform impulse model predicts that the peak plastic response is linear in the total impulse (given by the product of the uniform specific impulse and the membrane's area) and inversely proportional to $(h\rho c_p)$, where h, ρ, and c_p are, respectively, the plate's thickness, density, and plastic wave speed;
- The uniform model is shown to reasonably agree with the validation data, which consists of a large set of experimental measurements, available in the literature, and numerical results obtained from well-detailed numerical analyses using LS-DYNA;
- The uniform model can, as indicated above, then be considered as an already-validated fast-running tool to provide a reasonable and relatively instant assessment of the likely plastic response of a target subjected to a uniform blast load of extremely short duration;
- As some practical ductile materials exhibit substantial strain-hardening and the present model assumes perfect plasticity behaviour, simplified elasto-plastic (with hardening) SDOF analysis and additional LS-DYNA plate response simulations (in which the hardening modulus is varied) were undertaken to assess the effect of neglecting the work-hardening phenomena. It was shown that the rigid-perfectly plastic model is reasonably adequate to capture the overall (or global) plastic response provided that the initial kinetic energy (e.g., from the blast-generated specific impulse and the associated initial velocity field) is relatively larger than the additional energy dissipation offered by the inclusion of the work-hardening. Detailed discussion of the overall model limitations was provided in Section 4.7.

- Chapter 5, the conclusions below are taken directly from Section 5.7:
  - The sequential termination strategy, which is adopted for the response of plates under uniform specific impulse, is found to overestimate the plastic response when the specific impulse is highly non-uniform;
  - A new solution termination strategy is introduced and greatly improves the accuracy of the membrane model for the non-uniform specific impulse (i.e., that arises from an actual near-field blast event). The new strategy requires

the termination of the solution (of the plastic wave equation) when the local kinetic energy (i.e., the kinetic energy at a particular point) reaches zero for the first time after it was initially non-zero. Thus, the solution is terminated when the total velocity (the sum of dominant modes) reaches zero;

- The membrane model (based on the new termination strategy) is found to agree well with the used validation data, from experiments performed by Curry and Langdon (2017) and results from LS-DYNA simulations performed as part of the present work;
- The numerical simulations of near-field blast events using the MM-ALE in LS-DYNA are shown to provide reliable predictions of the near-field blast-generated reflected positive specific impulse distributions. The profiles of the specific impulse appear to capture the important features of near-field blasts, such as the high sensitivity to variations of stand-off distances and angles of incidence. These profiles follow the Gaussian spatial distribution as predicted by Pannell et al. (2021). The total impulse (obtained by spatial integration of the specific impulse) compares reasonably with the corresponding experimental measurements in Curry and Langdon (2017) when the findings of Rigby et al. (2019b) and Rigby et al. (2019a) are taken into account;
- Despite the good performance of the model for the predictions of the gross (or global) response, it is found that the model is incapable of providing accurate representation of the response on the local level. In particular, the distribution of the effective plastic strains in the membrane are incorrect when compared to the numerical predictions from relevant Lagrangian LS-DYNA analyses and the experimental observations presented in Cloete and Nurick (2014). This crucial limitation is attributed to the neglect, from the material perspective, of strain-hardening and strain-rate sensitivity and, from kinematics perspective, of the in-plane displacements effects on the evaluation of the plastic membrane strains. This has been discussed in Section 6.6. The more accurate distributions for the effective stresses, plastic strains, and strain-rates in near-field blast-loaded thin plates are presented in Section 5.7.
- In the structural LS-DYNA analyses, where thin Domex-355 steel plates are subjected to non-uniform specific impulse, it is found that plasticity (as measured by the effective total plastic strains) of the plates develops and progresses through the majority of the domain (the planar areas of the plates), in the early phase of the response. The responses of the targets are, hence, mainly plastic. Furthermore, the peak displacements are attained in the early phase.
- The model predictions and LS-DYNA numerical results on the plastic responses of the thin targets both show a linear dependence on the energy-equivalent total impulse, as first developed and discussed in Rigby et al. (2019a) and Tyas and Pope (2003).

In addition to the above per chapter conclusions, the conclusions for the overall work is the following. The thesis developed analytical model to predict the transverse response of thin ductile plates when subjected to impulsive blast loading. The model consists of the plastic wave equation, its solution, and an appropriate solution termination strategy. The uniform model, as presented in Chapter 4 with the sequential solution termination strategy (based on the individual modal velocities), has been found to be reasonably accurate for the uniform specific impulse case. On the other hand, when the specific impulse is non-uniform, then the non-uniform model, which is described in Chapter 5 with the total solution termination strategy (based on the total velocity), provides the accurate predictions. That is, there are two solution termination strategies, and the choice of the appropriate strategy depends on the distribution of the specific impulse. The reader should be kindly aware that inaccurate predictions could be obtained when the wrong solution termination strategy is used. This topic has been discussed in Section 6.5.

The model accuracy has been confirmed to be reasonably excellent only regarding the global response in terms of the transverse deformed profile. That is, concerning the transverse motion of a thin target plate, the target is very likely to respond to a near-field blast loading through the following basic mechanisms: an impulsive response, purely plastic material behaviour, and a membrane action that is solely due to the transverse displacement being large. And, this transverse motion is governed by the plastic wave equation, with the wave speed being $c_p = [2\sigma_0/(\sqrt{3}\rho)]^{1/2}$, where σ_0 and ρ are the membrane's tensile yield stress and density, respectively.

However, on the local level, the model predictions considerably deviate from the corresponding experimental and numerical observations regarding the distribution of the plastic strains. This is a crucial limitation as the plastic strain distribution is an important design parameter. For this reason, this issue has been, to some extent, addressed in Section 6.6, where suggestions for future work to enhance the predictions of plastic strains by the incorporation of the in-plane displacement effect are provided. Throughout Chapter 6, the engineering applicability of the model is provided, and discussions on the need for future work are highlighted to address certain limitations of the present theory.

7.2 Final Remarks and Future Work

The thesis derives a simple analytical model that provides fast predictions of the plastic response of thin targets when subjected to near-field blast loadings. The results and final models developed as part of the thesis have the significant potential to be added to the toolbox of practising blast engineers, where reasonably accurate fast-running predictive models are used to obtain reliable initial designs for blast-related structural protection and strengthening.

Despite the simplicity of the model and its underlying idealising assumptions, the model is found to agree with the validation data from real experiments (performed by others on

ductile plates) and sophisticated finite element simulations (in which most of all complexities are incorporated). As such, the model shows that the dominant and fundamental mechanisms responsible for the first-order representation of the overall behaviour of near-field blast-loaded thin plates are: impulsive response, membrane action, and pure perfect plasticity, as these are the retained structural response features in the model development. Additionally, on the journey during the development of the plastic wave equation (that governs the response of the target), further results were derived that can be of practical interest. Namely, the model predicts thinning of the membrane as the transverse normal strains are necessarily compressive and non-zero whenever in-plane strains are non-zero. As the in-plane strains' expressions are given in terms of the derivatives of the transverse displacement, necking (or thinning) of the plates can be predicted, and its contour can be determined and investigated. Also, the thin plates are predicted to be in a state of uni-axial stretch (in terms of principal in-plane strains) on their mid-planes as implied by the principal stresses' state. The directions (or trajectories) of this uni-axial stretching are predicted also as the directions of the principal normal stress. The model predicts that the magnitudes of the principal stresses are constant (on the whole plate's mid-plane) whenever the plate is under active yielding (i.e., when the transverse displacement is actively changing in time).

Concerning the global transverse response, the model can accommodate strain- or work-hardening, and an efficient method to modify the initial uni-axial yield stress is discussed in the thesis if deemed necessary. However, the thesis does not provide an assessment of the application of the suggested method. The effect of strain rate, when applicable, on the uni-axial yield stress is more challenging to incorporate in the model. This is mainly because the magnitudes and the range of strain rates that would be generated in a non-uniformly and impulsively loaded plate are unknown and can vary greatly based on the magnitude and distribution of the blast-generated specific impulse.

The membrane solution, developed and validated herein, has an additional potential application if thin ductile (e.g., steel) membranes are supplemented in blast protection construction to (externally) strengthen existing under-rated thick plates. The present membrane model can be used in initial designs to limit the likely plastic response. Other practical considerations were discussed in Section 6.7. As a concluding potential significance of the derived results, the present membrane solutions can be regarded as exact (or analytical) solutions to validate numerical schemes and their associated solutions in which the rigid-plastic ductile thin plates are loaded by uniform or non-uniform specific impulses, e.g., when the dynamic plastic (or limit) analysis of thin plates is solved numerically by a special-purpose (or non-traditional) finite element technique.

There are mainly two issues that need further research to improve the present model as given in the thesis. The first is related to the dilemma introduced by the two proposed solution termination strategies. The solution termination is a required step since the main mathematical model is based on the total flow rule instead of the incremental flow rule. Without the solution termination, the total flow rule would lead to completely

non-physical behaviour. The total flow rule in combination of the solution termination should be equivalent to the incremental flow rule-based solution, i.e., the physically correct behaviour. The main reason is that, in contrast to the total flow rule, the incremental flow rule never allow negative plastic work rate. As just mentioned above, two termination strategies were proposed to adhere to the plastic work rate' non-negativity, and each of the strategies gives accurate predictions depending on the distribution of the impulsive loading, i.e., whether uniform or non-uniform. The thesis suggests that the sequential solution termination strategy should be used when the impulsive loading distribution is uniform, whereas the total solution termination is found to provide the accurate predictions when the loading is non-uniform, as the case in typical near-field blasts. This proposed approach is considered practical and justified based on the accuracy observations. Future work is needed to obtain a practical unified strategy for the solution termination and/or to provide theoretical explanation on why should one of the two strategies be avoided for a given class of the distribution of the specific impulse. This issue was discussed in Section 6.5.

The second issue that needs additional research is discussed next. The model has been shown to provide reasonably accurate predictions only for the overall (or global) response, i.e., in terms of the evolution of global (kinetic and internal plastic) energies and transverse motion of the target. In particular, the model has been found to be qualitatively incorrect with respect to the local behaviour of the impulsively loaded thin plate with respect to the distribution of the plastic membrane strains. This issue has been attributed to two assumptions during the model's development, which are the neglect of the in-plane displacements' contributions to the membrane strains and (possibly) to the strain-hardening and strain-rate effects on the dynamic yield stress. This is an important issue as the design of a target against material failure would, typically, be based on the maximum (or failure) strains and the likely spatial regions where they occur. It is clear, to the author, that the model needs to be improved first by incorporating the in-plane displacement effect on the plastic strains. The improved rigid-perfectly plastic predictions of membrane strains could, then, be compared to more realistic profiles that are influenced by the strain-hardening and visco-plasticity to provide further insights for additional theoretical refinement to even improve the predictions on the local level. Relevant discussion was given in Section 6.6.

References

Abouzeid, M., R. R. Habib, S. Jabbour, A. H. Mokdad, and I. Nuwayhid (2020). "Lebanon's humanitarian crisis escalates after the Beirut blast". In: *Lancet* 396.10260, pp. 1380–1382. ISSN: 01406736. DOI: 10.1016/S0140-6736(20)31908-5.

Alotaibi, S. A., S. E. Rigby, M. Guadagnini, and A. Tyas (2023). "Rigid-plastic membrane response of thin plates under impulsive blast loads using the extended Hamilton principle". In: *Int. J. Impact Eng.* 178, p. 104624. ISSN: 0734743X. DOI: 10.1016/J.IJIMPENG.2023.104624.

Arnold, J. L., P. Halpern, M. C. Tsai, and H. Smithline (2004). "Mass Casualty Terrorist Bombings: A Comparison of Outcomes by Bombing Type". In: *Ann. Emerg. Med.* 43.2, pp. 263–273. ISSN: 01960644. DOI: 10.1016/S0196-0644(03)00723-6.

Aune, V., E. Fagerholt, K. O. Hauge, M. Langseth, and T. Børvik (2016). "Experimental study on the response of thin aluminium and steel plates subjected to airblast loading". In: *Int. J. Impact Eng.* 90, pp. 106–121. ISSN: 0734743X. DOI: 10.1016/j.ijimpeng.2015.11.017.

Aune, V., G. Valsamos, F. Casadei, M. Larcher, M. Langseth, and T. Børvik (2017). "Numerical study on the structural response of blast-loaded thin aluminium and steel plates". In: *Int. J. Impact Eng.* 99, pp. 131–144. ISSN: 0734743X. DOI: 10.1016/j.ijimpeng.2016.08.010.

Baker, W. E., P. S. Westine, and F. T. Dodge (1991). *Theory and Practice of Scale Modeling Revised Edition*. Revised. Vol. 12. Elsevier Science Publishers, p. 368. ISBN: 0444881565.

Bathe, K.-J. (1996). *Finite Element Procedures*. New Jersey: Prentice-Hall Inc., p. 1050. ISBN: 0-13-301458-4.

Belytschko, T., W. K. Liu, B. Moran, and K. I. Elkhodary (2014). *Nonlinear finite elements for continua and structures*. 2nd ed. John Wiley & Sons, Inc. ISBN: 978-1-118-63270-3. arXiv: 1011.1669.

Biggs, J. M. (1964). *Introduction to Structural Dynamics*. New York, NY, USA: McGraw-Hill Book Company, p. 355.

Blaauwendraad, J. (2010). *Plates and FEM*. Vol. 171, pp. 1–439. ISBN: 9789048135950.

Bodner, S. R. and P. S. Symonds (1979). "Experiments on viscoplastic response of circular plates to impulsive loading". In: *J. Mech. Phys. Solids* 27.2, pp. 91–113. ISSN: 00225096. DOI: 10.1016/0022-5096(79)90013-9.

Bogosian, D., J. Ferritto, and Y. Shi (2002). "Measuring uncertainty and conservatism in simplified blast models". In: *30th Explos. Saf. Semin.* August.

Bogosian, D., M. Yokota, and S. E. Rigby (2016). *TNT equivalence of C-4 and PE4: a review of traditional sources and recent data*. Tech. rep.

Capurso, M. (1972). "A quadratic programming approach to the impulsive loading analysis of rigid plastic structures". In: *Meccanica* 7.1 Supplement, pp. 45–57. ISSN: 00256455. DOI: 10.1007/BF02133604.

Chen, W.-F. and D.-J. Han (1988). *Plasticity for Structural Engineers*. New York: Springer-Verlag, p. 606.

Cheval, K., O. Loiseau, and V. Vala (2010). "Laboratory scale tests for the assessment of solid explosive blast effects. Part I: Free-field test campaign". In: *J. Loss Prev. Process Ind.* 23.5, pp. 613–621. ISSN: 09504230. DOI: 10.1016/j.jlp.2010.05.001.

Cheval, K., O. Loiseau, and V. Vala (2012). "Laboratory scale tests for the assessment of solid explosive blast effects. Part II: Reflected blast series of tests". In: *J. Loss Prev. Process Ind.* 25.3, pp. 436–442. ISSN: 0950-4230. DOI: 10.1016/J.JLP.2011.11.008.

Chung Kim Yuen, S., G. N. Nurick, G. S. Langdon, Y. Iyer, S. C. K. Yuen, G. N. Nurick, G. S. Langdon, and Y. Iyer (2016). "Deformation of thin plates subjected to impulsive load: Part III an update 25 years on". In: *Int. J. Impact Eng.* 107, pp. 108–117. ISSN: 0734743X. DOI: 10.1016/j.ijimpeng.2016.06.010.

Clarke, S. D., S. D. Fay, J. A. Warren, A. Tyas, S. E. Rigby, and I. Elgy (2015). "A large scale experimental approach to the measurement of spatially and temporally localised loading from the detonation of shallow-buried explosives". In: *Meas. Sci. Technol.* 26.1, p. 015001. ISSN: 0957-0233. DOI: 10.1088/0957-0233/26/1/015001.

Cloete, T. J. and G. N. Nurick (2014). "On the influence of radial displacements and bending strains on the large deflections of impulsively loaded circular plates". In: *Int. J. Mech. Sci.* 82, pp. 140–148. ISSN: 00207403. DOI: 10.1016/j.ijmecsci.2014.02.026.

Command, A. M. (1975). *Engineering Design Handbook. Explosions in Air. Part One*. Alexandria, VA.

Cooper, P. W. (1994). "Comments on TNT Equivalence". English. In: United States.

Cormie, D., G. Mays, and P. D. Smith (2009). *Blast effects on buildings, Second edition*, p. 338. ISBN: 978-0-7277-3403-7.

Cowper, G. R. and P. S. Symonds (1957). *Strain-Hardening and Strain-Rate Effects in The Impact Loading of Cantilever Beams (Technical Report No. 28)*. Tech. rep. Providence, R. I.: Office of Naval Research (ONR), Contract No. 562(10), NR-064-406, Division of Applied Mathematics, Brown University, p. 46.

Cox, A. D. and L. W. Morland (1959). "Dynamic plastic deformations of simply-supported square plates". In: *J. Mech. Phys. Solids* 7.4, pp. 229–241. ISSN: 00225096. DOI: 10.1016/0022-5096(59)90022-5.

Cranz, C. (1926). *Lehrbuch der Ballistik*. Berlin, Germany: Springer.

Curry, R. J. and G. S. Langdon (2017). "Transient response of steel plates subjected to close proximity explosive detonations in air". In: *Int. J. Impact Eng.* 102, pp. 102–116. ISSN: 0734743X. DOI: 10.1016/j.ijimpeng.2016.12.004.

Curry, R. (2017). "Response of plates subjected to air-blast and buried explosions". PhD Thesis. University of Cape Town, p. 318.

Dennis, A. and S. Rigby (2023). "Prediction of Blast Loads using Machine Learning Approaches". In: *SECED 2023 Conf. Earthq. Eng. Dyn. a Sustain. Futur. 14-15th Sept. 2023*. Society for Earthquake and Civil Engineering Dynamics (SECED).

Denny, J., A. Dickinson, and G. Langdon (2021). "Defining blast loading zones of relevance' for primary blast injury research: A consensus of injury criteria for idealised explosive scenarios." In: *Med. Eng. Phys.*, p. 21. ISSN: 1350-4533. DOI: 10.1016/j.medengphy.2021.05.014.

Donea, J., A. Huerta, J.-P. Ponthot, and A. Rodriguez-Ferran (2004). "Arbitrary Lagrangian-Eulerian Methods". In: *Encycl. Comput. Mech.* Vol. 1. Wiley. Chap. 14, pp. 413–437.

Drucker, D. C. (1956). *Variational Principles in The Mathematical Theory of Plasticity*. Tech. rep. Providence, R. I.: DIVISION OF APPLIED MATHEMATICS, BROWN UNIVERSITY, p. 24.

Drucker, D. C., W. Prager, and H. J. Greenberg (1952). "Extended limit design theorems for continuous media". In: *Q. Appl. Math.* 9.4, pp. 381–389. ISSN: 0033-569X. DOI: 10.1090/qam/45573.

Drucker, D. C. (1957). *A Definition of Stable Inelastic Material*. Tech. rep. Providence, Rhode Island: Division of Engineering, Brown University, p. 23.

Duffey, T. A. (1967). *Large Deflection Dynamic Response of Clamped Circular Plates Subjected to Explosive Loading*. Tech. rep.

Edwards, D. S., L. McMenemy, S. A. Stapley, H. D. L. Patel, and J. C. Clasper (2016). "40 years of terrorist bombings-A meta-analysis of the casualty and injury profile". In: *Injury* 47.3, pp. 646–652. ISSN: 18790267. DOI: 10.1016/j.injury.2015.12.021.

Elveli, B. S., M. B. Iddberg, T. Børvik, and V. Aune (2022). "On the strengthductility trade-off in thin blast-loaded steel plates with and without initial defects An experimental study". In: *Thin-Walled Struct.* 171.November 2021, p. 108787. ISSN: 02638231. DOI: 10.1016/j.tws.2021.108787.

Esparza, E. D. (1986). "Blast measurements and equivalency for spherical charges at small scaled distances". In: *Int. J. Impact Eng.* 4.1, pp. 23–40. ISSN: 0734743X. DOI: 10.1016/0734-743X(86)90025-4.

Florence, A. L. (1966). "Circular plate under a uniformly distributed impulse". In: *Int. J. Solids Struct.* 2.1, 37–40, IN1, 41–47. ISSN: 00207683. DOI: 10.1016/0020-7683(66)90005-9.

Frykberg, E. R. and J. J. Tepas (1988). "Terrorist bombings: Lessons learned from Belfast to Beirut". In: *Ann. Surg.* 208.5, pp. 569–576. ISSN: 00034932. DOI: 10.1097/00000658-198811000-00005.

Gel'fand, B. E., I. M. Voskoboinikov, and S. V. Khomik (2004). "Recording the position of a blast-wave front in air". In: *Combust. Explos. Shock Waves* 40.6, pp. 734–736. ISSN: 00105082. DOI: 10.1023/B:CESW.0000048281.33696.ed.

Gharababaei, H. and A. Darvizeh (2010). "Experimental and analytical investigation of large deformation of thin circular plates subjected to localized and uniform impulsive loading". In: *Mech. Based Des. Struct. Mach.* 38.2, pp. 171–189. ISSN: 15397734. DOI: 10.1080/15397730903554633.

Granum, H., V. Aune, T. Børvik, and O. S. Hopperstad (2019). "Effect of heat-treatment on the structural response of blast-loaded aluminium plates with pre-cut slits". In: *Int. J. Impact Eng.* 132.February, p. 103306. ISSN: 0734743X. DOI: 10.1016/j.ijimpeng.2019.05.020.

Hallquist, J. O. (2006). *LS-DYNA Theory Manual.* Vol. 22. 4. Livermore Software Technology Corporation, pp. 241–244. ISBN: 0-9778540-0-0.

Hopkins, H. G. (1957). "On the plastic theory of plates". In: *Proc. R. Soc. A Math. Phys. Eng. Sci.* 241.1225, pp. 153–179.

Hopkins, H. G. and W. Prager (1953). "The load carrying capacities of circular plates". In: *J. Mech. Phys. Solids* 2, pp. 1–13.

Hopkins, H. G. and W. Prager (1954). "On the dynamics of plastic circular plates". In: *Zeitschrift Für Angew. Math. Und Phys. Zamp* 5.4, pp. 317–330. ISSN: 00442275. DOI: 10.1007/BF01587827.

Hopkinson, B. (1915). "British ordnance board minutes 13565". In: *Natl. Arch. Kew, UK* 11.

Hudson, G. E. (1951). "A Theory of the Dynamic Plastic Deformation of a Thin Diaphragm". In: *J. Appl. Phys.* 22.1, pp. 1–11.

Hughes, T. J. R. (2012). *The Finite Element Method: Linear Static and Dynamic Finite Element Analysis*. Dover Civil and Mechanical Engineering. Dover Publications. ISBN: 9780486135021.

Hyde, D. (1992). "CONWEP-application of TM5-855-1". In: *Struct. Mech. Div. Struct. Lab. USAE Waterw. Exp. Station. Vicksburg, MS*.

Ioannou, O. and C. J. Gantes (2021). "Membrane Action of Cladding Subjected to Blast Loading and Effects on the Supporting Structure". In: *Vibration* 4.4, pp. 768–786. ISSN: 2571-631X. DOI: 10.3390/vibration4040043.

J. Chakrabarty (2010). *Applied Plasticity*. Second. l: Springer Science+Business Media, p. 544. ISBN: 9780387263960. DOI: 10.1007/b22134. arXiv: arXiv:1011.1669v3.

Johnson, G. R. and W. H. Cook (1985). "Fracture characteristics of three metals subjected to various strains, strain rates, temperatures and pressures". In: *Eng. Fract. Mech.* 21.1, pp. 31–48. ISSN: 0013-7944. DOI: 10.1016/0013-7944(85)90052-9.

Jones, N. (2010). "Inelastic response of structures due to large impact and blast loadings". In: *J. Strain Anal. Eng. Des.* 45.6, pp. 451–464. ISSN: 03093247. DOI: 10.1243/03093247JSA611.

Jones, N. (1967). "Impulsive Loading of a Simply Supported Circular Plate". In: February.

Jones, N. (1978). "Recent Progress in The Dynamic Plastic Behavior of Structures". In: p. 44.

Jones, N. (1989). "Recent studies on the dynamic plastic behavior of structures". In: *Appl. Mech. Rev.* 49.4, S112–S117. ISSN: 00036900. DOI: 10.1115/1.3101962.

Jones, N. (1996). "Recent Studies on the Dynamic Plastic Behavior of Structures - An Update". In: *Appl. Mech. Rev.* 49.10S, S112–S117. ISSN: 0003-6900. DOI: 10.1115/1.3101962.

Jones, N. (2012). *Structural Impact*. Second. New York: Cambridge University Press, p. 584. ISBN: 9781107010963. DOI: 10.1155/1999/124792.

Jones, N. (2014). "Dynamic inelastic response of strain rate sensitive ductile plates due to large impact, dynamic pressure and explosive loadings". In: *Int. J. Impact Eng.* 74.June, pp. 3–15. ISSN: 0734743X. DOI: 10.1016/j.ijimpeng.2013.05.003.

Kingery, C. N. and G. Bulmash (1984). *Air blast parameters from TNT spherical air burst and hemispherical surface burst*. Tech. rep. Aberdeen Proving Ground, MD, USA: Ballistic Research Laboratories.

Kinney, G. F. and K. J. Graham (1985). *Explosive Shocks in Air*. Second. New York: Springer Science+Business Media, p. 281. ISBN: 0387151478.

Komatitsch, D., J.-P. Vilotte, R. Vai, J. M. Castillo-Covarrubias, and F. J. Sánchez-Sesma (1999). "The spectral element method for elastic wave equationsapplication to 2-D and 3-D seismic problems". In: *Int. J. Numer. Methods Eng.* 45.9, pp. 1139–1164. ISSN: 0029-5981. DOI: 10.1002/(SICI)1097-0207(19990730)45:9<1139::AID-NME617>3.0.CO;2-T.

Li, Q. M. (2016). "An Appreciation of Professor Norman Jones' Contributions to Impact Engineering". In: DOI: 10.1115/OMAE2016-54251.

Liu, X., Y. Ji, and Q. Liang (2010). "Expression of strain tensor in orthogonal curvilinear coordinates". In: *Geod. Geodyn.* 1.1, pp. 48–56. ISSN: 1674-9847. DOI: 10.3724/SP.J.1246.2010.00048.

Livermore Software Technology Corporation (2019). *LS-DYNA Theory Manual*. R11. Vol. Theory. Livermore Software Technology Corporation, p. 886. ISBN: 9254492507.

Lomazzi, L., M. Giglio, and A. Manes (2021). "Analytical and empirical methods for the characterisation of the permanent transverse displacement of quadrangular metal plates subjected to blast load: Comparison of existing methods and development of a novel methodological approach". In: *Int. J. Impact Eng.* 154.March, p. 103890. ISSN: 0734743X. DOI: 10.1016/j.ijimpeng.2021.103890.

LST (2021a). *LS-DYNA Keyword User's Manual Volume I (R13)*. R13. Vol. I. October. Troy, Michigan: Livermore Software Technology, p. 3826. ISBN: 9254492507.

LST (2021b). *LS-DYNA Keyword User's Manual Volume II Material Models (R13)*. R13. Vol. II. Livermore Software Technology Corporation, p. 1993. ISBN: 9254492507.

LSTC (2019). *LS-OPT User's Manual*. 6th ed. February. Livermore Software Technology Corporation, p. 802. ISBN: 9254492507.

Maier, G. and A. Nappi (1984). "On the unified framework provided by mathematical programming to plasticity." In: *Stud. Appl. Mech.* Vol. 6. Elsevier, pp. 253–273. ISBN: 0444421696. DOI: 10.1016/b978-0-444-42169-2.50022-x.

Maier, G. (1968). "Quadratic programming and theory of elastic-perfectly plastic structures*". In: *Meccanica* 3, pp. 265–273. DOI: https://doi.org/10.1007/BF02186946.

Marfurt, K. J. (1984). "Accuracy of finite-difference and finite-element modeling of the scalar and elastic wave equations." In: *Geophysics* 49.5, pp. 533–549. ISSN: 00168033. DOI: 10.1190/1.1441689.

Marker, D. and C. Jenkins (1997). "Surface Precision of Optical Membranes with Curvature". In: *Opt. Express* 1.11, p. 324. ISSN: 1094-4087. DOI: 10.1364/oe.1.000324.

Martin, J. B. (1983). *Convergence to Mode Form Solutions in Impulsively Loaded Piecewise Linear Rigid-Plastic Structures*. Tech. rep. 2. Great Britain: Pergamon Press Ltd., pp. 125–141.

Martin, J. B. (1964). "Impulsive Loading Theorems for Rigid-Plastic Continua". In: *J. Eng. Mech. Div.* 90.5, pp. 27–42.

Martin, J. B. and P. S. Symonds (1965). *Mode Approximations for Impulsively Loaded Rigid Plastic Structures*. Tech. rep. Providence, R. I.: Division of Engineering, Brown University, p. 61.

McDonald, B., H. Bornstein, G. S. Langdon, R. Curry, A. Daliri, and A. C. Orifici (2018). "Experimental response of high strength steels to localised blast loading". In: *Int. J. Impact Eng.* 115.January, pp. 106–119. ISSN: 0734743X. DOI: 10.1016/j.ijimpeng.2018.01.012.

Mehreganian, N., A. S. Fallah, and L. A. Louca (2019a). "Nonlinear dynamics of locally pulse loaded square Föpplvon Kármán thin plates". In: *Int. J. Mech. Sci.* 163.September. ISSN: 00207403. DOI: 10.1016/j.ijmecsci.2019.105157.

Mehreganian, N., A. S. Fallah, and L. A. Louca (2019b). "Plastic dynamic response of simply supported thick square plates subject to localised blast loading". In: *Int. J. Impact Eng.* 126, pp. 85–100. ISSN: 0734743X. DOI: 10.1016/j.ijimpeng.2018.12.010.

Mehreganian, N., A. S Fallah, and L. A. Louca (2018a). "Inelastic dynamic response of square membranes subjected to localised blast loading". In: *Int. J. Mech. Sci.* 148, pp. 578–595. ISSN: 00207403. DOI: 10.1016/j.ijmecsci.2018.09.017.

Mehreganian, N., L. A. Louca, G. S. Langdon, R. J. Curry, and N. Abdul-Karim (2018b). "The response of mild steel and armour steel plates to localised air-blast loading-comparison of numerical modelling techniques". In: *Int. J. Impact Eng.* 115.May 2017, pp. 81–93. ISSN: 0734743X. DOI: 10.1016/j.ijimpeng.2018.01.010.

Micallef, K., A. S. Fallah, D. J. Pope, and L. A. Louca (2012). "The dynamic performance of simply-supported rigid-plastic circular steel plates subjected to localised blast loading".

In: *Int. J. Mech. Sci.* 65.1, pp. 177–191. ISSN: 00207403. DOI: 10.1016/j.ijmecsci.2012.10.001.

Micallef, K., A. S. Fallah, D. J. Pope, and L. A. Louca (2014). "Dynamic Performance of Simply Supported Rigid Plastic Circular Thick Steel Plates Subjected to Localized Blast Loading". In: *J. Eng. Mech.* 140.1, pp. 159–171. ISSN: 0733-9399. DOI: 10.1061/(asce)em.1943-7889.0000645.

Mihailescu-Suliciu, M. and T. Wierzbicki (2002). "Wave solution for an impulsively loaded rigid-plastic circular membrane". In: *Arch. Mech.* 54.5-6, pp. 553–575. ISSN: 03732029.

Nicholson, J. (2022). *Bessel Zero Solver - File Exchange - MATLAB Central*.

Nurick, G. N., M. E. Gelman, and N. S. Marshall (1996). "Tearing of blast loaded plates with clamped boundary conditions". In: *Int. J. Impact Eng.* 18.7-8, pp. 803–827. ISSN: 0734743X. DOI: 10.1016/s0734-743x(96)00026-7.

Nurick, G. N. and J. B. Martin (1989a). "Deformation of Thin Plates Subjected Impulsive Loading–A Review PART II: Experimental Studies". In: *Int. J. Impact Eng.* 8.2, pp. 171–186.

Nurick, G. N. and J. B. Martin (1989b). "Deformation of Thin Plates Subjected To Impulsive Loading - A Review Part I: Theoretical Considerations". In: *Int. J. Impact Eng.* 8.2, pp. 159–170.

Nurick, G. N., H. T. Pearce, and J. B. Martin (1985). "The Deformation of Thin Plates Subjected to Impulsive Loading". In: *Inelast. Behav. Plates Shells IUTAM Symp. Rio Janeiro*. Ed. by L. Bevilacqua, R. Feijno, and R. Valid. Rio de Janeiro, pp. 597–616. DOI: 10.1007/978-3-642-82776-1_29.

Nurick, G. N. and G. C. Shave (1996). "The deformation and tearing of thin square plates subjected to impulsive loads - An experimental study". In: *Int. J. Impact Eng.* 18.1, pp. 99–116. ISSN: 0734743X. DOI: 10.1016/0734-743X(95)00018-2.

Pannell, J. J. (2022). "Surrogate modelling strategies for the prediction of near-field blast impulse". PhD Thesis. The University of Sheffield.

Pannell, J. J., G. Panoutsos, S. B. Cooke, D. J. Pope, and S. E. Rigby (2021). "Predicting specific impulse distributions for spherical explosives in the extreme near-field using a Gaussian function". In: *Int. J. Prot. Struct.*, pp. 1–23. ISSN: 2041420X. DOI: 10.1177/2041419621993492.

Parkes, E. W. (1955). "The permanent deformation of a cantilever struck transversely at its tip". In: *Proc. R. Soc. London. Ser. A, Math. Phys.* Vol. 228. 1175. Royal Society, pp. 462–476.

Parkes, E. W. (1958). "The Permanent Deformation of an Encastre Beam Struck Transversely at Any Point In Its Span". In: *Proc. Inst. Civ. Eng.* 10.3, pp. 277–304.

Pasman, H. J., C. Fouchier, S. Park, N. Quddus, and D. Laboureur (2020). "Beirut ammonium nitrate explosion: Are not we really learning anything?" In: *Process Saf. Prog.* 39.4, pp. 1–18. ISSN: 1066-8527. DOI: 10.1002/prs.12203.

Ploch, J. and T. Wierzbicki (1981). "Bounds for large plastic deformations of dynamically loaded continua and structures". In: *Int. J. Solids Struct.* 17.2, pp. 183–195. ISSN: 00207683. DOI: 10.1016/0020-7683(81)90074-3.

Pope, D. J. (2002). "Response prediction of plate-reinforced concrete panels exposed to near field blast." PhD Thesis. The University of Sheffield.

Prager, W. (1942). "Fundamental theorems of a new mathematical theory of plasticity". In: *Duke Math. J.* 9.1, pp. 228–233. ISSN: 00127094. DOI: 10.1215/S0012-7094-42-00915-3.

Prager, W. (1948). "Theory of Plastic Flow versus Theory of Plastic Deformation". In: *J. Appl. Phys.* 19.6, pp. 540–543. ISSN: 0021-8979. DOI: 10.1063/1.1698170.

Prager, W. and P. G. Hodge (1951). *Theory of Perfectly Plastic Solids*. Ed. by I. S. Sokolnikoff. New York: John Wiley & Sons, Inc., p. 264.

Rajendran, R. and J. M. Lee (2009). "Blast loaded plates". In: *Mar. Struct.* 22.2, pp. 99–127. ISSN: 09518339. DOI: 10.1016/j.marstruc.2008.04.001.

Rao, S. S. (2019a). "Transverse Vibration of Strings". In: *Vib. Contin. Syst.* Wiley, pp. 209–238. DOI: 10.1002/9781119424284.ch8.

Rao, S. S. (2019b). "Vibration of Membranes". In: *Vib. Contin. Syst.* John Wiley & Sons, Ltd. Chap. 13, pp. 427–463. ISBN: 9781119424284. DOI: https://doi.org/10.1002/9781119424284.ch13.

Rayleigh, J. (1894). *The Theory of Sound*. The Theory of Sound v. 1. Macmillan.

Reddy, J. N. (2007). *Theory and Analysis of Elastic Plates and Shells*. 2nd ed. New York: Taylor & Francis Group LLC, p. 547. ISBN: 5856420187.

Reddy, J. N. (2002). *Energy Principles and Variational Methods in Applied Mechanics*. John Wiley & Sons, Inc., p. 592. DOI: 10.1016/0307-904x(85)90131-3.

Rigby, S., B. Fuller, and A. Tyas (2018). "Validation of Near-Field Blast Loading in LS-DYNA". In: 1.August, pp. 1–8.

Rigby, S. E., O. I. Akintaro, B. J. Fuller, A. Tyas, R. J. Curry, G. S. Langdon, and D. J. Pope (2019a). "Predicting the response of plates subjected to near-field explosions using

an energy equivalent impulse". In: *Int. J. Impact Eng.* 128.January, pp. 24–36. ISSN: 0734743X. DOI: 10.1016/j.ijimpeng.2019.01.014.

Rigby, S. E., C. Osborne, G. S. Langdon, S. B. Cooke, and D. J. Pope (2021). "Spherical equivalence of cylindrical explosives: Effect of charge shape on deflection of blast-loaded plates". In: *Int. J. Impact Eng.* 155, p. 103892. ISSN: 0734743X. DOI: 10.1016/j.ijimpeng.2021.103892.

Rigby, S. E., A. Tyas, R. J. Curry, and G. S. Langdon (2019b). "Experimental Measurement of Specific Impulse Distribution and Transient Deformation of Plates Subjected to Near-Field Explosive Blasts". In: *Exp. Mech.* 59.2, pp. 163–178. ISSN: 17412765. DOI: 10.1007/s11340-018-00438-3.

Rigby, S. E., A. Tyas, S. D. Fay, S. D. Clarke, and J. A. Warren (2014a). "Validation of Semi-Empirical Blast Pressure Predictions for Far Field Explosions - Is There Inherent Variability in Blast Wave Parameters?" In: *6th Int. Conf. Prot. Struct. Against Hazards, 16-17 Oct.* October, pp. 1–9.

Rigby, S. E., R. Knighton, S. D. Clarke, and A. Tyas (2020a). "Reflected Near-field Blast Pressure Measurements Using High Speed Video". In: *Exp. Mech.* 60.7, pp. 875–888. ISSN: 0014-4851. DOI: 10.1007/s11340-020-00615-3.

Rigby, S., A. Tyas, R. Curry, and G. Langdon (2019c). "The Response of Plates Under Non-Uniform Impulsive Loads". In: *Proc. SECED 2019 Conf. Soc. Earthq. Civ. Eng. Dyn. Conf. 09-10 Sep 2019, Greenwich, London, UK.* Vol. 3. September. Society for Earthquake and Civil Engineering Dynamics (SECED), pp. 1–7.

Rigby, S. E., A. Tyas, S. D. Clarke, S. D. Fay, J. J. Reay, J. A. Warren, M. Gant, and I. Elgy (2015). "Observations from preliminary experiments on spatial and temporal pressure measurements from near-field free air explosions". In: *Int. J. Prot. Struct.* 6.2, pp. 175–190. ISSN: 2041420X. DOI: 10.1260/2041-4196.6.2.175.

Rigby, S. E., A. Tyas, T. Bennett, S. D. Clarke, and S. D. Fay (2014b). "The negative phase of the blast load". In: *Int. J. Prot. Struct.* 5.1, pp. 1–19. ISSN: 2041420X. DOI: 10.1260/2041-4196.5.1.1.

Rigby, S. E. (2014). "Blast Wave Clearing Effects on Finite-Sized Targets Subjected to Explosive Loads". PhD thesis. The University of Sheffield, p. 192. DOI: 10.1088/1741-2560/8/4/046017.

Rigby, S. E., T. J. Lodge, S. Alotaibi, A. D. Barr, S. D. Clarke, G. S. Langdon, and A. Tyas (2020b). "Preliminary yield estimation of the 2020 Beirut explosion using video footage from social media". In: *Shock Waves* 30.6, pp. 671–675. ISSN: 0938-1287. DOI: 10.1007/s00193-020-00970-z.

Rigby, S. E., A. Tyas, and T. Bennett (2014c). "Elastic-plastic response of plates subjected to cleared blast loads". In: *Int. J. Impact Eng.* 66, pp. 37–47. ISSN: 0734743X. DOI: 10.1016/J.IJIMPENG.2013.12.006.

Ronter, A. R. S. and J. B. Martin (1972). "Bounds for Impulsively Loaded Plastic Structures". In: *J. Eng. Mech. Div.* 98.EM1, pp. 107–119.

Seisson, G., T. Lacaze, and A. Rouquand (2020). "Uncertainty estimation of external blast effects using the Monte-Carlo method". In: pp. 81–92. DOI: 10.2495/SUSI200071.

Spranghers, K., D. Lecompte, H. Sol, and J. Vantomme (2012a). "Material characterization of blast loaded plates". In: *Meca.Rma.Ac.Be* May, pp. 9–10.

Spranghers, K., I. Vasilakos, D. Lecompte, H. Sol, and J. Vantomme (2012b). "Full-Field Deformation Measurements of Aluminum Plates Under Free Air Blast Loading". In: *Exp. Mech.* 52.9, pp. 1371–1384. ISSN: 17412765. DOI: 10.1007/s11340-012-9593-5.

Spranghers, K., I. Vasilakos, D. Lecompte, H. Sol, and J. Vantomme (2013). "Numerical simulation and experimental validation of the dynamic response of aluminum plates under free air explosions". In: *Int. J. Impact Eng.* 54, pp. 83–95. ISSN: 0734743X. DOI: 10.1016/j.ijimpeng.2012.10.014.

Strategy& (2020). *Beirut explosion impact assessment.* Report September. Middle East, pp. 1–45.

Symonds, P. S. and W. T. Fleming (1984). "Parkes revisited: On rigid-plastic and elastic-plastic dynamic structural analysis". In: *Int. J. Impact Eng.* 2.1, pp. 1–36. ISSN: 0734743X. DOI: 10.1016/0734-743X(84)90013-7.

Symonds, P. S. and C. W. G. Fryer (1988). "On the relation between rigid-plastic and elastic-plastic predictions of response to pulse loading". In: *Int. J. Impact Eng.* 7.2, pp. 139–149.

Symonds, P. S. and T. J. Mentel (1958). "Impulsive loading of plastic beams with axial constraints". In: *J. Mech. Phys. Solids* 6.3, pp. 186–202. ISSN: 00225096. DOI: 10.1016/0022-5096(58)90025-5.

Symonds, P. S. (1967). *Survey of Methods of Analysis for Plastic Deformation of Structures Under Dynamic Loading (Final Report BU/NSRDC/1-67).* Tech. rep. Providence, R. I.: Office of Naval Research (ONR), Contract No. 3248(01)(X), Naval Ship Research and Development Center, NR-064-406, Division of Applied Mathematics, Brown University, p. 251.

Teague, D. C. (2004). "Mass Casualties in the Oklahoma City Bombing". In: *Clin. Orthop. Relat. Res.* 422.422, pp. 77–81. ISSN: 0009-921X. DOI: 10.1097/01.blo.0000131201.20418.82.

Teeling-Smith, R. G. and G. N. Nurick (1991). "The deformation and tearing of thin circular plates subjected to impulsive loads". In: *Int. J. Impact Eng.* 11.1, pp. 77–91. ISSN: 0734743X. DOI: 10.1016/0734-743X(91)90032-B.

Tetlow, L., S. Rigby, G. Langdon, A. Tyas, and G. Pezzola (2023). "Probabilistic analysis of the response of plates subjected to near-field blast loading". In.

Thil, N., N. Mehreganian, M. Moatamedi, L. A. Louca, and A. Soleiman Fallah (2019). "Dynamic plastic response of beams subjected to localised pulse loads". In: *Int. J. Prot. Struct.* 10.2, pp. 198–228. ISSN: 2041420X. DOI: 10.1177/2041419618807721.

Timoshenko, S. and S. Woinowsky-Krieger (1959). *Theory of Plates and Shells*. Second. Singapore: McGraw-Hill Inc., p. 609. ISBN: 0070858209. DOI: 10.1038/148606a0.

Timoshenko, S. and D. H. Young (1955). *Vibration Problems in Engineering*. Van Nostrand. ISBN: 9780608327990.

Tyas, A. and D. J. Pope (2003). "The energy take-up of panels subjected to near-field blast loading". In: *Int. Conf. Response Struct. to Extrem. Load.* 1.C.

Tyas, A. and D. J. Pope (2004). "Response number analysis of the response of steel plate panels to near-field blast loading". In: *2nd Asia-Pacific Conf. Prot. Struct. Against Hazards* December, pp. 311–316.

Tyas, A. (2018). "Experimental Measurement of Pressure Loading from Near-Field Blast Events: Techniques, Findings and Future Challenges". In: *18th Int. Conf. Exp. Mech.* Vol. 2. 8. Basel Switzerland: MDPI, 471(1)–471(7). DOI: 10.3390/ICEM18-05364.

Tyas, A. (2019). "Blast loading from high explosive detonation: What we know and don't know". In: *13th Int. Conf. Shock Impact Loads Struct. SILOS 2019, 14-15 December 2019, Guangzhou, China*. December. Guangzhou, China, pp. 65–76. ISBN: 9789811426896.

U.S. Army, C. o. E. (2008). *Structures To Resist The Effects of Accidental Explosions UFC 3-340-02*. Tech. rep. U.S. Army Corps of Engineers, p. 1796.

UFC (2022). *Unified Facilities Criteria (UFC)*.

Ventsel, E. and T. Krauthammer (2001). *Thin Plates and Shells: Theory: Analysis, and Applications*. CRC Press, p. 688. ISBN: 9780203908723.

Wang, A. J. (1955). "The Permanent Deflection of a Plastic Plate Under Blast Loading". In: *J. Appl. Mech.* 22.3, pp. 375–376. ISSN: 0021-8936. DOI: 10.1115/1.4011092.

Wang, A. J. and H. G. Hopkins (1954). "On the plastic deformation of built-in circular plates under impulsive load". In: *J. Mech. Phys. Solids* 3.1, pp. 22–37. ISSN: 00225096. DOI: 10.1016/0022-5096(54)90036-8.

Wang, X. D. and T. X. Yu (1991). "Parkes Revisited: Effect of Elastic Deformation at The Root of A Cantilever Beam". In: *Int. J. Impact Eng.* 11.2, pp. 197–209.

Washizu, K. (1975). *Variational Methods in Elasticity And Plasticity.* 2nd ed. Vol. 9. 2. Exeter, Great Britain: Pergamon Press, pp. 70–71. ISBN: 0080267238. DOI: 10.1002/zamm.19840640121.

Weisstein, E. W. (2022). *Parseval's Theorem - from Wolfram MathWorld.*

Wierzbicki, T. (1974). "Application of an Eigenfunction Expansion Method in Plasticity." In: *Am. Soc. Mech. Eng.* 74 -APM-C, pp. 448–452. ISSN: 04021215.

Wierzbicki, T. and G. N. Nurick (1996). "Large deformation of thin plates under localised impulsive loading". In: *Int. J. Impact Eng.* 18.7-8, pp. 899–918. ISSN: 0734743X. DOI: 10.1016/s0734-743x(96)00027-9.

Appendix A

Alternative Approach to Derive the Equilibrium Equation for the Rectangular Simple Membrane

By applying the principle of virtual work to a simple membrane (i.e., with $u_0 = v_0 = 0$) without specialising it as a rigid-perfectly plastic material, the following equilibrium equation can be obtained

$$\frac{\partial}{\partial x}\left(\sigma_x \frac{\partial w_0}{\partial x} + \sigma_{xy}\frac{\partial w_0}{\partial y}\right) + \frac{\partial}{\partial y}\left(\sigma_{xy}\frac{\partial w_0}{\partial x} + \sigma_y \frac{\partial w_0}{\partial y}\right) + \frac{p}{h} = \rho \ddot{w}_0,$$

that applies to any material.

Herein, the above equilibrium equation is made the starting point, and the aim is to re-derive the equation of motion, Eq. (3.6.10), that were presented in Section 3.6 when the simple membrane is made of a rigid-perfectly plastic von Mises material. First, the normal stresses σ_x and σ_y are expanded in terms of their deviatoric and hydrostatic pressure parts, i.e., $\sigma_x = s_x + \hat{p}$ and $\sigma_y = s_y + \hat{p}$, where $\hat{p}$ is the internal pressure, and s_x and s_y are the corresponding deviatoric stresses. $\sigma_{xy} = s_{xy}$. Substituting these in the equilibrium equation, one eventually obtains,

$$\frac{\partial}{\partial x}\left(s_x \frac{\partial w_0}{\partial x} + s_{xy}\frac{\partial w_0}{\partial y}\right) + \frac{\partial}{\partial y}\left(s_{xy}\frac{\partial w_0}{\partial x} + s_y \frac{\partial w_0}{\partial y}\right) + \frac{\partial}{\partial x}\left(\hat{p}\frac{\partial w_0}{\partial x}\right) + \frac{\partial}{\partial y}\left(\hat{p}\frac{\partial w_0}{\partial y}\right) + \frac{p}{h} = \rho \ddot{w}_0.$$

According to the rigid-plastic material assumption, strains when they develop are plastic strains; hence, when they are non-zero, then the yield condition is satisfied. From the flow rule, $\dot{\varepsilon}_{ij} = \dot{\lambda} s_{ij}$, see Section 3.4, the following, for a plane-stress problem, holds

$$\dot{\lambda} = \frac{\dot{\varepsilon}_x}{s_x} = \frac{\dot{\varepsilon}_y}{s_y} = \frac{\dot{\varepsilon}_{xy}}{s_{xy}} = \frac{\dot{\varepsilon}_z}{s_z},$$

while recalling that $\dot{\lambda} > 0$ when the yield is satisfied. So, one can write

$$s_{xy} = \frac{\dot{\varepsilon}_{xy}}{\dot{\varepsilon}_x} s_x = \frac{\dot{\varepsilon}_{xy}}{\dot{\varepsilon}_y} s_y$$

In a plane-stress problem, one also has $\sigma_z = 0 = s_z + \hat{p}$, which gives $s_z = -\hat{p}$. Moreover, due to the material assumption, the membrane is plastically incompressible, i.e., one must have $\dot{\varepsilon}_x + \dot{\varepsilon}_y + \dot{\varepsilon}_z = 0$; therefore, one can write $\dot{\varepsilon}_z = -(\dot{\varepsilon}_x + \dot{\varepsilon}_y)$.

The above relations hold as long as the material is rigid-perfectly plastic, obeying von Mises yield when the yield condition is satisfied. However, since these are expressed in incremental ("rate") form, they will not result in a simpler expression of the equilibrium equation if they were substituted into it. From now, it will be reverted to the "total" form of the flow rule, i.e., when $\varepsilon_{ij} = \lambda s_{ij}$ holds as in Section 3.4, since the aim in the present material is to re-derive the equilibrium equation given in Section 3.6.

It will be assumed now that $\varepsilon_{ij} = \lambda s_{ij}$ holds, and hence (in a very analogous way to the above) one can write

$$\lambda = \frac{\varepsilon_x}{s_x} = \frac{\varepsilon_y}{s_y} = \frac{\varepsilon_{xy}}{s_{xy}} = \frac{\varepsilon_z}{s_z}$$

and based on this, one further has

$$s_{xy} = \frac{\varepsilon_{xy}}{\varepsilon_x} s_x = \frac{\varepsilon_{xy}}{\varepsilon_y} s_y$$

The incompressibility now takes the "total" form: $\varepsilon_z = -(\varepsilon_x + \varepsilon_y)$. In addition, one still has $s_z = -\hat{p}$.

Now the equilibrium equation can be re-written as

$$\frac{\partial}{\partial x}\left(s_x \frac{\partial w_0}{\partial x} + s_y \frac{\varepsilon_{xy}}{\varepsilon_y}\frac{\partial w_0}{\partial y}\right) + \frac{\partial}{\partial y}\left(s_x \frac{\varepsilon_{xy}}{\varepsilon_x}\frac{\partial w_0}{\partial x} + s_y \frac{\partial w_0}{\partial y}\right) + \frac{\partial}{\partial x}\left(-s_z \frac{\partial w_0}{\partial x}\right) + \frac{\partial}{\partial y}\left(-s_z \frac{\partial w_0}{\partial y}\right) + \frac{p}{h} = \rho \ddot{w}_0,$$

in which use has been made of: $s_{xy} = (\varepsilon_{xy}/\varepsilon_y)s_y = (\varepsilon_{xy}/\varepsilon_x)s_x$ (twice) and $\hat{p} = -s_z$.

The terms involving quotients of strains can be evaluated according to the definitions of the in-plane strains in terms of the derivatives of displacement. That is,

$$\frac{\varepsilon_{xy}}{\varepsilon_y}\frac{\partial w_0}{\partial y} = \frac{(1/2)\frac{\partial w_0}{\partial x}\frac{\partial w_0}{\partial y}}{(1/2)\left[\frac{\partial w_0}{\partial y}\right]^2}\frac{\partial w_0}{\partial y} = \frac{\partial w_0}{\partial x}$$

$$\frac{\varepsilon_{xy}}{\varepsilon_x}\frac{\partial w_0}{\partial x} = \frac{(1/2)\frac{\partial w_0}{\partial x}\frac{\partial w_0}{\partial y}}{(1/2)\left[\frac{\partial w_0}{\partial x}\right]^2}\frac{\partial w_0}{\partial x} = \frac{\partial w_0}{\partial y}.$$

By substituting the above two relations in the equilibrium equation and collecting common

terms, it becomes

$$\frac{\partial}{\partial x}\left[\frac{\partial w_0}{\partial x}(s_x+s_y)\right]+\frac{\partial}{\partial y}\left[\frac{\partial w_0}{\partial y}(s_x+s_y)\right]+\frac{\partial}{\partial x}\left(-s_z\frac{\partial w_0}{\partial x}\right)+\frac{\partial}{\partial y}\left(-s_z\frac{\partial w_0}{\partial y}\right)+\frac{p}{h}=\rho\ddot{w}_0.$$

Next, since the deviatoric stress, by definition, has the property that $s_x+s_y+s_z\equiv 0$, then one has $s_x+s_y=-s_z$, which, when substituted in the last equilibrium equation, leads to

$$\frac{\partial}{\partial x}\left[-s_z\frac{\partial w_0}{\partial x}\right]+\frac{\partial}{\partial y}\left[-s_z\frac{\partial w_0}{\partial y}\right]+\frac{\partial}{\partial x}\left(-s_z\frac{\partial w_0}{\partial x}\right)+\frac{\partial}{\partial y}\left(-s_z\frac{\partial w_0}{\partial y}\right)+\frac{p}{h}=\rho\ddot{w}_0,$$

or,

$$2\left[\frac{\partial}{\partial x}\left(-s_z\frac{\partial w_0}{\partial x}\right)+\frac{\partial}{\partial y}\left(-s_z\frac{\partial w_0}{\partial y}\right)\right]+\frac{p}{h}=\rho\ddot{w}_0$$

Therefore, the equilibrium equation (in terms of stresses) depends on the value of $(-s_z)$ at yield. By the total form of the flow rule, one has

$$s_z=\sqrt{(2/3)}\sigma_0\frac{\varepsilon_z}{\sqrt{\varepsilon_{ij}\varepsilon_{ij}}}.$$

From the incompressibility, $\varepsilon_z=-(\varepsilon_x+\varepsilon_y)$, and it was shown in the previous section that $\varepsilon_{ij}\varepsilon_{ij}=\varepsilon_x^2+2\varepsilon_{xy}^2+\varepsilon_y^2+\varepsilon_z^2=2(\varepsilon_x+\varepsilon_y)^2$, according to the definition of the strains (in terms of derivatives of displacement) and the incompressibility. Hence, one has

$$s_z=\sqrt{(2/3)}\sigma_0\frac{-(\varepsilon_x+\varepsilon_y)}{\sqrt{2}(\varepsilon_x+\varepsilon_y)}=\frac{-1}{\sqrt{3}}\sigma_0.$$

Observe that from the above result, one also has $\hat{p}=-s_z=1/(\sqrt{3})\sigma_0$, and from the latter one has $\sigma_x+\sigma_y=3\hat{p}=\sqrt{3}\sigma_0$.

Finally, the substitution is made for $s_z=-1/(\sqrt{3})\sigma_0$, which is a constant, in the last equilibrium equation to obtain

$$\frac{2}{\sqrt{3}}\sigma_0\left(\frac{\partial^2 w_0}{\partial x^2}+\frac{\partial^2 w_0}{\partial y^2}\right)+\frac{p}{h}=\rho\ddot{w}_0,$$

which is identical to Eq. (3.6.10), given in Section 3.6. Again, the validity of this equation is limited to the cases for which the "total" form of the flow rule holds, $\varepsilon_{ij}=\lambda s_{ij}$.

Appendix B

Axi-Symmetric Membranes and the In-Plane Displacement Effect

B.1 Axi-Symmetric Circular Membranes

B.1.1 Overview and the Problem Definition

The equation of motion for circular membranes under axi-symmetric conditions will be derived using the virtual work principle. As such, the starting point is the definition of the membrane strains. The problem to be investigated is as follows. Consider a general membrane, i.e., a very thin plate where its flexure provides no resistance, and the plate undergoes large transverse displacement. The membrane's parameters are thickness h, density ρ, radius R, and the externally applied pressure is p. The membrane is assumed to be fully restrained along the outer periphery. The radial and transverse coordinates are denoted by r and z, and the z-axis originates at the plate's mid-plane. Furthermore, let the loading and boundary conditions be axi-symmetric. Hence, the membrane motion is completely characterised by the transverse, w, and radial, u, displacements, and all mechanical quantities are independent of the circumferential coordinate, θ.

It should be noted that the present problem derives from the von Kármán plate by assuming negligible flexure action, i.e., in the Föpple kinematics sense. Therefore, all quantities are uniform across the thickness. That is, for the present axi-symmetric case, all motion variables are functions of the radial coordinate, r, only. Furthermore, due to the plate's thinness, the transverse shear stresses are zero.

B.1.2 Membrane Strains

The in-plane strains for the above defined membrane are

$$\begin{aligned} \varepsilon_r^M &= \frac{\partial u}{\partial r} + \frac{1}{2}\left(\frac{\partial w}{\partial r}\right)^2, \\ \varepsilon_\theta^M &= \frac{u}{r}, \\ \varepsilon_{r\theta}^M &= 0, \end{aligned} \tag{B.1.1}$$

while the three remaining (transverse) strains are identically zero; the superscript M refers to the general membrane, or Föpple's plate.

According to the zero transverse shear stresses, the plate's mid-plane is the principal plane. Furthermore, since the transverse in-plane stress, $\sigma_{r\theta}$, is zero due to the axi-symmetry, the polar coordinates', r and θ, directions are the principal axes.

B.1.3 Equilibrium Equations for a General Membrane

The virtual work equation for the present problem is written as

$$\int_R \left(h\sigma_r \delta\varepsilon_r + h\sigma_\theta \delta\varepsilon_\theta + h\rho\ddot{w}\delta w - p\delta w\right) r\, dr = 0, \tag{B.1.2}$$

where it has been assumed that $\ddot{u} = 0$, and p is a surface pressure that is applied in the z-direction. Upon substituting for the in-plane strains, $\delta\varepsilon_r = \delta\varepsilon_r^M$, etc., and, subsequently, carrying out integration by parts, and noting $\delta u = 0$ and $\delta w = 0$ at $r = R$ (since the corresponding actual displacements are prescribed), and $\delta u = 0$ at the origin $r = 0$ (due to the axi-symmetry), one obtains

$$\int_R \left[-h\frac{\partial}{\partial r}\left(r\sigma_r\right) + h\sigma_\theta\right]\delta u + \left[-h\frac{\partial}{\partial r}\left(r\sigma_r\frac{\partial w}{\partial r}\right) + rh\rho\ddot{w} - rp\right]\delta w dr = 0, \tag{B.1.3}$$

Then, the virtual displacements, δu and δw, are made arbitrary within the domain to obtain the following two equilibrium equations, after some arrangements of terms,

$$\begin{aligned} \frac{\partial}{\partial r}\left(r\sigma_r\right) - \sigma_\theta &= 0 \\ \frac{\partial}{\partial r}\left(r\sigma_r\frac{\partial w}{\partial r}\right) + \frac{rp}{h} &= r\rho\ddot{w}, \end{aligned}$$

or, after expanding the derivatives of the products,

$$\begin{aligned} \frac{\partial \sigma_r}{\partial r} + \frac{\sigma_r - \sigma_\theta}{r} &= 0 \\ \frac{\partial \sigma_r}{\partial r}\frac{\partial w}{\partial r} + \sigma_r \frac{\partial^2 w}{\partial r^2} + \frac{\sigma_r}{r}\frac{\partial w}{\partial r} + \frac{p}{h} &= \rho \ddot{w} \end{aligned} \tag{B.1.4}$$

B.1.4 Equilibrium Equation for a Simple Membrane

The simple membrane is considered the special case of the general one where the in-plane displacement, namely u, is zero. Thus, the only non-zero strain is $\varepsilon_r = (1/2)\left(\frac{\partial w}{\partial r}\right)^2$, and $\varepsilon_\theta = 0$.

Therefore, by simple application of the virtual work in which the only degree-of-freedom is the transverse displacement, w, whose variation is δw, the following single equilibrium equation governs its motion

$$\frac{\partial \sigma_r}{\partial r}\frac{\partial w}{\partial r} + \sigma_r \frac{\partial^2 w}{\partial r^2} + \frac{\sigma_r}{r}\frac{\partial w}{\partial r} + \frac{p}{h} = \rho \ddot{w} \tag{B.1.5}$$

which is the transverse equilibrium equation of the general membrane.

For the sake of completion, a special case of the above equilibrium equation will be derived when the simple membrane is made of a rigid-perfectly plastic von Mises's material with tensile yield stress σ_0, and the total flow rule is assumed valid, $\varepsilon_{ij} = \lambda s_{ij}$, where the total plastic multiplier, λ, is $\sqrt{(3/2)}/(\sigma_0)\sqrt{\varepsilon_{ij}\varepsilon_{ij}}$. Accordingly, the deviatoric stress is $s_{ij} = \sqrt{(2/3)}\sigma_0 \varepsilon_{ij}/\sqrt{\varepsilon_{kl}\varepsilon_{kl}}$.

Since the only non-zero in-plane strain is ε_r, and from the incompressibility, $\varepsilon_r + \varepsilon_\theta + \varepsilon_z = \varepsilon_r + \varepsilon_z = 0$, one has $\sqrt{\varepsilon_{ij}\varepsilon_{ij}} = \sqrt{2}\varepsilon_r$. Furthermore, from $\sigma_z = s_z + \hat{p} = 0$, the internal (hydrostatic) pressure, $\hat{p}$, is given by $\hat{p} = -s_z$. For the present axi-symmetric problem, $s_{r\theta} = \sigma_{r\theta} = 0$.

By applying the flow rule, the deviatoric stresses are $s_r = \sigma_0/\sqrt{3}$, $s_\theta = 0$ (since $\varepsilon_\theta \equiv 0$ in the simple membrane), and $s_z = -\sigma_0/\sqrt{3} = -\hat{p}$. Therefore, the normal stresses are $\sigma_r = s_r + \hat{p} = 2/\sqrt{3}\sigma_0$, and $\sigma_\theta = \hat{p} = 1/\sqrt{3}\sigma_0 = (1/2)\sigma_r$. Note that the radial and circumferential stresses are the principal (in-plane) stresses.

Lastly, since $\sigma_r = 2/\sqrt{3}\sigma_0$, and noting that σ_0 is constant (i.e., σ_r is independent of the strains provided the total flow rule is valid, and the membrane is yielding), namely $\frac{\partial \sigma_r}{\partial r} \equiv 0$, then the earlier equilibrium equation of the simple membrane takes the following form

$$\frac{2}{\sqrt{3}}\sigma_0 \left(\frac{\partial^2 w}{\partial r^2} + \frac{1}{r}\frac{\partial w}{\partial r} \right) + \frac{p}{h} = \rho \ddot{w}, \tag{B.1.6}$$

which governs the transverse motion of the simple membrane. This equation is valid provided that the simple membrane is under active yielding and is loaded monotonically (i.e., when the total flow rule applies). For clarity, it is implied that the membrane is in

axi-symmetric conditions. This equation, if $p = 0$ (for an impulsive loading), is identical to Eq. (4.3.14) which is presented in Section 4.3.2.

B.2 In-Plane Displacement Effect

B.2.1 Cloete and Nurick's Case of Axi-symmetric Membranes

Cloete and Nurick (2014) considered a general membrane that is made of a rigid-perfectly plastic material which obeys the von Mises's yield criterion. The authors argued that the radial stress is constant throughout the (circular) domain; that is, $\frac{\partial \sigma_r}{\partial r} \equiv 0$. Hence, the radial equilibrium equation

$$r\frac{\partial \sigma_r}{\partial r} + (\sigma_r - \sigma_\theta) = 0,$$

requires that the normal in-plane stresses (which are the principal stresses) are equal, i.e.,

$$\sigma_r = \sigma_\theta \tag{B.2.1}$$

for all r.

Furthermore, the membrane's stresses must be non-negative (for stability). Hence, the stress state that satisfies the von Mises's yield condition, $\sigma_r = \sigma_\theta$, and $\sigma_r \geq 0$ is $\sigma_r = \sigma_\theta = \sigma_0$, where σ_0 is the uni-axial tensile yield stress. This can be shown by noting that the von Mises condition in the σ_r-σ_θ space, which is the principal in-plane space, can be written as

$$\sigma_r\left(\sigma_r - \sigma_\theta\right) + \sigma_\theta^2 = \sigma_0^2 \tag{B.2.2}$$

which, for $\sigma_r = \sigma_\theta$, gives $\sigma_\theta^2 = \sigma_0^2$. Lastly, for the stresses to be positive, then $\sigma_r = \sigma_\theta = \sigma_0$.

The associated "incremental" flow rule, $\dot{\varepsilon}_{ij} = \dot{\lambda} s_{ij}$, for a von Mises's material, requires that at the point $(\sigma_r, \sigma_\theta) = (\sigma_0, \sigma_0)$, the rates of normal in-plane strains are also equal; this is because

$$\sigma_r = \sigma_\theta$$

$$\hat{p} + s_r = \hat{p} + s_\theta$$

for any hydrostatic pressure, $\hat{p}$. Hence, $s_r = s_\theta$, and by using the incremental flow rule

$$s_r = s_\theta$$

$$\frac{\dot{\varepsilon}_r}{\dot{\lambda}} = \frac{\dot{\varepsilon}_\theta}{\dot{\lambda}}$$

that directly gives

$$\dot{\varepsilon}_r = \dot{\varepsilon}_\theta, \tag{B.2.3}$$

for any arbitrary positive value of the rate of plastic multiplier, $\dot{\lambda}$. Lastly, since the material is incompressible, i.e., the deviatoric and total strains are identical, then the above rates of strains are the rates of the total radial, $\dot{\varepsilon}_r$, and circumferential, $\dot{\varepsilon}_\theta$, strains.

Note that the hydrostatic pressure is given by $\hat{p} = (1/3)(\sigma_r + \sigma_\theta) = (2/3)\sigma_0$, where $\sigma_z = 0$ has been used. Thus, $s_r = s_\theta = \sigma_0 - (2/3)\sigma_0 = (1/3)\sigma_0$, which is positive. Hence, the (equal) rates of normal in-plane strains are also positive since $\dot{\lambda}$ is non-negative. As a result, a membrane element is under bi-axial in-plane stretching in the membrane's mid-plane. In addition, since $\sigma_z = s_z + \hat{p}$, then it follows that $s_z = -(2/3)\sigma_0$, which is negative. As a result, $\dot{\varepsilon}_z$ is non-positive which, in turn, indicates necking (or shortening of the thickness). The incompressibility also requires $\dot{\varepsilon}_z = -(\dot{\varepsilon}_r + \dot{\varepsilon}_\theta) = -2\dot{\varepsilon}_r$, which, again, confirms the negativity of the transverse normal strain rates.

The effect of the in-plane displacement, u, on the total plastic work is discussed next. The total plastic work of the present axi-symmetric problem can be written as

$$W_p = \int_R \left[rh\sigma_r \frac{\partial u}{\partial r} + rh\sigma_r \frac{1}{2}\left(\frac{\partial w}{\partial r}\right)^2 + h\sigma_\theta u \right] dr \tag{B.2.4}$$

where the first two terms are associated with radial stress and the last term is associated with the circumferential stress. Note that the second term is the only non-zero term for the plastic work of a corresponding *simple* membrane, i.e., when $u = 0$.

When the radial and circumferential stresses are made equal (and noting that their common value, σ_0, is constant), Cloete and Nurick derives the following interesting and important result

$$W_p = \int_R h\sigma_0 \left[r\frac{\partial u}{\partial r} + r\frac{1}{2}\left(\frac{\partial w}{\partial r}\right)^2 + u \right] dr \tag{B.2.5}$$

Hence, when the first term is integrated by parts, and assuming $u = 0$ on the boundary and at $r = 0$ (due to the axi-symmetric condition), the plastic work of the *general* membrane evaluates to

$$\begin{aligned} W_p &= \int_R h\sigma_0 \left[-\frac{\partial r}{\partial r}u + r\frac{1}{2}\left(\frac{\partial w}{\partial r}\right)^2 + u \right] dr \\ &= \int_R h\sigma_0 \left[(u-u) + r\frac{1}{2}\left(\frac{\partial w}{\partial r}\right)^2 \right] dr \\ &= \int_R h\sigma_0 r\frac{1}{2}\left(\frac{\partial w}{\partial r}\right)^2 dr \end{aligned} \tag{B.2.6}$$

The last result indicates that there is no contribution to the plastic work of the general membrane by the in-plane displacement, which is the radial displacement, u, provided the membrane is under axi-symmetric conditions and is fixed at the outer boundary, i.e., $u = 0$ at the limits $r = 0$ and $r = R$. As indicated by the above, the contributions of

the radial displacement to the radial and circumferential internal work cancel each other. This important result is due to Cloete and Nurick (2014). An important implication of the result is the transverse motion of a general (axi-symmetric circular) membrane, in which $\sigma_r = \sigma_\theta = \sigma_0$, is completely independent of the in-plane (or radial) displacement.

Using $\sigma_r = \sigma_0$, which is constant (i.e., $\frac{\partial \sigma_r}{\partial r} = 0$), in the transverse equilibrium equation, the latter becomes

$$\frac{\sigma_0}{\rho}\left(\frac{\partial^2 w}{\partial r^2} + \frac{1}{r}\frac{\partial w}{\partial r}\right) + \frac{p}{\rho h} = \ddot{w} \tag{B.2.7}$$

This equation is independent of the radial displacement, u, and the solution of which is the response of transverse motion, w. Thus, w is assumed to be known (by solving this equilibrium equation when subjected to some initial and boundary conditions on w and $\dot{w}$).

The membrane strains are to be discussed next. The rates of the normal strains, $\dot{\varepsilon}_r$ and $\dot{\varepsilon}_\theta$, are equal, as was shown earlier, based on the incremental flow rule and the condition that $\sigma_r = \sigma_\theta$. Although, Cloete and Nurick (2014) argued that the normal strains, ε_r and ε_θ, themselves, are also equal. This appears to be due to an implied assumption that the total flow rule is applicable, i.e., the membrane is loaded monotonically, and the stress state $\sigma_r = \sigma_\theta = \sigma_0$ is fixed throughout the deformation path. Therefore, the authors state that

$$\frac{u}{r} = \frac{\partial u}{\partial r} + \frac{1}{2}\left(\frac{\partial w}{\partial r}\right)^2 \tag{B.2.8}$$

where the left-hand side is the circumferential strain, ε_θ, whereas the right-hand side is the radial strain, ε_r. This (differential) equation relates u to the priorly known w. Multiplying both sides of the above equation by r and rearranging terms, it can be rewritten as

$$r\frac{\partial u}{\partial r} - u = -\frac{r}{2}\left(\frac{\partial w}{\partial r}\right)^2 \tag{B.2.9}$$

Since $r^2 \frac{\partial}{\partial r}(u/r)$ equals to the left-hand side of the above differential equation, then it becomes

$$\frac{\partial}{\partial r}\left(\frac{u}{r}\right) = -\frac{1}{2r}\left(\frac{\partial w}{\partial r}\right)^2 \tag{B.2.10}$$

It is noticed that the left-hand side is the derivative, with respect to r, of the circumferential strain, ε_θ. Since the right-hand side is always negative (because r and $(\frac{\partial w}{\partial r})^2$ both are non-negative), then ε_θ is monotonically decreasing as r increases. The solution (u/r) is obtained by direct integration over r to get

$$\frac{u}{r} = \varepsilon_\theta^0 - \frac{1}{2}\int_0^r \frac{1}{r}\left(\frac{\partial w}{\partial r}\right)^2 dr \tag{B.2.11}$$

where ε_θ^0 is the constant of integration which corresponds to the value of $\varepsilon_\theta = (u/r)$ at the circular plate's centre, $r = 0$. The integral in the second term of the right-hand side is assumed to be given since w is already known from the solution of the transverse

equilibrium equation, Eq. (B.2.7). From the boundary condition $u = 0$ at $r = R$, it is found that

$$\varepsilon_\theta^0 = \frac{1}{2}\int_0^R \frac{1}{r}\left(\frac{\partial w}{\partial r}\right)^2 dr \tag{B.2.12}$$

Note that $\frac{\partial w}{\partial r} = 0$ at $r = 0$ (due to the axi-symmetry), and, hence, the integral is finite. The circumferential strain, ε_θ, has a maximum value, ε_θ^0, at the centre, and it decreases (monotonically) to the zero value at $r = R$ (since $\varepsilon_\theta = u/r$ and $u = 0$ at the mentioned limit).

Lastly, since $\varepsilon_\theta = \varepsilon_r$, then ε_θ^0 is also the value of ε_r at the centre. All results on ε_θ applies equally to ε_r, namely ε_r is monotonically decreasing, and its maximum is ε_θ^0 that is located at the plate's centre.

The above treatment gives qualitative information on the distribution of membranes strains and an important quantitative estimate on the maximum membrane's strain, i.e., the primary parameter of interest to control material failure. The in-plane displacement, u, can be found by simply multiplying (u/r) by r. The above solution for u/r also says that u is non-negative throughout the domain, $r = [0, R]$; this is because

$$\varepsilon_\theta^0 \geq \frac{1}{2}\int_0^r \frac{1}{r}\left(\frac{\partial w}{\partial r}\right)^2 dr$$

for $0 \leq r \leq R$.

The contribution of u to the radial strain, ε_r, can be found, using Eqs. (B.2.8) and (B.2.11), as

$$\begin{aligned}\frac{\partial u}{\partial r} &= \frac{u}{r} - \frac{1}{2}\left(\frac{\partial w}{\partial r}\right)^2 \\ &= \varepsilon_\theta^0 - \frac{1}{2}\int_0^r \frac{1}{r}\left(\frac{\partial w}{\partial r}\right)^2 dr - \frac{1}{2}\left(\frac{\partial w}{\partial r}\right)^2\end{aligned}$$

which, when evaluated at $r = R$, the first two terms on the right-hand side cancel each other, and it can be found that the value of $\frac{\partial u}{\partial r}$ is the negative of $(1/2)\left(\frac{\partial w}{\partial r}\right)^2$ at the same point, $r = R$. Hence, it is confirmed that the radial strain, ε_r, is zero at the membrane's periphery.

An additional property on the distribution of u can be inferred as follows. By multiplying the differential equation, Eq. (B.2.10), by r^2, integrating both sides over r, carrying integration by parts on the left-hand side, and then using the boundary conditions on u at $r = 0$ and $r = R$, it can be shown that the following identity holds

$$2\int_0^R u dr = \frac{1}{2}\int_0^R \left(\frac{\partial w}{\partial r}\right)^2 r dr \tag{B.2.13}$$

which confirms that the area under (the non-negative) u is positive. The right-hand side of the last relation is proportional to the total plastic work (which depends completely on w alone). When the plate is impulsively loaded, i.e., $p = 0$ and $\dot{w}_0$ is given by the specific

impulse $i(r)$, according to $\dot{w}_0 = i/(\rho h)$, then the total plastic work can be made equal to the total upper-bound (initial) kinetic energy to get

$$\frac{\sigma_0 h}{2} \int_0^R \left(\frac{\partial w}{\partial r}\right)^2 r dr = \frac{1}{2\rho h} \int_0^R i^2 \, r dr \tag{B.2.14}$$

which, then, leads to

$$\int_0^R u dr = \frac{1}{2\sigma_0 h} \left(\frac{1}{2\rho h} \int_0^R i^2 \, r dr\right) \tag{B.2.15}$$

in which the quantity inside the parenthesis, on the right-hand side, is the initial kinetic energy (per unit radian). By noting that u is non-negative, see Eq. (B.2.11), and since it must be smooth and finite, the small area under its curve, as estimated by the above relation (and noting the large factor $2\sigma_0$ in the denominator), implies that u, itself, is small in an impulsively loaded axi-symmetric membrane.

The result of Cloete and Nurick underlies the work of the present thesis, based on which the in-plane displacements were neglected. Note that Cloete and Nurick result is general regardless of the distribution of u and w, provided that the in-plane strains are tensile throughout the domain, as required for $\sigma_r = \sigma_\theta = \sigma_0$. Although, the result is only ensured for the axi-symmetric circular problem. The circular axi-symmetric membrane is a problem that is expressed in the principal plane. However, it remains equally important to attempt to generalise Cloete and Nurick's result to non-circular problems. Thus, for general problems that are described in rectangular Cartesian system, the starting point can be based on rewriting the plastic work in the principal plane as the original work of the above-cited authors applies to a problem in the principal plane.

B.2.2 Extension of the Cloete and Nurick's Result

B.2.2.1 Motivation

The analytical result of Cloete and Nurick (2014), which was introduced and discussed in Section B.2.1, is of great importance as it allows crucial simplifications when analysing membranes under intense lateral loadings. In particular, the authors show that the in-plane displacements can be neglected when the transverse motion of the membrane is the primary concern. Although their result initially appears to be applicable for an axi-symmetric circular problem, it suggests the possibility to be generalised since the mentioned problem is one that is described in the principal (stress) plane. Hence, the starting point, herein, is to describe the general problem in the corresponding principal plane.

B.2.2.2 Principal Stress Analysis

A general membrane (i.e., with in-plane displacements) is considered. The membrane's mid-plane is the principal plane since the transverse shear stresses are identically zero.

The strains, stresses, and in-plane displacements, in the following, refer to the principal coordinate system even though the principal directions are unknown in advance. Let x_1 and x_2 be the principal (in-plane) axes, and the corresponding components of the in-plane displacement are u_1 and u_2; for example, u_1 is measured along x_1. The transverse displacement w is along the out-of-plane direction. By the definition of the principal directions, the in-plane shear stress is zero, i.e., $\sigma_{12} = 0$.

In the following, the equilibrium equations and the internal work expressions will be derived using the same basic procedure that has been used throughout the thesis, i.e., the principle of virtual work. Thus, the starting point is determining the expressions of the strains. As mentioned above, the present problem is to be investigated in the principal plane. The expression of the strain tensor in an orthogonal curvlinear coordinate system is derived by Liu et al. (2010), from which the following expressions are adopted since the principal axes are orthogonal and curvlinear.

The (principal) in-plane stains are

$$\varepsilon_1 = \frac{\partial u_1^*}{\partial {x_1}^*} + \frac{1}{2}\left(\frac{\partial w^*}{\partial {x_1}^*}\right)^2$$

$$\varepsilon_2 = \frac{\partial u_2^*}{\partial {x_2}^*} + \frac{1}{2}\left(\frac{\partial w^*}{\partial {x_2}^*}\right)^2$$

In the above strain definitions, the (starred) partial differentials include corrections since the (orthogonal curvlinear) coordinates, x_1 and x_2, are, in general, curved; note that u_1 and u_2 are measured along these curves. The partial differentials are

$$\partial x_1^* = \xi_1 \partial x_1,$$

$$\partial x_2^* = \xi_2 \partial x_2,$$

$$\partial u_1^* = \partial u_1 - u_2 \partial f,$$

$$\partial u_2^* = \partial u_2 + u_1 \partial f,$$

where ξ_i is the scale length associated with x_i, and the correction operator, ∂f, is a pure function of (the two) ξ_i's and (the two) ∂x_i's. Their expressions will be given later. Note that the out-of-plane coordinate, z, and the corresponding displacement, w, neither influence nor are influenced by the differentials of the in-plane displacements. This is because the direction of z (and, hence, w) is not curved. That is, $\xi_3 = 1$ and $\partial w^* = \partial u_3 = \partial w$.

The scaling length ξ_i is defined as

$$\xi_i = \left[\left(\frac{\partial x}{\partial x_i} \right)^2 + \left(\frac{\partial y}{\partial x_i} \right)^2 + \left(\frac{\partial z}{\partial x_i} \right)^2 \right]^{1/2},$$

in which x, y, and z are the usual rectangular Cartesian coordinates. The correction operator is

$$\partial f = -\frac{\partial \xi_1}{\partial x_2} \frac{\partial x_1}{\xi_2} + \frac{\partial \xi_2}{\partial x_1} \frac{\partial x_2}{\xi_1}$$

However, in the following, it is unnecessary to substitute the explicit expressions of ξ_i's and ∂f. For the derivations of the above expressions for ξ_i and ∂f, the reader is referred to the work of Liu et al. (2010).

The principal (normal) stresses, which are work-conjugates to ε_1 and ε_2, respectively, are denoted by σ_1 and σ_2.

The virtual work, with reference to the principal plane, takes the form

$$\int_A \left(h\sigma_1 \delta\varepsilon_1 + h\sigma_2 \delta\varepsilon_2 + h\rho\ddot{w}\delta w - p\delta w \right) \xi_1 \xi_2 dx_1 dx_2 = 0 \tag{B.2.16}$$

or,

$$\begin{aligned} \int_A \left[h\frac{\sigma_1}{\xi_1} \left(\frac{\partial \delta u_1}{\partial x_1} - \delta u_2 \frac{\partial f}{\partial x_1} + \frac{1}{\xi_1} \frac{\partial w}{\partial x_1} \frac{\partial \delta w}{\partial x_1} \right) \right] \xi_1 \xi_2 dx_1 dx_2 \\ + \int_A \left[h\frac{\sigma_2}{\xi_2} \left(\frac{\partial \delta u_2}{\partial x_2} + \delta u_1 \frac{\partial f}{\partial x_2} + \frac{1}{\xi_2} \frac{\partial w}{\partial x_2} \frac{\partial \delta w}{\partial x_2} \right) \right] \xi_1 \xi_2 dx_1 dx_2 \\ + \int_A \left[h\rho\ddot{w}\delta w - p\delta w \right] \xi_1 \xi_2 dx_1 dx_2 = 0 \end{aligned} \tag{B.2.17}$$

where $\ddot{u}_1 = \ddot{u}_2 = 0$, and $(p\,\xi_1 \xi_2\, dx_1 dx_2)$ is assumed to be work-conjugate to w. The virtual work statement can be shown, through carrying integration by parts and requiring δu_1, δu_2, and δw to be arbitrary everywhere except on the boundary of the surface domain, A, to lead into the following three equilibrium equations

$$\frac{\partial}{\partial x_1}(\sigma_1 \xi_2) - \sigma_2 \xi_1 \frac{\partial f}{\partial x_2} = 0 \tag{B.2.18}$$

$$\frac{\partial}{\partial x_2}(\sigma_2 \xi_1) + \sigma_1 \xi_2 \frac{\partial f}{\partial x_1} = 0 \tag{B.2.19}$$

$$\frac{1}{\xi_1 \xi_2} \left[\frac{\partial}{\partial x_1} \left(\frac{\sigma_1 \xi_2}{\xi_1} \frac{\partial w}{\partial x_1} \right) + \frac{\partial}{\partial x_2} \left(\frac{\sigma_2 \xi_1}{\xi_2} \frac{\partial w}{\partial x_2} \right) \right] + \frac{p}{h} = \rho\ddot{w} \tag{B.2.20}$$

The internal actual work is

$$W_{\text{int}} = \int_A h \left[\frac{\sigma_1 \xi_2}{2\xi_1} \left(\frac{\partial w}{\partial x_1} \right)^2 + \frac{\sigma_2 \xi_1}{2\xi_2} \left(\frac{\partial w}{\partial x_2} \right)^2 \right] dx_1 dx_2 + \int_A h \left[-\frac{\partial}{\partial x_1}(\sigma_1 \xi_2) + \sigma_2 \xi_1 \frac{\partial f}{\partial x_2} \right] u_1 \, dx_1 dx_2 + \int_S h \left[u_1 \sigma_1 \xi_2 \right] \, dx_2 + \int_A h \left[-\frac{\partial}{\partial x_2}(\sigma_2 \xi_1) - \sigma_1 \xi_2 \frac{\partial f}{\partial x_1} \right] u_2 \, dx_1 dx_2 + \int_S h \left[u_2 \sigma_2 \xi_1 \right] \, dx_1 \quad \text{(B.2.21)}$$

which, in view of the first two (in-plane) equilibrium equations, simplifies to

$$W_{\text{int}} = \int_A h \left[\frac{\sigma_1 \xi_2}{2\xi_1} \left(\frac{\partial w}{\partial x_1} \right)^2 + \frac{\sigma_2 \xi_1}{2\xi_2} \left(\frac{\partial w}{\partial x_2} \right)^2 \right] dx_1 dx_2 + \int_S h \left[u_1 \sigma_1 \xi_2 \right] \, dx_2 + \int_S h \left[u_2 \sigma_2 \xi_1 \right] \, dx_1 \quad \text{(B.2.22)}$$

Thus, when the membrane is restrained with respect to u_1 and u_2 along the entire boundary, i.e., when the line integrals in above vanish completely, then the internal actual work becomes

$$W_{\text{int}} = \int_A h \left[\frac{\sigma_1 \xi_2}{2\xi_1} \left(\frac{\partial w}{\partial x_1} \right)^2 + \frac{\sigma_2 \xi_1}{2\xi_2} \left(\frac{\partial w}{\partial x_2} \right)^2 \right] dx_1 dx_2 \quad \text{(B.2.23)}$$

As can be seen from the above result, the internal work is independent of u_1 and u_2 whenever the normal principal stresses, σ_1 and σ_2, are themselves independent of those in-plane displacements. Hence, if the principal normal stresses are considered to be constant in a rigid-perfectly plastic membrane, then it can be said that the internal actual work, W_{int}, and the transverse equilibrium equation (governing the transverse motion, w) do not depend on the in-plane displacements, u_1 and u_2. For a rectangular membrane that is expressed in the usual rectangular coordinate system, the in-plane displacements u (measured along x) and v (measured along y) are linear combinations of the in-plane displacements u_1 and u_2, which appear in the above expressions. Thus, the internal work is independent of u and v as well.

Before closing the present subsection, it can be constructive to rewrite (or expand) the in-plane equilibrium equations. For this, the fractions $\frac{\partial f}{\partial x_2}$ (in the first equilibrium equation) and $\frac{\partial f}{\partial x_1}$ (in the second equation) need to be evaluated (while noting that $\frac{\partial x_i}{\partial x_j} = \delta_{ij}$, in which δ_{ij} is the Kronecker delta, due to the orthogonality of the coordinates)

$$\frac{\partial f}{\partial x_2} = \frac{1}{\xi_1} \frac{\partial \xi_2}{\partial x_1}$$

$$\frac{\partial f}{\partial x_1} = -\frac{1}{\xi_2} \frac{\partial \xi_1}{\partial x_2}$$

The first two equilibrium equations, then, become

$$\frac{\partial}{\partial x_1}(\sigma_1 \xi_2) - \sigma_2 \frac{\partial \xi_2}{\partial x_1} = 0 \tag{B.2.24}$$

$$\frac{\partial}{\partial x_2}(\sigma_2 \xi_1) - \sigma_1 \frac{\partial \xi_1}{\partial x_2} = 0 \tag{B.2.25}$$

To appreciate the physical interpretation of the above in-plane equilibrium equations, consider the following brief example. In an axi-symmetric membrane, the principal axes are the radial and circumferential axes. Here $x_1 = r$, $x_2 = \theta$. Since $(x, y, z) = (r\cos\theta, r\sin\theta, z)$, then

$$\begin{aligned}
\xi_1 \equiv \xi_r &= \left[\left(\frac{\partial x}{\partial r}\right)^2 + \left(\frac{\partial y}{\partial r}\right)^2 + \left(\frac{\partial z}{\partial r}\right)^2\right]^{1/2} \\
&= \left[\cos^2\theta + \sin^2\theta\right]^{1/2} \\
&= 1, \\
\xi_2 \equiv \xi_\theta &= \left[\left(\frac{\partial x}{\partial \theta}\right)^2 + \left(\frac{\partial y}{\partial \theta}\right)^2 + \left(\frac{\partial z}{\partial \theta}\right)^2\right]^{1/2} \\
&= \left[r^2\left(\sin^2\theta + \cos^2\theta\right)\right]^{1/2} \\
&= r
\end{aligned}$$

Therefore, the first equilibrium equation (i.e., along the r-axis) becomes $\frac{\partial}{\partial r}(r\sigma_r) - \sigma_\theta = 0$, and the second equilibrium equation becomes $\frac{\partial}{\partial \theta}(\sigma_\theta) - 0 = 0$, which is an expected result since the considered problem is axi-symmetric, i.e., all motion variables, including σ_θ, are independent of θ. These are the familiar equations for axi-symmetric problems in polar coordinates. The axi-symmetric example will not be discussed any futher.

B.2.2.3 Simplified Principal Analysis

The preceding equations, in the previous subsection, for rectangular membranes might be simplified by proceeding as follows. Let the direction of the first principal axis, x_1, be denoted with θ_1 (defining the angle between the x_1-axis and the rectangular Cartesian x-axis), and likewise, let θ_2 be the angle that the second principal axis, x_2, makes with respect to the x-axis. It is important to appreciate that θ_1 and θ_2 are not the principal coordinates themselves, and they are measured from the same reference, i.e., the rectangular x-axis; for the sake of completeness, $\theta_2 = \theta_1 \pm \pi/2$ (since x_1 and x_2 are mutually orthogonal).

Thus, by emphasising that θ_1 and θ_2 are the angles that the x_1- and x_2-axes, respectively, make relative to the Cartesian x-axis, where θ_1 and θ_2 are (distinct) functions of (x_1, x_2),

the coordinate x might be determined from,

$$x = \int_0^{x_1} \cos\theta_1 \, dx_1 + \int_0^{x_2} \cos\theta_2 \, dx_2 + x^{(0)}, \tag{B.2.26}$$

where $x^{(0)}$ is the x-coordinate at the origin $(x_1, x_2) = (0, 0)$. Note that along the trajectory $x_2 = 0$, $x = \int_0^{x_1} \cos\theta_1 \, dx_1 + x^{(0)}$. This expression would give x for any x_1 along the curve $x_2 = 0$. The angle θ_1 varies with x_1 (and x_2), since the prinicpal axes are, in general, curved. From the above general expression, it can be found that $\frac{\partial x}{\partial x_1} = \cos\theta_1$, and $\frac{\partial x}{\partial x_2} = \cos\theta_2$. An analogous expression can be written to determine y, given a pair (x_1, x_2), which involves $\sin\theta_1$ and $\sin\theta_2$. Namely, it can be written that $\frac{\partial y}{\partial x_1} = \sin\theta_1$ and $\frac{\partial y}{\partial x_2} = \sin\theta_2$. However, the foregoing treatment assumes that dx_1 and dx_2 both have dimensional units of length (i.e., as dx and dy). This can be justified by noting, e.g., that dx_1 is the (infinitesimal) arc length along the curve $x_2 = \text{const.}$, i.e., $dx_1^2 = dx^2 + dy^2$.

Using the above set-up and geometrical justification, it can be written that,

$$\frac{\partial x}{\partial x_1} = \cos\theta_1, \qquad \frac{\partial y}{\partial x_1} = \sin\theta_1, \qquad \frac{\partial z}{\partial x_1} = 0,$$
$$\frac{\partial x}{\partial x_2} = \cos\theta_2, \qquad \frac{\partial y}{\partial x_2} = \sin\theta_2, \qquad \frac{\partial z}{\partial x_2} = 0,$$

thus,

$$\begin{aligned} \xi_1 &= \left(\cos^2\theta_1 + \sin^2\theta_1\right)^{1/2} \\ &= 1 \\ \xi_2 &= \left(\cos^2\theta_2 + \sin^2\theta_2\right)^{1/2} \\ &= 1 \end{aligned}$$

In addition, it is found that $\frac{\partial \xi_i}{\partial x_j} = 0$ for $(i, j) = 1$ and 2, which leads to $\frac{\partial f}{\partial x_1} = \frac{\partial f}{\partial x_2} = 0$. Therefore, the equilibrium equations would take the simpler forms,

$$\frac{\partial \sigma_1}{\partial x_1} = 0 \tag{B.2.27}$$

$$\frac{\partial \sigma_2}{\partial x_2} = 0 \tag{B.2.28}$$

$$\left[\frac{\partial}{\partial x_1}\left(\sigma_1 \frac{\partial w}{\partial x_1}\right) + \frac{\partial}{\partial x_2}\left(\sigma_2 \frac{\partial w}{\partial x_2}\right)\right] + \frac{p}{h} = \rho \ddot{w} \tag{B.2.29}$$

and, in view of the first two (in-plane) equilibrium equations, the third (transverse) equa-

tion reduces to the final form,

$$\sigma_1 \frac{\partial^2 w}{\partial {x_1}^2} + \sigma_2 \frac{\partial^2 w}{\partial {x_2}^2} + \frac{p}{h} = \rho \ddot{w} \tag{B.2.30}$$

According to the in-plane equilibrium equations, σ_1 is constant along x_1, and, likewise, σ_2 is constant along x_2. Since the x_1-x_2 space spans the entire membrane area (or domain), the transverse motion (as given by the transverse equilibrium equation) is independent of the in-plane displacements if it can be shown that σ_1 is constant along x_2 and, also, σ_2 is constant along x_1.

For this purpose, the von Mises yield condition (which is assumed to govern the rigid-perfect plasticity of the membrane)

$$\sigma_1^2 - \sigma_1 \sigma_2 + \sigma_2^2 = \sigma_0^2$$

is differentiated with respect to x_2 to get

$$\frac{\partial \sigma_1}{\partial x_2} (2\sigma_1 - \sigma_2) = 0$$

where the equilibrium equation in the x_2-direction has been used, i.e., $\frac{\partial \sigma_2}{\partial x_2} = 0$. From the above, it is either $\frac{\partial \sigma_1}{\partial x_2} = 0$ or $2\sigma_1 = \sigma_2 = (2/\sqrt{3})\sigma_0$. Either of the two conditions indicates that σ_1 is constant along x_2. This means that σ_1 is constant throughout, as it is already constant along x_1 (see the first in-plane equilibrium equation).

Similarly, when the yield condition is differentiated with respect to x_1, the following is obtained

$$\frac{\partial \sigma_2}{\partial x_1} (2\sigma_2 - \sigma_1) = 0$$

in view of the equilibrium equation along the x_1-axis, i.e., $\frac{\partial \sigma_1}{\partial x_1} = 0$. The last relation requires $2\sigma_2 = \sigma_1 = (2/\sqrt{3})\sigma_0$ or $\frac{\partial \sigma_2}{\partial x_1} = 0$. Hence, σ_2 is, also, constant throughout.

Using the conclusion that $\xi_1 = \xi_2 = 1$, the internal actual work of the membrane (which is assumed to be restrained along its entire boundary) simplifies to

$$W_{\text{int}} = \int_A \left[h\sigma_1 \frac{1}{2} \left(\frac{\partial w}{\partial x_1} \right)^2 + h\sigma_2 \frac{1}{2} \left(\frac{\partial w}{\partial x_2} \right)^2 \right] dx_1 dx_2 \tag{B.2.31}$$

In summary, it is found that both σ_1 and σ_2 are constant throughout the membrane, and the total plastic internal work, W_{int}, and the transverse motion of the membrane (as governed by the transverse equilibrium equation) are both completely independent of the in-plane displacements. That is the case provided that the membrane is rigid-perfectly plastic, is restrained along its boundary, and the in-plane accelerations are negligible (and the externally applied load is along z-axis).

B.2.2.4 Discussion and Conclusions

The internal work is a scalar quantity, and as such, it is independent of the coordinate system. In other words, the total contribution by the in-plane displacement to the internal work is always zero. Namely, it is so in the (usual) rectangular Cartesian coordinate system, i.e., in which the in-plane displacements are u and v (measured along the x- and y-axes, respectively), and for which the in-plane shear stress σ_{xy} can be arbitrarily non-zero.

The in-plane displacement components along the principal axes, u_1 and u_2, can be related to the rectangular components, u and v by $u_1 = u\cos(\theta_1)+v\sin(\theta_1)$ and $u_2 = -u\sin(\theta_1)+v\cos(\theta_1)$, where θ_1 is the angle that the principal axis x_1 makes with the rectangular x-axis. Although, this transformation was not necessary to derive any of the above results.

The principal coordinate system was chosen for convenience as it is not clear that the usual Cartesian components of the stresses, σ_x, σ_{xy}, and σ_y, are constants. In addition, the in-plane shear stress in the principal in-plane space is identically zero. Once the conclusion has been reached in the principal space for the total internal work, it should hold for any other coordinate system, namely for the usual x-y coordinate system, due to the scalar nature of the internal work. The approach, used herein, to utilise the principal in-plane plane is inspired by the neat work of Cloete and Nurick (2014) when analysing the in-plane displacement effect in rigid-perfectly plastic axi-symmetric circular membranes.

The main result achieved by the above is the generalisation of the important result of Cloete and Nurick (2014) that the transverse motion and total internal work of membranes are not affected by the in-plane displacements. It can be instructive to identify the conditions for which the above result holds; these are: the membrane is fixed along the entire outer boundary; the in-plane displacements accelerations, $\ddot{u}_1$ and $\ddot{u}_2$ are negligible; and the external loading, if any, is normal to the membrane's plane, and the principal in-plane stresses are constant.

B.2.2.5 Closing Remarks

An additional interesting observations can be derived for the simple membrane (i.e., without in-plane displacements) from the transverse equilibrium equation in the principal plane, i.e.,

$$\frac{1}{\xi_1\xi_2}\left[\frac{\partial}{\partial x_1}\left(\frac{\sigma_1\xi_2}{\xi_1}\frac{\partial w}{\partial x_1}\right)+\frac{\partial}{\partial x_2}\left(\frac{\sigma_2\xi_1}{\xi_2}\frac{\partial w}{\partial x_2}\right)\right]+\frac{p}{h}=\rho\ddot{w} \tag{B.2.32}$$

In section 3.8.2, the general stress state of the simple membrane, which is made of a von Mises material, was derived as $\sigma_1 = (2/\sqrt{3})\sigma_0$ and $\sigma_2 = (1/2)\sigma_1$, which are both constant (since σ_0 is so). This stress state is a direct consequence of the "total" flow rule and the specific forms of the membrane strains, in particular when the in-plane displacements are identically zero. For the von Mises material, the outward normal to the yield curve in the principal stress plane at the point $(\sigma_1,\sigma_2) = \left(2/\sqrt{3}\sigma_0, 1/\sqrt{3}\sigma_0\right)$ is parallel to the

σ_1-axis. Accordingly, the plastic strain component ε_2, which is work-conjugate with σ_2, is zero, provided the total flow rule is applicable. For the present simple membrane, $\varepsilon_2 = [1/(2\,\xi_2^2)]\left(\frac{\partial w}{\partial x_2}\right)^2$. Therefore, for ε_2 to be zero, then

$$\frac{\partial w}{\partial x_2} = 0 \tag{B.2.33}$$

From the above, two results follow. First, w is constant along x_2, for fixed x_1 and time, t. That is, the direction of x_2 is the contour of constant transverse displacement, w. Since x_1 must be orthogonal to x_2, then the x_1-axis is direction of descent of w, which is perpendicular to the contours of constant w.

The second observation is that when the last equation is substituted in the transverse equilibrium equation, the second term in the latter vanishes, and the equation of motion becomes

$$\frac{1}{\xi_1\xi_2}\left[\frac{\partial}{\partial x_1}\left(\frac{\sigma_1\xi_2}{\xi_1}\frac{\partial w}{\partial x_1}\right)\right] + \frac{p}{h} = \rho\ddot{w} \tag{B.2.34}$$

or, noting that $\sigma_1 = 2/\sqrt{3}\sigma_0$ where σ_0 is a constant,

$$\frac{2\sigma_0}{\sqrt{3}\rho\xi_1\xi_2}\left[\frac{\partial}{\partial x_1}\left(\frac{\xi_2}{\xi_1}\frac{\partial w}{\partial x_1}\right)\right] + \frac{p}{\rho h} = \ddot{w}. \tag{B.2.35}$$

When $\xi_1 = \xi_2 = 1$, the above becomes a one-dimensional wave equation,

$$\frac{2\sigma_0}{\sqrt{3}\rho}\left(\frac{\partial^2 w}{\partial {x_1}^2}\right) + \frac{p}{\rho h} = \ddot{w}. \tag{B.2.36}$$

with $\left[2\sigma_0/\left(\sqrt{3}\,\rho\right)\right]^{1/2}$ as the wave speed.

The observations, which were presented throughout Section B.2.2, give profound insights on the overall response. However, it is less practical to work with the equilibrium equations in the principal axes as their directions are unknown in advance, and the specification of the boundary conditions, e.g., can be difficult. Lastly, for the stress states to be determined, and for a specific problem to be solved, the values of σ_1 and σ_2 must be specified.

B.2.3 A General Membrane in Which $\sigma_1 = \sigma_2$

In the previous section, it was only shown that the total plastic work is independent of the in-plane displacements. However, the magnitude of the membrane strains, in the local level, depends on the latter displacements. This is partly discussed in this section for the general rectangular membranes. The following is inspired by the work of Cloete and Nurick (2014) on the predictions of the in-plane displacements for axi-symmetric circular membranes, which was reviewed and discussed in Section B.2.1.

The (three) equilibrium equations, in the rectangular Cartesian coordinate system, for a general membrane (with non-zero in-plane displacements) were given in Section 3.3.2 by

Eqs. (3.3.2), which are repeated below,

$$\begin{aligned} \frac{\partial \sigma_x}{\partial x} + \frac{\partial \sigma_{xy}}{\partial y} &= 0 \\ \frac{\partial \sigma_{xy}}{\partial x} + \frac{\partial \sigma_y}{\partial y} &= 0 \\ \sigma_x \frac{\partial^2 w}{\partial x^2} + 2\sigma_{xy} \frac{\partial^2 w}{\partial x \partial y} + \sigma_y \frac{\partial^2 w}{\partial y^2} + \frac{p}{h} &= \rho \ddot{w}, \end{aligned} \tag{B.2.37}$$

where h and ρ are the membrane's thickness and density, respectively.

The stress state $\sigma_1 = \sigma_2$, i.e., equal in-plane principal normal stresses, directly leads to a set of important results. First, the von Mises yield condition is satisfied, and $\sigma_1 = \sigma_2 = \sigma_0$, where σ_0 is the tensile yield stress of the membrane's material. Second, the radius, R, of the Mohr's circle, associated with the membrane stresses, is zero since $R = (1/2)(\sigma_1 - \sigma_2)$. The latter, in turn, implies that $\sigma_x = \sigma_y = \sigma_1 = \sigma_0$. Since the radius of Mohr's circle is zero, then it must be the case that $\sigma_{xy} = 0$. Third, the total flow rule gives that $\varepsilon_{xy} = 0$ since $\sigma_{xy} = 0$ and, also, that $\varepsilon_x = \varepsilon_y$.

Now, the stress state given by $\sigma_x = \sigma_y = \sigma_0$ (where σ_0 is a constant) and $\sigma_{xy} = 0$ satisfies the first two (i.e., the in-plane) equilibrium equations, in Eq. (B.2.37), identically. Note that this state already satisfies the yield condition. In addition, the third (or transverse) equilibrium equation simplifies to

$$\sigma_0 \left(\frac{\partial^2 w}{\partial x^2} + \frac{\partial^2 w}{\partial y^2} \right) + \frac{p}{h} = \rho \ddot{w}, \tag{B.2.38}$$

The transverse response can be found by solving the above (transverse) equation of motion and the prescribed initial and boundary conditions on the transverse displacement, w. It is vital to recognise that the system of the transverse motion does not depend on the in-plane displacements, and it can be solved independently. Note that the above equation differs only slightly from the one governing the transverse motion of the simple membrane (in which the in-plane displacements were set zero); the difference is the factor σ_0 instead of $(2/\sqrt{3})\sigma_0$ in the simple membrane; again, this was due to the present assumption that $\sigma_1 = \sigma_2$ (which led to $\sigma_1 = \sigma_2 = \sigma_0$) for the general membrane in which $\sigma_1 = \sigma_2$.

Having obtained the solution of the transverse displacement, w, one might investigate the in-plane displacements as the following. It was mentioned that $\varepsilon_x = \varepsilon_y$ (from the total flow rule and the condition that $\sigma_x = \sigma_y$), and $\varepsilon_{xy} = 0$ (since $\sigma_{xy} = 0$, which is due to the assumption that $\sigma_1 = \sigma_2$ and the properties of the Mohr's circle).

The above conditions on the in-plane strains provide two set of equations

$$\varepsilon_x = \varepsilon_y$$

$$\varepsilon_{xy} = 0$$

which when rewritten in terms of the derivatives of the displacements (and re-arranging terms) become

$$\begin{aligned} \frac{\partial u}{\partial x} - \frac{\partial v}{\partial y} &= \frac{1}{2}\left[\left(\frac{\partial w}{\partial y}\right)^2 - \left(\frac{\partial w}{\partial x}\right)^2\right] \\ \frac{\partial v}{\partial x} + \frac{\partial u}{\partial y} &= -\frac{\partial w}{\partial x}\frac{\partial w}{\partial y} \end{aligned} \tag{B.2.39}$$

Note that the right-hand sides of the above equations, in Eq. (B.2.39), are assumed already known since w can be solved independently using Eq. (B.2.38). Thus, Eq. (B.2.39), in addition to some appropriate initial and/or boundary conditions, provides a set of two (linear) equations to determine the in-plane displacements, u and v.

It can be convenient to differentiate, separately, the first and second equations in Eq. (B.2.39) with respect to x and y, respectively, add the resulting two equations to eliminate v, and obtain a single equation involving u only. A similar operation can be done to eliminate u, and obtain an equation in v only.

Once u and v are known, then ε_x (and $\varepsilon_y = \varepsilon_x$) can be calculated, and $\varepsilon_1 = \varepsilon_x$ (and $\varepsilon_2 = \varepsilon_1$); thus, the principal membrane strains (including the contributions of the in-plane displacement) are obtained. The maximum strains can be found and (if desirable) be verified against material failure.

The reader is reminded that the foregoing treatment and results hinge on the validity of the assumption that $\sigma_1 = \sigma_2$. It has been discussed that this special stress state satisfies the yield condition and the in-plane equilibrium equation. As was shown, this special state led to several fruitful consequences. However, the author could not find a procedure to prove that σ_1 must be equal to σ_2, i.e., it is not guaranteed that the stress state $\sigma_1 = \sigma_2$ is the only valid state that satisfies the in-plane equilibrium equations and, simultaneously, the yield condition. Therefore, the material in this subsection was presented to highlight the importance of proving that $\sigma_1 = \sigma_2$ in future research, again, since it directly leads to all the above very practical results. If $(\sigma_1 = \sigma_2)$ cannot be derived analytically, then its consequences can be verified by performing numerical simulations for validation purposes. For example, one can verify that $\varepsilon_1 = \varepsilon_2$ throughout a (von Mises) membrane, say, at selective time instants; if this is the case, then $\sigma_1 = \sigma_2$ since the normality rule (or the associated flow rule) requires the equality of the principal in-plane stresses. Lastly, the interest in studying the special stress state, i.e., $\sigma_1 = \sigma_2$, became important after the neat and attractive work of Cloete and Nurick (2014) on the in-plane displacement effect on axi-symmetric circular membranes in which the in-plane principal stresses (which are the circumferential and radial stresses) are made to be equal.

Appendix C

Assessment of the Error Due to Series Truncation

Unless the specific impulse distribution identically matches the shape of a particular mode, the exact solution, as given by Eqs. (4.4.8) and (4.4.9), requires taking an infinite number of terms in the sum. However, in practice, a finite number of terms is used to approximate the solution within reasonable accuracy. An appropriate measure to evaluate the sufficiency of the approximation is the total kinetic energy. Suppose that the kinetic energy computed by including a finite number of modes is close to the "exact" kinetic energy, which is a strict upper bound due to the non-negativity of kinetic energies. Then, the discarded modes will be insignificant as their total contribution is bounded from above by the implied error (or difference). It is the *initial* kinetic energy that is referred to, which is

$$\begin{aligned} E_k &= \int_0^{L_x} \int_0^{L_y} \frac{1}{2} \rho h \dot{w}_0^2 \, dy \, dx \\ &= \frac{1}{2\rho h} \int_0^{L_x} \int_0^{L_y} i(x,y)^2 \, dy \, dx. \end{aligned} \tag{C.1}$$

Again, this is taken as the "exact" kinetic energy at time $t = 0$, and it is termed the "upper bound kinetic energy" uptake in Tyas and Pope (2003) and Rigby et al. (2019a).

Due to the assumption of deformation monotonicity, the total plastic work is associated with the total strain at the final time (as the problem is path-independent). That is, after $t \geq t_{1,1}$, the plastic work W_p^* is evaluated using the final displacement field, $w_p(x,y)$, and hence is given by

$$W_p^* = \frac{2}{\sqrt{3}} \sigma_0 h \int_0^{L_x} \int_0^{L_y} \left[\frac{1}{2} \left(\frac{\partial w_p}{\partial x} \right)^2 + \frac{1}{2} \left(\frac{\partial w_p}{\partial y} \right)^2 \right] dy \, dx. \tag{C.2}$$

By exploiting the modal orthogonality property and after some lengthy algebraic simpli-

fications, the plastic work evaluates to

$$W_p^* = \frac{1}{2\rho h}\frac{4}{L_x L_y}\sum_{m,n=1}^{\infty} I_{mn}^2. \tag{C.3}$$

The above, Eq. (C.3), is precisely the expression for the (initial) kinetic energy if it would be evaluated by time differentiating the general solution $w(x, y, t)$, Eq. (4.4.1), then set $t = 0$, which confirms that the initial kinetic energy is converted into (plastic) internal energy.

Now, when the expressions of the exact initial kinetic energy, E_k, from Eq. (C.1), and the final plastic work, W_p^*, are set equal, the following condition, known as Parseval's formula, see Weisstein (2022), is obtained

$$\sum_{m,n=1}^{\infty} I_{mn}^2 = \frac{L_x L_y}{4}\int_0^{L_x}\int_0^{L_y} i(x,y)^2\, dy\, dx \;=\; \|\phi_{mn}\|^2 \cdot \|i\|^2, \tag{C.4}$$

where $\|f(x,y)\| = \sqrt{\int_A f(x,y)^2\, dA}$, is the norm of a function f, and $\|\phi_{mn}\|$ is $\sqrt{(L_x L_y/4)}$. Therefore,

$$\sum_{m,n=1}^{\infty} I_{mn}^2 = \left(\frac{I_k}{2}\right)^2, \tag{C.5}$$

in which I_k is the energy-equivalent impulse due to Rigby et al. (2019a), which, for a rectangular target with loaded area $A = L_x L_y$, is given by

$$\begin{aligned} I_k &= \sqrt{A\int_A i(x,y)^2\, dA} \\ &= \sqrt{A} \times \|i\|. \end{aligned} \tag{C.6}$$

It should be noted that in Rigby et al. (2019a), I_k was derived directly from the physical problem using equivalence between kinetic energies due to non-uniform and uniform specific impulses.

Now, defining an angular parameter, which measures how much the actual specific impulse field is along the direction of one particular mode (in the inner product sense), by

$$\cos\theta_{mn} = \frac{2I_{mn}}{I_k}, \tag{C.7}$$

then, one reaches the following general condition,

$$\sum_{m,n=1}^{\infty} \cos^2\theta_{mn} = 1. \tag{C.8}$$

It is vital to recognise that there is no single component in the infinite series above, Eq. (C.8), with a magnitude larger than unity since each term is always positive while the right-hand side is one. Hence, if one term is identically one, then all other terms must vanish, which is the situation when the specific impulse field matches the shape of the surviving (or resonating) mode.

Finally, if only a finite number of terms is used to calculate w_p or w_c, then it is sufficient to verify that the sum of $\cos^2\theta_{mn}$, for those modes included, is close to unity (from below). In other words, the error, ϵ, due to truncation at $m = M$ and $n = N$, can be estimated as

$$\epsilon_{MN} = 1 - \sum_{m,n=1}^{M,N} \cos^2\theta_{mn} \equiv \sum_{M,N}^{\infty} \cos^2\theta_{mn}. \tag{C.9}$$

The quantity $\cos\theta_{mn}$, on its own, gives the absolute *physical* importance of the $(m,n)^{\text{th}}$ mode in relation to all other modes since it compares the modal energy (through I_{mn}) to the strict upper bound kinetic energy, E_k, (through I_k).

Appendix D

A Practical Method to Compute I_{mn} for Rectangular Membranes

For smoothly varying distribution of specific impulse, I_{mn} decreases as m and n increase due to cancellations associated with high spatial oscillations. Thus, practically, a finite number of modes suffices to estimate the displacement accurately.

In the expression for w_c, instead of carrying out the numerical integrations directly by the trapezoidal rule, it is observed that the two-dimensional Fast Fourier Transform (FFT) could be utilised to reduce the computational time. However, according to the form of I_{mn}, the specific impulse distribution should be slightly manipulated first. The procedure is straightforward to derive, and it is briefly described below and followed by a practical MATLAB code for the implementation.

From the actual specific impulse, $i(x, y)$, defined on the actual membrane that spans the domain $[0, L_x] \times [0, L_y]$, construct a fictitious specific impulse $i^*(x, y)$ that covers an extended rectangular region $[-L_x, L_x] \times [-L_y, L_y]$, which is defined as

$$i^*(x,y) = \begin{cases} i(x,y), & (x,y) \in [0,L_x] \times [0,L_y], \\ -i(-x,y), & (x,y) \in [-L_x,0] \times [0,L_y], \\ -i(x,-y), & (x,y) \in [0,L_x] \times [-L_y,0], \\ i(-x,-y), & (x,y) \in [-L_x,0] \times [-L_y,0]. \end{cases} \tag{D.1}$$

Now, the real components of the two-dimensional discrete Fourier transform of $i^*(x, y)$ is denoted by b_{mn} and given by

$$b_{mn} = \frac{1}{L_x L_y} \int_{-L_x}^{L_x} \int_{-L_y}^{L_y} i^*(x,y) \sin\left(\frac{2m\pi x}{2L_x}\right) \sin\left(\frac{2n\pi y}{2L_y}\right) dy\, dx. \tag{D.2}$$

It is important to note that the x-interval is $2L_x$ and that along y is $2L_y$.

Next, $b_{mn} = b(m, n)$ is related to the complex Fourier coefficients by

$$b_{mn} = -c(m,n) + c(-m,n) + c(m,-n) - c(-m,-n), \tag{D.3}$$

where m and n are indices corresponding to positive integers, and $-m$ and $-n$ are indices corresponding to negative integers. Then, using the piecewise definition of $i^*(x,y)$, it can be shown that b_{mn} reads

$$\begin{aligned} b_{mn} &= \frac{4}{L_x L_y}\int_0^{L_x}\int_0^{L_y} i(x,y)\sin\left(\frac{m\pi x}{L_x}\right)\sin\left(\frac{n\pi y}{L_y}\right)dy\,dx \\ &= \frac{4I_{mn}}{L_x L_y}. \end{aligned} \tag{D.4}$$

Finally,

$$I_{mn} = \frac{L_x L_y}{4}\left[-c(m,n)+c(-m,n)+c(m,-n)-c(-m,-n)\right]. \tag{D.5}$$

The values of $c(m,n)$, $c(-m,n)$, $c(m,-n)$, and $c(-m,-n)$ are the standard outputs of an FFT, to within a constant multiplier. FFT gives the amplitudes of the modes, e.g., $c(0,0)$ reflects the amplitude of the mode associated with $m=0$ and $n=0$. In MATLAB, this is achieved using the built-in function `fft2()`. Note that inMATLAB, the output sorts the number of modes in each direction in a special order: first, the zeroth mode (which we do not need), followed by positive modes in ascending order, and lastly negative modes in descending order.

The specific procedure to be implemented in MATLAB is what follows. Let the actual specific impulse, $i(x,y)$, be stored in 2D array `I`. Further, let the plate lengths along x and y be `Lx` and `Ly`, respectively.

Then, denote $i^*(x,y)$ by `Istar`, which can easily be formed in MATLAB using the built-in function `flip()`. Finally, say the total modal impulse, I_{mn}, will be stored in the array `Imn` and be evaluated using FFT. The MATLAB procedure is given in Script D.1.

```
%% start of script
% I =specific impulse matrix (2D array)...
% rows of I --> variation along x
% cols of I --> variation along y

Istar=[flip(flip(I,1),2),-flip(I,1);-flip(I,2),I];

C0=fft2(Istar);
C0=real(C0);
C0=1/(numel(Istar))*C0; %undo multiplier
C1=C0(2:end,2:end); %skip zeroth mode
B=zeros(ceil((size(C1)-1)/2));

for i=1:size(B,1)
    for j=1:size(B,2)
        B(i,j) = -C1(i,j)+C1(end-i+1,j)+C1(i,end-j+1)-C1(end-i+1,end-j+1);
    end
end

Imn=Lx*Ly*B/4;

% Imn stores total modal impulses, Imn.
% Use this directly in expressions for displacement w_p or w_c.
%% end of script.
```

Script D.1. MATLAB script to compute I_{mn} efficiently using FFT

By comparing the results (not shown herein) from computing I_{mn} via the trapezoidal rule for many modes in each direction to those using the FFT, the observations are FFT is superiorly efficient and very reasonably accurate. Hence, the use of FFT to evaluate I_{mn} is recommended. This computational strategy is rarely pointed out in the literature as an efficient method to compute the modal amplitudes appearing in the displacement response of plates.

Appendix E

Effect of Work-Hardening on the Response of an SDOF and a 2D Steel Plate

E.1 Forced Response - SDOF

In this section, an assessment of the effect of work-hardening is presented based on the response of a single-degree-of-freedom (SDOF). The system consists of a mass m, a massless spring with resistance R, and an applied dynamic force, and its general equation of motion is

$$m\ddot{x} + R = F$$

For simplicity, we are concerned with motion up to a half cycle beyond the first maximum response. The SDOF is assumed as initially at rest.

The resistance R is of bilinear form during loading and has an elastic unloading

$$R = \begin{cases} kx & t \leq t_{y,0}, \\ R_{y,0} + H(x - x_{y,0}) & t_{y,0} \leq t \leq t_m, \\ R_{y,0} + H(x_m - x_{y,0}) + k(x - x_m) & t_m \leq t, \end{cases}$$

where k and H are the elastic stiffness and the hardening modulus; $R_{y,0}$, $x_{y,0}$, and $t_{y,0}$ are the initial yield force, the corresponding yield displacement, and the time at which first yielding occurs. The maximum displacement is x_m. The last expression for R describes the elastic unloading for sufficiently small-time interval after $t = t_m$.

The applied force F is assumed to be a rectangular pulse with amplitude F_0 and duration t_d.

The elasto-plastic response of the SDOF was solved numerically using an explicit time integration scheme. The solution is terminated after completing a half cycle from the

first occurrence of maximum displacement (i.e., after sufficient time during the elastic unloading/rebound), to obtain a sufficient response for the computation of the residual displacement, x_r.

We considered the following input data. The elastic period $T_e = 2\pi\sqrt{m/k}$ is 0.0811 s. The ratio of the external force to the initial yield limit $F_0/R_{y,0}$ is 5.0. The ratio of load duration to the elastic period t_d/T_e and the ratio of hardening modulus to elastic stiffness H/k are varied independently; some practical ratios of H/k are considered. The results for the normalised residual displacement $x_r/x_{y,0}$ are given in Fig. E.1.

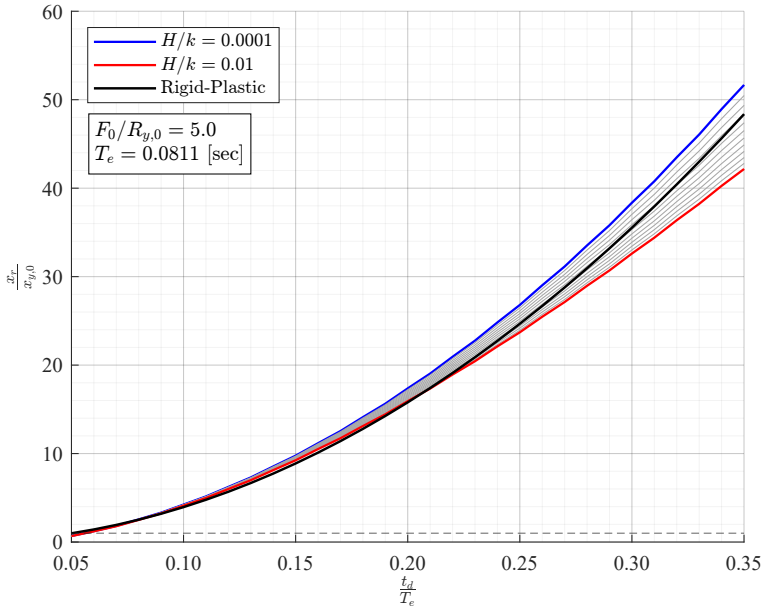

Fig. E.1. Normalised residual displacement $x_r/x_{y,0}$ of elasto-plastic SDOF as function of the ratios of load duration to elastic period t_d/T_e and hardening modulus to elastic stiffness H/k. The grey curves are for intermediate ratios of H/k, which are bounded by the values of the blue and red curves.

The Rigid-plastic response of the SDOF is obtained by substituting $R = R_{y,0}$ in the equation of motion, which is valid since $F_0 > R_{y,0}$, and hence it is expected that $\dot{x} \geq 0$. Therefore, the maximum displacement is

$$x_{m,rp} = x_{t_d} + \dot{x}_{t_d}(t_m - t_d) - \frac{R_{y,0}}{2m}(t_m - t_d)^2$$

where,

$$x_{t_d} = \left(\frac{F_0 - R_{y,0}}{2m}\right) t_d^2, \tag{E.1.1}$$

$$\dot{x}_{t_d} = \frac{F_0 t_d}{m} - \frac{R_{y,0} t_d}{m}, \tag{E.1.2}$$

$$t_m = \frac{\dot{x}_{t_d}}{\left(\frac{R_{y,0}}{m}\right)} + t_d \tag{E.1.3}$$

The maximum rigid-perfectly plastic displacement $x_{m,rp}$ is plotted in Fig. E.1 as a func-

tion of the ratio of load duration to elastic period t_d/T_e and compared to the residual displacement of the elasto-plastic problem.

It can be seen, from the figure, that the rigid-perfectly plastic solution gives reliable predictions as compared to the elasto-plastic solution with various work-hardening, in particular as the load duration to elastic period ratio, t_d/T_e, becomes very small. In Fig. E.1, the difference between the responses for the rigid-perfectly plastic (black) and elasto-plastic with $H/k = 0.0001$ (blue) is attributed to elastic deformations of the elasto-plastic SDOF. Such difference should decrease as the external force to initial yield limit ratio, $(F_0/R_{y,0})$, increases while small t_d is maintained.

E.2 Impulsive Response - SDOF

In this section, we present additional assessment of the effect of work-hardening on the response of the same SDOF as in the previous section. However, we consider the system where the external force is absent and assume the response to be driven by initial velocity. The initial displacement is assumed zero.

We consider the initial velocity, $\dot{x}_0$, to be large enough to cause initial yielding.

Denoting the time of initial yielding by $t_{y,0}$, the response for $(0 \leq t \leq t_{y,0})$ is governed by $m\ddot{x} + kx = 0$ with initial conditions $x_0 = 0$ and $\dot{x}_0 > 0$. The response is

$$\omega_e = \sqrt{\frac{k}{m}},$$

$$x(t) = \frac{\dot{x}_0}{\omega_e} \sin(\omega_e t).$$

From which, the state at $t = t_{y,0}$ is

$$x_{y,0} = \frac{R_{y,0}}{k},$$

$$t_{y,0} = \frac{\sin^{-1}\left(\frac{x_{y,0}\omega_e}{\dot{x}_0}\right)}{\omega_e},$$

$$\dot{x}_{y,0} = \dot{x}_0 \cos(\omega_e t_{y,0}).$$

Denoting the time at maximum response (i.e., just prior to elastic unloading) by t_m, the response for $(t_{y,0} \leq t \leq t_m)$ is governed by $m\ddot{x} + R_{y,0} + H(x - x_{y,0}) = 0$ with initial

conditions $x(t_{y,0}) = x_{y,0}$ and $\dot{x}(t_{y,0}) = \dot{x}_{y,0}$. The response is

$$\begin{aligned}\omega_H =& \sqrt{\frac{H}{m}},\\ x(t) =& x_{y,0}\cos\left[\omega_H\left(t-t_{y,0}\right)\right] + \frac{\dot{x}_{y,0}}{\omega_H}\sin\left[\omega_H\left(t-t_{y,0}\right)\right] +\\ & -\left(\frac{R_{y,0}-Hx_{y,0}}{H}\right)\left\{1-\cos\left[\omega_H\left(t-t_{y,0}\right)\right]\right\}.\end{aligned}$$

By definition, t_m is the time when velocity becomes zero for the first time, i.e., $\dot{x}(t_m) = 0$. From which, the state at $t = t_m$ is

$$\begin{aligned}\beta &= \tan^{-1}\left[\frac{\dot{x}_{y,0}}{\omega_H x_{y,0} + \left(\frac{R_{y,0}+Hx_{y,0}}{m\omega_H}\right)}\right],\\ t_m &= \frac{\beta}{\omega_H} + t_{y,0},\\ x_m &= x_{y,0}\cos\left(\beta\right) + \frac{\dot{x}_{y,0}}{\omega_H}\sin\left(\beta\right) - \left(\frac{R_{y,0}-Hx_{y,0}}{H}\right)\left[1-\cos\left(\beta\right)\right].\end{aligned}$$

For $(t \geq t_m)$, the response is an elastic rebound, which is governed by $m\ddot{x} + R_{y,0} + H(x_m - x_{y,0}) + k(x - x_m) = 0$, with initial conditions $x(t_m) = x_m$ and $\dot{x}(t_m) = 0$. The rebound response, for $t \geq t_m$, is

$$\begin{aligned}x(t) =& x_m\cos\left[\omega_e(t-t_m)\right] +\\ & -\left(\frac{R_{y,0}+H(x_m-x_{y,0})-kx_m}{k}\right)\left\{1-\cos\left[\omega_e(t-t_m)\right]\right\}.\end{aligned}$$

The residual (plastic) displacement, x_r, is obtained from the above rebound solution when the vibration terms (i.e., the cosine terms) are eliminated. With the elastic period

$$T_e = 2\pi\sqrt{\frac{m}{k}},$$

so that the residual displacement is

$$x_r = \frac{2}{T_e}\int_{t_m}^{t_m+\frac{T_e}{2}} x(t)\,dt$$

which simplifies to

$$x_r = -\frac{\left[R_{y,0}+H(x_m-x_{y,0})-kx_m\right]}{k}.$$

The initial kinetic energy, $E_{k,0}$, of the SDOF is

$$E_{k,0} = \frac{1}{2}\, m\, \dot{x}_0^2,$$

and, the maximum (initial) elastic energy, $E_{e,m}$, is

$$E_{e,m} = \frac{1}{2}\, k\, x_{y,0}^2$$

For a given ratio of $E_{k,0}/E_{e,m}$ and a ratio of H/k, one can study the response in terms of the ratio of maximum (or residual) displacement, x_m (or x_r), to the initial yield displacement, $x_{y,0}$. This gives direct assessment of the influence of work-hardening.

The rigid-perfectly plastic solution is characterised by the maximum response time $t_{m,rp}$ (when velocity reaches, and subsequently held constant at, zero) and the corresponding maximum displacement $x_{m,rp}$. These are defined by

$$t_{m,rp} = \frac{\dot{x}_0}{\left(\frac{R_{y,0}}{m}\right)},$$

$$x_{m,rp} = \dot{x}_0 t_{m,rp} - \frac{1}{2}\frac{R_{y,0}}{m} t_{m,rp}^2.$$

The rigid-perfectly plastic response $x_{m,rp}$ can be compared to the response of the elasto-plastic with hardening solutions, the maximum x_m or residual x_r displacements, to assess the effects of both work-hardening and elasticity.

We consider a particular case for which the ratio of initial kinetic energy to maximum elastic energy is large, $\frac{E_{k,0}}{E_{e,m}} = 9.0$. The elastic period is $T_e = 0.0811$ [s]. Moreover, the ratio of the hardening modulus to the elastic stiffness H/k is taken as (0.01). The comparison of the time history responses of the elasto-plastic with hardening SDOF and the corresponding rigid-perfectly plastic SDOF is shown for the present case in Fig. E.2. The displacement x is normalised by $x_{y,0}$, and the time axis is normalised by t_y. The figure indicates that the rigid-perfectly plastic solution is suitable and highly efficient for response of the SDOF for the considered ratio of $E_{k,0}/E_{e,m} = 9.0$.

As a second example, we consider a problem with $E_{k,0}/E_{e,m} = 25.0$, $T_e = 0.1147$ s, and $H/k = 0.002$. The responses from the elasto-plastic with hardening model and the rigid-perfectly plastic model are compared in Fig. E.3.

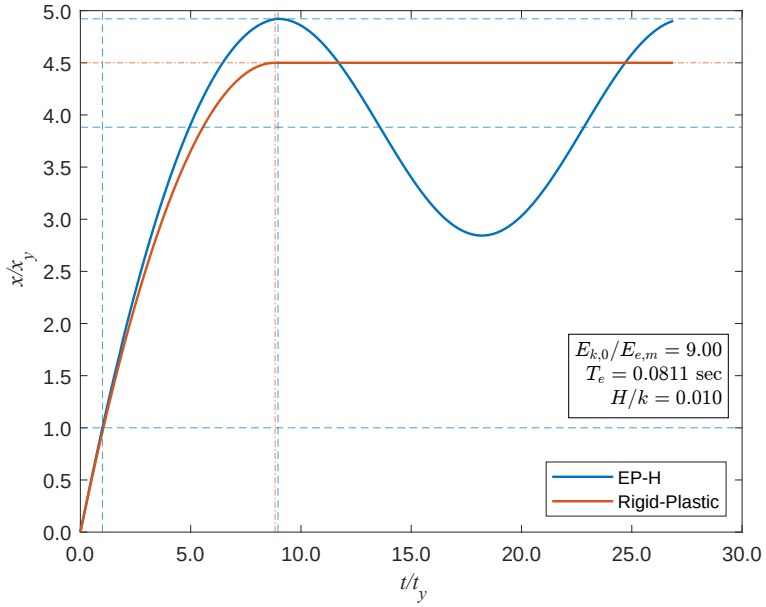

Fig. E.2. Normalised transient displacement $x(t)/x_{y,0}$ of elasto-plastic SDOF (with work-hardening) as function of normalised time $t/t_{y,0}$; hardening modulus to elastic stiffness ratio is $H/k = 0.01$. The response is for an impulsively loaded SDOF, i.e., with non-zero initial velocity and zero external force. The initial kinetic energy $\left(E_{k,0} = (1/2)\, m\, \dot{x}_0^2\right)$ is nine times larger than the maximum elastic energy $\left(E_{e,m} = (1/2)\, k\, x_y^2\right)$. Horizontal (blue) dashed lines are drawn at $x_{y,0}$, x_r, and x_m for the elasto-plastic response, and the additional (red) dashed line corresponds to $x_{m,rp}$ for the rigid-plastic response.

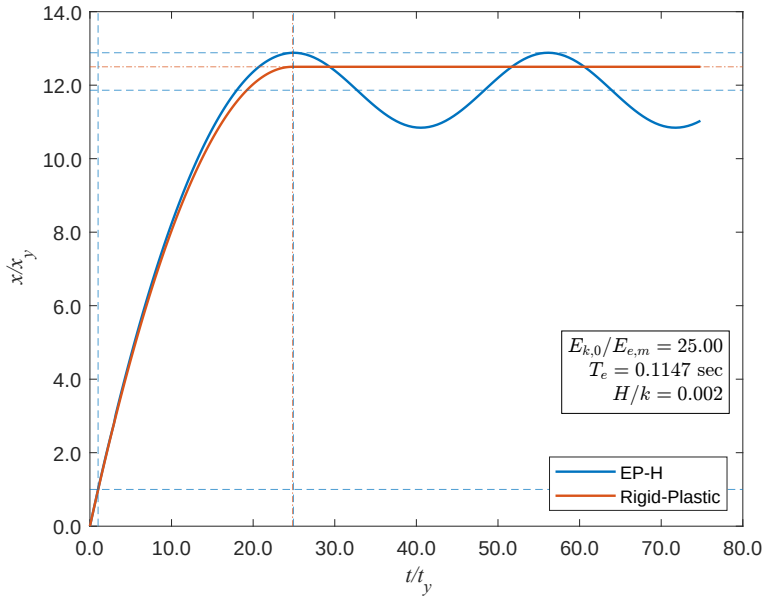

Fig. E.3. Normalised transient displacement $x(t)/x_{y,0}$ of elasto-plastic SDOF (with work-hardening) as function of normalised time $t/t_{y,0}$; hardening modulus to elastic stiffness ratio is $H/k = 0.002$. The response is for an impulsively loaded SDOF, i.e., with non-zero initial velocity and zero external force. The initial kinetic energy $\left(E_{k,0} = (1/2)\, m\, \dot{x}_0^2\right)$ is 25 times larger than the maximum elastic energy $\left(E_{e,m} = (1/2)\, k\, x_y^2\right)$. Horizontal (blue) dashed lines are drawn at $x_{y,0}$, x_r, and x_m for the elasto-plastic response, and the additional (red) dashed line corresponds to $x_{m,rp}$ for the rigid-plastic response.

E.3 Plate Response Using LS-DYNA

In this section, results from LS-DYNA simulations are presented to assess the influence of work-hardening on the response of a ductile thin plate loaded by a uniform impulse.

Flexural, shear, and membrane effects are all considered. Furthermore, a general elasto-plastic material behaviour is adopted. Plasticity follows a von Mises yield function in which the yielding stress is given by Johnson-Cook (JC) model. In this study, the hardening saturation stress B is varied while all other material (and geometry and loading) parameters fixed.

The plate is impulsively loaded using a prescribed uniform initial transverse velocity $\dot{w}_0$

$$\dot{w}_0 = \frac{i_0}{\rho h},$$

where the uniform specific impulse, density, and uniform thickness are denoted by i_0, ρ, and h.

According to JC model without Voce's hardening, the current yield stress, σ_y, is influenced by current effective plastic strain ε_{eff}, the instantaneous effective plastic strain rate $\dot{\varepsilon}_{\text{eff}}$, and the absolute temperature T using

$$\sigma_y = (A + B\,\varepsilon_{\text{eff}}^n)\left[1 + \left(\frac{\dot{\varepsilon}_{\text{eff}}}{\dot{\varepsilon}_0}\right)\right]^c (1 - T^{*m})$$

where T^* is

$$T^* = \frac{T - T_r}{T_m - T_r},$$

in which T_m and T_r are the (absolute) melting and room temperatures.

B and n are power-law hardening parameters, c is a strain-rate sensitivity parameter. A is the initial quasi-static yield stress at the threshold strain rate $\dot{\varepsilon}_0$. Note that n is typically in the range $0 \leq n \leq 1$, and then B could be regarded as an increase in σ_y (from A) due to strain-hardening. A further strengthening in the strain-hardened σ_y occurs at high strain rates. On the other hand, two softening mechanisms (thermal softening when m is non-zero and/or damage-induced softening) can lower σ_y. We assume that softening is absent for simplicity (i.e., $m = 0$ and damage threshold $= \infty$).

In the study, we considered the following values for the material constants.

Three values of B as multiples of A are considered. In particular, we consider ratios of B/A of 1.7, 0.89, and 0.05. These ratios correspond to the (true) yield stress-effective plastic strain curves in Fig E.4.

The other input parameters are the following. The plate is square with a side length of 0.089 [m] and thickness of 1.6 [mm]. Additionally, a total impulse of -16.1 [N.m]. is applied uniformly to the plate to give a uniform initial transverse velocity of -162.24

Table E.1. JC material parameters

Parameter	Value	Unit
E	206×10^9	Pa
ρ	7830	kg/m^3
ν	0.29	-
A	296×10^6	Pa
n	0.5597	-
m	0	-
c	0.032	-
$\dot{\varepsilon}_0$	1.4×10^{-6}	1/s

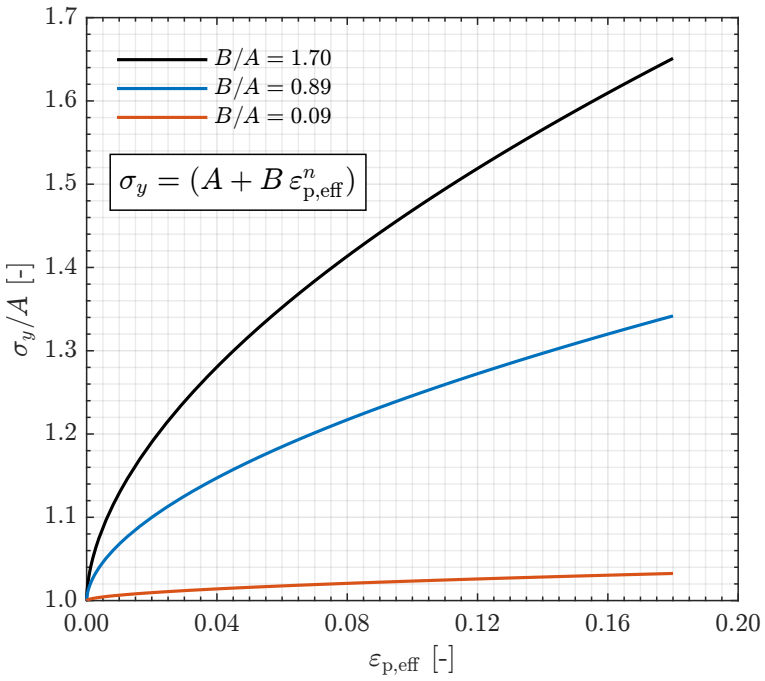

Fig. E.4. Variation of JC current yield stress σ_y versus effective (von Mises) plastic strain $\varepsilon_{\mathrm{p,eff}}$ at the quasi-static plastic strain rate $\dot{\varepsilon}_0$. The curves correspond to different amount of strain-hardening in terms of B/A ratio.

[m/s]. The input values correspond to the square plate tests of Nurick et al., cited and discussed in Section 4.4.2. All boundary nodes are restrained in all translational and rotational degrees of freedom. A fine element mesh is selected. The plate is modelled with two-dimensional shell elements using ELFORM=7 (selectively reduced integrated Hughes-Liu co-rotational formulation) and 10 Gauss integration points to better represent the extent of plasticity through the plate's thickness.

Nodal, element, and energy databases are requested with fine sampling rates. The transverse (z-) displacement and energy histories are post-processed in MATLAB. The residual displacement is computed by time integration averaging beyond the first peak response.

The history results obtained from LS-DYNA for the three ratios of B/A are compared to the predictions of the present model. Namely, the displacements at the plate's centre, the time to maximum response, and the evolution of different energies are analysed. In the model predictions, the characteristic yield strength σ_0 is taken as the static yield strength A.

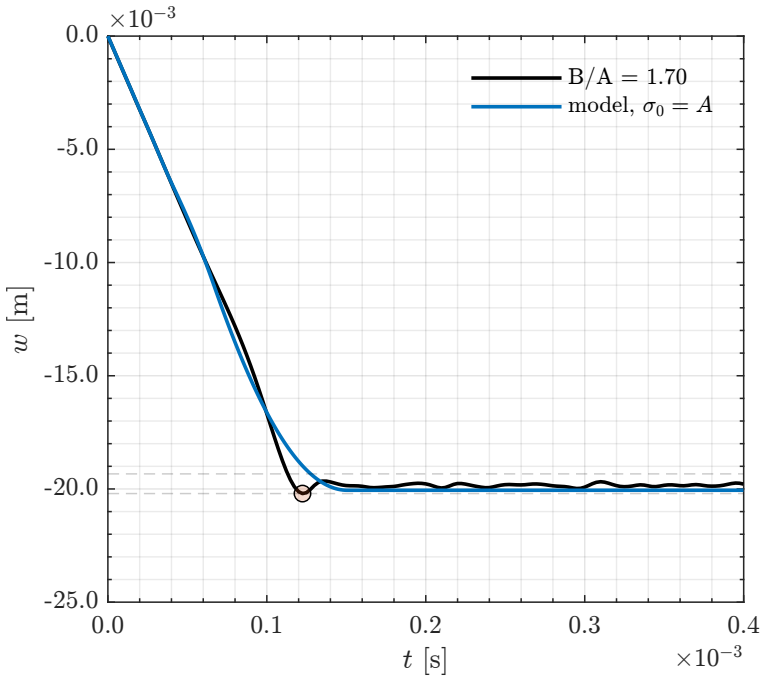

Fig. E.5. Central transverse displacement w time history from LS-DYNA simulation (for $B/A = 1.7$) and the corresponding model prediction.

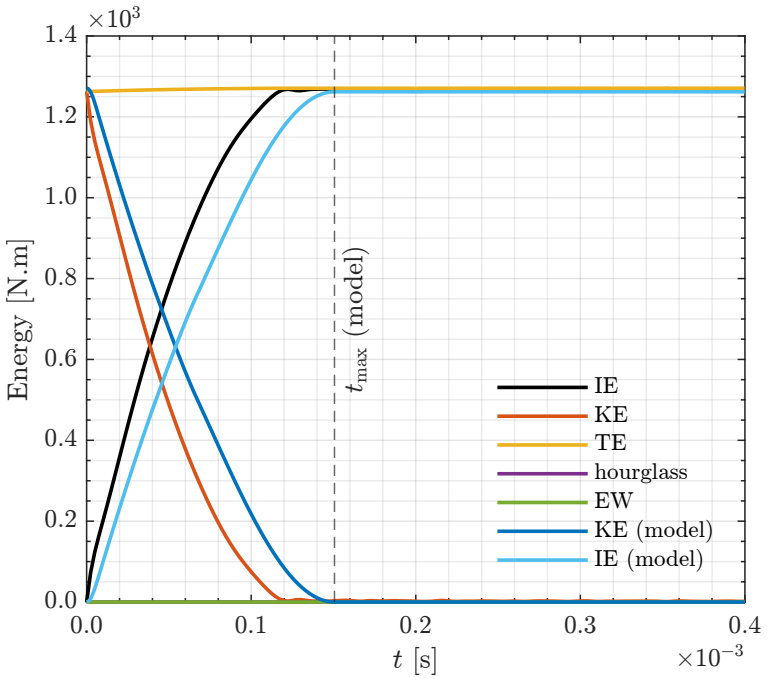

Fig. E.6. Histories of global energies from LS-DYNA (for $B/A = 1.7$), and the corresponding kinetic (KE) and plastic internal (IE) energies predicted by the model. From LS-DYNA, the internal (IE), kinetic (KE), total (TE), and hour-glass energies and external work (EW) are shown. The maximum response time t_{max} predicted by the model is shown as a vertical dashed line.

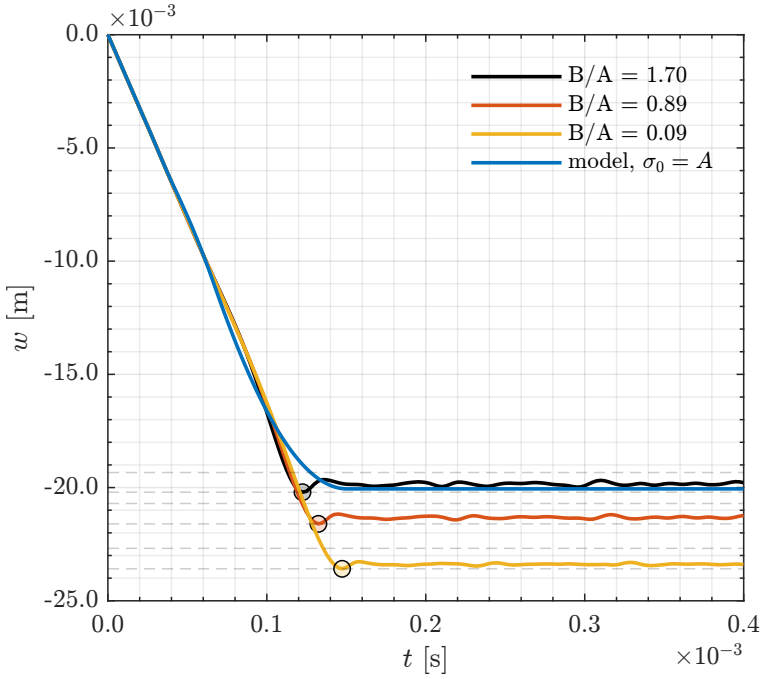

Fig. E.7. Effect of the degree of strain-hardening (in terms of B/A ratio) on the transient and residual central displacements from LS-DYNA. The model prediction assumes $\sigma_0 = A$.

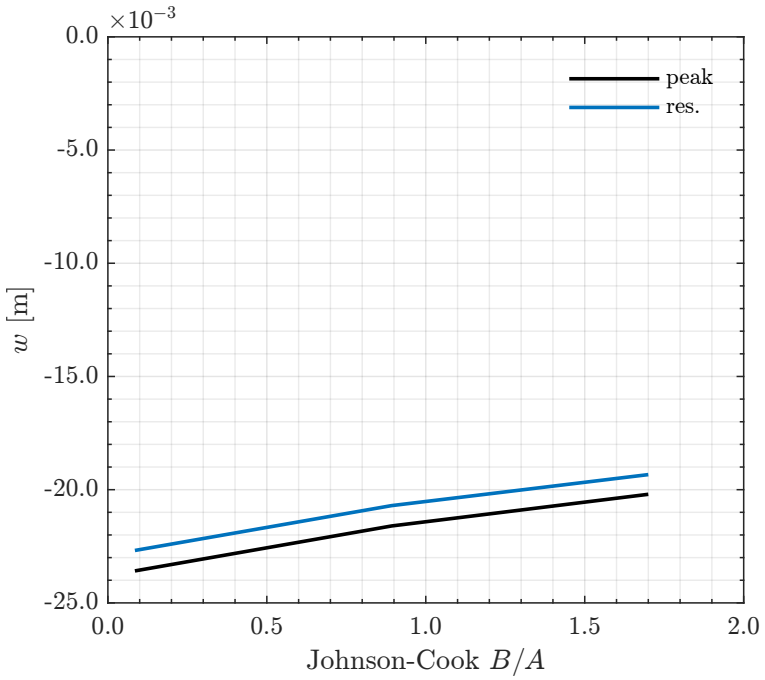

Fig. E.8. LS-DYNA maximum (peak) and residual (res.) displacements at the plate's centre as functions of the degree of hardening (in terms of B/A).

Appendix F

MATALB Function to Read LS-DYNA's binout Files

F.1 Overview

A MATALB function is developed to read the whole binary data from an LS-DYNA's `binout` file. The function syntax is

```
binin = get_binout_data(<path/to/binout>)
```

where the input argument is either a `char` or `string` specifying the path (relative or absolute) to the binout file. The output is a MATALB `struct` that contains all data in the binout file (all directories, subdirectories, and their arrays). The main directories (e.g., `nodout` or `elout`, etc) present in the binout file become the root fields of the `binin` structure. The original hierarchy and variables' labels (or names) of data in the binout are preserved, with the exception that replacing a "-" with "_" in some labels to make them valid MATALB field names. For example, if the binout file has `matsum` and `nodout` data in it, then the `binin` will have two root fields with names "matsum" and "nodout", each of which is a root structure. Each of most of these root structures has exactly two fields: `data` and `metadata`, each of which is again a structure.

The `data` structure will have the actual data as arrays, with their labels borrowed from the binout file. For example, to get the kinetic energy stored in the "matsum", one can use `binin.matsum.data.kinetic_energy`, which returns the array of kinetic energy with rows corresponding to the time states and columns (if more than one) corresponding to the IDs of the parts whom data were requested from LS-DYNA. The time vector for all variables present in the "matsum" can be accessed using `binin.matsum.data.time`. The term "kinetic" may be replaced with "internal" or "hourglass" to get the corresponding energy data. All numeric arrays are of MATALB type `double`, even if the corresponding original data in the `binout` file were stored as integers or floats of "single" precision.

The `metadata` structure contains mostly metadata; however, it also contains important variables, in particular the IDs of the various entities, such as those of parts, nodes, etc.

For example, if there are more than one part whom data is requested, then one needs to first get their IDs from the vector `binin.matsum.metadata.ids`. For example, if the 3rd entry of the IDs vector is 99, then the 3rd column of the "kinetic energy" array is the time-history of kinetic energy for the part with id = 99. The length of the `ids` vector is also the number of columns of the kinetic energy array and of similar arrays, discussed earlier.

Since the content of the `binin` merely reflects what is present in the `binout`, and the field names are borrowed directly from the `binout`, which are almost self-explanatory, thus detailed documentation of the `binin` is omitted. As a demonstration, the displacement of the nodes in the x-direction can be accessed using `binin.nodout.data.x_displacement`, which returns the 2D array of x-components of displacement for all nodes (columns map to node IDs) and at all time instants (rows map to time instants); the vector `binin.nodout.metadata.ids` gives the IDs of the nodes (and the length of this vector equals to the number of columns of arrays in `binout.nodout.data`, if that number is greater than one). The time vector for all arrays (i.e., displacements, coordinates, velocities, etc) in `binin.nodout.data` is stored in `binin.nodout.data.time`.

To further illustrate how the structure of the `binin` is laid out in a real case, consider the following example, which is based on an actual `binout` file. The latter file contained `matsum`, `glstat`, `nodout`, and `elout` and was outputted by LS-DYNA after running a (shell) plate model. Fig. F.1 shows the structure tree of the main `binin`, in which the terminal leaves (i.e., fields under each of the `data` and `metadata` nodes) were suppressed for clarity. On the other hand, Fig. F.2 shows the actual content (with the terminal leaves displayed) of `binin.matsum`, which is representative of the other root fields under the main `binin`.

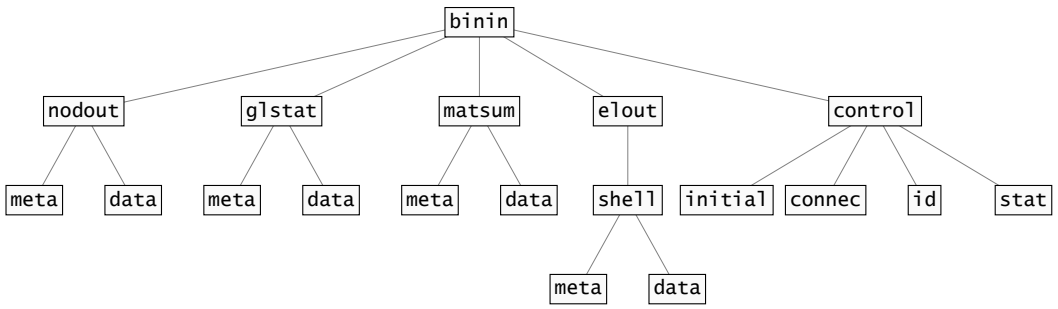

Fig. F.1. A sample `binin` structure corresponding to a `binout` file that contains `matsum`, `glstat`, `nodout`, and `elout` databases. The `elout` field contains only `shell` since it is the type that was requested from LS-DYNA in the original model. The actual data are the fields of every `data` but are not shown here for simplicity; see Fig. F.2 that provides all details for the `matsum` database, as an example. Note: the `control` and all its children are not part of the `binout`, but they were retrieved from the root `d3plot` for convenience for later post-processing.

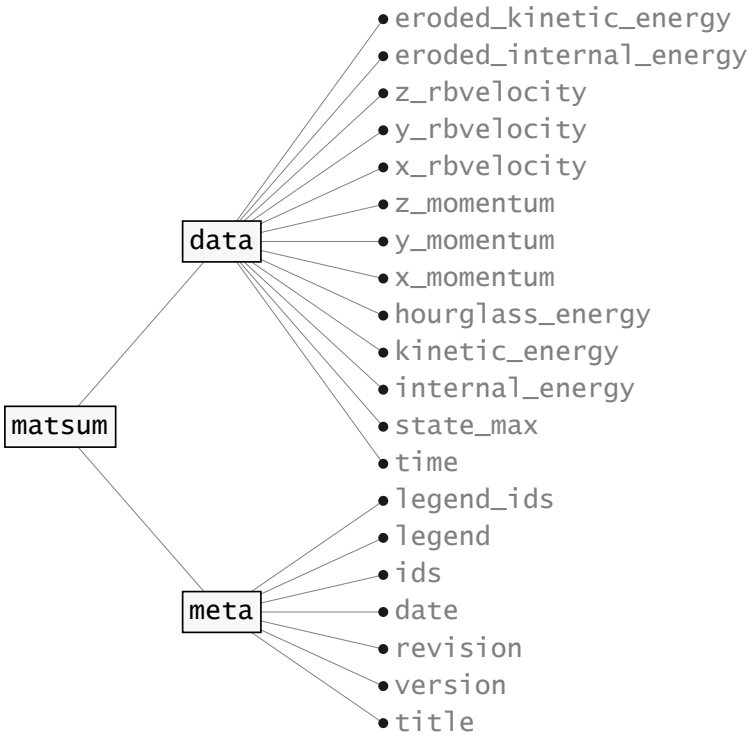

Fig. F.2. Content of the `matsum` database returned as part of the `binin`. To obtain the time vector (as an example), use `binin.matsum.data.time`.

F.2 Additional Functionality

LS-DYNA binout files do not contain the element-node connectivity arrays. If this information is needed for certain post-processing, one can either directly import this data from the LS-DYNA keyword "`.k`" file, or make use of the root output `d3plot` file. Another supplementary Matalb function is also developed to get all control data from the root `d3plot` file. Among the control data are the element-node connectivity arrays and the initial coordinates of the input mesh. The function that reads such control data is called `get_d3plot_d3thdt_control_data()`. This function is called from within the previously discussed `binout` reader function, and the control data are fed into a new field (called `control`) in the `binin` structure, as was already shown in Fig. F.1 in the previous section.

F.3 Performance Remarks

Although the `binout` reader function requires the specification of the path to the (root) binout file, it will read all binout files sequentially (if there are more than one), and all data are stored in the single `binin` variable. Only the binout files sharing the same root name of the root file will be read. It is the caller's responsibility to ensure that the accumulated size of data does not exceed the available RAM. Note: the function code includes commands to pre-allocate reasonable memory before reading the data (whose exact size is initially unknown) to speed up the execution time; however, this process is done in segments (i.e.,

as dynamically needed) to make it as economical as possible. After completion of reading the actual data, the remaining unused entries are eliminated before returning the output.

The reason for having to request results from LS-DYNA in binary format so that a binout file gets written is that binary data are compact and small compared to the same data in ASCII format. To be specific, the size of "`3.1415927`" is 9 bytes in ASCII (since there are 9 characters, including the period mark), while it is 4 bytes if written as a binary number in "single" precision (any number is always 4 bytes in single precision). Furthermore, the ASCII formatted files written by LS-DYNA have many delimiters and repeated text labels that considerably add to the overall size of the file. This is why LS-DYNA splits data in different ASCII files, while it combines them in the same binout file. To make certain data written to the binout, one can use `binary=2` in the `*database_<option>`, where `<option>` can be `matsum`, `nodout`, etc.

Finally, recall that the binout reader function converts all numeric data to the type "double". Hence, it is not recommended to store the returned `binin` structure as a replacement for the original binout file because, (assuming it was produced by LS-DYNA single-precision solver), the binout file will be (by far) smaller.

F.4 Source Code of the Matalb Function

The source code for the `binout` reader and the root `d3plot` control data reader functions have been made public and are published on `GitHub`.

The source code is available at the following `GitHub`'s `binout` repository:

`https://github.com/saudbinayed/binout`

and the direct link to the `GitHub`'s page of the Matalb's `get_binout_data.m` source code is:

`https://github.com/saudbinayed/binout/blob/master/src/get_binout_data.m`

The `GitHub` page includes adequate description and example of the code and its usage. Furthermore, the Matalb source code has, also, been published on the University of Sheffield's Online Research Data, `ORDA`, repository, and it can be accessed using:

`https://doi.org/10.15131/shef.data.26018836`

Appendix G

Illustration of the Solution Termination for a Rigid-Perfectly Plastic SDOF

G.1 Overview

The aim of the present material is to increase confidence on the importance of the concept of the solution termination strategy for a mechanical system that is rigid-perfectly plastic. Therefore, it is vital to focus on the most simple version of the problem without unneeded mathematical complexity. That is, the motion of a rigid-perfectly plastic single-degree-of-freedom (SDOF) system will be investigated. For further simplicity and direct relevance to the membrane problem, the SDOF will be assumed to be impulsively loaded.

G.2 Problem Definition

The SDOF is non-damped and consists of a mass, m, that is attached to a rigid-perfectly plastic spring, whose resistance force is R; the mass is subjected to an external force, F. The motion of the SDOF is uni-dimensional, and the mass has zero initial displacement, $x_0 = 0$, before the load application (or when the spring is undeformed). Therefore, the system's equation of motion is

$$m\ddot{x} + R = F \tag{G.2.1}$$

As mentioned, the spring is rigid-perfectly plastic. The resultant stress is the spring resistance force, R, and the corresponding (work-conjugate) strain measure (or resultant) is the displacement of the mass, x. Furthermore, the strain-rate resultant is, hence, the mass's velocity, $\dot{x}$. The yield condition (defining the onset of plasticity of the spring) can be written as

$$Y = |R| - R_y = 0, \tag{G.2.2}$$

where R_y is the yield limit, which is constant in tension and compression, and $|z|$ is the absolute value of z. Herein, Y is the relevant yield function. The spring is said to be rigid whenever $Y < 0$ (or when $-R_y < R < R_y$), and yielding can take place only when $Y = 0$; note that $Y \not> 0$.

Hence, assuming the spring's material obeys the classical associated flow rule, the increment of the resultant strain-rate is described by

$$\begin{aligned} \dot{x} &= \dot{\lambda}\frac{\partial}{\partial R}(Y) \\ &= \dot{\lambda}\frac{\partial}{\partial R}\left(|R| - R_y\right) \\ &= \dot{\lambda}\,\mathrm{sgn}\,(R) \\ \dot{\lambda} &\geq 0 \end{aligned} \tag{G.2.3}$$

in which, $\mathrm{sgn}\,(z)$ is the sign function which returns $+1$ when $z > 0$, -1 when $z < 0$, and 0 when $z = 0$; herein, the sign function is taken as the derivative of the absolute value function.

In the last set of equations, $\dot{\lambda}$ is the rate of plastic multiplier that is non-negative and must satisfy the following consistency condition

$$\begin{aligned} \dot{\lambda} &> 0 \quad \text{when} \quad Y = 0 \\ \dot{\lambda} &= 0 \quad \text{when} \quad Y < 0 \end{aligned} \tag{G.2.4}$$

As can be seen from Eqs. (G.2.3), a positive velocity, $\dot{x} > 0$, implies that $R = R_y$, and, likewise, when $\dot{x} < 0$ implies that $R = -R_y$. In addition, when $Y < 0$ (or equivalently when $|R| < R_y$), then $\dot{x} = 0$ since $\dot{\lambda} = 0$ because, in this case, that the yield condition is not satisfied. Moreover, it can be inferred that whenever $\dot{x}$ is non-zero (which corresponds to the satisfaction of the yield condition), the value of $\dot{\lambda}$ is the absolute value of $\dot{x}$; that is,

$$\dot{\lambda} = |\dot{x}| \quad \text{when } Y = 0, \tag{G.2.5}$$

otherwise, $\dot{\lambda} = 0$ if $Y < 0$.

Therefore, it can be deduced that the value of the resistance force, R, of the spring during its plastic flow can be taken as

$$R = R_y\,\mathrm{sgn}\,(\dot{x}) \tag{G.2.6}$$

since, again, $R = R_y$ implies $\dot{x} > 0$, and $R = -R_y$ implies $\dot{x} < 0$. Note that when $|R| < R_y$ (i.e., $Y < 0$) corresponds to a state of rigid spring so that the mass is not moving (i.e., its velocity and acceleration are zero). The value $(R_y\,\mathrm{sgn}\,(\dot{x}))$ is important, since it will, at all times, ensure that the rate of plastic work, $R\dot{x} = R_y\,\mathrm{sgn}\,(\dot{x})\dot{x} = R_y|\dot{x}|$, is non-negative since R_y is positive. When $|R| < R_y$, then no plastic flow occurs, i.e., $\dot{x} = 0$, and hence

the rate of plastic work is identically zero.

Consequently, substituting Eq. (G.2.6) into the equation of motion, Eq. (G.2.1), the latter takes the following form

$$m\ddot{x} + R_y \operatorname{sgn}(\dot{x}) = F \tag{G.2.7}$$

where R_y is a positive constant, and the equilibrium equation applies when $\dot{x} \neq 0$.

Next, to further simplify the discussion and makes the SDOF problem more relevant to the main work in the thesis, the external loading is assumed to be impulsive such that during the load application the SDOF is at rest. By the end of load application, the system acquires some non-zero initial velocity. Hence, the equilibrium equation becomes

$$m\ddot{x} + R_y \operatorname{sgn}(\dot{x}) = 0 \tag{G.2.8}$$

where motion is induced by the non-zero initial velocity, $\dot{x}_0$.

G.3 Solution

In general, the above equation is non-linear differential equation in time due to $\operatorname{sgn}(\dot{x})$. By the definition of the sign function, the value of $\operatorname{sgn}(\dot{x})$ can be 1, -1, or 0, depending on the sign of the instantaneous velocity, $\dot{x}$. The non-linear equation can be solved numerically to obtain the response (or motion) of a given system under prescribed initial velocity.

However, when the sign of the given initial velocity is known, e.g., positive, $\dot{x}_0 > 0$, then the non-linearity disappears temporarily. For such case, i.e., $\dot{x}_0 > 0$, one can arrive at the following equation

$$m\ddot{x} + R_y = 0 \tag{G.3.1}$$

as long as $\dot{x} > 0$. The solution of the above equation can, easily, be obtained by direct integration of $\ddot{x} = -R_y/m$. Namely, the velocity of the mass is

$$\dot{x} = \dot{x}_0 - \left(\frac{R_y}{m}\right) t \tag{G.3.2}$$

This (analytical) solution is valid as long as the condition that $\dot{x} > 0$ is not violated. Clearly, the critical time instant is when $\dot{x} = 0$ for the first time. Let such instant be denoted by t^*. It is given by

$$t^* = \frac{m\dot{x}_0}{R_y}. \tag{G.3.3}$$

Since the analytical solution of the instantaneous velocity, as given by Eq. (G.3.2), predicts that the velocity decreases (linearly) with time from the initial positive velocity, $\dot{x}_0$, beyond $t = t^*$, the current velocity would turn negative. Hence, the valid equilibrium equation would become $m\ddot{x} - R_y = 0$ (for $\dot{x} < 0$). In turn, the velocity solution, for $t \geq t^*$, becomes $\dot{x} = \dot{x}^* + (R_y/m)(t - t^*)$, where $\dot{x}^* \equiv \dot{x}(t = t^*)$. This latter solution is valid until $\dot{x} = 0$ for the first time beyond $t = t^*$, and let such new time instant denoted by t^{**}. Hence, t^{**} can

be determined by the following equation, $-\dot{x}^* = (R_y/m)(t^{**} - t^*)$. Since, by definition, $\dot{x}^* = 0$, then it is concluded that $t^{**} = t^*$; that is, the two critical time instants coincide with each other. Subsequently, $\dot{x} = 0 + (R_y/m)(t^* - t^*) = 0$. In other words, the system reached its final state, and there is no subsequent motion beyond the first occurrence of zero velocity, i.e., when $t = t^*$.

Alternatively, the same conclusion can be arrived at by recalling that the non-linear equilibrium equation, given in Eq. (G.2.8), also states that $R = 0$ at $t = t^*$ since $\dot{x} = \dot{x}^*$ is instantaneously zero; therefore, the instantaneous acceleration is zero, and the initial velocity at $t = t^*$ is zero. The overall effect is that the (SDOF) system ceases motion at and beyond the first critical time instant, $t = t^*$.

The response of the impulsively loaded SDOF is therefore

$$x(t) = \begin{cases} \dot{x}_0 t - \frac{1}{2}\frac{R_y}{m}t^2, & t < t^* \\ \frac{1}{2}\dot{x}_0 t^*, & t \geq t^* \end{cases} \tag{G.3.4}$$

G.4 Discussion

It is crucially important to note that the solution of $x(t) = \dot{x}_0 t - \frac{1}{2}\frac{R_y}{m}t^2$ is valid only conditionally; it holds, as shown above, until the time instant t^*. That is, the solution is terminated. The subsequent solution is held constant at $x = x(t^*) = \frac{1}{2}\dot{x}_0 t^*$. For the academic sake, the problem of an impulsively loaded and rigid-perfectly plastic SDOF is mathematically equivalent to the problem of a sliding block on frictional surface where the block is given an initial positive velocity and allowed to slide in the presence of a (constant) Coulomb friction force. The work done by the friction force, as the irreversible plastic work, is dissipative. The friction force is non-zero whenever the current velocity is non-zero; the yield force by the rigid-perfectly plastic spring in the SDOF is R_y only whenever the current velocity is non-zero and positive. In the two problems, the problem can be linearised and, easily, solved provided that the solution is terminated as soon as the current velocity becomes zero for the first time (beyond this time instant, the initial linearised problem is irrelevant, and a new linearisation should be established to account for the new sign of the current velocity).

Therefore, given an impulsively loaded SDOF with a non-zero initial velocity, the solution can be predicted analytically by simplifying the equation of motion based on the sign of the initial velocity. This solution, however, is valid as long as the underlying equilibrium equation is valid (with the assumed sign of the current velocity). The analytical solution is terminated whenever the equation of motion becomes invalid. In this simplified analysis of an impulsive SDOF system, the termination criterion is the first occurrence of zero current velocity. The solution termination is, further, predicted analytically by determining the critical time instant, t^*.

The starting equilibrium equation of the impulsive motion of the SDOF with positive

initial velocity, in Eq. (G.3.1), is assumed to hold under the assumed condition that the current velocity is and continues to be positive. This was done to linearise the equation of motion, see Eq. (G.2.8). The current velocity of the SDOF problem is the version of the strain-rate measure of the rigid-perfectly plastic spring; a non-zero current velocity, thus, is an assumption of active yielding of the spring. In the main text of the thesis concerns the motion of an impulsively loaded rigid-perfectly plastic membrane. The equation of motion of the membrane, developed therein, was linearised with a subsidiary condition that the membrane is under active yielding. Since the condition is anticipated to be violated at some time instant as motion evolves, then the developed equation of motion and the solution based on it were complemented by the suitable strategies to terminate the (conditional) solution. The termination strategies were introduced and addressed in Chapters 3, 4, and 5.

G.5 Systematic Derivation of the Non-Linear Equilibrium Equation of the SDOF

The non-linear equation of motion for the impulsive case, in Eq. (G.2.8), will be derived by simple application of the (rate of) virtual work principle, which states that

$$\delta W = R\delta\dot{x} + m\ddot{x}\delta\dot{x} = 0, \tag{G.5.1}$$

where the first term is the internal virtual work, and the second is the virtual work due to inertia. The latter will remain unaltered, and focus is made on the former. In the internal work, R is the spring force (which needs not satisfy the yield condition, $|R| = R_y$, although it cannot violate the yield inequality, $|R| \leq R_y$).

The flow rule was given earlier by $\dot{x} = \dot{\lambda}\,\mathrm{sgn}\,(R)$, see Eq. (G.2.3), and recall that the non-negative $\dot{\lambda}$ is non-zero only if $|R| = R_y$, i.e., when the yield condition is satisfied. Furthermore, $\dot{\lambda} = \sqrt{\dot{x}^2} = |\dot{x}|$, which is obtained by squaring both sides of the flow rule, and solving for $\dot{\lambda}$ while noting that $\dot{\lambda}$ is non-negative, and $[\mathrm{sgn}\,(R)]^2 = 1$ (when R is non-zero).

Therefore, the internal virtual work takes the form

$$\begin{aligned} R\delta\dot{x} &= R\,\mathrm{sgn}\,(R)\delta\dot{\lambda} \\ &= R\,\mathrm{sgn}\,(R)\delta(|\dot{x}|) \end{aligned} \tag{G.5.2}$$

In the above, note that $R\,\mathrm{sgn}\,(R)$ is, identically, $|R|$. Hence,

$$R\delta\dot{x} = |R|\delta(|\dot{x}|) \tag{G.5.3}$$

Now, since $\dot{\lambda}$ (and accordingly $|\dot{x}|$) can be non-zero only if $|R| = R_y$, then the internal

virtual work is

$$R\delta\dot{x} = R_y\delta(|\dot{x}|) \tag{G.5.4}$$

Note that if $R \neq R_y$, then $\delta\dot{\lambda} = \delta(|\dot{x}|) \equiv 0$.

The variation of $|\dot{x}|$ is

$$\begin{aligned}\delta(|\dot{x}|) &= \frac{\partial}{\partial\dot{x}}\left(|\dot{x}|\right)\delta\dot{x} \\ &= \operatorname{sgn}(\dot{x})\delta\dot{x}\end{aligned} \tag{G.5.5}$$

Using the above in the internal virtual work, one gets

$$R\delta\dot{x} = R_y \operatorname{sgn}(\dot{x})\delta\dot{x} \tag{G.5.6}$$

When the last expression is substituted into the total virtual work equation, it becomes

$$\delta W = R_y \operatorname{sgn}(\dot{x})\delta\dot{x} + m\ddot{x}\delta\dot{x} = 0, \tag{G.5.7}$$

or,

$$\left[R_y \operatorname{sgn}(\dot{x}) + m\ddot{x}\right]\delta\dot{x} = 0 \tag{G.5.8}$$

Then, when $\delta\dot{x}$ is made arbitrary, its coefficient vanishes, i.e.,

$$R_y \operatorname{sgn}(\dot{x}) + m\ddot{x} = 0 \tag{G.5.9}$$

The derivation is complete as the above is the equation of motion for an impulsively loaded rigid-perfectly plastic SDOF, as given in Eq. (G.2.8). Motion is induced by any arbitrary initial velocity, $\dot{x}_0$. This equation ensures that if plastic work rate takes place, it will be, at all times, non-negative. Again, this equation is non-linear due to the presence of $\operatorname{sgn}(\dot{x})$ in the first term of the left-hand side.